Journal of
Mechanics of Materials and Structures

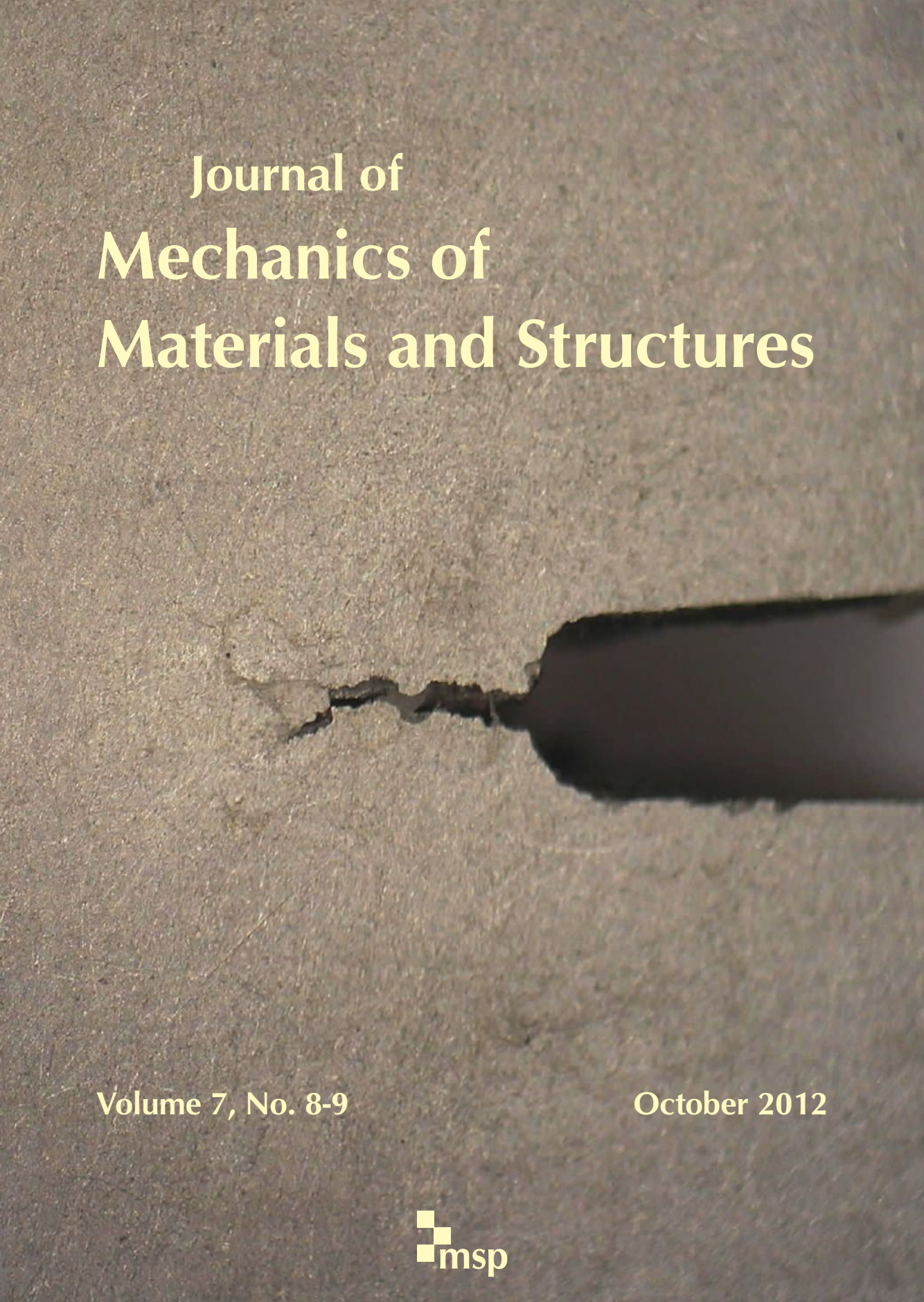

Volume 7, No. 8-9 October 2012

msp

JOURNAL OF MECHANICS OF MATERIALS AND STRUCTURES

jomms.net

Founded by Charles R. Steele and Marie-Louise Steele

See http://jomms.net for submission guidelines.

JoMMS (ISSN 1559-3959) is published in 10 issues a year. The subscription price for 2012 is US $555/year for the electronic version, and $735/year (+$60 shipping outside the US) for print and electronic. Subscriptions, requests for back issues, and changes of address should be sent to Mathematical Sciences Publishers, Department of Mathematics, University of California, Berkeley, CA 94720–3840.

JoMMS peer-review and production is managed by EditFLOW® from Mathematical Sciences Publishers.

PUBLISHED BY

mathematical sciences publishers

http://msp.org/

A NON-PROFIT CORPORATION

Typeset in LaTeX

JOURNAL OF MECHANICS OF MATERIALS AND STRUCTURES
Vol. 7, No. 8-9, 2012
dx.doi.org/10.2140/jomms.2012.7.735

msp

A MODEL FOR THE SHEAR DISPLACEMENT DISTRIBUTION OF A FLOW LINE IN THE ADIABATIC SHEAR BAND BASED ON GRADIENT-DEPENDENT PLASTICITY

XUE-BIN WANG AND BING MA

Based on second-order gradient-dependent plasticity (GDP), we establish the shear displacement distribution of material points of a flow line beyond the occurrence of the adiabatic shear band (ASB) at a position on a thin-walled tubular specimen in dynamic torsion. In the ASB, the shear displacements of a material point include two parts caused by homogeneous and inhomogeneous strain components, respectively. The former is assumed to be a linear function of the material point coordinate, while the latter is found to be a sinusoidal function of the coordinate due to the microstructural effect. For the Ti-6Al-4V alloy and two kinds of steels, the coefficients of the constant, linear, and nonlinear terms in the expression for the shear displacement distribution are determined by least-squares fitting for different widths and positions of the ASB. During the localized shear process, the coefficients of the linear and nonlinear terms are found to have increasing tendencies, while the deformed ASB width (which is larger than the width of the ASB central region) is slightly decreased. This investigation shows that second-order GDP may be successfully applied in simulation of the shear displacement distribution of material points at flow lines in the ASBs.

1. Introduction

Thin-walled tubular metal specimens, providing a homogeneous state of stress [Bai and Bodd 1992], are usually subjected to adiabatic shear failures in dynamic torsional experiments. Dynamic experiments can create a high enough strain rate in the tested materials that the condition for the occurrence of adiabatic shear bands (ASBs) is satisfied, that is, thermal softening outweighs plastic hardening. To observe the initiation and development of ASBs, many fine grid lines are deposited photographically on the outside surface of a specimen before experiments [Giovanola 1988; Marchand and Duffy 1988; Duffy and Chi 1992; Cho et al. 1993; Liao and Duffy 1998]. Initially, these lines are oriented parallel to the axis of the specimen; see Figure 1(a). During the deformation, high-speed photographs of grid lines are taken, in which the slopes of lines provide a measure of the shear strain distribution along the gage length; see Figure 1(b–d).

Marchand and Duffy [1988] conducted dynamic torsional experiments on steels, and concluded that the plastic straining process might be divided into three consecutive stages; see Figure 1(b–d). In the first stage, the grid lines incline but remain straight, which implies that shear deformation within the specimen is homogeneous. In the second stage, the grid lines become slightly curved, as in Figure 1(c), indicating inhomogeneous or localized deformation. Curved grid lines are usually called flow lines. In

Keywords: adiabatic shear band, shear displacement distribution, fitting least-squares method, gradient-dependent plasticity, Ti-6Al-4V, steel.

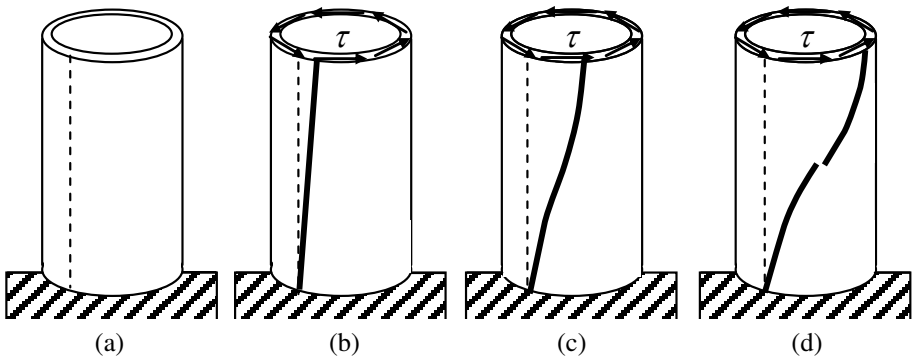

Figure 1. A thin-walled tube specimen without deformation (a), the uniform shear deformation in the elastic and strain-softening stages (b), the nonuniform deformational stage (c), and the discontinuous deformational stage (d). The dotted straight line is the initial grid line parallel to the axis of the specimen. The thick straight and curved lines are the curved flow lines, and τ is the shear stress acting on the sectional area of the specimen.

this stage, shear strain begins to concentrate first in a broad deformed ASB, and then, as deformation continues, becomes more localized until a narrow ASB is formed, marking the beginning of the third stage. In the third stage, flow lines appear discontinuous, as in Figure 1(d), indicating the formation of macroscopic fractures. ASBs are found to begin in the second stage, especially its later stage. Accordingly, the measured shear stress-nominal shear strain curve shows three distinct stages: a sharp rise in stress, followed by a long plateau, and then a steep drop in stress. In general, many kinds of steels and titanium alloys follow this process of deformation [Giovanola 1988; Marchand and Duffy 1988; Duffy and Chi 1992; Cho et al. 1993; Liao and Duffy 1998].

The nonlinear shear displacement distribution of material points at a flow line suggests that different points have different shear strains. Approximately, different material points may possess the same shear stress due to the use of a thin-walled tubular metal specimen. The phenomenon of the same shear stress corresponding to different shear strains cannot be uniquely described by classical continuum models where no internal length parameter is included, so that the nonuniform strain distribution and nonlinear displacement distribution in the localized zone, as well as the zone size, cannot be accurately obtained. Among the enriched continuum models, nonlocal and gradient continua have been widely used to avoid pathological localization in numerical simulation [De Borst and Mühlhaus 1992; Pamin and De Borst 1995; Askes et al. 2000; Menzel and Steinmann 2000; Peerlings et al. 2001; Simone et al. 2004; Voyiadjis and Abu Al-Rub 2005; Peerlings 2007; Poh et al. 2011], as have the Cosserat continuum and viscoplastic theories [Bažant and Pijaudier-Cabot 1988; Shawki and Clifton 1989]. In gradient continua, second-order gradient-dependent plasticity (GDP) is usually adopted, and a few analytical solutions of the strain and strain rate distribution in the localized band have been derived in the one-dimensional tensile and shear cases [De Borst and Mühlhaus 1992; Pamin and De Borst 1995; Menzel and Steinmann 2000]. However, a bilinear (linearly elastic and strain-softening) constitutive relation is used, and no plastic strain occurs within the specimen before strain localization. These assumptions are possibly even applicable for brittle materials, such as rocks, concretes, and ceramics, not just for metal materials, such as titanium alloys

and steels. For these metal materials in dynamic torsion, the measured shear stress-nominal shear strain curve enters a wide plateau stage prior to the localized shear deformation due to shear yield [Giovanola 1988; Marchand and Duffy 1988; Duffy and Chi 1992; Cho et al. 1993; Liao and Duffy 1998].

Assuming that the plastic shear strain corresponding to the ASB onset (also called *critical plastic shear strain*) is not zero, an expression for the local plastic shear strain in the ASB was derived for arbitrary strain-softening materials based on second-order GDP [Wang 2006a; 2006b]. This expression is an even more general formulation than expressions in [De Borst and Mühlhaus 1992; Pamin and De Borst 1995; Menzel and Steinmann 2000], applicable for metal materials. Introducing Johnson–Cook and Zerilli–Armstrong models in the expression, the shear strain, shear displacement, and temperature distribution in the ASB were studied for some metals and alloys in [Wang 2006a; 2006b; 2006c; 2007]. If the local temperature in the deformed ASB exceeds the transformation temperature, then a transformed ASB can appear at the central part of the deformed ASB. The transformed ASB thickness, local plastic shear strain, and shear displacement at interfaces between the deformed and transformed ASBs were investigated [Wang 2008]. The usually reported ASB width is the size of the ASB central region, rather than the total thickness of the deformed ASB. The ASB thickness at the central region was defined as the width of the region surrounding the ASB center over which the temperature differed from its peak value by less than 5% [Wang 2009], and effects of all parameters on the ASB thickness at the central region were studied. The peak and average temperatures in the ASB were calculated from the shear stress-average plastic shear strain curve of the ASB, which was back-calculated from the measured shear stress-nominal shear strain curve of the specimen [Wang 2010].

Based on second-order GDP, the aim of the present study is to discuss the applicability of an expression for the shear displacement distribution of material points at a flow line in dynamic torsion. Based on an expression for the local plastic shear strain in the ASB based on second-order GDP [Wang 2006a; 2006b; 2010], we proposed an expression for the local shear displacement around the ASB considering the following two assumptions: first, the plastic shear strain outside the ASB is treated as uniform, and does not change during the localized shear deformation; second, certain elastic shear strains are stored within the ASB and outside. After establishing the expression, for different widths and positions of the ASB, the experimental data about the shear displacement distribution and evolution with loading time or straining for three kinds of metal materials are fitted using least-squares methods. Among the candidate widths and positions of the ASB, the values minimizing the squared errors are believed to be true. The coefficients of the constant, linear, and sinusoidal terms in the expression are presented, together with their evolution with loading time or straining, and the deformed ASB widths.

2. Shear displacement distribution of a flow line

Before an ASB is initiated, the shear strain within a specimen in torsion can be seen as uniform. After the occurrence of the ASB, the shear strain within the specimen becomes nonuniform. At the ASB position, the local shear strain is higher and increases with straining, while outside the ASB, the local shear strain is relatively lower and approximately remains constant. Figure 2 shows an ideal model for the shear displacement distribution within the gage length after an ASB appears. The model includes three parts: one middle ASB, shown in part (b) of the figure, and two surrounding regions with uniform deformations, shown in parts (a) and (c).

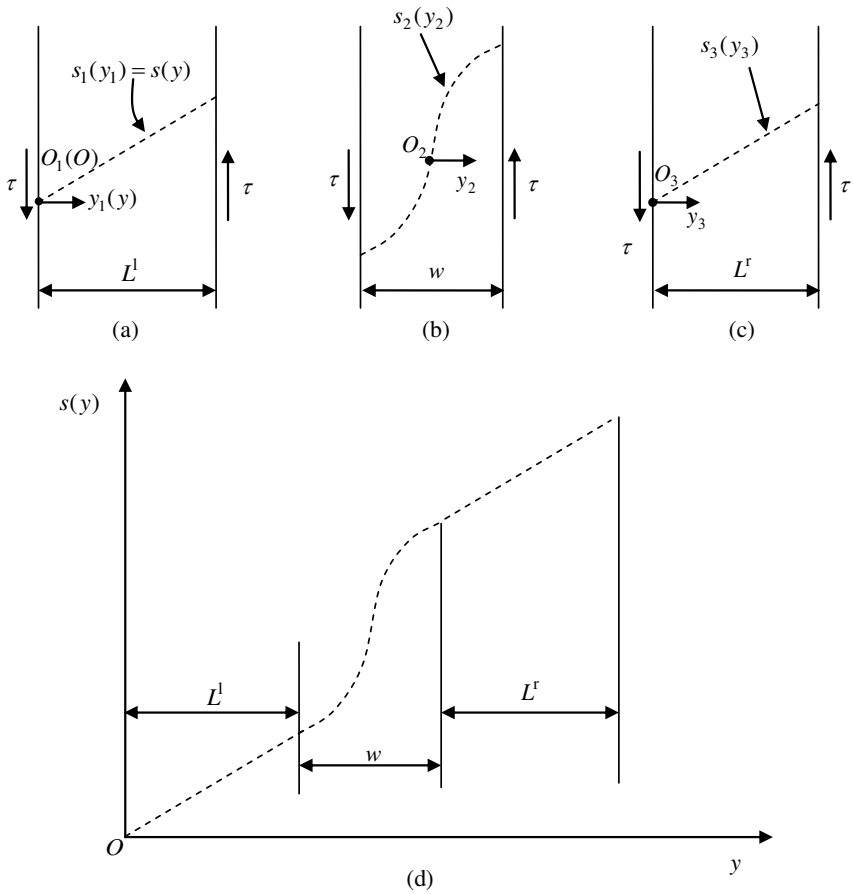

Figure 2. An ideal model for the shear displacement distribution of a flow line within the gage length: (a) the uniformly deformational region at the left side of the ASB, (b) the central deformed ASB, (c) the uniformly deformational region at the right side of the ASB, and (d) the continuous shear displacement distribution of material points at a flow line.

Based on second-order GDP, for a one-dimensional shear problem, an expression for the local plastic shear strain $\gamma_p(y)$ in the ASB was derived [Wang 2006a; 2006b; 2010]:

$$\gamma_p(y_2) = \gamma_c + (\bar{\gamma}_p - \gamma_c)\left(1 + \cos\frac{y_2}{l}\right), \tag{1}$$

where y_2 is the coordinate whose origin O_2 is set at the ASB center (Figure 2(b)); $\bar{\gamma}_p$ (also called the nonlocal plastic shear strain [Menzel and Steinmann 2000]) is the average plastic shear strain of the ASB, which is a variable dependent on the level of shear stress acting on the ASB during the localized shear process; γ_c is the critical plastic shear strain; and l is the internal length parameter in GDP, describing the effect of microstructures of heterogeneous metal materials. The critical plastic shear strain is referred to as the average plastic shear strain corresponding to the onset of the ASB. Prior to the occurrence of the

ASB, certain plastic shear strains have accumulated within metal materials. When the accumulated strain reaches the critical strain, then an ASB takes place. After the occurrence of the ASB, the accumulated strain is increased continuously. In GDP, the spatial gradient terms of plastic strain and their coefficients enter the yield function in order to describe interactions and interplay among microstructures [Askes et al. 2000; Peerlings et al. 2001]. The internal length parameter is believed to be related to the average grain diameter [Peerlings et al. 2001], defining the size of the localized band in numerical and analytical results. Otherwise, pathological numerical results will occur once standard continuum models are used in numerical models. For metal materials, such as Ti-6Al-4V alloy, grains ranged from 2–10 μm in diameter [Liao and Duffy 1998]. During shear deformation, grains can be rotated and elongated along the shear direction, and intense slip lines within grains are well-aligned with the shear direction, as found through transmission electron micrographs [Liao and Duffy 1998]. These observations suggest that interactions and interplay are more intense during the process of localized deformation, and must be taken into account.

Equation (1) is applicable for linear and nonlinear strain-softening cases at postpeak. Moreover, when strain localization is just initiated, the nonzero plastic shear strain accumulated within metal materials due to shear yield is permitted, that is, $\gamma_c > 0$. It is usually assumed that shear stress τ reaches its maximum $\tau_{\max}$ when the ASB just appears via instability analysis. In fact, (1) is also applicable for the case that the ASB appears beyond the peak stress. Rittel et al. [2006] argued that energy factors are the main criterion for the onset of ASB failure, while the strain or stress criterion applies in more restricted conditions.

For a one-dimensional shear problem, an expression for the local shear strain in the localized shear band was derived in [Menzel and Steinmann 2000]. It is only applicable for linear strain-softening materials at postpeak. Equation (1) can be seen as a generalization from this expression. Neglecting the plastic shear strain accumulated within the materials before the localized shear deformation, that is, $\gamma_c = 0$, (1) is simplified as

$$\gamma_p(y_2) = \bar{\gamma}_p\left(1 + \cos\frac{y_2}{l}\right). \tag{2}$$

This means that the localized shear is initiated just at the end of the linear elastic stage. For the linear strain-softening case at postpeak, $\bar{\gamma}_p$ is related to the shear stress difference $\tau_c - \tau$ and the softening modulus c (positive for strain-softening materials):

$$\bar{\gamma}_p = \frac{\tau_c - \tau}{c}. \tag{3}$$

In fact, (2) and (3) are identical to the expression in [Pamin and De Borst 1995]. Differentiating (2) on both sides with respect to time leads to

$$\dot{\gamma}_p(y_2) = -\frac{\dot{\tau}}{c}\left(1 + \cos\frac{y_2}{l}\right). \tag{4}$$

Equation (4) is identical to the result in [Pamin and De Borst 1995]. The derivation of (1) is similar to [De Borst and Mühlhaus 1992; Pamin and De Borst 1995; Menzel and Steinmann 2000]. In these studies, the shear band width w is

$$w = 2\pi l. \tag{5}$$

It is found from (1) that at the ASB's two boundaries ($y_2 = \pm w/2$), $\gamma_p(\pm w/2) = \gamma_c$, while at its center ($y_2 = 0$), $\gamma_p(0) = \gamma_c + 2(\bar{\gamma}_p - \gamma_c)$. At this position, the local plastic shear strain reaches its maximum. Therefore, the plastic shear strain distribution in the ASB is nonuniform. The value of γ_c may be specific for a material if the strain rate and ambient temperature are known. During the localized deformational process, $\bar{\gamma}_p$ ($\bar{\gamma}_p \geq \gamma_c$) is increased with straining. Thus, the profile of the local plastic shear strain becomes steeper until a final fracture occurs.

Herein, differentiating (1) one time with respect to the coordinate y_2 results in

$$\frac{d\gamma_p(y_2)}{dy_2} = -\frac{\bar{\gamma}_p - \gamma_c}{l} \sin \frac{y_2}{l}. \tag{6}$$

Differentiating (6) leads to

$$\frac{d^2\gamma_p(y_2)}{dy_2^2} = -\frac{\bar{\gamma}_p - \gamma_c}{l^2} \cos \frac{y_2}{l}. \tag{7}$$

Thus, using (1) and (7), we have

$$\gamma_p(y_2) + l^2 \frac{d^2\gamma_p(y_2)}{dy_2^2} = \bar{\gamma}_p. \tag{8}$$

In fact, (8) is a special case of (explicit) GDP [Peerlings et al. 2001], that is, one-dimensional GDP in simple shear. Equation (8) establishes a relation between the local $\gamma_p(y_2)$ and nonlocal $\bar{\gamma}_p$ variables. The nonlocal variable is related to the shear stress, which is the plastic shear strain in the context of classical elastoplastic theories. When the nonlocal variable $\bar{\gamma}_p$ and the critical plastic shear strain γ_c are specific, different material points will have different local plastic shear strains, and a unique solution can be ensured. Averaging these local plastic shear strains over the entire ASB will lead to the nonlocal plastic shear strain, as can be easily confirmed through integrating (1) with respect to the coordinate y_2 ($\int_{-w/2}^{w/2} \gamma_p(y_2)\, dy_2$), and then divided by the ASB width. For two and three-dimensional cases, the Laplacian will appear in GDP [Askes et al. 2000; Peerlings et al. 2001; Simone et al. 2004; Voyiadjis and Abu Al-Rub 2005; Peerlings 2007; Poh et al. 2011]. GDP can be derived from the nonlocal theory [Askes et al. 2000; Peerlings et al. 2001] by expanding the plastic strain into a Taylor series, and by neglecting gradient terms of order four and higher.

Integrating (1) with respect to the coordinate y_2, the local plastic shear displacement $s_p(y_2)$ in the ASB can be obtained:

$$s_p(y_2) = \int_0^{y_2} \gamma_p(y_2)\, dy_2 = \bar{\gamma}_p y_2 + l(\bar{\gamma}_p - \gamma_c) \sin \frac{y_2}{l}. \tag{9}$$

Equation (9) describes the relative shear displacements of different material points in the y_2 direction with respect to the origin O_2. Evolution of shear displacements of different material points on the outside surface of a specimen can be measured through high-speed photography of a grid pattern previously printed on the specimen's outer surface [Giovanola 1988; Marchand and Duffy 1988; Duffy and Chi 1992; Cho et al. 1993; Liao and Duffy 1998]. Initially, fine lines are oriented parallel to the axis of the specimen; then, during the deformation, the slopes of lines will change, providing a measure of the local shear strain distribution along the axis of the specimen. Curved flow lines describe the local deformational characteristics within the entire gage section, not only within the ASB; see Figure 2(d).

During the deformational process, certain recoverable elastic shear strains γ^e will be stored within the specimen. These parts of the strains can be seen as uniform. Thus, the total shear displacement $s_2(y_2)$ in the ASB can be expressed as

$$s_2(y_2) = s_p(y_2) + s^e = (\bar{\gamma}_p + \gamma^e)y_2 + l(\bar{\gamma}_p - \gamma_c)\sin\frac{y_2}{l}, \tag{10}$$

where s^e is the elastic shear displacement caused by γ^e.

For the sake of simplicity, the plastic shear strain outside the ASB can be also treated as uniform, equal to γ_c. This suggests that it no longer increases during the localized shear process. Thus, the relative shear displacements with respect to origins O_1 and O_3 in two uniformly deformational regions — see Figure 2(a, c) — can be given by

$$s_1(y_1) = (\gamma_c + \gamma^e)y_1, \tag{11}$$

$$s_3(y_3) = (\gamma_c + \gamma^e)y_3, \tag{12}$$

where $y_1 \in [0, L^l]$, $y_3 \in [0, L^r]$, and L^l and L^r are the sizes of the uniformly deformational regions on the left and right sides of the ASB, respectively. A coordinate transformation is introduced to replace y_2 and y_3 with y_1. Let $y_1 = y$ whose origin O is also set at O_1. Thus, we have

$$y_2 = y - \frac{w}{2} - L^l, \quad y_3 = y - w - L^l. \tag{13}$$

For $y \in [0, L^l]$, the local shear displacement $s(y)$ relative to the origin O according to (11) is

$$s(y) = (\gamma_c + \gamma^e)y. \tag{14}$$

When $y \in [L^l, L^l + w]$, $s(y) = s(L^l) + s_2(y_2) + (\bar{\gamma}_p + \gamma^e)w/2$. Thus, $s(y)$ can be written as

$$s(y) = (\gamma_c + \gamma^e)L^l + (\bar{\gamma}_p + \gamma^e)(y - L^l) + l(\bar{\gamma}_p - \gamma_c)\sin\frac{y - w/2 - L^l}{l}. \tag{15}$$

Apparently, when $y = L^l$, $s(L^l) = (\gamma_c + \gamma^e)L^l$; when $y = L^l + w$, $s(L^l + w) = (\gamma_c + \gamma^e)L^l + (\bar{\gamma}_p + \gamma^e)w$. When $y \in [L^l + w, L^l + L^r + w]$, we have

$$s(y) = (\gamma_c + \gamma^e)L^l + (\bar{\gamma}_p + \gamma^e)w + (\gamma_c + \gamma^e)(y - L^l - w). \tag{16}$$

It can be found from (14)–(16) that at the outside of the ASB, the local shear displacement is a linear function of the coordinate y, and that at the position of the ASB, it is a nonlinear function. The coefficients of the constant, linear, and nonlinear terms are not easy to determine mainly due to the geometrically inhomogeneous deformation defects and inertial effect. Therefore, these coefficients require a fitting.

3. Fitting least-squares method

Four flow lines (#1–#4) in Table 1 are selected for fitting. All tests are conducted under dynamic torsional conditions by use of a torsional split Hopkinson bar [Giovanola 1988; Marchand and Duffy 1988; Cho et al. 1993; Liao and Duffy 1998]. Only high-speed photographs of the grid pattern taken during the formation of the ASB are presented in [Marchand and Duffy 1988; Cho et al. 1993; Liao and Duffy 1998]. However, a time sequence of the shear displacement profiles has been provided [Giovanola 1988]. These profiles are obtained by digitizing a flow line in high-speed photographs, and then smoothing the

Flow lines	Material	Nominal strain rate	Stress or strain state	Flow line data origin
#1	4340 steel	$6000\,s^{-1}$	After strain localization from 45–52.5 μs	[Giovanola 1988, Figure 4]
#2	Ti-6Al-4V	$1100\,s^{-1}$	Before rapid stress drop for frames #1–#4	Frames #1–#5 in [Liao and Duffy 1998, Figure 5]
#3	HY-100 steel	$1200\,s^{-1}$	Prior to the stress peak for frame #4	Frames #4 and #5 in [Cho et al. 1993, Figures 1 and 2]
#4	HY-100 steel	$1600\,s^{-1}$	After the stress peak	Frames "camera #2" and "camera #3" in [Marchand and Duffy 1988, Figure 14]

Table 1. Selected four flow lines from dynamic torsional tests.

digitized records. In order to obtain the relative shear displacements of different material points at the other three flow lines (#2–#4), we use a method similar to [Giovanola 1988]. The three flow lines in high-speed photographs [Marchand and Duffy 1988; Cho et al. 1993; Liao and Duffy 1998] in the present work are marked in Figure 3. In Figure 3(a), taken from [Liao and Duffy 1998], in Figure 3(b), taken from [Cho et al. 1993], and in Figure 3(c), taken from [Marchand and Duffy 1988], there exist many flow lines. In the present work, only the results for a typical flow line in each figure are presented since selecting different flow lines from a figure results in the basically same results. For different frames in the same figure, data points on the same flow line are considered.

For the sake of simplicity, only a portion of the material points with the same horizontal spacing at each flow line is selected. Let the number of the selected material points be N_0. The leftmost material point is the first point. During the dynamic torsion, a short thin-walled tubular specimen is sandwiched between two long elastic bars, called the input bar and output bar. Near the loading ends, the stress and strain within the specimen is quite complex, possibly deviating from the simple pure shear state. Therefore, the data from material points near the two ends must be omitted in fitting. The remaining data will be fitted, and the total number of fitted data points is $N = N_0 - N_0^l - N_0^r$, where N_0^l and N_0^r are the numbers of omitted data points near the left and right ends of the specimen, respectively. Those data points, deviating from the slopes of the grid lines of the uniformly deformational regions outside the ASB, are omitted. Thus, the values of N_0^l and N_0^r can be determined easily.

These fitted data can be divided into three groups. The number of data points in the groups is denoted by N_1, N_2, and N_3, respectively. The first group is from the (N_0^l+1)-th to the $(N_0^l+N_1)$-th data point; the second from the $(N_0^l+N_1)$-th to the $(N_0^l+N_1+N_2-1)$-th; and the third from the $(N_0^l+N_1+N_2-1)$-th to the $(N_0^l+N_1+N_2+N_3-2)$-th. For the first and third groups, the line-fitting least-squares method is used, while for the second the curve-fitting least-squares method is used.

The extracted position and corresponding relative shear displacement of a material point is expressed as (y_i, d_i), $i = N_0^l + 1, N_0^l + 2, \ldots, N_0^l + N$. For the first group data, no special requirement on the theoretical expression (14) is enforced in fitting:

$$s(y, c_{11}, c_{12}) = c_{11} + c_{12}y. \tag{17}$$

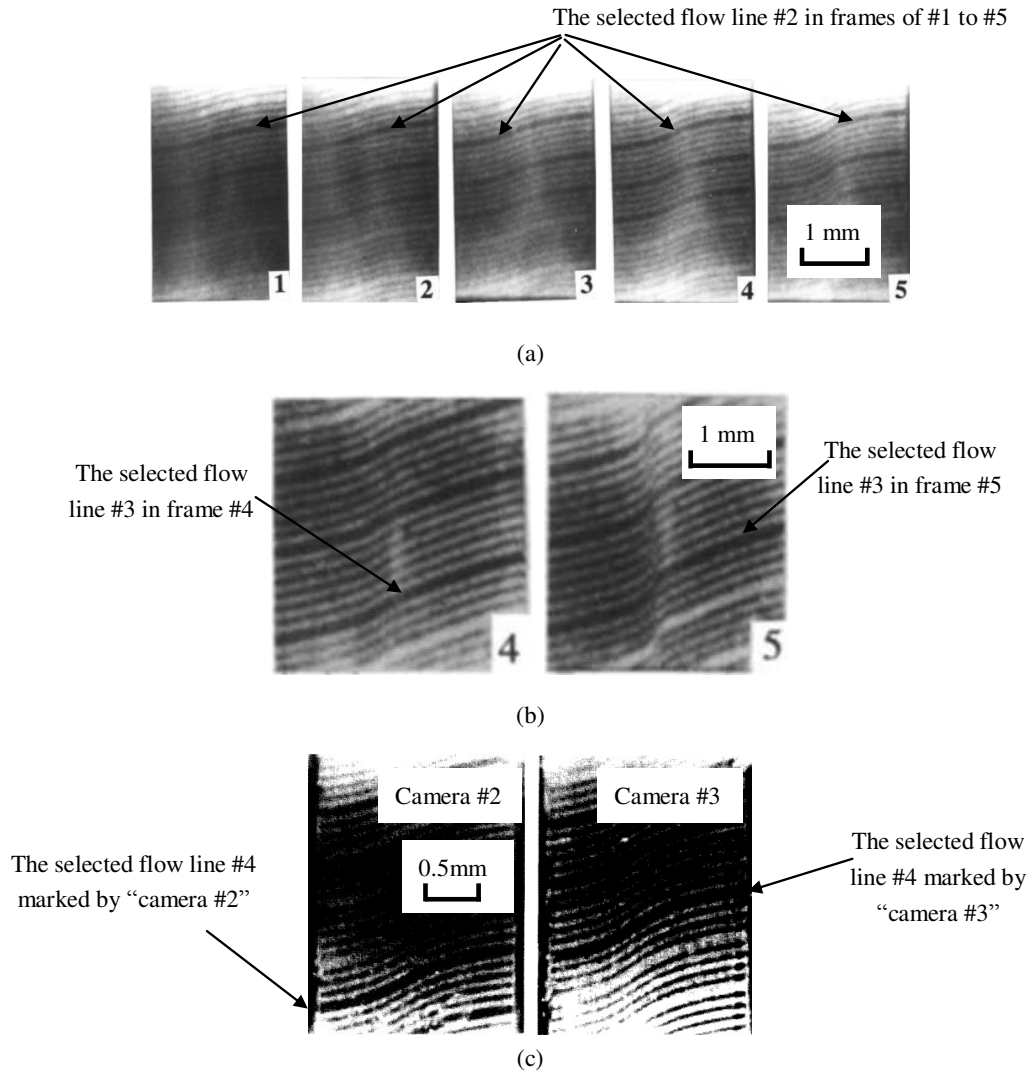

Figure 3. Selected flow lines from which coordinates and corresponding shear displacements are extracted: (a) the evolution of flow line #2 with straining for Ti-6Al-4V [Liao and Duffy 1998], (b) the evolution of flow line #3 with straining for HY-100 steel [Cho et al. 1993], and (c) flow line #4 in photographs taken at different positions using different cameras for HY-100 steel [Marchand and Duffy 1988].

For the second group data, it is required that the point $(y_{N_0^l+N_1}, d_{N_0^l+N_1})$ is at the theoretical curve, that is, (15), when $y = L^l$:

$$s(y, c_{21}, c_{22}) = d_{N_0^l+N_1} + c_{21}(y - L^l) + c_{22} \sin \frac{y - w/2 - L^l}{l}. \tag{18}$$

Similarly to the first group data, no special requirement is imposed on the theoretical expression, that

is, (16), for the third group data in fitting:

$$s(y, c_{31}, c_{32}) = c_{31} + c_{32}(y - L^l - w). \tag{19}$$

For the known N_1, N_2, and N_3 (or N_1, N_2, and N), using the fitting least-squares method results in values of c_{11}, c_{12}, c_{21}, c_{22}, c_{31}, and c_{32}. These values minimize the sum of the squared errors ($R_1^2 + R_2^2 + R_3^2$, R_1^2, R_2^2, and R_3^2 are the squared errors in the three groups of fitted data):

$$J_0 = \min(R_1^2 + R_2^2 + R_3^2) = \min\Big\{ \sum_{i=N_0^l+1}^{N_0^l+N_1} [d_i - s(y_i, c_{11}, c_{12})]^2 + \sum_{i=N_0^l+N_1}^{N_0^l+N_1+N_2-1} [d_i - s(y_i, c_{21}, c_{22})]^2 + \sum_{i=N_0^l+N_1+N_2-1}^{N_0^l+N} [d_i - s(y_i, c_{31}, c_{32})]^2 \Big\}. \tag{20}$$

For the given N, and different N_1 and N_2, the value of J_0 will be different. It is assumed that the true values of c_{11}, c_{12}, c_{21}, c_{22}, c_{31}, and c_{32} minimize J_0:

$$J = \min J_0. \tag{21}$$

During the search process, the ranges of N_1 and N_2 need to be specified. Thus, J_0 will be a spatially curved surface whose height is dependent on the values of N_1 and N_2. Finding a global minimum J_0 is easy. After that, the corresponding values of N_1 and N_2 are known. Thus c_{11}, c_{12}, c_{21}, c_{22}, c_{31}, and c_{32} will be specific, and the ASB width will also be obtained, which is only dependent on the data number N_2 in the second group, and the horizontal distance Δh of two adjacent data points. The ASB width w is then expressed as

$$w = (N_2 - 1)\Delta h. \tag{22}$$

Using (5), the internal length parameter will be obtained:

$$l = (N_2 - 1)\Delta h/2\pi. \tag{23}$$

Table 2 shows the selected parameters (N, N_0, N_0^l, N_0^r, and Δh) and obtained results (N_1, N_2, c_{12}, c_{21}, c_{22}, c_{32}, and w) corresponding to the minimum J_0. It is found that c_{21} and c_{22} have an increasing tendency with time (for flow line #1) and frame number (for flow lines of #2 and #3). The values of c_{11} (small enough) and c_{31} are not presented in Table 2 since the two parameters are independent of strain, that is, the slope of the local shear displacement. During the shear localization, the ASB width is found to become narrow or thin. Using the gradient plasticity theory with a variable length scale parameter, Voyiadjis and Abu Al-Rub [2005] argued that the length scale parameter should not be seen as a constant, and decreases with an increase of the plastic deformation. This finding is in agreement with the present work. Physically, the occurrence of highly elongated and fine grains, parallel to the shear direction due to the severe plastic shear deformation, is responsible for this phenomenon. Figures 4–7 show comparisons between the measured results and the best theoretical results with the obtained parameters after fitting listed in Table 2. Displacements of material points are relative to the first material point (the leftmost material point among the selected material points). The omitted material points outside the uniformly deformational regions and corresponding shear displacements are not depicted in Figures 4–7. The best

	Flow line #1			
Loading time =	45 μs	47.5 μs	50 μs	52.5 μs
N_0	76	76	76	76
N	43	43	43	43
N_0^l	17	17	17	17
N_0^r	17	17	17	17
$\Delta h/10^{-5}$ m	2.0	2.0	2.0	2.0
$J/10^{-10}$ m^2	0.1	0.2	1.2	7.6
N_1	17	17	17	19
N_2	10	9	9	4
c_{12}	0.127	0.130	0.138	0.147
c_{21}	0.241	0.457	0.830	2.565
$c_{22}/10^{-6}$ m	0.33	8.35	21.12	32.21
c_{32}	0.175	0.180	0.192	0.237
$w/10^{-4}$ m	2.0	1.8	1.8	0.8

	Flow line #2					Flow line #3		Flow line #4	
	Frame #1	Fr. #2	Fr. #3	Fr. #4	Fr. #5	Fr. #4	Fr. #5	Camera #2	Cam. #3
N_0	41	41	41	41	41	46	43	43	43
N	36	36	36	36	36	45	42	42	42
N_0^l	4	4	4	4	4	1	1	1	1
N_0^r	2	2	2	2	2	1	1	1	1
$\Delta h/10^{-5}$ m	4.9	4.9	4.9	4.9	4.9	6.2	6.7	4.3	4.3
$J/10^{-10}$ m^2	1.4	3.0	2.7	4.8	6.7	15.3	24.1	7.0	5.0
N_1	6	8	6	9	4	14	14	9	8
N_2	21	21	20	18	23	12	9	21	20
c_{12}	0.167	0.167	0.157	0.190	0.167	0.274	0.274	0.211	0.191
c_{21}	0.278	0.297	0.332	0.410	0.418	0.495	0.858	0.409	0.509
$c_{22}/10^{-6}$ m	5.59	4.60	8.37	8.01	33.05	12.67	57.28	22.23	19.18
c_{32}	0.162	0.160	0.183	0.167	0.177	0.334	0.385	0.204	0.208
$w/10^{-4}$ m	10	10	9.8	8.8	11	7.5	6.0	9.1	8.6

Table 2. Parameters used in fitting least-squares methods and fitted results for four flow lines.

theoretical results correspond to the minimum J_0. It is found that the agreement between the two kinds of results is good. This means that the second-order plastic strain gradient plays an important role in the postlocalization deformational stage of metal materials. The displacement distribution of a flow line in the deformed ASB can be described accurately by the linear and sinusoidal terms with respect to the material point coordinate beside a constant term.

It is also found that shear strains (c_{12} and c_{32}) in uniformly deformational bodies outside the ASB are slightly different. The wall thickness of the specimen, showing small variations along the length of the specimen [Liao and Duffy 1998], can be the reason for this phenomenon.

The calculated ASB width is usually larger than reported results [Giovanola 1988; Marchand and Duffy 1988; Cho et al. 1993; Liao and Duffy 1998]. In fact, the calculated width is the width of the

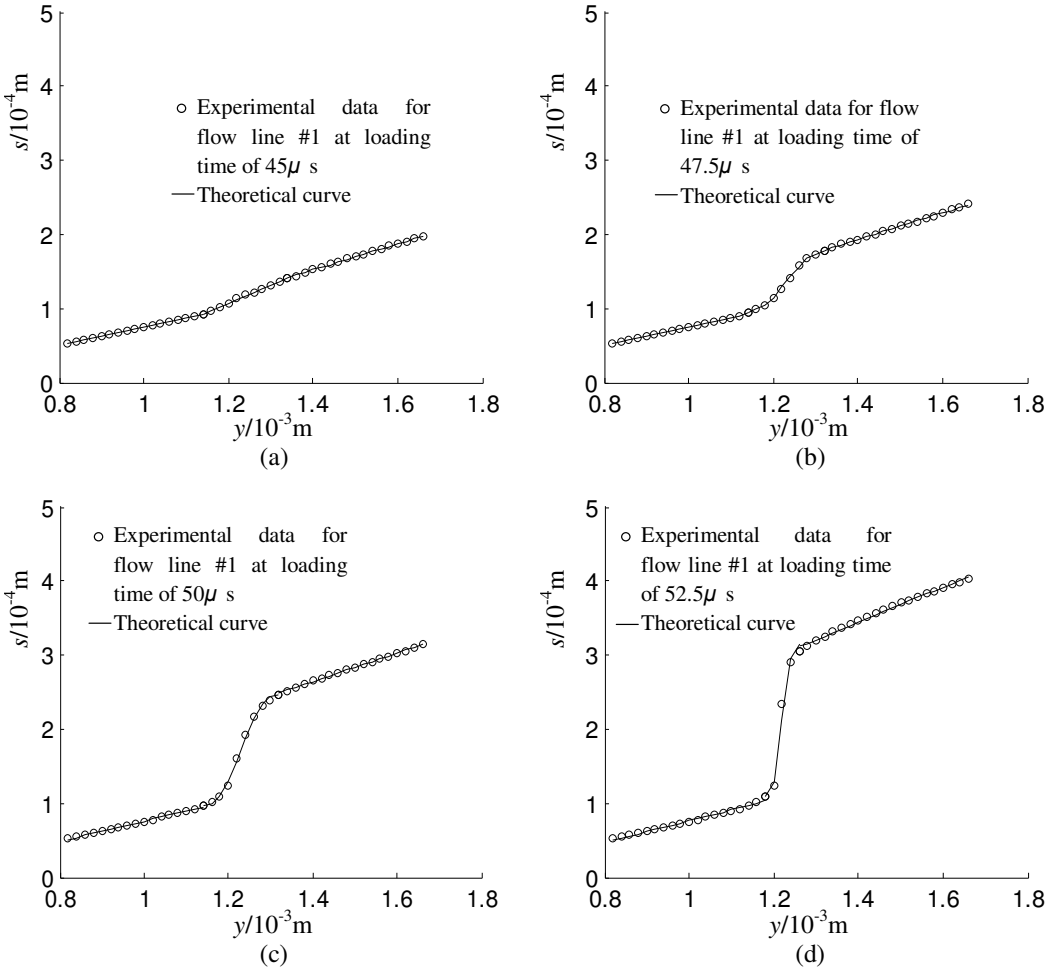

Figure 4. Comparisons of the measured shear displacements of material points at flow line #1 with loading time for 4340 steel [Giovanola 1988], and the fitted theoretical results based on second-order GDP with best parameters.

region with nonuniform strains, that is, the width of the deformed ASB. However, the reported width is usually the width of the ASB at its central region, over which the shear strain remains constant [Giovanola 1988; Marchand and Duffy 1988; Cho et al. 1993; Liao and Duffy 1998].

As mentioned before, theoretically, the critical plastic shear strain γ_c may be a constant for a flow line during the localized shear process. When the plastic shear strain within the specimen reaches γ_c, shear localization is assumed to occur. From (15) and (18), we can obtain the following expression:

$$c_{21} = \bar{\gamma}_p + \gamma^e, \quad c_{22} = l(\bar{\gamma}_p - \gamma_c), \tag{24}$$

$$\gamma_c = c_{21} - \frac{c_{22}}{l} - \gamma^e. \tag{25}$$

If the static shear Hooke's law ($\gamma^e = \tau/G$, where G is the shear elastic modulus that is the slope of the measured shear stress-nominal shear strain curve prior to the yield plateau) is used, then it is found that

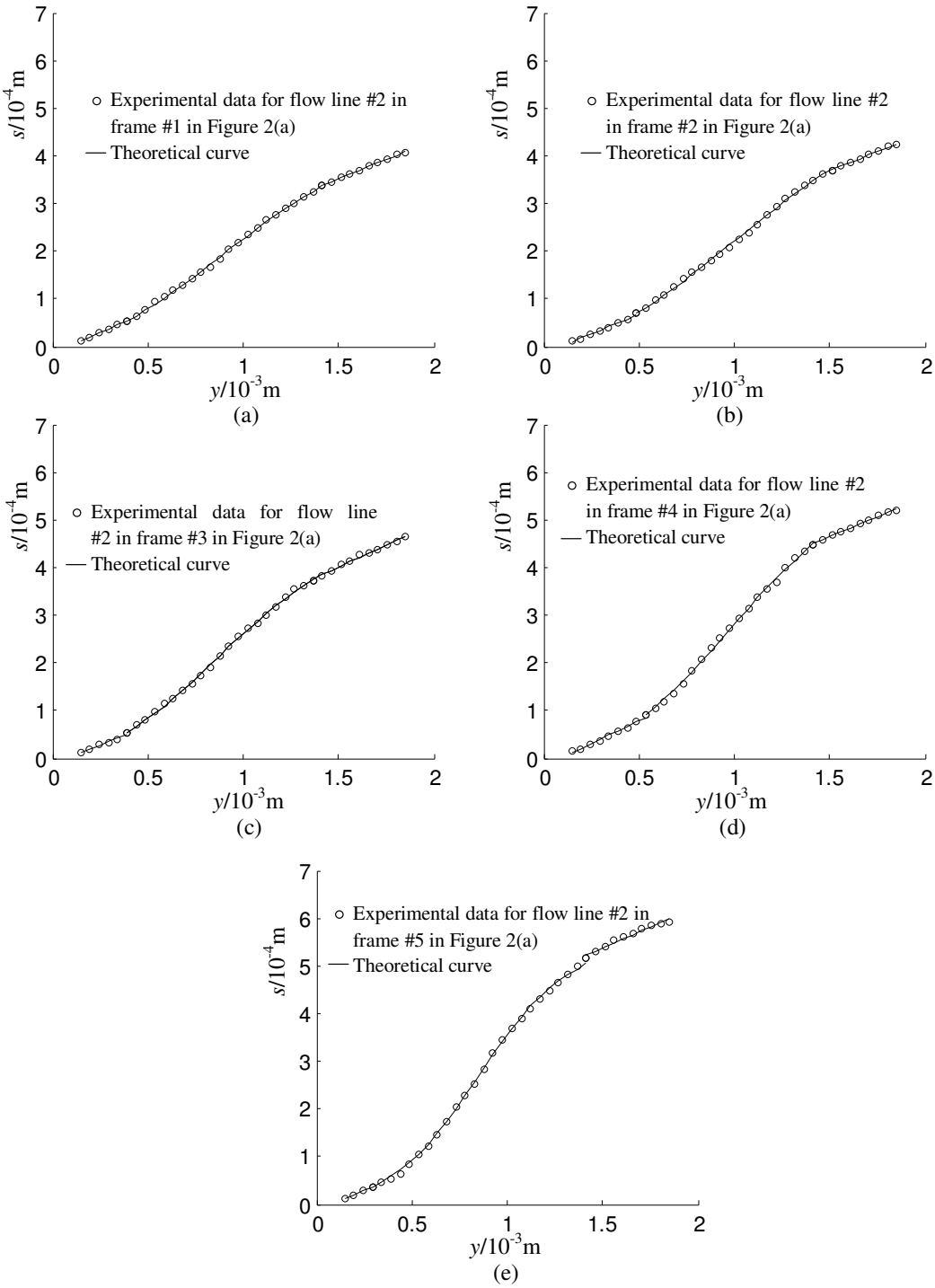

Figure 5. Comparisons of the measured shear displacements of material points at flow line #2 with straining for Ti-6Al-4V [Liao and Duffy 1998], and the fitted theoretical results based on second-order GDP with best parameters.

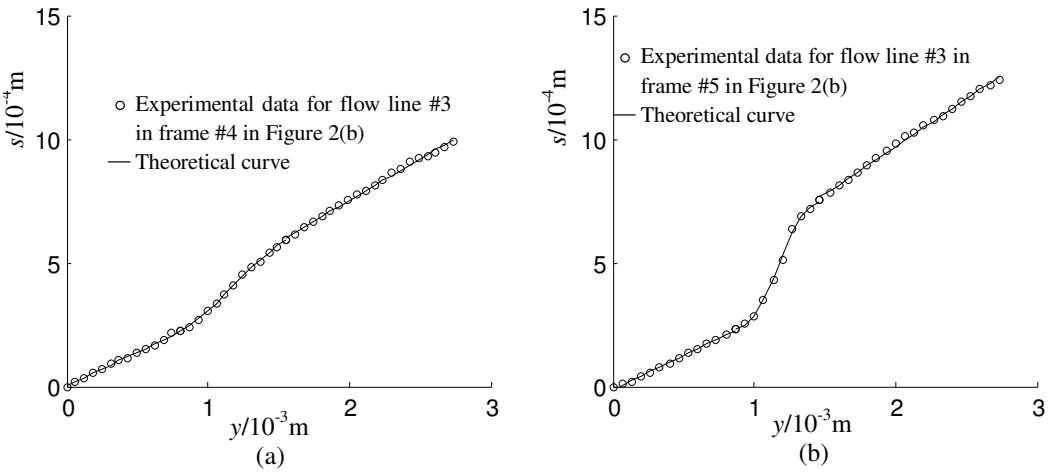

Figure 6. Comparisons of the measured shear displacements of material points at flow line #3 with straining for HY-100 steel [Cho et al. 1993], and the fitted theoretical results based on second-order GDP with best parameters.

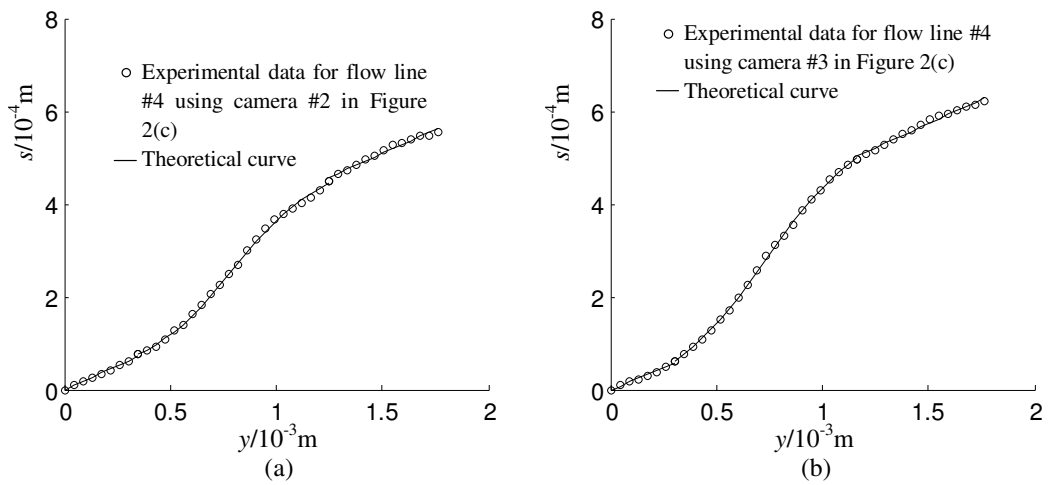

Figure 7. Comparisons of the measured shear displacements of material points at flow line #4 for HY-100 steel at the same time using different cameras [Marchand and Duffy 1988], and the fitted theoretical results based on second-order GDP with best parameters.

the calculated values of γ_c are variant using the obtained values of parameters (c_{21}, c_{22}, N_2, and Δh), the measured shear stress τ, and the shear elastic modulus G. The reason for this is still unclear. Seemingly, the static shear Hooke's law should not be used. An inertial effect must exist in dynamic torsional tests, possibly leading to a nonuniform shear stress distribution within the specimen to some extent. On the other hand, local perturbation (such as a microstructural inhomogeneity or machining marks) [Giovanola 1988] also possibly results in the nonuniform shear stress, even before shear localization. Even shear localization is initiated at postpeak, not at the highest shear strain within the specimen [Giovanola 1988].

Geometric defects have a key influence on the ASB initiation [Liao and Duffy 1998]. These factors are difficult to take into account in analyses. Obtaining a constant γ_c will require further investigation.

Damage during the shear yield process and beyond, and local rapid temperature rise in the ASB and the following heat conduct, possibly increase the plastic shear strain and displacement of material points. Thus, the expressions for c_{21} and c_{22} can be different from those in (24). The present expression is limited to the conditions without the damage and heat conduct. An analytical expression considering these factors is quite necessary.

4. Conclusions

During shear localization, the thin-walled tubular specimen within the gage length in dynamic torsion is simplified into three parts: two uniformly deformational regions surrounding the adiabatic shear band (ASB) and a central localized deformational region. Deformations in these regions are treated as one-dimensional shear problems. A linear distribution is assumed for the shear displacements of material points outside the ASB at a flow line. For arbitrary strain-softening materials in which certain plastic shear strains have accumulated before the ASB initiation, an expression for the shear displacement distribution in the ASB is established based on second-order gradient-dependent plasticity (GDP) considering the microstructural effect, including the linear and nonlinear (sinusoidal) terms with respect to the material point coordinate as well as a constant term.

To obtain the coefficients of the constant, linear, and nonlinear terms, which are not easy to determine due to the influence of geometric defects, line and curve-fitting least-squares methods are used for data in the uniform and localized deformational regions, respectively. For three kinds of materials, results show that the agreement between the measured shear displacements of flow lines using high-speed photography and the theoretical results is good. Moreover, the coefficients of the linear and sinusoidal terms with respect to the material point coordinate basically increase with loading time or straining during the shear localization process, while the ASB width has a decreasing tendency. The agreement suggests that second-order GDP is suitable for measuring the relative shear displacement distribution of flow lines in the ASBs.

If various parameters are known, flow lines can be numerically calculated by use of finite-element methods where enriched continuum models are necessarily included, avoiding pathological mesh sensitivity. However, these parameters are possibly difficult to specify. Using the proposed analytical expression for the local shear displacement in the ASB and outside, under the condition of unknown parameters, these parameters, such as the width of the ASB, and the critical plastic shear strain corresponding to the onset of the localized deformation, can be determined together by fitting with experimental observations. The fitted width of the ASB is apparently higher than the experimentally reported value. If the parameters obtained through fitting are used in the gradient-enhanced finite-element methods, then more accurate numerical results can be expected.

Acknowledgement

We are grateful to two anonymous reviewers for their helpful comments and suggestions in improving the manuscript. This work was supported by the Doctor Startup Foundation of Liaoning Province, China, No. 20081102, and supported by the Program for Liaoning Excellent Talents in University (LJQ2011030).

References

[Askes et al. 2000] H. Askes, J. Pamin, and R. De Borst, "Dispersion analysis and element-free Galerkin solutions of second- and fourth-order gradient-enhanced damage models", *Int. J. Numer. Methods Eng.* **49** (2000), 811–832.

[Bai and Bodd 1992] Y. Bai and B. Bodd, *Adiabatic shear localization: occurrence, theories and applications*, Pergamon Press, Oxford, 1992.

[Bažant and Pijaudier-Cabot 1988] Z. P. Bažant and G. Pijaudier-Cabot, "Nonlocal continuum damage, localization instability and convergence", *J. Appl. Mech.* (*ASME*) **55** (1988), 287–293.

[Cho et al. 1993] K. M. Cho, S. Lee, S. R. Nutt, and J. Duffy, "Adiabatic shear band formation during dynamic torsional deformation of an HY-100 steel", *Acta Metall. Mater.* **41** (1993), 923–932.

[De Borst and Mühlhaus 1992] R. De Borst and H. B. Mühlhaus, "Gradient-dependent plasticity: formulation and algorithmic aspects", *Int. J. Numer. Methods Eng.* **35** (1992), 521–539.

[Duffy and Chi 1992] J. Duffy and Y. C. Chi, "On the measurement of local strain and temperature during the formation of adiabatic shear bands", *Mater. Sci. Eng. A* **157** (1992), 195–210.

[Giovanola 1988] J. H. Giovanola, "Adiabatic shear banding under pure shear loading, I: Direct observation of strain localization and energy dissipation measurements", *Mech. Mater.* **7** (1988), 59–72.

[Liao and Duffy 1998] S. C. Liao and J. Duffy, "Adiabatic shear bands in a Ti-6Al-4V titanium alloy", *J. Mech. Phys. Solids* **46** (1998), 2201–2231.

[Marchand and Duffy 1988] A. Marchand and J. Duffy, "An experimental study of the formation process of adiabatic shear bands in a structural steel", *J. Mech. Phys. Solids* **36** (1988), 251–283.

[Menzel and Steinmann 2000] A. Menzel and P. Steinmann, "On the continuum formulation of higher gradient plasticity for single and polycrystals", *J. Mech. Phys. Solids* **48**:8 (2000), 1777–1796.

[Pamin and De Borst 1995] J. Pamin and R. De Borst, "A gradient plasticity approach to finite element predictions of soil instability", *Arch. Mech.* **47**:2 (1995), 353–377.

[Peerlings 2007] R. H. J. Peerlings, "On the role of moving elastic-plastic boundaries in strain gradient plasticity", *Model. Simul. Mater. Sci. Eng.* **15**:1 (2007), s109–s120.

[Peerlings et al. 2001] R. H. J. Peerlings, M. G. D. Geers, R. De Borst, and W. A. M. Brekelmans, "A critical comparison of nonlocal and gradient-enhanced softening continua", *Int. J. Solids Struct.* **38** (2001), 7723–7746.

[Poh et al. 2011] L. H. Poh, R. H. J. Peerlings, M. G. D. Geers, and S. Swaddiwudhipong, "An implicit tensorial gradient plasticity model-formulation and comparison with a scalar gradient model", *Int. J. Solids Struct.* **48** (2011), 2595–2604.

[Rittel et al. 2006] D. Rittel, Z. G. Wang, and M. Merzer, "Adiabatic shear failure and dynamic stored energy of cold work", *Phys. Rev. Lett.* **96**:7 (2006), Article ID #075502.

[Shawki and Clifton 1989] T. G. Shawki and R. J. Clifton, "Shear band formation in thermal visco-plastic materials", *Mech. Mater.* **8** (1989), 13–43.

[Simone et al. 2004] A. Simone, H. Askes, R. H. J. Peerlings, and L. J. Sluys, "Interpolation requirements for implicit gradient-enhanced continuum damage models", *Commun. Numer. Methods Eng.* **20** (2004), 163–165.

[Voyiadjis and Abu Al-Rub 2005] G. Z. Voyiadjis and R. K. Abu Al-Rub, "Gradient plasticity theory with a variable length scale parameter", *Int. J. Solids Struct.* **42** (2005), 3998–4029.

[Wang 2006a] X. B. Wang, "Temperature-dependent shear strain localization of aluminum-lithium alloy in uniaxial compression using Zerilli–Armstrong and gradient plasticity models", *Mater. Sci. Forum* **519-521** (2006), 789–794.

[Wang 2006b] X. B. Wang, "Temperature distribution in adiabatic shear band for ductile metal based on Johnson–Cook and gradient plasticity models", *Trans. Nonferr. Met. Soc. China* **16** (2006), 333–338.

[Wang 2006c] X. B. Wang, "Effects of constitutive parameters on adiabatic shear localization for ductile metal based on Johnson–Cook and gradient plasticity models", *Trans. Nonferr. Met. Soc. China* **16** (2006), 1362–1369.

[Wang 2007] X. B. Wang, "Adiabatic shear localization for steels based on Johnson–Cook model and second- and fourth-order gradient plasticity models", *J. Iron Steel Res. Int.* **14** (2007), 56–61.

[Wang 2008] X. B. Wang, "Effects of temperature and strain rate on the evolution of thickness of transformed adiabatic shear band", *Solid State Phenom.* **138** (2008), 385–392.

[Wang 2009] X. B. Wang, "Theoretical analysis of the adiabatic shear band width and strain rate effect of Ti-6Al-4V", *Rare Met. Mater. Eng.* **38** (2009), 214–218. In Chinese.

[Wang 2010] X. B. Wang, "A new method for calculating the peak temperature evolution in the adiabatic shear band of steel", *J. Mech. Mater. Struct.* **5** (2010), 95–106.

Received 27 Oct 2011. Revised 28 Jun 2012. Accepted 27 Jul 2012.

XUE-BIN WANG: wxbbb@263.net
Department of Mechanical Science and Engineering, Liaoning Technical University, Fuxin City, 123000, China

BING MA: bingandna@263.net
Department of Mechanical Science and Engineering, Liaoning Technical University, Fuxin City, 123000, China

JOURNAL OF MECHANICS OF MATERIALS AND STRUCTURES
Vol. 7, No. 8-9, 2012
dx.doi.org/10.2140/jomms.2012.7.753

A PULL-OUT MODEL FOR PERFECTLY BONDED CARBON NANOTUBE IN POLYMER COMPOSITES

KHONDAKER SAKIL AHMED AND ANG KOK KENG

A pull-out model for carbon nanotube (CNT) reinforced composite is presented to obtain the interface characteristic in which perfect bonding at the interface is considered. In the model, a partially embedded CNT in a cylindrical polymer matrix is subjected to an axial load at the open end. By using representative volume element (RVE) concept, analytical solutions are derived for axial and interfacial shear stresses in the CNT. Parametric studies are also conducted to obtain the influence of aspect ratio, modulus ratio and relative size of RVE on stress components. Variation of critical pull-out stress with embedded length and CNT/polymer Young's modulus ratio are also investigated.

1. Introduction

One of the major applications of carbon nanotube is its use as high strength reinforcements for high performance composite materials [Ajayan et al. 2000; Frankland and Harik 2003; Haque and Ramasetty 2005; Qian et al. 2000; 2002; Thostenson et al. 2001; Tserpes et al. 2008; Wang et al. 2008]. Many factors affecting the performance of CNT-reinforced composites include [Ailin et al. 2010] mechanical properties of nanotubes as well as matrix, purity, interface characteristics such as interfacial bonding, interactions with host and orientation of CNTs in the matrix. Similar to conventional composites, many research studies also suggested that the performance of CNT-reinforced composites depends critically on the interfacial characteristics between CNT and the matrix material [Kin and Sean 2001; Liao and Li 2001; Manoharan et al. 2009; Qian 2003; 2000; Salehikhojin and Jalili 2008; Wang et al. 2008].

One of the major challenges in the CNT-reinforced composites is load transfer efficiency across the CNT/matrix interface. Research studies suggest that the main contributing factors for interfacial load transfer between CNT and polymer are mechanical interlocking (friction), chemical bonding and noncovalent bonding like $v\,dW$ interactions [Haque and Ramasetty 2005; Jiang et al. 2006; 2008].

In the literature, several researchers also found the presence of strong bonding at the interface when nanotubes were dispersed in PHAE or polystyrene [Qian et al. 2000; 2002]. Chemical bonding or surface treatment is difficult between CNT and polymer matrix but it certainly improves the interface strength by a significant order. As an example, chemisorptions to as little as 5.0% of the nanotube carbon atoms increases the shear stress of at the interface by about 1000% [Zheng et al. 2008]. It is also well known that surface to volume ratio (SVR) and aspect ratio (AR) of nanotubes are higher in magnitudes than those of traditional composites. Though there is a huge difference in strength between nanotube and polymer matrix, high frictional forces may prevent slipping of the tube and ensure good load transfer even in chemically nonbonded CNT/matrix interface. Therefore, all the aforementioned properties of CNT ensure that weak CNT/matrix interface can also be assumed as perfectly bonded.

Keywords: perfectly bonded interface, representative volume element, stress transfer, aspect ratio, critical pull-out stress.

In conventional fiber-reinforced composites [Cox 1952; Kim and Mai 1998; Li-Min et al. 1992], pull-out tests are widely used to measure the interface characteristics, stress distributions, maximum pull-out force or effective pull-out length. However, it is very difficult to conduct experimental pull-out tests on CNT embedded in polymer matrix due to the challenges involved in griping, manipulation and stress, strain measurements. The load transfer mechanism in conventional fiber-reinforced composites has been studied by using the pull-out model for many years [Li-Min et al. 1992; Seshadri and Saigal 2007]. Some researchers have conducted molecular dynamic (MD) simulations [Frankland and Harik 2003; Kin and Sean 2001] on CNT pull-out models. Though MD simulation is generally accepted to be more accurate, it is however highly time consuming and costly.

Recently, some researchers have proposed various pull-out models for CNT-reinforced composites using continuum mechanics approach [Ahmed and Ang 2010; Kin-tak 2003; Natsuki et al. 2007; Tan and Kin 2004]. A number of previous studies have considered the case of frictionally bonded interface that are valid only for very weak CNT/matrix interface. In [Wagner 2002], the interfacial shear strength in polymer composites reinforced by SWNT has been estimated using a modified Kelly–Tyson approach which however assumes the interfacial shear and axial normal stresses to be uniform. A perfectly bonded CNT/matrix interface using RVE concept was considered in [Gao and Li 2005]. This study, however, was on a shear lag model which assumes the CNT to be fully embedded within the matrix and is aimed at estimating the average stress components of the matrix and CNT. On the other hand, a pull-out test model is designed to estimate the critical pull-out force, the mechanism of stress transfer from CNT to matrix as well as the factors that influence the composite behavior. Surprisingly, no research study on CNT pull-out model has been reported in the literature for perfectly bonded interface.

The main objective of the current work is to develop an analytical pull-out model of a perfectly bonded CNT/matrix using linear elasticity theory. The proposed continuum-based model is capable of predicting axial and interfacial shear stress distributions of the CNT as well as the critical pull-out force. Analytical results obtained from the model are verified by comparing with those available in the literature. To illustrate the application of the proposed model, parametric studies are conducted to examine the effects of aspect ratio, radius ratio and modulus ratio on the average axial and interfacial shear stresses in CNT. Therefore, this model aims to provide a more convenient solution that would help to provide a design guideline for stress transferring of CNT in composites.

2. Proposed pull-out model

In this study, a 3D cylindrical representative volume element (RVE) is selected from a cracked section of CNT-reinforced composite shown in Figure 1(a) to define the pull-out model, as shown in Figure 1(b). The pull-out model comprises of a CNT of radius a partially embedded within a cylindrical matrix of radius b. The z and r coordinates are assigned along the axial and radial directions of the CNT, respectively. The embedded length of the CNT in the polymer matrix is denoted by L and F is the axial normal force applied at the open end of the CNT.

To investigate the pull-out characteristics of the CNT, it is proposed that the CNT be replaced by an effective solid fiber having the same length and outer diameter as shown in Figure 1(c). The modulus of the effective fiber E_f can be expressed in terms of the elastic modulus of the nanotube E_t as follows

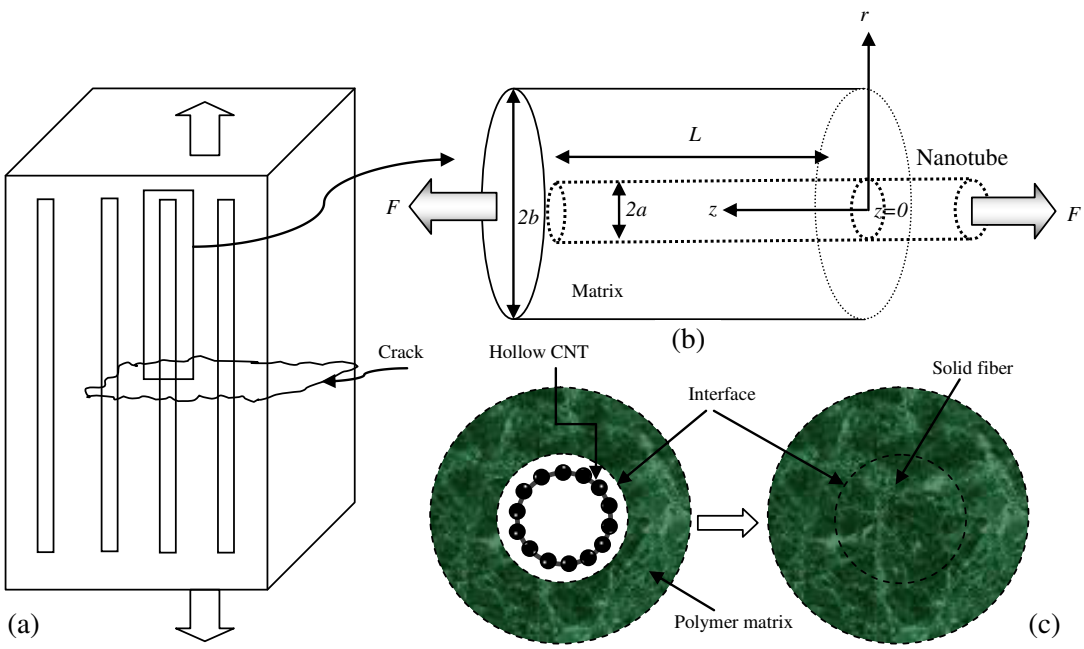

Figure 1. Schematics of the CNT pull-out model: (a) cracked section of CNT-reinforced composite; (b) partially embedded CNT in 3-D RVE; (c) conversion of typical hollow CNT to equivalent effective fiber in polymer matrix.

(see [Ailin et al. 2010; Gao and Li 2005; Thostenson et al. 2001]):

$$E_f = \frac{A_t}{A_{eff}} E_t = \frac{2at - t^2}{a^2} E_t; \tag{1}$$

this is determined by setting the cross-sectional areas of the hollow CNT and solid fiber to be equal to each other. Here, t denotes the thickness of the nanotube.

The governing equilibrium equations for the axisymmetric problem in terms of polar coordinates (r, θ, z) may be written as

$$\frac{d\sigma_{rr}}{dr} + \frac{d\tau_{rz}}{dz} + \frac{\sigma_{rr} - \sigma_{\theta\theta}}{r} = 0, \quad \frac{d\sigma_{zz}}{dz} + \frac{1}{r}\frac{d(r\tau_{rz})}{dr} = 0, \tag{2}$$

where σ_{zz}, σ_{rr}, $\sigma_{\theta\theta}$, τ_{rz} are the axial, radial, hoop and shear stress components, respectively, ϵ_{rr}, ϵ_{zz}, $\epsilon_{\theta\theta}$, γ_{rz} the corresponding strain components, respectively and w, u the axial and radial displacements, respectively.

Assuming that the material obeys Hooke's law, the constitutive equations may be written as

$$\epsilon_{zz} = \frac{1}{E}\{\sigma_{zz} - \nu(\sigma_{rr} + \sigma_{\theta\theta})\}, \quad \epsilon_{rr} = \frac{1}{E}\{\sigma_{rr} - \nu(\sigma_{zz} + \sigma_{\theta\theta})\}, \quad \epsilon_{\theta\theta} = \frac{1}{E}\{\sigma_{\theta\theta} - \nu(\sigma_{rr} + \sigma_{zz})\}, \tag{3a}$$

$$\gamma_{rz} = \frac{\tau_{rz}}{G}, \tag{3b}$$

where E, G and ν are the Young's modulus, shear modulus and Poisson's ratio, respectively.

The strain-displacement relationships may be written as

$$\epsilon_{rr} = \frac{du}{dr}, \quad \epsilon_{zz} = \frac{dw}{dz}, \quad \epsilon_{\theta\theta} = \frac{u}{r}, \quad \gamma_{rz} = \frac{du}{dz} + \frac{dw}{dr}. \tag{4}$$

Note that Equations (2)–(4) are valid for both the effective solid fiber and matrix.

The mechanical equilibrium equation at any section of the RVE can be written as

$$\pi a^2 \sigma = \int_0^a \sigma_{zz}^f (2\pi r)\, dr + \int_a^b \sigma_{zz}^m (2\pi r)\, dr, \tag{5}$$

where $\sigma (= F/\pi a^2)$ denotes the average stress applied in the effective fiber at $z = 0$. (Superscript f and m refer to the effective fiber and matrix, respectively.) The average axial stresses of CNT and matrix can be expressed as

$$\overline{\sigma}_{zz}^f = \frac{2}{a^2} \int_0^a \sigma_{zz}^f r\, dr, \quad \overline{\sigma}_{zz}^m = \frac{2}{b^2 - a^2} \int_a^b \sigma_{zz}^m r\, dr. \tag{6}$$

The boundary conditions of the pull-out model are

$$\begin{aligned} &\overline{\sigma}_{zz}^f(0) = \sigma, \quad \overline{\sigma}_{zz}^f(L) = \overline{\sigma}_{zz}^m(L), \quad \tau_{rz}^f(a) = \tau_i, \qquad \tau_{rz}^m(b) = 0, \\ &\overline{\sigma}_{rr}^m(b) = 0, \quad \epsilon_z^f(a) = \epsilon_z^m(a), \quad w_z^f(a) = w_z^m(a), \end{aligned} \tag{7}$$

where τ_i is the interfacial shear stress.

Upon integrating $(2)_2$ with respect to r from 0 to a and applying the boundary conditions given in $(7)_3$ for the effective fiber, we obtain

$$\frac{d\overline{\sigma}_{zz}^f}{dz} = -\frac{2}{a}\tau_i. \tag{8}$$

In view that the matrix shear stress (τ_{rz}^m) has to be compatible with interfacial shear stress (τ_i) and the fact that the outer surface of matrix cylinder is stress free, τ_{rz}^m at any radial distance r can be derived by integrating $(2)_2$ to give

$$\tau_{rz}^m = \frac{a}{b^2 - a^2} \frac{(b^2 - r^2)}{r} \tau_i. \tag{9}$$

Since $\frac{du}{dz} \ll \frac{dw}{dr}$, we can assume $\frac{du}{dz} + \frac{dw}{dr} \equiv \frac{dw}{dr}$. Therefore, $(4)_4$ may be rewritten as

$$\gamma_{rz} = \frac{dw}{dr}. \tag{10}$$

In view of (10), Equation (3b) for both the fiber and matrix may then be rewritten as

$$\tau_{rz}^f = \frac{E_f}{1 + \nu_f} \frac{dw^f}{dr}, \quad \tau_{rz}^m = \frac{E_m}{1 + \nu_m} \frac{dw^m}{dr}. \tag{11}$$

By substituting $(11)_2$ into (9), we obtain

$$\frac{E_m}{1 + \nu_m} \frac{dw^m}{dr} = \frac{\gamma}{a} \frac{(b^2 - r^2)}{r} \tau_i, \tag{12}$$

where

$$\gamma = \frac{a^2}{b^2 - a^2}. \tag{13}$$

By integrating (12) from a to b, we obtain

$$\tau_i = \frac{a}{\gamma} \frac{E_m(w_b^m - w_a^m)}{(1+\nu_m)(b^2 \ln \frac{b}{a} - a^2/2\gamma)}. \tag{14}$$

Finally, by substituting (14) into (12) and integrating from a to b, we obtain

$$w^m(r,z) = w_a^m + \frac{(b^2 \ln \frac{r}{a} - (r^2 - a^2)/2)(w_b^m - w_a^m)}{b^2 \ln \frac{b}{a} - a^2/2\gamma}. \tag{15}$$

Since the axial stress is the predominant stress component, we assume that $\sigma_{rr} + \sigma_{\theta\theta} \ll \sigma_{zz}$. Equation $(3a)_1$ may therefore be rewritten as

$$\sigma_{zz}^f = E_f \frac{dw^f}{dz}, \quad \sigma_{zz}^m = E_m \frac{dw^m}{dz}. \tag{16}$$

Equation $(16)_2$ becomes, in view of (15),

$$\sigma_{zz}^m(r,z) = \sigma_{zz}^m(a,z) + \frac{\{b^2 \ln \frac{r}{a} - (r^2 - a^2)/2\}\{\sigma_{zz}^m(b,z) - \sigma_{zz}^m(a,z)\}}{b^2 \ln \frac{b}{a} - a^2/2\gamma}. \tag{17}$$

Upon substituting (17) into (5) and after rearranging, we obtain

$$\sigma_{zz}^m(b,z) = \frac{\sigma - \gamma(\overline{\sigma}_{zz}^f - \sigma)}{\beta} + \left(1 - \frac{1}{\beta}\right)\sigma_{zz}^m(a,z) \tag{18}$$

where

$$\beta = \frac{b^2(1+\gamma)\ln \frac{b}{a} - (3b^2 - a^2)/4}{b^2 \ln \frac{b}{a} - a^2/2\gamma}. \tag{19}$$

Now, by substituting (14) into (8), we obtain

$$\frac{d\overline{\sigma}_{zz}^f}{dz} = -\frac{2}{\gamma} \frac{E_m(w_b^m - w_a^m)}{(1+\nu_m)(b^2 \ln \frac{b}{a} - a^2/2\gamma)}. \tag{20}$$

By differentiating (20) with respect to z and making use of $\sigma_{zz}^m(b,z)$ given in (18), we obtain the second order differential equation

$$\frac{d^2\overline{\sigma}_{zz}^f}{dz^2} = -\frac{2}{\gamma(1+\nu_m)} \frac{\frac{\sigma - \overline{\sigma}_{zz}^f}{\beta} - \frac{\sigma_{zz}^m(a,z)}{\gamma\beta}}{b^2 \ln \frac{b}{a} - a^2/2\gamma}. \tag{21}$$

As it is assumed that there is perfect bonding at the interface, i.e., $\epsilon_z^f(a) = \epsilon_z^m(a)$, the stress-strain relationship given in $(3a)_1$ reduces to

$$\sigma_{zz}^m(a,z) = \alpha\overline{\sigma}_{zz}^f, \tag{22}$$

where

$$\alpha = E_m/E_f. \tag{23}$$

Now, by substituting $\sigma_{zz}^m(a, z)$ from (22) and β from (19) into (21) and after rearranging, we obtain

$$\frac{d^2\overline{\sigma}_{zz}^f}{dz^2} = -\frac{2}{a^2\gamma^2(1+\nu_m)}\frac{\gamma\sigma - (\alpha+\gamma)\overline{\sigma}_{zz}^f}{(\frac{b}{a})^4\ln\frac{b}{a} - (3b^2-a^2)/4a^2\gamma}, \tag{24}$$

which may be simplified and written as

$$\frac{d^2\overline{\sigma}_{zz}^f}{dz^2} - C_1\overline{\sigma}_{zz}^f + C_1\frac{\gamma}{\alpha+\gamma}\sigma = 0, \tag{25}$$

where

$$C_1 = \frac{2}{a^2\gamma^2(1+\nu_m)}\frac{\alpha+\gamma}{(\frac{b}{a})^4\ln\frac{b}{a} - (3b^2-a^2)/4a^2\gamma}. \tag{26}$$

By using the boundary conditions given in (7), the analytical solution for the average axial stress of CNT may be expressed as

$$\overline{\sigma}_{zz}^f = \left[\frac{(R-\alpha S)\exp(pz) - (R-\alpha/S)\exp(-pz)}{q} + \gamma\right]\frac{\sigma}{\alpha+\gamma}. \tag{27}$$

The solution for the interfacial shear stress can be obtained by using (8) and (24) and written as

$$\tau_i = \left[(R-\alpha S)\exp(pz) + (R-\alpha/S)\exp(-pz)\right]\frac{ap\sigma}{2q(\alpha+\gamma)} \tag{28}$$

where

$$p = C_1^{1/2}, \quad q = 2\sinh(pL), \quad R = \gamma^2(\alpha+\gamma) - \gamma, \quad S = \exp(-pL). \tag{29}$$

3. Analytical results

To examine the accuracy of the derived analytical formulas, results are presented and compared with available results in the literature. Various values of key parameters, namely the aspect ratio ($AR = L/2a$), radius ratio (b/a), and modulus ratio (α) are considered to examine the effect of these parameters on the axial and interfacial stresses developed in the CNT. In addition, critical values of embedded length (L) and modulus ratio (α) are estimated based on the maximum shear stress developed just before debonding occurs at the interface. Available experimental data for various parameters that are used in the computations of the analytical results are given in Table 1.

F	12.566 nN	E_m	20 Gpa
a	2 nm	E_f	560 GPa
b	12 nm	ν_f	0.28
L	50 nm	ν_m	0.35

Table 1. Parameter values.

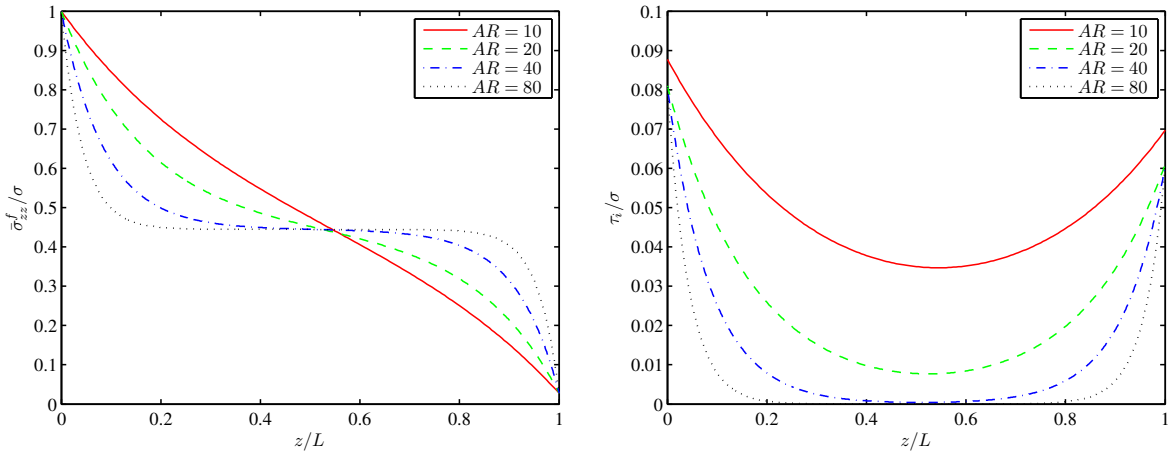

(a) (b)

Figure 2. (a) Average axial stress of CNT along the length for different aspect ratios (AR). (b) Interfacial shear stress of CNT along the length for different aspect ratios.

Figure 2 shows the average axial and interfacial shear stress distributions along the length, for different AR. Both the axial and interfacial shear stress distribution trends are quite similar to the recent friction-based pull-out model proposed in [Tan and Kin 2004]. It can be seen from Figure 2a that the axial stress decreases towards the end for all AR. The result also shows that larger stress saturation zone has been found for higher AR. In contrast, the axial stress distributions are linear for smaller AR. This happens because applied stress can be distributed over larger surface area as well as longer length for higher AR. It can be seen from Figure 2b that the shear stress is maximum at $z = 0$. It gradually decreases and reaches the lowest value near the middle of the length. It then gradually increases towards the end. As the uniform stress is applied at $z = 0$, it is to be expected that the interfacial shear stress developed will be maximum at the same location.

Since the tip of the embedded CNT is assumed to be perfectly bonded with the matrix, it is expected that the interfacial shear stress will also show another peak at the tip, i.e., at $z = L$. Figure 2b also shows that the interfacial shear stress tends to be smaller for higher AR. This happens because a higher AR indicates a relatively longer length for a given diameter. Consequently, the shear stress can be distributed over a longer embedded length, thereby resulting in smaller shear stress distribution. It is interesting to note that all the curves in Figure 2b coincide at approximately $z/L = 0.55$. The minimum value of shear stress for all distributions is also noted to occur at this value of z/L.

Figure 3 shows the axial and interfacial shear stress distributions along the length for different radius ratios (b/a). Note that the radius ratio represents different RVE size as well as volume fraction of CNT in the composite. Figure 3a shows that higher axial stress is found for smaller RVE size (smaller b/a). This is to be expected since for a smaller RVE, a bigger proportion of the applied axial stress is to be carried by the CNT. It is also found that the stress distribution is approximately the same for about 10% of the length measured from the open end. The stress distributions deviate significantly from each other in the vicinity of the middle of the embedded length for different (b/a) ratios. Figure 3b shows that

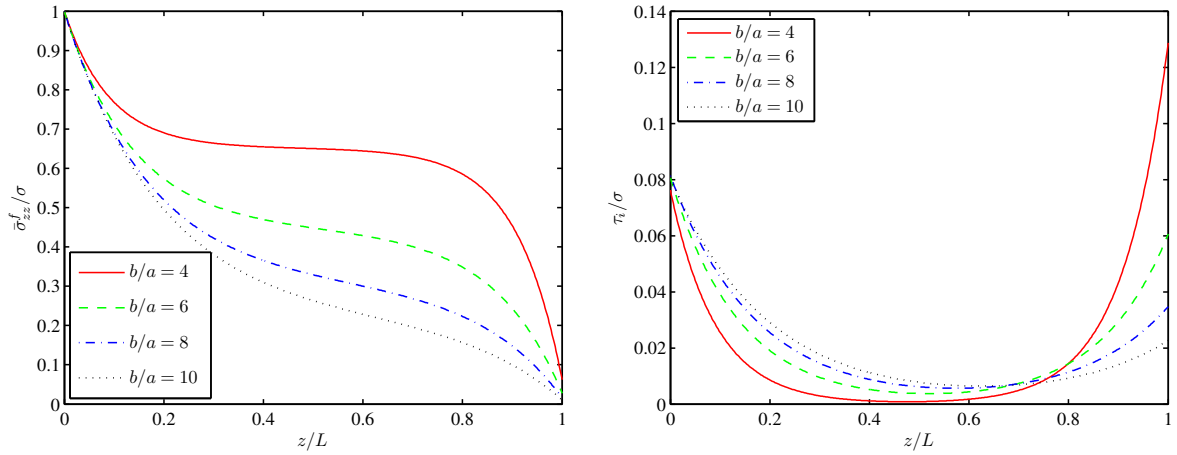

(a) (b)

Figure 3. (a) Average axial stress of CNT along the length for different RVE sizes (b/a). (b) Interfacial shear stress of CNT along the length for different RVE sizes.

the interfacial shear stress is close to zero near the middle and rises to large values at the open end and the extreme embedded end. It is also observed that the interfacial shear stress is generally smaller at the extreme embedded end compared to the open end, except when the (b/a) ratio is small. This observation is similar to the results of [Li-Min et al. 1992] for fiber-reinforced composite.

Figure 4 shows the average axial and interfacial shear stress distributions, for different Young's modulus ratios $\alpha = E_m/E_f$ — that is, for different relative matrix strengths. Figure 4a shows that axial stress distribution for any value of α decreases sharply up to 20% of the embedded length from the tip before

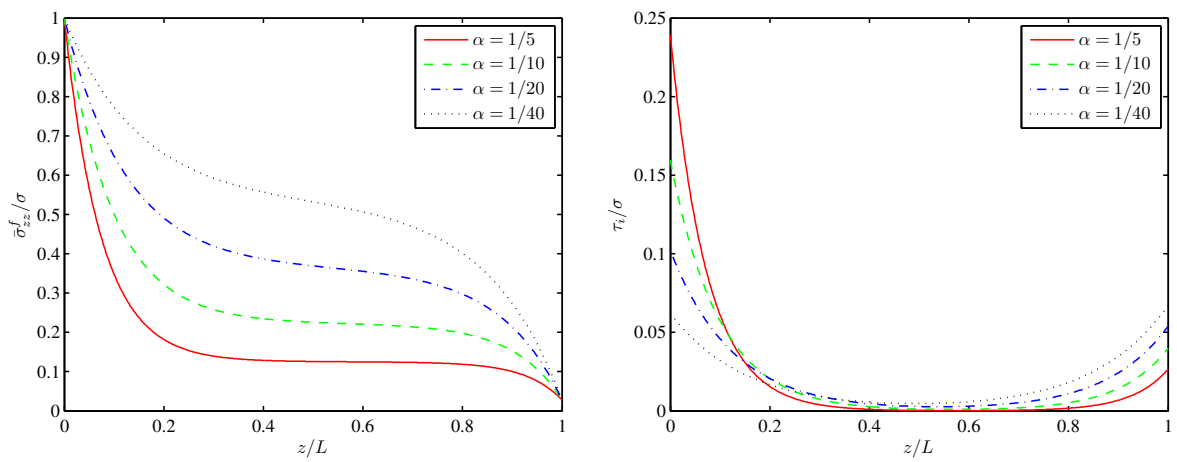

(a) (b)

Figure 4. (a) Average axial stress of CNT along the length for different modulus ratios (α). (b) Interfacial shear stress of CNT along the length for different modulus ratios.

reaching a stress constant region and then finally meets a common point at the end. It can be seen from the figure that as larger the value of α is, the axial stress of CNT for different modulus ratios is smaller. For weaker matrix, i.e., smaller modulus ratios, the axial stress distribution is higher as compared to stronger matrix, thereby indicating that the proportion of axial stress carried by CNT decreases as the matrix gets stronger. In contrast, Figure 4b shows that the interfacial shear stress is noted to be virtually zero over most part of the CNT except near the ends with the open end achieving a much larger value than the other end. Interestingly, the interfacial shear stress is noted to be much larger for higher modulus ratios at the open end but the opposite happens at the extreme embedded end.

The current study as well as several previous studies [Ahmed and Ang 2010; Li-Min et al. 1992; Natsuki et al. 2007; Xiao and Liao 2004] show that the maximum interfacial shear stress for the pull-out problem is found at the open end, i.e., at $z = 0$. Thus, it is expected that debonding between the CNT and the matrix will occur at the open end. By rearranging (27), the critical pull-out stress (σ_{cr}) defined as the maximum pull-out force per unit cross-sectional area of CNT at impending debonding can be determined as a function of the allowable interfacial shear stress as follows

$$\sigma_{cr} = \frac{2(\alpha + \gamma)}{ap(2R - \alpha S - \alpha/S)}\tau_{max} \tag{30}$$

The allowable interfacial shear stress is dependent on the nature of the CNT/matrix interface. Manoharan et al. [2009] has measured this value for CNT-reinforced epoxy composite experimentally using a scanning electron microscope to be nearly 200 MPa. Liao and Li [2001] have determined the maximum interfacial shear stress to be about 160 MPa through molecular dynamic simulation on the pull-out problem of a nanotube/polymer system. Knowing the maximum interfacial shear stress (τ_{max}) and other physical and mechanical properties of composite, the critical pull-out stress (σ_{cr}) can be determined using (30).

Based on (30), the critical pull-out stress (σ_{cr}) may be determined for any embedded length of CNT. Figure 5 shows the variation of the critical pull-out stress with the embedded length for the case of an epoxy matrix where the allowable interfacial shear stress is taken to be 200 MPa. It can be seen from the curve shown in Figure 5 that σ_{cr} increases gradually with increasing embedded length up to 20 nm and thereafter stays virtually constant. Hence, it is interesting to note that any increase in the embedded length beyond a critical embedded length is unable to prevent debonding at the open end in view that the shear stress induced has already reached the allowable interfacial stress value. Thus, for the case examined here, the critical embedded length is estimated to be approximately 20 nm.

Figure 6 shows the variation of critical pull-out stress (σ_{cr}) with the CNT/matrix modulus ratio, $\alpha(E_m/E_f)$. It can be seen that the σ_{cr} decreases as the modulus ratio increases which agrees with the friction based model for fiber-reinforced model proposed in [Chiang 2001]. This happens because a higher α represents a stronger matrix. As explained previously, a stronger matrix would result in a larger shear stress at the open end as well as a smaller axial stress induced in the CNT. Consequently, the critical pull-out stress is expected to decrease. The figure also shows that σ_{cr} decreases sharply for smaller values of α and remains nearly constant after $\alpha > 0.3$. Similar to the explanation given with regards to the critical embedded length, there is thus a critical value of the modulus ratio beyond which there is no significant variation in the σ_{cr}. For the case discussed, the critical modulus ratio may be taken to be 0.3.

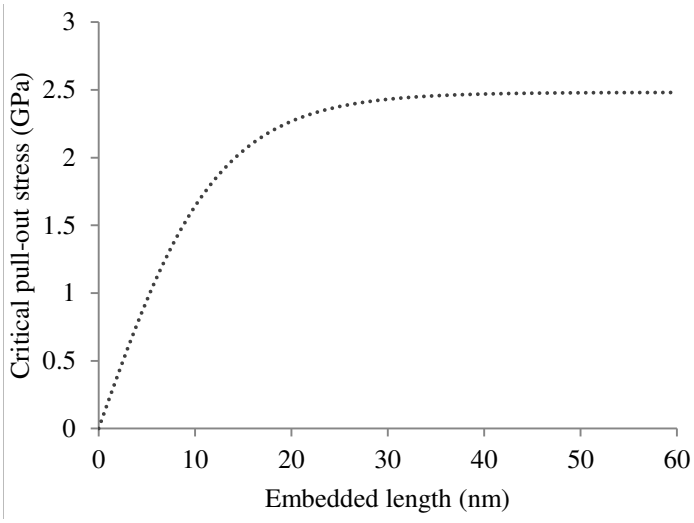

Figure 5. Variation of critical pull-out stress (σ_{cr}) with embedded length (L).

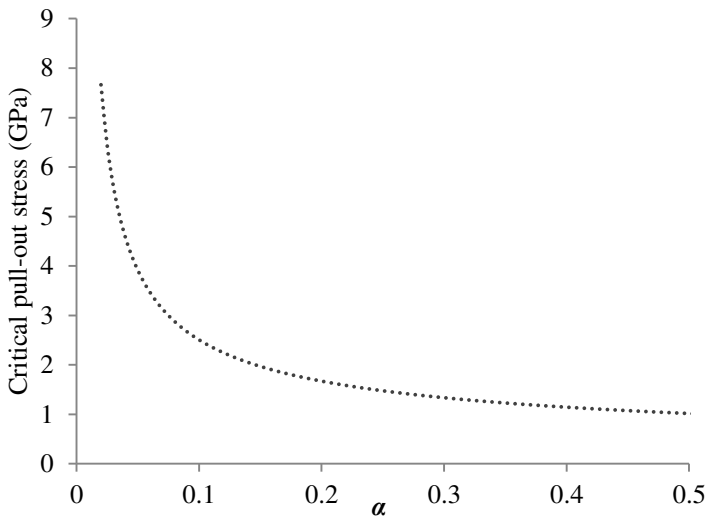

Figure 6. Variation of critical pull-out stress (σ_{cr}) with modulus ratio, α (E_m/E_f).

4. Conclusion

An analytical pull-out model has been proposed to investigate the stress transferring mechanism of CNT in polymer matrix by using classical continuum mechanics. Closed-form solutions have been derived for the axial and interfacial shear stress components. These formulas can be used to investigate the pull-out problem conveniently without resorting to more expensive and complicated experimental study. The present study revealed that the aspect ratio, modulus ratio and radius ratio (RVE size) are the key controlling parameters in CNT-reinforced polymer composites. Critical values of embedded length and modulus ratio for a sample case were also determined, which are the minimum embedded length of CNT

and strongest matrix that can be used effectively with CNT, respectively that correspond to the largest possible pull-out stress for perfectly bonded CNT/polymer interface.

It is to be noted that since we convert the hollow nanotube to be effective solid fiber, the proposed pull-out model is not limited to the CNT-reinforced composite only. The derived solution may therefore be used for other fiber-reinforced composite having similar physical properties, geometric shape and interface.

References

[Ahmed and Ang 2010] K. S. Ahmed and K. K. Ang, "An improved pull-out model for carbon nanotube reinforced composites", pp. 41–44 in *Proceedings of the Twenty-third KKCNN Symposium on Civil Engineering* (Taipei, 2010), 2010.

[Ailin et al. 2010] L. Ailin, K. W. Wang, and C. E. Bakis, "Multiscale damping model for polymeric composites containing carbon nanotube ropes", *J. Compos. Mater.* **44** (2010), 2301–2323.

[Ajayan et al. 2000] P. M. Ajayan, L. S. Schadler, C. Giannaris, and A. Rubio, "Single-walled carbon nanotube-polymer composites: strength and weakness", *Adv. Mater.* **12**:10 (2000), 750–753.

[Chiang 2001] Y.-C. Chiang, "The influence of Poisson contraction on matrix cracking stress in fiber reinforced ceramics", *J. Mater. Sci.* **36**:13 (2001), 3239–3246.

[Cox 1952] H. L. Cox, "The elasticity and strength of paper and other fibrous materials", *Br. J. Appl. Phys.* **3** (1952), 72–79.

[Frankland and Harik 2003] S. J. V. Frankland and V. M. Harik, "Analysis of carbon nanotube pull-out from a polymer matrix", *Surf. Sci.* **525** (2003), L103–L108.

[Gao and Li 2005] X. Gao and K. Li, "A shear-lag model for carbon nanotube-reinforced polymer composites", *Int. J. Solids Struct.* **42**:5 (2005), 1649–1667.

[Haque and Ramasetty 2005] A. Haque and A. Ramasetty, "Theoretical study of stress transfer in carbon nanotube reinforced polymer matrix composites", *Compos. Struct.* **71**:1 (2005), 68–77.

[Jiang et al. 2006] L. Jiang, Y. Huang, H. Jiang, G. Ravichandran, H. Gao, K. Hwang, and B. Liu, "A cohesive law for carbon nanotube/polymer interfaces based on the van der Waals force", *J. Mech. Phys. Solids* **54**:11 (2006), 2436–2452.

[Jiang et al. 2008] Y. Y. Jiang, W. Zhou, T. Kim, Y. Huang, and J. M. Zuo, "Measurement of radial deformation of single-wall carbon nanotubes induced by intertube van der Waals forces", *Phys. Rev. B* **77**:15 (2008), Art. ID #153405.

[Kim and Mai 1998] J.-K. Kim and Y.-W. Mai, *Engineered interfaces in fiber reinforced composites*, Elsevier, Amsterdam, 1998.

[Kin and Sean 2001] L. Kin and L. Sean, "Interfacial characteristics of a carbon nanotube-polystyrene composite system", *Appl. Phys. Lett.* **79** (2001), 4225–4227.

[Kin-tak 2003] L. Kin-tak, "Interfacial bonding characteristics of nanotube/polymer composites", *Chem. Phys. Lett.* **370** (2003), 399–405.

[Li-Min et al. 1992] Z. Li-Min, K. Jang-Kyo, and M. Yiu-Wing, "On the single fibre pull-out problem: effect of loading method", *Compos. Sci. Technol.* **45** (1992), 153–160.

[Liao and Li 2001] K. Liao and S. Li, "Interfacial characteristics of a carbon nanotube-polystyrene composite system", *Appl. Phys. Lett.* **79**:25 (2001), 4225–4227.

[Manoharan et al. 2009] M. P. Manoharan, A. Sharma, A. V. Desai, M. A. Haque, C. E. Bakis, and K. W. Wang, "The interfacial strength of carbon nanofiber epoxy composite using single fiber pull-out experiments", *Nanotechnology* **20**:29 (2009), Art. ID #295701.

[Natsuki et al. 2007] T. Natsuki, F. Wang, Q. Q. Ni, and M. Endo, "Interfacial stress transfer of fiber pull-out for carbon nanotubes with a composite coating", *J. Mater. Sci.* **42**:12 (2007), 4191–4196.

[Qian 2003] D. Qian, "Load transfer mechanism in carbon nanotube ropes", *Compos. Sci. Technol.* **63**:11 (2003), 1561–1569.

[Qian et al. 2000] D. Qian, E. C. Dickey, R. Andrews, and T. Rantell, "Load transfer and deformation mechanisms in carbon nanotube-polystyrene composites", *Appl. Phys. Lett.* **76**:20 (2000), 2868–2870.

[Qian et al. 2002] D. Qian, G. J. Wagner, W. K. Liu, M.-F. Yu, and R. S. Ruoff, "Mechanics of carbon nanotubes", *Appl. Mech. Rev.* (*ASME*) **55**:6 (2002), 495–533.

[Salehikhojin and Jalili 2008] A. Salehikhojin and N. Jalili, "A comprehensive model for load transfer in nanotube reinforced piezoelectric polymeric composites subjected to electro-thermo-mechanical loadings", *Compos. B Eng.* **39**:6 (2008), 986–998.

[Seshadri and Saigal 2007] M. Seshadri and S. Saigal, "Crack bridging in polymer nanocomposites", *J. Eng. Mech.* (*ASCE*) **133**:8 (2007), 911–918.

[Tan and Kin 2004] X. Tan and L. Kin, "A nonlinear pullout model for unidirectional carbon nanotube-reinforced composites", *Compos. B Eng.* **35**:3 (2004), 211–217.

[Thostenson et al. 2001] E. T. Thostenson, Z. Ren, and T.-W. Chou, "Advances in the science and technology of carbon nanotubes and their composites: a review", *Compos. Sci. Technol.* **61**:13 (2001), 1899–1912.

[Tserpes et al. 2008] K. Tserpes, P. Papanikos, G. Labeas, and S. Pantelakis, "Multi-scale modeling of tensile behavior of carbon nanotube-reinforced composites", *Theor. Appl. Fract. Mech.* **49**:1 (2008), 51–60.

[Wagner 2002] H. D. Wagner, "Nanotube-polymer adhesion: a mechanics approach", *Chem. Phys. Lett.* **361**:1–2 (2002), 57–61.

[Wang et al. 2008] W. Wang, P. Ciselli, E. Kuznetsov, T. Peijs, and A. H. Barber, "Effective reinforcement in carbon nanotube-polymer composites", *Phil. Trans. R. Soc. A* **366** (2008), 1613–1626.

[Xiao and Liao 2004] T. Xiao and K. Liao, "A nonlinear pull-out model for unidirectional carbon nanotube-reinforced composites", *Compos. B Eng.* **35**:3 (2004), 211–217.

[Zheng et al. 2008] Q. Zheng, Q. Xue, K. Yan, X. Gao, Q. Li, and L. Hao, "Effect of chemisorption on the interfacial bonding characteristics of carbon nanotube-polymer composites", *Polymer* **49**:3 (2008), 800–808.

Received 2 Apr 2012. Revised 29 Sep 2012. Accepted 16 Oct 2012.

KHONDAKER SAKIL AHMED: ksahmed@nus.edu.sg
Department of Civil and Environmental Engineering, 1 Engineering Drive 2, National University of Singapore, Singapore 117576

ANG KOK KENG: cveangkk@nus.edu.sg
Department of Civil and Environmental Engineering, 1 Engineering Drive 2, National University of Singapore, Singapore 117576

JOURNAL OF MECHANICS OF MATERIALS AND STRUCTURES
Vol. 7, No. 8-9, 2012
dx.doi.org/10.2140/jomms.2012.7.765

msp

A PERFECTLY MATCHED LAYER FOR PERIDYNAMICS IN TWO DIMENSIONS

RAYMOND A. WILDMAN AND GEORGE A. GAZONAS

A perfectly matched layer (PML) absorbing boundary is formulated for and numerically applied to peridynamics in two dimensions. Peridynamics is a nonlocal method, derived to be insensitive to discontinuities, more easily simulating fracture. A PML is an absorbing boundary layer, which decays impinging waves exponentially without introducing reflections at the boundary between the computational region and the absorbing layer. Here, we use state-based peridynamics as PMLs are essentially anisotropic absorbing materials, therefore requiring arbitrary material parameters. State-based peridynamics is also more convenient for auxiliary field formulations, facilitating the implementation of the PML. Results show the efficacy of the approach.

1. Introduction

Originally introduced in [Silling 2000], peridynamics is a nonlocal formulation of elastodynamics, which can more easily incorporate discontinuities such as cracks and damage. Derivatives of field variables in the classical continuum model are replaced by integrals over a small neighborhood of microelastic kernels that replace standard constitutive relations. In its discretized form, an elastic solid is treated as a collection of particles or nodes, each connected to its neighbors by breakable bonds. Bond breakage can be defined to occur when a bond is stretched past some predetermined limit. After a bond is broken, any supported force transfers to the remaining bonds, increasing their supported load, and encouraging more breakage. Eventually, this process autonomously leads to cracking and failure. The end result is a method capable of predicting crack growth in brittle elastic materials [Gerstle et al. 2005; Silling and Askari 2005; Emmrich and Weckner 2006; Demmie and Silling 2007; Kilic et al. 2009; Ha and Bobaru 2010].

Over the last decade, peridynamics has been extended past its original formulation. First, the numerical method originally outlined in [Silling and Askari 2005] has been extended to include adaptive refinement [Bobaru et al. 2009], replaced with different quadrature rules [Emmrich and Weckner 2007], and implemented in a parallel, molecular dynamics code [Parks et al. 2008]. In addition, it has been extended to different material types including viscoplastic [Foster et al. 2010], micropolar [Gerstle et al. 2011], and nanofiber networks [Bobaru 2007]. It has also been applied to different fields such as heat conduction [Bobaru and Duangpanya 2010] and electromigration [Gerstle et al. 2008]. Aside from practical applications, the mathematics behind the approach have been studied: Weckner et al. [2009] derived a Green's function for the peridynamic equation and Weckner and Abeyaratne [2005] discussed dispersion relations for various kernels. Most importantly for this work, state-based peridynamics was introduced,

Keywords: peridynamics, perfectly matched layer, absorbing boundary.

allowing for more flexible constitutive relations [Silling et al. 2007]. As will become clear later, state-based peridynamics allows for an auxiliary field formulation, which is necessary for the implementation of a perfectly matched layer (PML).

While most peridynamics work has focused on simulating problems with free or fixed boundary conditions, there are applications in which the simulation of an infinite medium may be useful, such as wave or crack propagation in a half-space. Absorbing boundary conditions are a way of simulating an infinite medium by absorbing any impinging waves at the computational boundaries so they do not reflect back into the simulation. A PML is such an absorbing boundary, and was originally introduced for electromagnetic simulations [Berenger 1994; Chew and Weedon 1994]. PMLs differ from traditional absorbing boundary conditions in that they are an absorbing layer, placed between the computational region of interest and the truncation of the grid or mesh. They can also be thought of as an anisotropic absorbing material, which is why the flexibility of a state-based peridynamics is necessary.

PMLs have two important qualities: First, waves in a PML decay exponentially, and second, in their analytic form, no waves reflect at the interface of a PML and the computational region. These properties make them ideal for simulating wave propagation in infinite, unbounded regions. Since their introduction, PMLs have been extended to many different types of media [Uno et al. 1997; Teixeira and Chew 1998; Dong et al. 2004], different numerical methods [Pissoort and Olyslager 2003; Pissoort et al. 2005; Alles and van Dongen 2009], and different fields [Chew and Liu 1996; Liu and Tao 1997; Festa and Nielsen 2003].

This paper implements a peridynamic formulation of elastodynamics in two dimensions and terminates the boundary with a PML. As is discussed, the use of a PML is facilitated with an auxiliary field formulation, derived from state-based peridynamics, and the peridynamic equation is broken into five coupled equations. A PML was applied to one-dimensional peridynamics in [Wildman and Gazonas 2011], which used the results of [Du et al. 2012] to formulate an auxiliary field equation. This approach required a matrix representation of the auxiliary field, which may be memory prohibitive in higher dimensions.

The remainder of the paper is organized as follows: Section 2 discusses the formulation of peridynamics, PMLs, and their numerical implementation; Section 3 gives some results; and Section 4 summarizes the report and details future work.

2. Formulation

In this section, a PML is formulated for state-based two-dimensional peridynamics. First, in Section 2A, a linear elastic, state-based peridynamics formulation will be reviewed. Next, Section 2B reviews the formulation of a PML. Section 2C then applies the PML to state-based peridynamics, and finally Section 2D discusses a discretization of the formulation using the standard node-based peridynamics method.

2A. ***Two-dimensional, state-based peridynamics.*** The continuum equation of motion in an elastic solid can be stated as

$$\rho \frac{\partial^2}{\partial t^2} \boldsymbol{u} = \nabla \cdot \bar{\boldsymbol{\sigma}} + \boldsymbol{b}, \tag{2-1}$$

where (in two dimensions) $\rho(\boldsymbol{x})$ [kg/m^2] is the density, $\boldsymbol{u}(\boldsymbol{x}, t)$ [m] is the displacement, $\bar{\boldsymbol{\sigma}}(\boldsymbol{x}, t)$ [N/m] is the stress tensor, and $\boldsymbol{b}(\boldsymbol{x})$ [N/m^2] is a body force [Malvern 1969]. (Throughout, boldface type denotes a vector and a boldface variable with an overbar denotes a tensor.) Equation (2-1) is a local formulation

because the divergence of the stress (and gradient of the displacement implied in its definition) represents a local operation on a variable. In other words, the action of $\nabla \cdot \bar{\boldsymbol{\sigma}}$ only depends on $\bar{\boldsymbol{\sigma}}$ at a single spatial point. In problems involving discontinuities, such as cracks, the divergence at such discontinuities is not well defined, leading to numerical implementation problems. Peridynamics proposes replacing $\nabla \cdot \bar{\boldsymbol{\sigma}}$ with a nonlocal operation that nonetheless also represents a force

$$\rho \frac{\partial^2}{\partial t^2} \boldsymbol{u} = \int_{\mathcal{H}_{\boldsymbol{x}}} \boldsymbol{f}(\boldsymbol{u}' - \boldsymbol{u}, \boldsymbol{x}' - \boldsymbol{x})\, dV_{\boldsymbol{x}'} + \boldsymbol{b}, \tag{2-2}$$

where $\boldsymbol{f}(\boldsymbol{x}' - \boldsymbol{x}, \boldsymbol{u}' - \boldsymbol{u})$ [N/m^4] represents a micromodulus force function (or kernel) that defines a force between two points and $\mathcal{H}_{\boldsymbol{x}}$ represents a horizon or maximum distance over which two points can influence each other [Silling 2000]. The micromodulus function becomes the constitutive response in the formulation, replacing Hooke's law in the continuum case. In its original form, the micromodulus function was developed as a simple elastic response following

$$\boldsymbol{f}(\boldsymbol{\eta}, \boldsymbol{\xi}) = c \frac{\boldsymbol{\xi} + \boldsymbol{\eta}}{|\boldsymbol{\xi} + \boldsymbol{\eta}|} \frac{|\boldsymbol{\xi} + \boldsymbol{\eta}| - |\boldsymbol{\eta}|}{|\boldsymbol{\eta}|} H(\delta - |\boldsymbol{\xi}|), \tag{2-3}$$

where c is some constant, $H(\cdot)$ is the Heaviside step function, and δ is the radius of the horizon region, which defines $\mathcal{H}_{\boldsymbol{x}}$ [Silling 2000]. Note that in contrast to [Silling 2000], for simplicity there is no history-dependent failure term in (2-3). Equation (2-3) is isotropic, though not strictly linear in terms of $\boldsymbol{u}$. Linearizing (2-3) gives

$$\boldsymbol{f}(\boldsymbol{\eta}, \boldsymbol{\xi}) = \bar{\boldsymbol{C}}(\boldsymbol{\xi})\boldsymbol{\eta}, \quad \bar{\boldsymbol{C}}(\boldsymbol{\xi}) = C(\boldsymbol{\xi}) \frac{\boldsymbol{\xi} \otimes \boldsymbol{\xi}}{|\boldsymbol{\xi}|^3}, \quad C(|\boldsymbol{\xi}|) = cH(\delta - |\boldsymbol{\xi}|), \tag{2-4}$$

where $\otimes$ denotes an outer product [Silling 2000]. The function $C(|\boldsymbol{\xi}|)$ is the kernel function, typically taken to be a Heaviside function. Here, we will also use a Gaussian kernel function, which tends to give smoother results with less apparent ringing in the solution. A Gaussian kernel is defined as

$$C_{\text{Gauss}}(|\boldsymbol{\xi}|) = ce^{-(|\boldsymbol{\xi}|/\delta)^2}. \tag{2-5}$$

For the Gaussian kernel, the horizon δ does not delineate a strict bond family as the Heaviside function, but describes the decay of the kernel. To determine the bond family, $\mathcal{H}_{\boldsymbol{x}}$, a small, arbitrary value can be chosen as a cutoff for the kernel. Note that the cutoff has a large impact on the efficiency of the method: too small a cutoff and a large number of bonds must be included in each calculation. Throughout, we set the cutoff to 10^{-6}.

A PML application requires an auxiliary field formulation, as it is essentially an anisotropic absorbing material, if a nonphysical one. Consequently, a state-based peridynamic formulation [Silling et al. 2007] is necessary to implement the required constitutive relations in the absorber. State-based peridynamics uses a family of bonds to determine a given force rather than a single bond independently. This more general approach allows for inelastic behavior and more general elastic behavior, and is governed by

$$\rho \frac{\partial^2}{\partial t^2} \boldsymbol{u} = \int_{\mathcal{H}_{\boldsymbol{x}}} (\bar{\boldsymbol{T}}[\boldsymbol{x}, t]\langle \boldsymbol{x}' - \boldsymbol{x} \rangle - \bar{\boldsymbol{T}}[\boldsymbol{x}', t]\langle \boldsymbol{x} - \boldsymbol{x}' \rangle)\, dV_{\boldsymbol{x}'} + \boldsymbol{b}, \tag{2-6}$$

where $\bar{\boldsymbol{T}}[\boldsymbol{x}, t]\langle \boldsymbol{x}' - \boldsymbol{x} \rangle$ is a peridynamic vector state, with the parameters in the square brackets indicating variables that act as arguments to any functions referenced in the vector state and the variables in the

angle brackets acting as arguments to the vector state itself. In the state-based formulation of [Foster et al. 2010], the deformation gradient, given by

$$\bar{\boldsymbol{F}} = \bar{\boldsymbol{I}} + \boldsymbol{u}\nabla, \tag{2-7}$$

can be approximated as a vector state as

$$\bar{\boldsymbol{F}}[\boldsymbol{x}, t] = \left[\int_{\mathcal{H}_x} C(|\boldsymbol{\xi}|)(\boldsymbol{Y}[\boldsymbol{x}, t]\langle\boldsymbol{\xi}\rangle \otimes \boldsymbol{\xi})\, dV_{\boldsymbol{x}'}\right]\bar{\boldsymbol{K}}^{-1}, \tag{2-8}$$

where $\boldsymbol{\xi} = \boldsymbol{x}' - \boldsymbol{x}$, $\bar{\boldsymbol{K}}$ is a shape tensor given by

$$\bar{\boldsymbol{K}}[\boldsymbol{x}, t] = \int_{\mathcal{H}_x} C(|\boldsymbol{\xi}|)(\boldsymbol{\xi} \otimes \boldsymbol{\xi})\, dV_{\boldsymbol{x}'}, \tag{2-9}$$

and $\boldsymbol{Y}$ is a deformation vector state given by

$$\boldsymbol{Y}[\boldsymbol{x}, t]\langle\boldsymbol{\xi}\rangle = \boldsymbol{\eta} + \boldsymbol{\xi}, \tag{2-10}$$

with $\boldsymbol{\eta} = \boldsymbol{u}[\boldsymbol{x}', t] - \boldsymbol{u}[\boldsymbol{x}, t]$ [Foster et al. 2010].

The deformation gradient can now be substituted into Hooke's law and strain-displacement relations, giving a stress term $\bar{\boldsymbol{\sigma}}$ in terms of $\boldsymbol{u}$ in plane strain

$$\rho\frac{\partial^2}{\partial t^2}\boldsymbol{u} = \nabla\cdot\bar{\boldsymbol{\sigma}} = \nabla\cdot(\bar{\boldsymbol{c}} : \bar{\boldsymbol{\epsilon}}), \tag{2-11}$$

where

$$\bar{\boldsymbol{\epsilon}}[\boldsymbol{x}, t] = \tfrac{1}{2}(\nabla\boldsymbol{u} + \boldsymbol{u}\nabla) = \tfrac{1}{2}(\bar{\boldsymbol{F}}[\boldsymbol{x}, t] + \bar{\boldsymbol{F}}[\boldsymbol{x}, t]^{\boldsymbol{T}} - 2\bar{\boldsymbol{I}}), \tag{2-12}$$

$$\bar{\boldsymbol{c}} = \frac{E}{(1+\nu)(1-2\nu)}\begin{bmatrix} 1-\nu & \nu & 0 \\ \nu & 1-\nu & 0 \\ 0 & 0 & 1-2\nu \end{bmatrix} = \begin{bmatrix} \lambda+2\mu & \lambda & 0 \\ \lambda & \lambda+2\mu & 0 \\ 0 & 0 & 2\mu \end{bmatrix}, \tag{2-13}$$

E is the Young's modulus, ν is the Poisson's ratio, and λ and μ are the Lamé parameters. Ultimately, the peridynamic vector state $\boldsymbol{T}$ for plane strain elasticity is given by

$$\bar{\boldsymbol{T}}[\boldsymbol{x}, t]\langle\boldsymbol{\xi}\rangle = C(|\boldsymbol{\xi}|)\bar{\boldsymbol{\sigma}}[\boldsymbol{x}, t]\bar{\boldsymbol{K}}^{-1}\boldsymbol{\xi}. \tag{2-14}$$

2B. ***Perfectly matched layer.*** The first step in formulating a PML is to construct an analytic continuation to the complex plane

$$\hat{x} = x + ig(x), \tag{2-15}$$

where $g(x)$ is a given function describing the deformation [Johnson 2010]. This mapping has the effect of transforming traveling waves of the form e^{ikx}, where $k = \omega/c$ is the wave number, into evanescent waves of the form $e^{ikx}e^{-kg(x)}$, thus attenuating such waves in the PML region.

Substituting $\hat{x}$ into the above equations would yield a viable method, though one that requires complex coordinates. A simpler solution is to change variables back to the real part x, which requires a relation for the differential quantities, given as

$$\partial\hat{x} = \left[1 + i\frac{d}{dx}g\right]\partial x; \tag{2-16}$$

partial differential quantities are used, as this is used as a substitution for the above equations involving functions of both x and t [Johnson 2010]. A convenient choice for $g(x)$ is

$$\frac{d}{dx}g(x) = \frac{\phi(x)}{\omega}, \tag{2-17}$$

because the $1/\omega$ factor creates a frequency-independent attenuation rate in dispersionless materials [Johnson 2010]. (Peridynamic formulations are not dispersionless, as discussed in [Weckner and Abeyaratne 2005], though this standard choice is used for simplicity.) Finally, the substitution that must be made for any spatial derivative can be written

$$\frac{\partial}{\partial x} \to \frac{1}{1+i\phi(x)/\omega}\frac{\partial}{\partial x}. \tag{2-18}$$

Before applying a PML directly to the peridynamic equation, (2-1) will be treated so that the PML application to peridynamics will be clear. It is convenient to convert (2-1) to the Laplace domain, assuming e^{-st} time dependence, giving

$$\rho s^2 \tilde{\boldsymbol{u}} = \nabla \cdot \tilde{\bar{\boldsymbol{\sigma}}}, \tag{2-19}$$

where the Laplace transform of a variable is indicated by $\mathcal{L}\{f\} = \tilde{f}$. Next, we express the wave equation as two coupled first-order partial differential equations, the first in $\tilde{\boldsymbol{u}}$ and the second in $s\tilde{\bar{\boldsymbol{\psi}}} = \tilde{\bar{\boldsymbol{\sigma}}}$:

$$\rho s\tilde{\boldsymbol{u}} = \nabla \cdot \tilde{\bar{\boldsymbol{\psi}}}, \quad s\tilde{\bar{\boldsymbol{\psi}}} = \bar{\boldsymbol{c}} : \tilde{\bar{\boldsymbol{\epsilon}}}. \tag{2-20}$$

Expanding (2-20) into components gives five coupled equations:

$$\begin{gathered}
\rho s\tilde{u}_x = \frac{\partial}{\partial x}\tilde{\psi}_x + \frac{\partial}{\partial y}\tilde{\psi}_\tau, \quad \rho s\tilde{u}_y = \frac{\partial}{\partial x}\tilde{\psi}_\tau + \frac{\partial}{\partial y}\tilde{\psi}_y, \\
s\tilde{\psi}_x = (\lambda+2\mu)\frac{\partial}{\partial x}\tilde{u}_x + \lambda\frac{\partial}{\partial y}\tilde{u}_y, \quad s\tilde{\psi}_y = \lambda\frac{\partial}{\partial x}\tilde{u}_x + (\lambda+2\mu)\frac{\partial}{\partial y}\tilde{u}_y, \quad s\tilde{\psi}_\tau = \mu\Big(\frac{\partial}{\partial y}\tilde{u}_x + \frac{\partial}{\partial x}\tilde{u}_y\Big).
\end{gathered} \tag{2-21}$$

Here, we will make the substitution given in (2-18) for all spatial derivatives, written as

$$\frac{\partial}{\partial x} \to \frac{s}{s+\phi(x)}\frac{\partial}{\partial x} \tag{2-22}$$

in the Laplace domain, and later define ϕ_x and ϕ_y in the desired absorbing boundary locations. Using $(2\text{-}21)_1$ as an example, we get

$$\begin{aligned}
\rho s\tilde{u}_x &= \frac{s}{s+\phi_x}\frac{\partial}{\partial x}\tilde{\psi}_x + \frac{s}{s+\phi_y}\frac{\partial}{\partial y}\tilde{\psi}_\tau \\
&\implies \rho(s+\phi_x)(s+\phi_y)\tilde{u}_x = (s+\phi_y)\frac{\partial}{\partial x}\tilde{\psi}_x + (s+\phi_x)\frac{\partial}{\partial y}\tilde{\psi}_\tau.
\end{aligned} \tag{2-23}$$

The remaining components of (2-21) can be expanded in a similar way.

Wherever $\phi > 0$, $\boldsymbol{u}$ and $\bar{\boldsymbol{\sigma}}$ will exponentially decay. Before discretization, any change in ϕ will not result in any reflections, so the region of interest would have $\phi = 0$, and the PML region could have a

discontinuity in applying ϕ. In practice, however, numerical reflections can result from discontinuous material parameters after discretization, so it is better to use a smooth transition for ϕ. Here, we divide the PML region into two parts, one in which ϕ is a constant value, and the other in which ϕ ramps up to that constant value following a Gaussian distribution. An example is shown in Figure 1, with the constant region set to 0.1 m and the Gaussian region 0.2 m. The variance of the distribution is set so that the minimum value in the Gaussian region is 10^{-6}.

2C. ***Auxiliary field formulation and PML application.*** Peridynamics is not typically stated in terms of Cartesian components as in (2-24), but we can expand the state-based formulation into components and match terms to (2-24). Following this approach yields a viable method for performing PML substitutions.

First, the state-based peridynamic equations (2-6)–(2-14) can be written explicitly as

$$\begin{aligned}
\rho s\tilde{u}_x[\boldsymbol{x},s] &= \int_{\mathcal{H}_{\boldsymbol{x}}} C(|\boldsymbol{\xi}|)\big[(\tilde{\psi}_x[\boldsymbol{x},s]k^{\mathrm{inv}}_{xx}+\tilde{\psi}_\tau[\boldsymbol{x},s]k^{\mathrm{inv}}_{yx})\xi_x+(\tilde{\psi}_x[\boldsymbol{x}',s]k'^{\mathrm{inv}}_{xx}+\tilde{\psi}_\tau[\boldsymbol{x}',s]k'^{\mathrm{inv}}_{yx})\xi_x\big]dV_{\boldsymbol{x}'}\\
&\quad+\int_{\mathcal{H}_{\boldsymbol{x}}} C(|\boldsymbol{\xi}|)\big[(\tilde{\psi}_x[\boldsymbol{x},s]k^{\mathrm{inv}}_{xy}+\tilde{\psi}_\tau[\boldsymbol{x},s]k^{\mathrm{inv}}_{yy})\xi_y+(\tilde{\psi}_x[\boldsymbol{x}',s]k'^{\mathrm{inv}}_{xy}+\tilde{\psi}_\tau[\boldsymbol{x}',s]k'^{\mathrm{inv}}_{yy})\xi_y\big]dV_{\boldsymbol{x}'},\\
\rho s\tilde{u}_y[\boldsymbol{x},s] &= \int_{\mathcal{H}_{\boldsymbol{x}}} C(|\boldsymbol{\xi}|)\big[(\tilde{\psi}_\tau[\boldsymbol{x},s]k^{\mathrm{inv}}_{xx}+\tilde{\psi}_y[\boldsymbol{x},s]k^{\mathrm{inv}}_{yx})\xi_x+(\tilde{\psi}_\tau[\boldsymbol{x}',s]k'^{\mathrm{inv}}_{xx}+\tilde{\psi}_y[\boldsymbol{x}',s]k'^{\mathrm{inv}}_{yx})\xi_x\big]dV_{\boldsymbol{x}'}\\
&\quad+\int_{\mathcal{H}_{\boldsymbol{x}}} C(|\boldsymbol{\xi}|)\big[(\tilde{\psi}_\tau[\boldsymbol{x},s]k^{\mathrm{inv}}_{xy}+\tilde{\psi}_y[\boldsymbol{x},s]k^{\mathrm{inv}}_{yy})\xi_y+(\tilde{\psi}_\tau[\boldsymbol{x}',s]k'^{\mathrm{inv}}_{xy}+\tilde{\psi}_y[\boldsymbol{x}',s]k'^{\mathrm{inv}}_{yy})\xi_y\big]dV_{\boldsymbol{x}'},\\
s\tilde{\psi}_x[\boldsymbol{x},s] &= (\lambda+2\mu)\left[\int_{\mathcal{H}_{\boldsymbol{x}}} C(|\boldsymbol{\xi}|)(\tilde{Y}_x[\boldsymbol{x},s]\xi_x k^{\mathrm{inv}}_{xx}+\tilde{Y}_x[\boldsymbol{x},s]\xi_y k^{\mathrm{inv}}_{yx})\,dV_{\boldsymbol{x}'}-1\right]\\
&\quad+\lambda\left[\int_{\mathcal{H}_{\boldsymbol{x}}} C(|\boldsymbol{\xi}|)(\tilde{Y}_y[\boldsymbol{x},s]\xi_x k^{\mathrm{inv}}_{xy}+\tilde{Y}_y[\boldsymbol{x},s]\xi_y k^{\mathrm{inv}}_{yy})\,dV_{\boldsymbol{x}'}-1\right],\\
s\tilde{\psi}_y[\boldsymbol{x},s] &= \lambda\left[\int_{\mathcal{H}_{\boldsymbol{x}}} C(|\boldsymbol{\xi}|)(\tilde{Y}_x[\boldsymbol{x},s]\xi_x k^{\mathrm{inv}}_{xx}+\tilde{Y}_x[\boldsymbol{x},s]\xi_y k^{\mathrm{inv}}_{yx})\,dV_{\boldsymbol{x}'}-1\right]\\
&\quad+(\lambda+2\mu)\left[\int_{\mathcal{H}_{\boldsymbol{x}}} C(|\boldsymbol{\xi}|)(\tilde{Y}_y[\boldsymbol{x},s]\xi_x k^{\mathrm{inv}}_{xy}+\tilde{Y}_y[\boldsymbol{x},s]\xi_y k^{\mathrm{inv}}_{yy})\,dV_{\boldsymbol{x}'}-1\right],\\
s\tilde{\psi}_\tau[\boldsymbol{x},s] &= \mu\int_{\mathcal{H}_{\boldsymbol{x}}} C(|\boldsymbol{\xi}|)\big(\tilde{Y}_x[\boldsymbol{x},s]\xi_x k^{\mathrm{inv}}_{xy}+\tilde{Y}_x[\boldsymbol{x},s]\xi_y k^{\mathrm{inv}}_{yy}\big)\,dV_{\boldsymbol{x}'}\\
&\quad+\mu\int_{\mathcal{H}_{\boldsymbol{x}}} C(|\boldsymbol{\xi}|)\big(\tilde{Y}_y[\boldsymbol{x},s]\xi_x k^{\mathrm{inv}}_{xx}+\tilde{Y}_y[\boldsymbol{x},s]\xi_y k^{\mathrm{inv}}_{yx}\big)\,dV_{\boldsymbol{x}'},
\end{aligned}\tag{2-24}$$

where

$$\overline{\boldsymbol{K}}^{-1}=\begin{bmatrix} k^{\mathrm{inv}}_{xx} & k^{\mathrm{inv}}_{xy}\\ k^{\mathrm{inv}}_{yx} & k^{\mathrm{inv}}_{yy}\end{bmatrix}.\tag{2-25}$$

Though no derivatives appear in (2-24), the correspondence of each term to those in (2-21) is apparent — with partial derivatives following the component of $\boldsymbol{\xi}$ — and the PML substitutions can be made. For

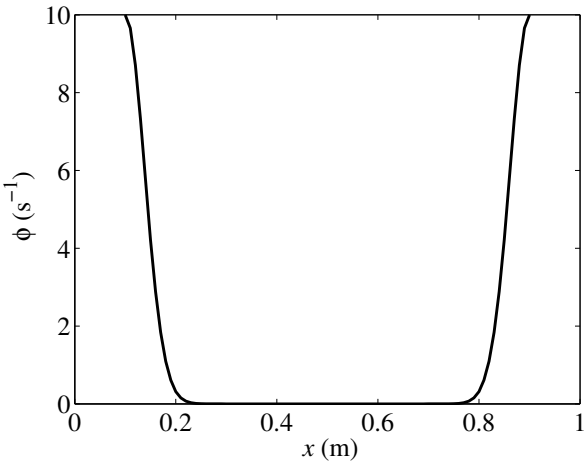

Figure 1. An example of a PML across one dimension using a Gaussian ramp.

example, the first equation in (2-24) can be rewritten as

$$\begin{aligned}\rho(s+\phi_x)(s+\phi_y)\tilde{u}_x = {} & (s+\phi_y)\int_{\mathcal{H}_{\boldsymbol{x}}} C(|\boldsymbol{\xi}|)\big(\tilde{\psi}_x[\boldsymbol{x},s]k_{xx}^{\text{inv}}+\tilde{\psi}_{xy}[\boldsymbol{x},s]k_{yx}^{\text{inv}}\big)\xi_x\,dV_{\boldsymbol{x}'}\\ & +(s+\phi_y)\int_{\mathcal{H}_{\boldsymbol{x}}} C(|\boldsymbol{\xi}|)\big(\tilde{\psi}_x[\boldsymbol{x}',s]k_{xx}'^{\text{inv}}+\tilde{\psi}_{xy}[\boldsymbol{x}',s]k_{yx}'^{\text{inv}}\big)\xi_x\,dV_{\boldsymbol{x}'}\\ & +(s+\phi_x)\int_{\mathcal{H}_{\boldsymbol{x}}} C(|\boldsymbol{\xi}|)\big(\tilde{\psi}_x[\boldsymbol{x},s]k_{xy}^{\text{inv}}+\tilde{\psi}_{\tau}[\boldsymbol{x},s]k_{yy}^{\text{inv}}\big)\xi_y\,dV_{\boldsymbol{x}'}\\ & +(s+\phi_x)\int_{\mathcal{H}_{\boldsymbol{x}}} C(|\boldsymbol{\xi}|)\big(\tilde{\psi}_x[\boldsymbol{x}',s]k_{xy}'^{\text{inv}}+\tilde{\psi}_{\tau}[\boldsymbol{x}',s]k_{yy}'^{\text{inv}}\big)\xi_y\,dV_{\boldsymbol{x}'},\end{aligned}\tag{2-26}$$

with the remaining equations following similarly.

2D. ***Discretization.*** For the temporal discretization, forward Euler will be used to simplify the presentation and implementation. Higher-order temporal discretizations can be used, though they lead to more terms in what follows. The Laplace domain was used throughout to facilitate the temporal discretization of the final equations. Because differentiation in the Laplace domain is represented by s, approximations to s can be directly substituted in terms of the z-transform. This technique is used in the design of digital filters, where it is known as "filter design by approximation of derivatives" or "the bilinear transformation" [Proakis and Manolakis 1996], and in integral equation methods where it is known as "convolution quadrature" [Lubich 1988a; 1988b], or "finite difference delay modeling" [Wang et al. 2008]. A forward Euler approximation can be stated as the substitution

$$s \to \frac{z-1}{\Delta t},\tag{2-27}$$

where z is the z-transform[1] variable representing a unit advance and Δt is the time step size. Substitution

[1]The z-transform is defined here as $X(z) = Z\{x[n]\} = \sum_{n=0}^{\infty} x[n]z^{-n}$ for causal signals.

into (2-26) gives

$$\begin{aligned}\rho(z-1+\Delta t\phi_x)(z-1+\Delta t\phi_y)U_x &= (z-1+\Delta t\phi_y)\int_{\mathcal{H}_{\boldsymbol{x}}} C(|\boldsymbol{\xi}|)\big(\Psi_x[\boldsymbol{x},z]k^{\text{inv}}_{xx}+\Psi_\tau[\boldsymbol{x},z]k^{\text{inv}}_{yx}\big)\xi_x\,dV_{\boldsymbol{x}'}\\ &\quad+(z-1+\Delta t\phi_y)\int_{\mathcal{H}_{\boldsymbol{x}}} C(|\boldsymbol{\xi}|)\big(\Psi_x[\boldsymbol{x}',z]k'^{\text{inv}}_{xx}+\Psi_\tau[\boldsymbol{x}',z]k'^{\text{inv}}_{yx}\big)\xi_x\,dV_{\boldsymbol{x}'}\\ &\quad+(z-1+\Delta t\phi_x)\int_{\mathcal{H}_{\boldsymbol{x}}} C(|\boldsymbol{\xi}|)\big(\Psi_x[\boldsymbol{x},z]k^{\text{inv}}_{xy}+\Psi_\tau[\boldsymbol{x},z]k^{\text{inv}}_{yy}\big)\xi_y\,dV_{\boldsymbol{x}'}\\ &\quad+(z-1+\Delta t\phi_x)\int_{\mathcal{H}_{\boldsymbol{x}}} C(|\boldsymbol{\xi}|)\big(\Psi_x[\boldsymbol{x}',z]k'^{\text{inv}}_{xy}+\Psi_\tau[\boldsymbol{x}',z]k'^{\text{inv}}_{yy}\big)\xi_y\,dV_{\boldsymbol{x}'},\end{aligned}\tag{2-28}$$

where capital letters indicate the z-transform of a variable. Expanding the quadratic term on the left-hand side gives

$$\begin{aligned}(z-1+\Delta t\phi_x)(z-1+\Delta t\phi_y) &= \Delta t^2\phi_x\phi_y+\Delta t\phi_x z-\Delta t\phi_x+\Delta t\phi_y z+z^2-z-\Delta t\phi_y-z+1\\ &= z^2+(\Delta t\phi_x+\Delta t\phi_y-2)z+\Delta t^2\phi_x\phi_y-\Delta t\phi_x-\Delta t\phi_y+1.\end{aligned}\tag{2-29}$$

Multiplying by z^{-2} and rearranging gives an update equation in terms of z, which can be converted to a time-stepping method via the inverse z-transform[2] (assuming vanishing initial conditions and an appropriate region of convergence) as

$$\begin{aligned}u_x[\boldsymbol{x},l] &= -(\gamma_x+\gamma_y)u_x[\boldsymbol{x},l-1]-\gamma_x\gamma_y u_x[\boldsymbol{x},l-2]\\ &\quad+\frac{\Delta t}{\rho}\int_{\mathcal{H}_{\boldsymbol{x}}} C(|\boldsymbol{\xi}|)\big(\psi_x[\boldsymbol{x},l-1]k^{\text{inv}}_{xx}+\psi_\tau[\boldsymbol{x},l-1]k^{\text{inv}}_{yx}\big)\xi_x\,dV_{\boldsymbol{x}'}\\ &\quad+\frac{\Delta t}{\rho}\int_{\mathcal{H}_{\boldsymbol{x}}} C(|\boldsymbol{\xi}|)\big(\psi_x[\boldsymbol{x}',l-1]k'^{\text{inv}}_{xx}+\psi_\tau[\boldsymbol{x}',l-1]k'^{\text{inv}}_{yx}\big)\xi_x\,dV_{\boldsymbol{x}'}\\ &\quad+\frac{\Delta t}{\rho}\gamma_y\int_{\mathcal{H}_{\boldsymbol{x}}} C(|\boldsymbol{\xi}|)\big(\psi_x[\boldsymbol{x},l-2]k^{\text{inv}}_{xx}+\psi_\tau[\boldsymbol{x},l-2]k^{\text{inv}}_{yx}\big)\xi_x\,dV_{\boldsymbol{x}'}\\ &\quad+\frac{\Delta t}{\rho}\gamma_y\int_{\mathcal{H}_{\boldsymbol{x}}} C(|\boldsymbol{\xi}|)\big(\psi_x[\boldsymbol{x}',l-2]k'^{\text{inv}}_{xx}+\psi_\tau[\boldsymbol{x}',l-2]k'^{\text{inv}}_{yx}\big)\xi_x\,dV_{\boldsymbol{x}'}\\ &\quad+\frac{\Delta t}{\rho}\int_{\mathcal{H}_{\boldsymbol{x}}} C(|\boldsymbol{\xi}|)\big(\psi_x[\boldsymbol{x},l-1]k^{\text{inv}}_{xy}+\psi_\tau[\boldsymbol{x},l-1]k^{\text{inv}}_{yy}\big)\xi_y\,dV_{\boldsymbol{x}'}\\ &\quad+\frac{\Delta t}{\rho}\int_{\mathcal{H}_{\boldsymbol{x}}} C(|\boldsymbol{\xi}|)\big(\psi_x[\boldsymbol{x}',l-1]k'^{\text{inv}}_{xy}+\psi_\tau[\boldsymbol{x}',l-1]k'^{\text{inv}}_{yy}\big)\xi_y\,dV_{\boldsymbol{x}'}\\ &\quad+\frac{\Delta t}{\rho}\gamma_x\int_{\mathcal{H}_{\boldsymbol{x}}} C(|\boldsymbol{\xi}|)\big(\psi_x[\boldsymbol{x},l-2]k^{\text{inv}}_{xy}+\psi_\tau[\boldsymbol{x},l-2]k^{\text{inv}}_{yy}\big)\xi_y\,dV_{\boldsymbol{x}'}\\ &\quad+\frac{\Delta t}{\rho}\gamma_x\int_{\mathcal{H}_{\boldsymbol{x}}} C(|\boldsymbol{\xi}|)\big(\psi_x[\boldsymbol{x}',l-2]k'^{\text{inv}}_{xy}+\psi_\tau[\boldsymbol{x}',l-2]k'^{\text{inv}}_{yy}\big)\xi_y\,dV_{\boldsymbol{x}'},\end{aligned}\tag{2-30}$$

[2]The only necessary property is the delay: $x[n-k]\leftrightarrow z^{-k}X(z)$

where l is the time step number, $\gamma_x = \Delta t\phi_x - 1$, and $\gamma_y = \Delta t\phi_y - 1$. A stress component update equation becomes, for example,

$$\begin{aligned}\psi_x[\boldsymbol{x}, l] = &-(\gamma_x+\gamma_y)\psi_x[\boldsymbol{x}, l-1] - \gamma_x\gamma_y\psi_x[\boldsymbol{x}, l-2]\\ &+ \Delta t(\lambda+2\mu)\left[\int_{\mathcal{H}_{\boldsymbol{x}}} C(|\boldsymbol{\xi}|)(Y_x[\boldsymbol{x}, l-1]\xi_x k_{xx}^{\text{inv}} + Y_x[\boldsymbol{x}, l-1]\xi_y k_{yx}^{\text{inv}})\,dV_{\boldsymbol{x}'} - 1\right]\\ &+ \Delta t\gamma_y(\lambda+2\mu)\left[\int_{\mathcal{H}_{\boldsymbol{x}}} C(|\boldsymbol{\xi}|)(Y_x[\boldsymbol{x}, l-2]\xi_x k_{xx}^{\text{inv}} + Y_x[\boldsymbol{x}, l-2]\xi_y k_{yx}^{\text{inv}})\,dV_{\boldsymbol{x}'} - 1\right]\\ &+ \Delta t\lambda\left[\int_{\mathcal{H}_{\boldsymbol{x}}} C(|\boldsymbol{\xi}|)(Y_y[\boldsymbol{x}, l-1]\xi_x k_{xy}^{\text{inv}} + Y_y[\boldsymbol{x}, l-1]\xi_y k_{yy}^{\text{inv}})\,dV_{\boldsymbol{x}'} - 1\right]\\ &+ \Delta t\lambda\gamma_x\left[\int_{\mathcal{H}_{\boldsymbol{x}}} C(|\boldsymbol{\xi}|)(Y_y[\boldsymbol{x}, l-2]\xi_x k_{xy}^{\text{inv}} + Y_y[\boldsymbol{x}, l-2]\xi_y k_{yy}^{\text{inv}})\,dV_{\boldsymbol{x}'} - 1\right]. \quad (2\text{-}31)\end{aligned}$$

Finally, (2-30) can be discretized spatially using a simple one-point integration and point match testing, giving, for the x-component of displacement,

$$\begin{aligned}u_x[\boldsymbol{x}_i, l] = &-(\gamma_x+\gamma_y)u_x[\boldsymbol{x}_i, l-1] - \gamma_x\gamma_y u_x[\boldsymbol{x}_i, l-2]\\ &+ \frac{\Delta t}{\rho}\sum_{j=1}^{N_i} C(|\boldsymbol{\xi}_{ij}|)(\psi_x[\boldsymbol{x}_i, l-1]k_{i,xx}^{\text{inv}} + \psi_\tau[\boldsymbol{x}_i, l-1]k_{i,yx}^{\text{inv}})\xi_x V_j\\ &+ \frac{\Delta t}{\rho}\sum_{j=1}^{N_i} C(|\boldsymbol{\xi}_{ij}|)(\psi_x[\boldsymbol{x}_j, l-1]k_{j,xx}^{\text{inv}} + \psi_\tau[\boldsymbol{x}_j, l-1]k_{j,yx}^{\text{inv}})\xi_x V_j\\ &+ \frac{\Delta t}{\rho}\gamma_y\sum_{j=1}^{N_i} C(|\boldsymbol{\xi}_{ij}|)(\psi_x[\boldsymbol{x}_i, l-2]k_{i,xx}^{\text{inv}} + \psi_\tau[\boldsymbol{x}_i, l-2]k_{i,yx}^{\text{inv}})\xi_x V_j\\ &+ \frac{\Delta t}{\rho}\gamma_y\sum_{j=1}^{N_i} C(|\boldsymbol{\xi}_{ij}|)(\psi_x[\boldsymbol{x}_j, l-2]k_{j,xx}^{\text{inv}} + \psi_\tau[\boldsymbol{x}_j, l-2]k_{j,yx}^{\text{inv}})\xi_x V_j\\ &+ \frac{\Delta t}{\rho}\sum_{j=1}^{N_i} C(|\boldsymbol{\xi}_{ij}|)(\psi_x[\boldsymbol{x}_i, l-1]k_{i,xy}^{\text{inv}} + \psi_\tau[\boldsymbol{x}_i, l-1]k_{i,yy}^{\text{inv}})\xi_y V_j\\ &+ \frac{\Delta t}{\rho}\sum_{j=1}^{N_i} C(|\boldsymbol{\xi}_{ij}|)(\psi_x[\boldsymbol{x}_j, l-1]k_{j,xy}^{\text{inv}} + \psi_\tau[\boldsymbol{x}_j, l-1]k_{j,yy}^{\text{inv}})\xi_y V_j\\ &+ \frac{\Delta t}{\rho}\gamma_x\sum_{j=1}^{N_i} C(|\boldsymbol{\xi}_{ij}|)(\psi_x[\boldsymbol{x}_i, l-2]k_{i,xy}^{\text{inv}} + \psi_\tau[\boldsymbol{x}_i, l-2]k_{i,yy}^{\text{inv}})\xi_y V_j\\ &+ \frac{\Delta t}{\rho}\gamma_x\sum_{j=1}^{N_i} C(|\boldsymbol{\xi}_{ij}|)(\psi_x[\boldsymbol{x}_j, l-2]k_{j,xy}^{\text{inv}} + \psi_\tau[\boldsymbol{x}_j, l-2]k_{j,yy}^{\text{inv}})\xi_y V_j, \quad (2\text{-}32)\end{aligned}$$

where V_j is the volume of node j, N_i is the number of nodes in the neighborhood of node i, and $\boldsymbol{\xi}_{ij} = \boldsymbol{x}_j - \boldsymbol{x}_i$.

3. Results

The PML was tested on two types of problems, first a wave propagation problem, to demonstrate the effectiveness of the PML, and second a crack propagation problem.

3A. ***Wave propagation.*** The PML was first tested on a wave propagation problem with PML boundary layers and a Gaussian distribution as an initial condition. Specifically, the x-directed displacement was set to

$$u_x(\boldsymbol{x}, t = 0) = e^{-200|\boldsymbol{x}-\boldsymbol{p}_{\text{mid}}|^2}, \tag{3-1}$$

where $\boldsymbol{p}_{\text{mid}}$ is the midpoint of the region, which in this example was defined as $0 \le x, y \le 1$ and discretized with $\Delta x = \Delta y = 0.01$ m. The Young's modulus for the region was set to 1 Pa, the Poisson's ratio was $\frac{1}{4}$, and the density was $1\,\text{kg/m}^3$. The PML region was defined as the 0.3 m border around the $1\,\text{m} \times 1\,\text{m}$ region and used a Gaussian ramp with a width of 0.2 m, finally reaching a maximum of $50\,\text{s}^{-1}$ for the remaining 0.1 m. For the Gaussian kernel, a horizon size of $\delta = 1.1\Delta x$ was used, and for the Heaviside kernel, a horizon of $\delta = 3.1\Delta x$ was used. The kernel constant c in (2-4) and (2-5) is set to 1 throughout.

The simulation was run with both the Heaviside and Gaussian kernels, with the total strain energy shown in Figure 2. The Gaussian kernel (the dotted line) shows the largest drop in energy, reaching a minimum of 5.6×10^{-7}, and the Heaviside kernel (the dashed line) decreases to $1. \times 10^{-4}$. A bounded simulation is shown for reference (the solid line), which used a fixed displacement boundary condition and the Gaussian kernel. Figure 3 shows a waterfall plot of the x-directed displacement along the $y = 0.5$ line for the Gaussian kernel with the PML function ϕ_x shown in gray on the far end of the plot (corresponding to $t = 1$ s). Figure 4 shows the absolute value of the x-directed displacement at the edge of the PML region, in simulations terminated by a PML and with a fixed boundary condition. The wave

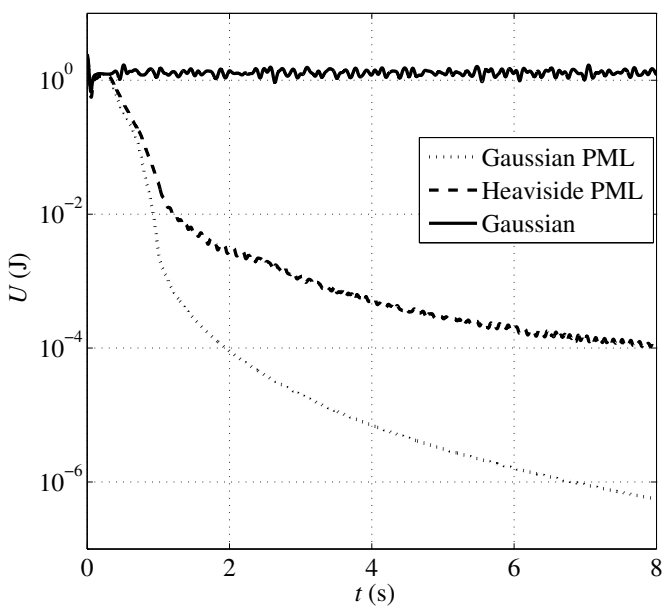

Figure 2. Total strain energy in a simulation terminated by a PML.

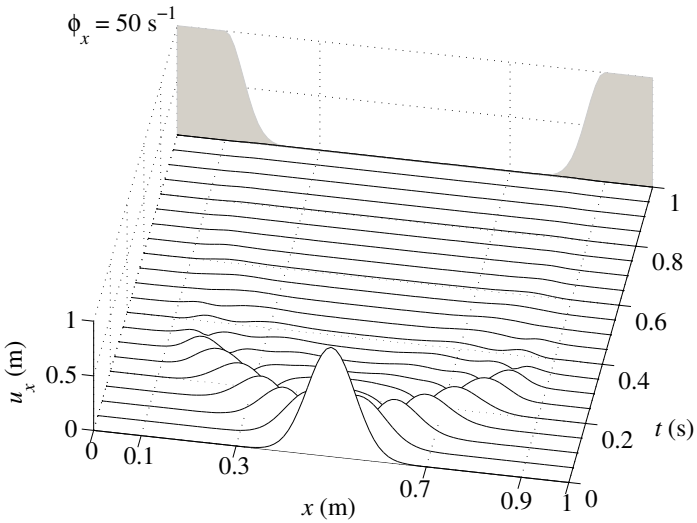

Figure 3. The x-directed displacement at $y = 0.5\,\mathrm{m}$, terminated by a PML.

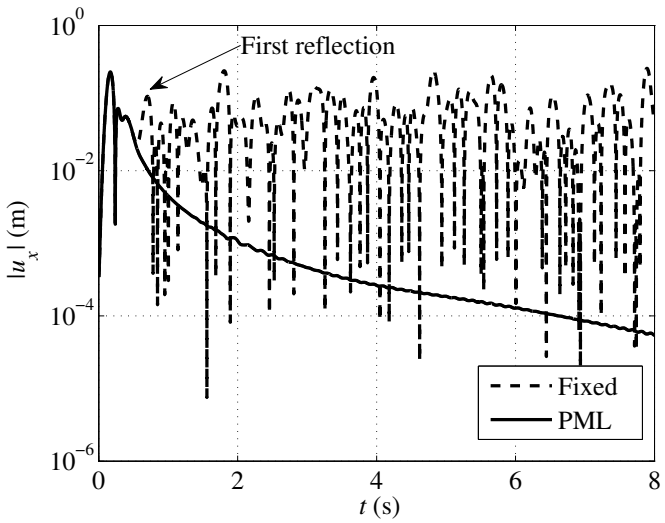

Figure 4. The x-directed displacement at $x = 0.3$, $y = 0.5\,\mathrm{m}$. The solid line shows results terminated by a PML, and the dashed line used a fixed boundary condition.

is absorbed at the boundary with minimal reflections: as can be seen, the plots align for a time, and where they deviate (indicating a reflection from the hard boundary), the PML simulation remains in decay.

For verification, the method was compared with an exact analytical solution. Consider a cylindrically symmetric wave propagating in an infinite elastic medium with the same constitutive parameters as the above example, and with an initial condition given by

$$u_0(r) = b\Big(\frac{r}{a}\Big)\Big[1 + \Big(\frac{r}{a}\Big)^2\Big]^{-3/2}, \tag{3-2}$$

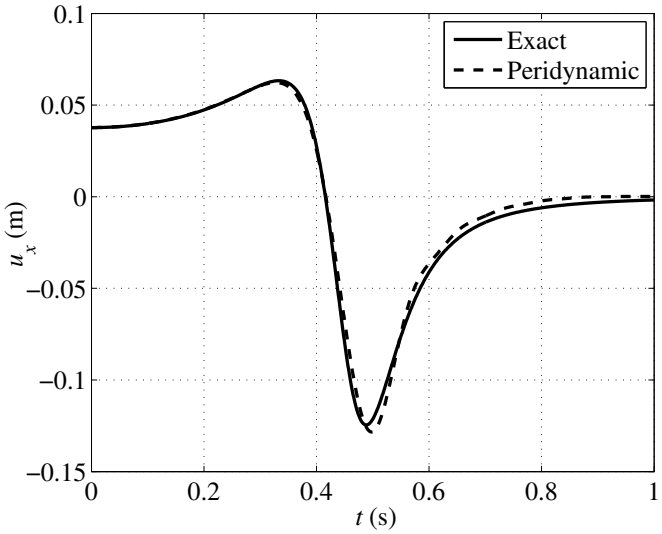

Figure 5. The x-directed displacement at $x = 0.5$, $y = 0$ m. The solid line shows the exact solution and the dashed line results terminated by a PML.

where here we take $b = 1$ and $a = 0.1$. The exact solution is given by [Eringen and Suhubi 1975]

$$u(r,t) = \frac{br}{\sqrt{2}aR^6}\sqrt{R^2+\alpha}(2\alpha - R^2), \quad \alpha = 1 + \frac{r^2 - c^2t^2}{a^2}, \quad R^2 = \sqrt{\alpha^2 + \frac{4c^2t^2}{a^2}}, \tag{3-3}$$

where c is the longitudinal wave speed. This problem was simulated in a two-dimensional region, 2 m × 2 m and $\Delta x = \Delta y = 0.01$ m, terminated by a PML with the same dimensions and magnitude as the above problem. The Gaussian kernel was used with a horizon size of $\delta = 0.75\Delta x$, with an actual cutoff of 0.028 m. The results are shown in Figure 5, with the exact solution shown as the solid line and the peridynamic solution shown as the dashed line. The peridynamic solution shows good agreement with the exact solution and minimal reflections from the PML boundary.

3B. ***Crack propagation.*** Crack propagation in a half-space can be useful for modeling physical phenomena such as indentation experiments. As an example, we model such a problem as a body force applied to a finite region with small precracks in a region terminated on three sides with PMLs. One addition to the algorithm for this problem was a drag term, used to reduce noise. For crack problems with a sudden force application, noise and oscillations can cause hot spots and undesirable cracking. To remedy this, a drag term can be added to smooth oscillations, by adjusting the nodal velocity as

$$\boldsymbol{v}^*[\boldsymbol{x}_i, l] = (1 - D)\boldsymbol{v}[\boldsymbol{x}_i, l] + \frac{D}{N_b}\sum_{j=1}^{N_b} \boldsymbol{v}[\boldsymbol{x}_j, l], \tag{3-4}$$

where D is the drag coefficient and N_b is the remaining number of bonds in the family of node n [Becker and Lucas 2011].

An absorbing boundary ensures that no reflections from the boundaries interfere with the crack propagation, possibly causing it to deviate. Figure 6 gives a schematic of the problem: the extent of the

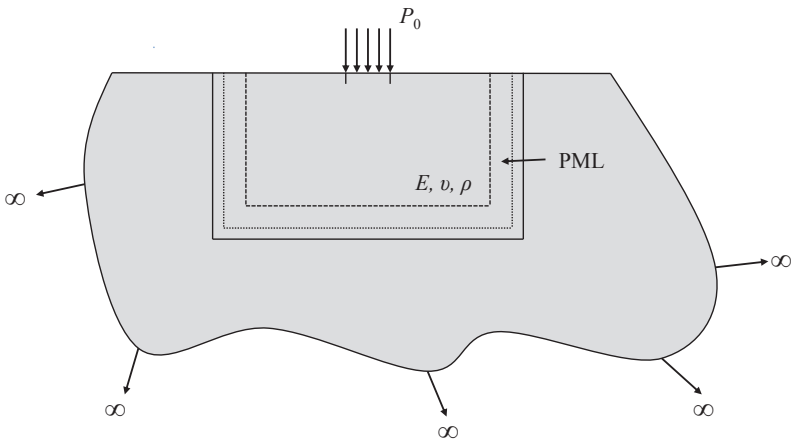

Figure 6. Schematic diagram of the problem for crack propagation in a half-space.

computation region is designated by the solid line, the PML ramp begins at the dashed line, and the PML plateaus at the dotted line. The computational region was 70 mm wide and 35.25 mm high, the PML region began at 15 mm from each edge (except the top) and peaked at 5 mm to a value of $5 \times 10^6\ \mathrm{s}^{-1}$. The node spacing was 0.496 mm and the time step size was 1 ns. For material values, the density was $2235\ \mathrm{kg/m}^3$, the Young's modulus was 65 GPa, the Poisson's ratio was 0.2, and the fracture criteria used a fracture energy of $204\ \mathrm{J/m}^2$. The failure criteria used in this simulation was bond-based, that is, a bond failed if it was stretched past a given limit, determined by the fracture energy [Ha and Bobaru 2010]. The maximum relative bond stretch was then 2.971×10^{-3}. The load was applied across a 10 mm region, centered at the top surface, with precracks on each edge with a length of two nodes or 0.993 mm. The simulation was run for a total of 10 μs, and the cracks were measured manually from the edge of the precracks to the extent of the damaged area.

Figure 7 shows a result which had an applied load of 250 N, yielding a 2.11 mm crack. Figure 8 shows a close-up of the damaged area from Figure 7. As can be seen, the crack extends three nodes down and

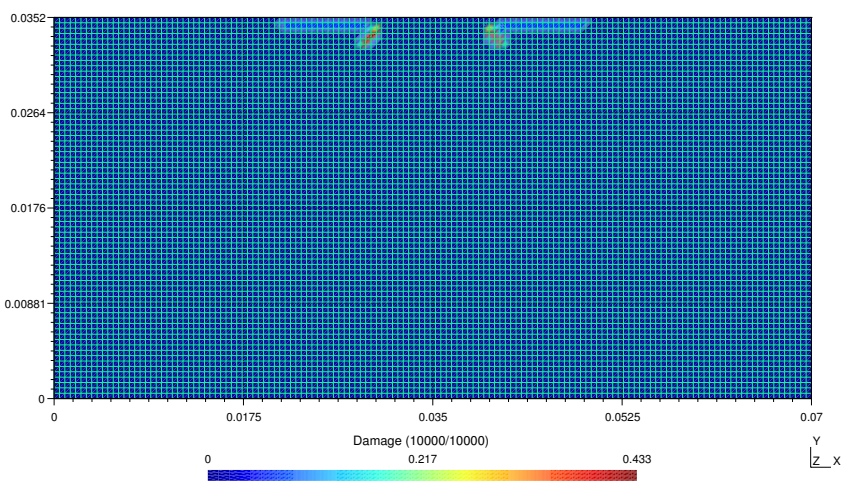

Figure 7. Damage map resulting from a 250 N applied load after 10 μs.

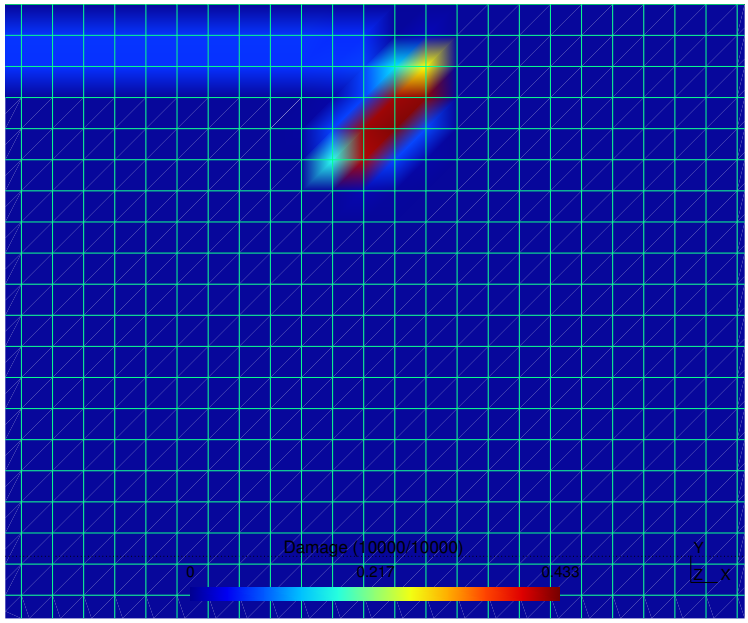

Figure 8. Close-up of damage map from Figure 7.

three nodes across. Finally, the applied load was varied between 140 N and 500 N, with the distance between the crack tips (the crack separation) versus the applied load shown as the dots in Figure 9. A curve, shown as the solid line in Figure 9, was fit using the form

$$d = Ap^s + B, \tag{3-5}$$

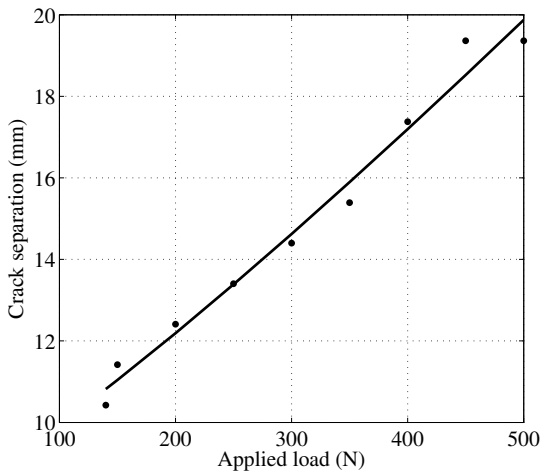

Figure 9. Crack separation versus applied force for indentation into an elastic half-space. Dots represent data points from the peridynamic simulation and the solid line is a curve fit.

where d is the crack tip separation distance, p is the applied load, and $A = 8.49 \times 10^{-3}$ mm/N^s, $s = 1.16$ and $B = 8.15$ mm were determined using least squares. The norm of the residual for the curve fit was 1.65×10^{-6}.

4. Conclusions

A perfectly matched layer (PML) was applied to peridynamics in two dimensions, allowing for the simulation of infinite regions. State-based peridynamics was used as more flexible constitutive relations are necessary to implement a perfectly matched layer, essentially an artificial anisotropic absorbing material. Standard discretization techniques were used: one-point integration and point-matching for the spatial discretization and forward Euler for the temporal discretization. Results show that the PML absorbs incoming waves and results in minimal reflections at the boundary between the absorbing layer and the computational region. A Gaussian function was used as a ramp to avoid these numerical reflections. Finally, a crack propagation problem was simulated in a half-space, modeling indentation problems. A three-dimensional implementation of the method would be straightforward, following an identical procedure for the peridynamics and PML formulation.

References

[Alles and van Dongen 2009] E. J. Alles and K. W. A. van Dongen, "Frequency domain perfectly matched layers for acoustic scattering integral equation problems", pp. 1610–1613 in *2009 IEEE International Ultrasonics Symposium* (Rome, 2009), edited by M. P. Yuhas, IEEE, Piscataway, NJ, 2009.

[Becker and Lucas 2011] R. Becker and R. J. Lucas, "An assessment of peridynamics for pre and post failure deformation", Technical report ARL-TR-5811, U.S. Army Research Laboratory, Aberdeen, MD, November 2011, Available at http://www.dtic.mil/cgi-bin/GetTRDoc?AD=ADA553977.

[Berenger 1994] J.-P. Berenger, "A perfectly matched layer for the absorption of electromagnetic waves", *J. Comput. Phys.* **114**:2 (1994), 185–200.

[Bobaru 2007] F. Bobaru, "Influence of van der Waals forces on increasing the strength and toughness in dynamic fracture of nanofibre networks: a peridynamic approach", *Model. Simul. Mater. Sci. Eng.* **15**:5 (2007), 397–417.

[Bobaru and Duangpanya 2010] F. Bobaru and M. Duangpanya, "The peridynamic formulation for transient heat conduction", *Int. J. Heat Mass Transf.* **53**:19-20 (2010), 4047–4059.

[Bobaru et al. 2009] F. Bobaru, M. Yang, L. F. Alves, S. A. Silling, E. Askari, and J. Xu, "Convergence, adaptive refinement, and scaling in 1D peridynamics", *Int. J. Numer. Methods Eng.* **77**:6 (2009), 852–877.

[Chew and Liu 1996] W. C. Chew and Q. H. Liu, "Perfectly matched layers for elastodynamics: a new absorbing boundary condition", *J. Comput. Acoust.* **4**:4 (1996), 341–359.

[Chew and Weedon 1994] W. C. Chew and W. H. Weedon, "A 3D perfectly matched medium from modified Maxwell's equations with stretched coordinates", *Microw. Opt. Tech. Lett.* **7**:13 (1994), 599–604.

[Demmie and Silling 2007] P. N. Demmie and S. A. Silling, "An approach to modeling extreme loading of structures using peridynamics", *J. Mech. Mater. Struct.* **2**:10 (2007), 1921–1945.

[Dong et al. 2004] X. T. Dong, X. S. Rao, Y. B. Gan, B. Guo, and W. Y. Yin, "Perfectly matched layer-absorbing boundary condition for left-handed materials", *IEEE Microw. Wirel. Compon. Lett.* **14**:6 (2004), 301–303.

[Du et al. 2012] Q. Du, M. D. Gunzburger, R. B. Lehoucq, and K. Zhou, "A nonlocal vector calculus, nonlocal volume-constrained problems, and nonlocal balance laws", *Math. Models Methods Appl. Sci.* (2012). Accepted for publication. Preprint SAND2010-8353J available from Sandia National Laboratories, 2010.

[Emmrich and Weckner 2006] E. Emmrich and O. Weckner, "The peridynamic model in non-local elasticity theory", *Proc. Appl. Math. Mech.* **6**:1 (2006), 155–156.

[Emmrich and Weckner 2007] E. Emmrich and O. Weckner, "The peridynamic equation and its spatial discretisation", *Math. Model. Anal.* **12**:1 (2007), 17–27.

[Eringen and Suhubi 1975] A. C. Eringen and E. S. Suhubi, *Elastodynamics*, Academic Press, New York, 1975.

[Festa and Nielsen 2003] G. Festa and S. Nielsen, "PML absorbing boundaries", *Bull. Seismol. Soc. Am.* **93**:2 (2003), 891–903.

[Foster et al. 2010] J. T. Foster, S. A. Silling, and W. W. Chen, "Viscoplasticity using peridynamics", *Int. J. Numer. Methods Eng.* **81**:10 (2010), 1242–1258.

[Gerstle et al. 2005] W. Gerstle, N. Sau, and S. A. Silling, "Peridynamic modeling of plain and reinforced concrete structures", pp. 54–88 in *18th International Conference on Structural Mechanics in Reactor Technology* (Beijing, 2005), edited by Y. Zhou, Atomic Energy Press, Beijing, 2005.

[Gerstle et al. 2008] W. Gerstle, S. A. Silling, D. Read, V. Tewary, and R. Lehoucq, "Peridynamic simulation of electromigration", *Comput. Mater. Continua* **8**:2 (2008), 75–92.

[Gerstle et al. 2011] W. Gerstle, N. Sau, and E. Aguilera, "Micropolar peridynamic constitutive model for concrete", pp. 1–8 in *19th International Conference on Structural Mechanics in Reactor Technology* (Toronto, ON, 2007), edited by V. C. Matzen, Elsevier, Amsterdam, 2011.

[Ha and Bobaru 2010] Y. D. Ha and F. Bobaru, "Studies of dynamic crack propagation and crack branching with peridynamics", *Int. J. Fract.* **162**:1-2 (2010), 229–244.

[Johnson 2010] S. G. Johnson, "Notes on perfectly matched layers", 2010, Available at http://math.mit.edu/~stevenj/18.369/pml.pdf.

[Kilic et al. 2009] B. Kilic, A. Agwai, and E. Madenci, "Peridynamic theory for progressive damage prediction in center-cracked composite laminates", *Compos. Struct.* **90**:2 (2009), 141–151.

[Liu and Tao 1997] Q.-H. Liu and J.-P. Tao, "The perfectly matched layer for acoustic waves in absorptive media", *J. Acoust. Soc. Am.* **102**:4 (1997), 2072–2082.

[Lubich 1988a] C. Lubich, "Convolution quadrature and discretized operational calculus, I", *Numer. Math.* **52**:2 (1988), 129–145.

[Lubich 1988b] C. Lubich, "Convolution quadrature and discretized operational calculus, II", *Numer. Math.* **52**:4 (1988), 413–425.

[Malvern 1969] L. E. Malvern, *Introduction to the mechanics of a continuous medium*, Prentice-Hall, Englewood Cliffs, NJ, 1969.

[Parks et al. 2008] M. L. Parks, P. Seleson, S. J. Plimpton, R. B. Lehoucq, and S. A. Silling, "Peridynamics with LAMMPS: a user guide", Technical report SAND2008-0135, Sandia National Laboratories, Albuquerque, NM, July 2008. Superseded by SAND2010-5549, version 0.2 Beta, August 2010.

[Pissoort and Olyslager 2003] D. Pissoort and F. Olyslager, "Termination of periodic waveguides by PMLs in time-harmonic integral equation-like techniques", *IEEE Antenn. Wirel. Propag. Lett.* **2**:20 (2003), 281–284.

[Pissoort et al. 2005] D. Pissoort, D. Vande Ginste, and F. Olyslager, "Including PML-based absorbing boundary conditions in the MLFMA", *IEEE Antenn. Wirel. Propag. Lett.* **4**:1 (2005), 312–315.

[Proakis and Manolakis 1996] J. G. Proakis and D. G. Manolakis, *Digital signal processing: principles, algorithms, and applications*, Prentice-Hall, Upper Saddle River, NJ, 1996.

[Silling 2000] S. A. Silling, "Reformulation of elasticity theory for discontinuities and long-range forces", *J. Mech. Phys. Solids* **48**:1 (2000), 175–209.

[Silling and Askari 2005] S. A. Silling and E. Askari, "A meshfree method based on the peridynamic model of solid mechanics", *Comput. Struct.* **83**:17-18 (2005), 1526–1535.

[Silling et al. 2007] S. A. Silling, M. Epton, O. Weckner, J. Xu, and E. Askari, "Peridynamic states and constitutive modeling", *J. Elasticity* **88**:2 (2007), 151–184.

[Teixeira and Chew 1998] F. L. Teixeira and W. C. Chew, "A general approach to extend Berenger's absorbing boundary condition to anisotropic and dispersive media", *IEEE Trans. Antenn. Propag.* **46**:9 (1998), 1386–1387.

[Uno et al. 1997] T. Uno, Y. He, and S. Adachi, "Perfectly matched layer absorbing boundary condition for dispersive medium", *IEEE Microw. Guided Wave Lett.* **7**:9 (1997), 264–266.

[Wang et al. 2008] X. Wang, R. A. Wildman, D. S. Weile, and P. Monk, "A finite difference delay modeling approach to the discretization of the time domain integral equations of electromagnetics", *IEEE Trans. Antenn. Propag.* **56**:8, part 1 (2008), 2442–2452.

[Weckner and Abeyaratne 2005] O. Weckner and R. Abeyaratne, "The effect of long-range forces on the dynamics of a bar", *J. Mech. Phys. Solids* **53**:3 (2005), 705–728.

[Weckner et al. 2009] O. Weckner, G. Brunk, M. A. Epton, S. A. Silling, and E. Askari, "Green's functions in non-local three-dimensional linear elasticity", *Proc. R. Soc. Lond. A* **465**:2111 (2009), 3463–3487.

[Wildman and Gazonas 2011] R. A. Wildman and G. A. Gazonas, "A perfectly matched layer for peridynamics in one dimension", Technical report ARL-TR-5626, U.S. Army Research Laboratory, Aberdeen, MD, 2011.

Received 2 Apr 2012. Revised 17 Jul 2012. Accepted 18 Jul 2012.

RAYMOND A. WILDMAN: raymond.a.wildman.civ@mail.mil
Weapons and Materials Research Directorate, U.S. Army Research Laboratory, Attn: RDRL-WMM-B, Aberdeen Proving Ground, MD 21005, United States

GEORGE A. GAZONAS: george.a.gazonas.civ@mail.mil
Weapons and Materials Research Directorate, U.S. Army Research Laboratory, ATTN: RDRL-WMM-B, Aberdeen Proving Ground, MD 21005, United States

JOURNAL OF MECHANICS OF MATERIALS AND STRUCTURES
Vol. 7, No. 8-9, 2012
dx.doi.org/10.2140/jomms.2012.7.783

DISPLACEMENT FIELD IN AN ELASTIC SOLID WITH MODE-III CRACK AND FIRST-ORDER SURFACE EFFECTS

TAMRAN H. LENGYEL AND PETER SCHIAVONE

We analyze a nonstandard boundary-value problem for Laplace's equation characterizing the displacement field arising from the antiplane deformations of an infinite elastic solid containing a sharp finite crack when first-order surface effects are included on the crack faces. The surface effects are incorporated using the continuum-based surface/interface model of Gurtin and Murdoch. We establish a uniqueness result for the displacement field and use complex variable methods to reduce the problem to a series of integral equations which are solved numerically using an efficient, stable, yet convenient finite element discretization method. Our results demonstrate the effect of the surface on the displacement field and its implications for the corresponding stress distributions in the vicinity of the crack.

1. Introduction

The incorporation of surface mechanics into mathematical models describing deformation of various elastic structures has drawn an increasing amount of attention in the literature recently (see, for example, [Gibbs 1906; Orowan 1970; Gurtin and Murdoch 1975; 1978; Chan and Larché 1982; Benveniste and Aboudi 1984; Thomson and Chuang 1986; Cammarata 1994; Steigmann and Ogden 1997a; 1997b; Wang et al. 2007; 2010a; 2010b; Zhu 2008; Altenbach et al. 2009; 2010a; 2010b; 2011] and the references contained therein). The concept is particularly significant when considering continuum models of deformation at the nanoscale where the high surface-area-to-volume ratio means that the separate contributions of the surface can no longer be ignored.

In the case of antiplane deformations of a linearly elastic and homogeneous isotropic solid containing a sharp crack, Kim et al. [2010a; 2010b] have incorporated surface effects on the faces of the crack using the Gurtin–Murdoch surface elasticity model [Gurtin and Murdoch 1975; 1978; Ru 2010]. The resulting mathematical model gave rise to a nonstandard boundary-value problem for the (harmonic) antiplane displacement. Using complex variable methods, Kim et al. presented various conclusions regarding the *stress* distributions in the vicinity of the crack and how they are affected by the surface mechanics. A rigorous analysis of the actual displacement boundary-value problem in terms of uniqueness and determination of the displacement solution was never conducted. The determination of the displacement field is important in identifying the deformation of the body; in particular, the change of shape of the crack faces in response to the presence of surface effects. To this end, it is extremely important to ensure that the mathematical model being used to describe the displacement field is "correct" or well-posed in the sense that any solution found by numerical methods is necessarily unique. In fact, as we discuss in Section 4, the uniqueness result, in particular, has significant implications not only for the determination

Keywords: displacement field, mode-III crack, antiplane deformations, surface elasticity, integral equations.

of the displacement field but also for the corresponding stress distributions in the vicinity of the crack tips.

In this paper we undertake a rigorous formulation and analysis of the displacement boundary-value problem first mentioned in [Kim et al. 2010a; 2010b]. We establish a uniqueness result for the displacement field and use complex variable methods to reduce the problem to a series of integral equations which are solved numerically using an efficient and stable, yet straightforward numerical method. Our results demonstrate the contribution of the mechanics of the crack surfaces on the displacement field and the implications for the corresponding stress distributions at the crack tips.

2. Formulation

We consider antiplane deformations of a linearly elastic and homogeneous isotropic solid occupying a cylindrical region in $\mathbb{R}^3$ with generators parallel to the x_3-axis of a rectangular Cartesian coordinate system (x_1, x_2, x_3). Suppose that the cylinder contains a single internal finite crack running the length of the cylinder and occupying the region $L = \{-a \le x_1 \le a, x_2 = 0^{\pm}\}$ of a typical cross section S. The crack length $2a$ is assumed to be much smaller than any characteristic length in S. The faces of the crack are assumed to have separate elasticities which is described by an adaptation of the Gurtin–Murdoch surface elasticity model [Ru 2010]. The theory of antiplane elasticity leads to a description of the deformation of the solid characterized by the unknown antiplane displacement function $w(x_1, x_2)$ defined in S.

In order to formulate the boundary-value problem for w, we first note that the nature of antiplane deformations are such that [Milne-Thompson 1962]

$$w^+ = -w^- \quad \text{everywhere in } S. \tag{2.1}$$

Here w^+ and w^- represent the antiplane displacements in the upper and lower half-planes $x_2 > 0$ and $x_2 < 0$, respectively. Consequently, since we assume that the material remains connected (no tearing), $w = 0$ at the crack tips $x_1 = \pm a$ and $x_2 = 0$. Finally, we assume that the crack faces are subjected to a loading $\sigma_{23} = P(x_1)$, where $P(x_1)$ is a Hölder-continuous function, and that the remote boundaries of the cross section are free of loading, that is, $\sigma_{23} = 0$ and $R^2 = x_1^2 + x_2^2 \to \infty$.

We obtain the following two-dimensional discontinuous boundary-value problem for the Laplace operator Δ:

$$\Delta w(x_1, x_2) = 0, \qquad (x_1, x_2) \in S \setminus L, \tag{2.2}$$

$$\mp\beta \frac{\partial^2 w}{\partial x_1^2}(x_1, 0^{\pm}) + P(x_1) = \mu \frac{\partial w}{\partial x_2}(x_1, 0^{\pm}), \qquad -a < x_1 < a. \tag{2.3}$$

For $R = \sqrt{x_1^2 + x_2^2} \to \infty$, as in the statement of the standard exterior Dirichlet problem for Laplace's equation [Kress 1999], it is required that

$$w(x_1, x_2) = w_\infty + O\Big(\frac{1}{R}\Big), \tag{2.4}$$

uniformly for all directions. Here β is a parameter representing the elasticity of the surface layer and μ is the shear modulus in the bulk material [Ru 2010]. We note that a variation of the boundary-value problem (2.2)–(2.4) has been solved numerically in an infinite strip using Fourier transforms and reduction to a Riemann–Hilbert problem [Antipov and Schiavone 2011].

It is convenient to introduce the dimensionless transformations

$$x \equiv \frac{x_1}{a}, \quad y \equiv \frac{x_2}{a}, \quad \tilde{P}(x) \equiv \frac{P(ax)}{P_0}, \quad \gamma \equiv \frac{\beta}{a\mu}, \quad u(x,y) \equiv \frac{\mu}{aP_0} w(ax, ay), \tag{2.5}$$

where P_0 is the root-mean-squared value of the input stress along the crack face defined by

$$P_0 = \sqrt{\frac{1}{2a}\int_{-a}^{a} [P(t)]^2 \, dt},$$

γ is defined as the dimensionless surface parameter, and u is the normalized antiplane displacement field. The boundary-value problem (2.2)–(2.4) then becomes

$$\Delta u(x,y) = 0, \qquad (x,y) \in S \setminus L, \tag{2.6}$$

$$\mp\gamma \frac{\partial^2 u}{\partial x^2}(x, 0^{\pm}) + \tilde{P}(x) = \frac{\partial u}{\partial y}(x, 0^{\pm}), \qquad -1 < x < 1, \tag{2.7}$$

$$u = u_\infty + O\big(1/\tilde{R}\big), \qquad \tilde{R} = \sqrt{x^2 + y^2} \to \infty, \tag{2.8}$$

where u_∞ is a constant. Finally, the corresponding dimensionless shear stresses τ_x and τ_y are defined using the above transformations as

$$\sigma_{13} = \mu \frac{\partial w}{\partial x_1} = P_0 \frac{\partial u}{\partial x} \equiv P_0 \tau_x, \quad \sigma_{23} = \mu \frac{\partial w}{\partial x_2} = P_0 \frac{\partial u}{\partial y} \equiv P_0 \tau_y,$$

with the total normalized stress magnitude τ given by

$$\tau^2 \equiv (\tau_x)^2 + (\tau_y)^2.$$

Note that (2.1) along with the assumption that the material remains connected (no tearing) at the crack tips implies that

$$\tau_x^+ = -\tau_x^-, \quad \tau_y^+ = \tau_y^-.$$

3. Uniqueness of solution

We shall prove that the boundary-value problem (2.6)–(2.8) can have at most one solution. Consider the difference $v(x, y)$ of any two solutions of the boundary-value problem (2.6)–(2.8). We prove that $v(x, y) \equiv 0$ in $S \setminus L$ by adapting the methods used in [Knowles and Pucik 1973]. Clearly v satisfies the corresponding homogeneous boundary-value problem. Referring to Figure 1, we surround the crack by a smooth curve $\partial\Omega$ of "radius" ϵ, contained entirely within the area $B \subset S$. The region exterior to $\partial\Omega$ is denoted by Ω and the outer boundary of B by ∂B. We decompose $\partial\Omega$ as

$$\partial\Omega = \bigcup_{i=1}^{4} \partial\Omega_i,$$

where $\partial\Omega_1$ and $\partial\Omega_2$ are the upper ($y = +\epsilon$) and lower ($y = -\epsilon$) portions of the straight portion of $\partial\Omega$, respectively ($\partial\Omega_{1,2} : x \in [-1, 1]$, $y = \pm\epsilon$); and $\partial\Omega_3$ ($\pi/2 \le \varphi \le 3\pi/2$) and $\partial\Omega_4$ ($-\pi/2 \le \varphi \le \pi/2$) are the left and right curved portions of $\partial\Omega$, respectively (in cylindrical polar coordinates).

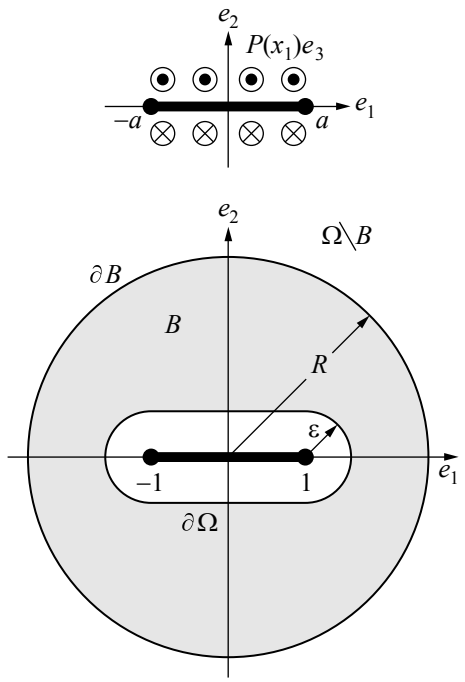

Figure 1. Crack surrounded by a smooth curve $\partial\Omega$ of "radius" ϵ, contained entirely within the area $B \subset S$.

We define the values of v on the boundary of $\partial\Omega$ to be

$$\begin{aligned} v_\epsilon^{\pm} &\equiv v(x, \pm\epsilon) && \text{on } \partial\Omega_{1,2}, \\ v_r &\equiv v(\mp 1 + \epsilon\cos(\varphi), \epsilon\sin(\varphi)) && \text{on } \partial\Omega_{3,4}. \end{aligned}$$

Green's first identity in the bounded domain B yields

$$\int_B |\nabla v|^2 dA = \oint_{\partial B} v\frac{\partial v}{\partial \boldsymbol{n}} ds - \oint_{\partial\Omega} v\frac{\partial v}{\partial \boldsymbol{n}} ds. \tag{3.1}$$

As $R \to \infty$ the region $B \to \Omega$ and further as $\epsilon \to 0$, the region $\Omega \to S \setminus L$. As $R \to \infty$, the asymptotic behavior of (2.8) yields for (3.1)

$$\begin{aligned} \int_\Omega |\nabla v|^2 dA &= -\oint_{\partial\Omega} v\frac{\partial v}{\partial \boldsymbol{n}} ds = -\sum_{i=1}^{4}\int_{\partial\Omega_i} v\frac{\partial v}{\partial \boldsymbol{n}} ds \\ &= -\int_{-1}^{1} v_\epsilon^+(\nabla v_\epsilon^+ \cdot (-\boldsymbol{e}_2))(-dx) - \int_{-1}^{1} v_\epsilon^-(\nabla v_\epsilon^- \cdot \boldsymbol{e}_2)dx - 2\epsilon\int_{-\pi/2}^{\pi/2} v_r(\nabla v_r \cdot (-\boldsymbol{e}_r))d\theta \\ &= -\int_{-1}^{1} v_\epsilon^+\frac{\partial v_\epsilon}{\partial y}^+ dx - \int_{-1}^{1} v_\epsilon^-\frac{\partial v_\epsilon}{\partial y}^- dx + 2\epsilon\int_{-\pi/2}^{\pi/2} v_r\frac{\partial v_r}{\partial r}d\theta = -I_1 - I_2 + 2\epsilon I_3. \end{aligned} \tag{3.2}$$

The integrals I_1 and I_2 are determined using the boundary condition (2.7) and the smoothness of the

solution v [Kress 1999]. Noting that $v^+ = -v^-$ for antiplane displacement, we have, as $\epsilon \to 0$,

$$\lim_{\epsilon\to 0} I_1 = \lim_{\epsilon\to 0} \int_{-1}^{1} v_\epsilon^+ \frac{\partial v_\epsilon}{\partial y}^+ dx = \int_{-1}^{1} v^+ \frac{\partial v}{\partial y}^+ dx = -\gamma \int_{-1}^{1} v^+ \frac{\partial^2 v}{\partial x^2}^+ dx \equiv \nu,$$

$$\lim_{\epsilon\to 0} I_2 = \lim_{\epsilon\to 0} \int_{-1}^{1} v_\epsilon^- \frac{\partial v_\epsilon}{\partial y}^- dx = \int_{-1}^{1} v^- \frac{\partial v}{\partial y}^- dx = \gamma \int_{-1}^{1} v^- \frac{\partial^2 v}{\partial x^2}^- dx = -\nu.$$

Also,

$$\lim_{\epsilon\to 0} |I_3| = \lim_{\epsilon\to 0} \left| \int_{-\pi/2}^{\pi/2} v_r \frac{\partial v_r}{\partial r} d\theta \right| = \left| \int_{-\pi/2}^{\pi/2} v(\pm 1, 0) \frac{\partial v}{\partial \boldsymbol{n}} (\pm 1, 0) d\theta \right|$$

$$\leq \int_{-\pi/2}^{\pi/2} |v(\pm 1, 0) \nabla v(\pm 1, 0)| d\theta = \int_{-\pi/2}^{\pi/2} V_0^2 d\theta = \pi V_0^2.$$

Taking the limit as $\epsilon \to 0$ on the right-hand side of (3.2) then yields:

$$\int_{S\setminus L} |\nabla v|^2 dA = 0.$$

Note that in the case when $\partial v/\partial \boldsymbol{n}$ has a logarithmic singularity at the crack tips, the integral I_3 remains uniformly bounded as $\epsilon \to 0^+$ since the integrand remains weakly singular [Kress 1999].

Hence, $v = \text{const.}$ in $S\setminus L$. However, given that $v^+ = -v^-$, $-1 \leq x \leq 1$, it follows that, at the crack tips, $v(-1, 0) = v(1, 0) = 0$, from which it follows that $v \equiv 0$ (or, $u_2 = u_1$) in $S \setminus L$. Consequently, as a result of the linearity of the problem there can be at most one solution of (2.6)–(2.8).

4. Integral equation

Define the complex antiplane displacement potential $\phi(z)$, $z \equiv x + iy$, as

$$\phi(z) \equiv u(x, y) + i v(x, y).$$

Here $u(x, y)$ is the displacement field from (2.6)–(2.8) with $u_\infty = 0$ and $v(x, y)$ is the conjugate function. Define the function $\theta(x)$ by $\theta(x) \equiv \lim_{y\to 0^+} u(x, y)$. Then θ is the normalized antiplane displacement on the upper crack face, where

$$u(x, 0^\pm) = \pm\theta(x), \quad -1 \leq x \leq 1.$$

Then, the displacement jump across the crack is given by

$$2\theta(t) = [\phi(t)]^+ - [\phi(t)]^-$$

and $\phi(z)$ can be represented in the form of a Cauchy integral [Muskhelishvili 1963]:

$$\phi(z) = \frac{1}{\pi i} \int_L \frac{\theta(t)}{t - z} dt,$$

so that, as a consequence of (2.1),

$$\theta(-1) = \theta(1) = 0. \tag{4.1}$$

Using the Plemelj formula [Muskhelishvili 1963], after some rearrangement, we obtain the following integrodifferential equation for the displacement on the crack:

$$\frac{1}{\pi}\frac{d}{dx}\left[\int_L \frac{\theta(t)}{t-x}\,dt\right] + \gamma\theta''(x) = \tilde{P}(x), \quad -1 \le x \le 1.$$

Using integration by parts, we can write this equation as a Fredholm equation of the second kind:

$$\gamma\theta(x) - \frac{1}{\pi}\int_L \theta(t)\ln|t-x|\,dt = \zeta_2(x) - C_1 x - C_2, \tag{4.2}$$

where the function $\zeta_2(x)$ is defined by

$$\zeta_2(x) = \int_0^x \int_0^t \tilde{P}(s)\,ds\,dt$$

and C_1 and C_2 are constants of integration.

The normalized displacement field in the bulk material is then described by

$$u(x, y) = \operatorname{Re}\phi(z) = \operatorname{Im}\left\{\frac{1}{\pi}\int_L \frac{\theta(t)}{t-z}\,dt\right\}.$$

The corresponding stresses on the crack are then given by

$$\tau_x(x, 0^{\pm}) = \pm\theta'(x)\ (\equiv \pm\theta_x),$$
$$\tau_y(x, 0^{\pm}) = \tilde{P}(x) \mp \gamma\theta''(x)\ (\equiv \theta_y), \quad -1 < x < 1,$$

where $\theta'(x)$ is given by

$$\gamma\theta'(x) - \frac{1}{\pi}\int_L \theta'(t)\ln|t-x|\,dt = \zeta_1(x) - C_3, \tag{4.3}$$

C_3 is an arbitrary constant, and

$$\zeta_1(x) = \int_0^x \tilde{P}(t)\,dt.$$

The constants C_1, C_2, C_3 are determined using the crack-tip conditions (4.1) and the requirement that

$$\int_{-1}^{1} \theta'(t)\,dt = 0$$

which follows from (4.1) as a result of the antiplane nature, (2.1), of the deformations considered here.

Note that (4.3) leads to

$$\gamma\theta''(x) - \frac{1}{\pi}\int_L \theta''(t)\ln|t-x|\,dt = \tilde{P}(x) - \left[\frac{1}{\pi}\theta'(t)\ln|t-x|\right]_{t=-1}^{t=1}. \tag{4.4}$$

From (4.4), if the stresses τ_x ($\propto \theta'(\pm 1)$) at the crack tips are finite and nonzero, then the stresses τ_y at the crack tips ($\tau_y \propto \theta''(\pm 1)$) cannot be finite even for a finite externally applied stress function ($\tilde{P}$). This result is in agreement with the recent papers [Kim et al. 2013; Walton 2012] where it was noted that by imposing the further condition $\theta' \equiv 0$ at the crack tips (to achieve finite stress [Kim et al. 2010a; 2010b]) we effectively overdetermine the problem so that, contrary to the results reported in these two references, there can be no solutions of (2.2)–(2.4) with finite stress at the crack tips. In fact, this is clear from the

uniqueness theorem proved above: once the unique displacement field is determined in the body one cannot then arbitrarily assign values to the derivatives of the displacement field at the crack tips. This fact is further reflected in the next section when we actually compute θ and its derivatives.

5. Numerical solution

The displacement and slope on the crack face can be found by solving (4.2) and (4.3), which are accommodated by the general form

$$\gamma f(x) - \frac{1}{\pi}\int_L f(t)\ln|t-x|\,dt = \zeta(x) \tag{5.1}$$

for corresponding functions f and ζ. Equation (5.1) is a Fredholm integral equation of the second kind, which (provided γ is not an eigenvalue for the corresponding integral operator) is well-known to have a unique continuous solution for each continuous $\zeta(x)$ on L. We have approximated the solution for appropriate values of γ using a discretized (finite-element) residual formulation based on a total of N linear elements leading to a system of $N+1$ linear equations for $N+1$ unknowns [Lengyel 2011].

The numerical method can accommodate different input load profiles ($\tilde{P}(x)$). However, if the crack length is relatively small, it is sufficient to assume a constant input stress ($\because \tilde{P} = \pm 1$). In this way, the solution to the classical antiplane crack problem with a constant mode-III input load ($\tilde{P} = -1$ for convenience) has been solved in [Muskhelishvili 1963; Sih 1965; Broberg 1998], where it is shown that on the (+) crack face:

$$\theta(x) = u(x,0^+) = \sqrt{1-x^2}, \qquad -1 \le x \le 1, \tag{5.2}$$

$$\theta_x(x) = \tau_x(x,0^+) = -\frac{x}{\sqrt{1-x^2}}, \qquad -1 < x < 1, \tag{5.3}$$

$$\theta_y(x) = \tau_y(x,0^+) = -1, \qquad -1 < x < 1. \tag{5.4}$$

Note the singularities in both normalized stress components at the crack tips (when $x = \pm 1$). Plots of (5.2) and (5.3) are compared with the numerical model used here (in the case $\gamma = 0$) in Figure 2. The method shows fast and stable convergence to the exact solution in this case. In Figure 3 we plot the

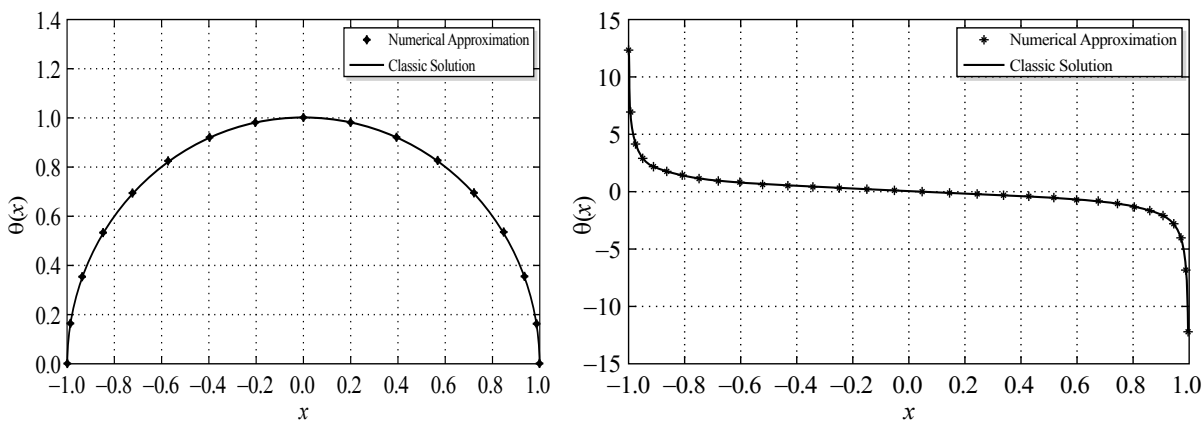

Figure 2. Plots of (5.2) and (5.3) compared with the numerical model.

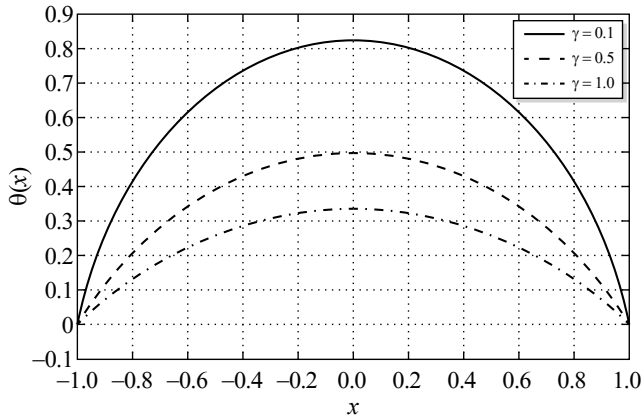

Figure 3. Effects of various surface parameters γ on the displacement of the (+) crack face.

effects of various surface parameters γ on the displacement of the (+) crack face. It is clear that the displacement is reduced on the crack face with increasing surface effect. We note also from Figure 4, left, that the stress θ_x is finite everywhere across the crack face, even at the crack tips. However, the unit stress θ_y, plotted on the right in Figure 4, remains singular at the crack tips. This result contradicts that presented in [Kim et al. 2010a; 2010b] but is not surprising. As mentioned above, the unique solution of (2.6) and (2.7) determines a priori the values of θ_x which are clearly never zero at the crack tips for any meaningful value of γ.

Figure 5 plots $\theta(0)$ ($\equiv \theta_{\max}$) with increasing N (the number of elements) using different values of the surface parameter (γ). These approximations demonstrate rapid convergence with less than 50 elements. Refinement convergence of the slope at the endpoints ($\theta_x(-1) \equiv \theta'_{\max}$) is shown in Figure 6. There is convergence here, however, more elements are required as the surface parameter decreases in value. This is not surprising since, as the surface parameter tends to zero (the classical model) the opposing stresses ($\tau_x \propto \theta_x$) at the crack tips become singular. Figure 7 shows the (decreased) stress in the bulk material

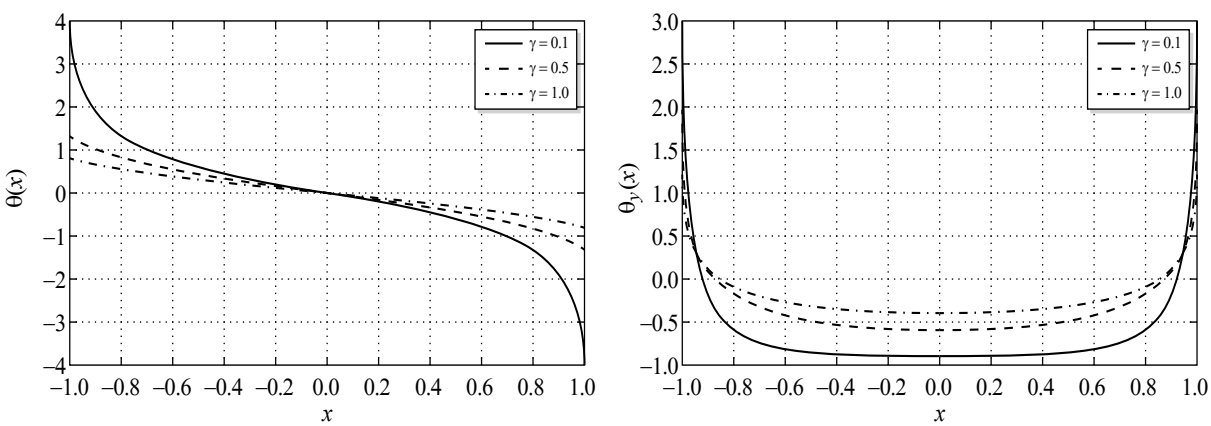

Figure 4. Stress θ_x (left) and unit stress θ_y (right) across the crack face.

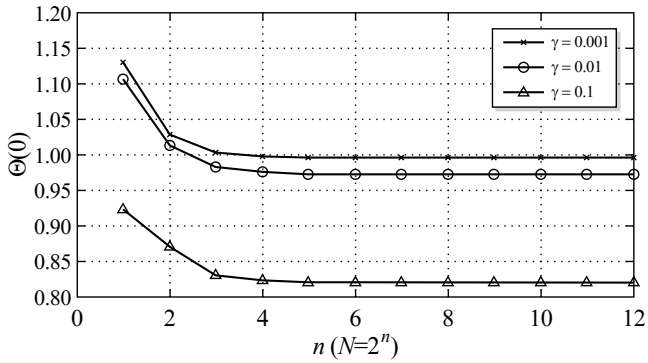

Figure 5. Plot of $\theta(0)$ ($\equiv \theta_{\max}$) with increasing number of elements, N, using different values of the surface parameter γ.

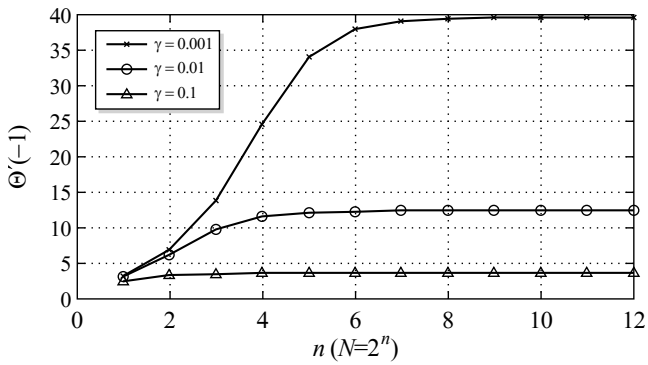

Figure 6. Refinement convergence of the slope at the endpoints ($\theta_x(-1) \equiv \theta'_{\max}$).

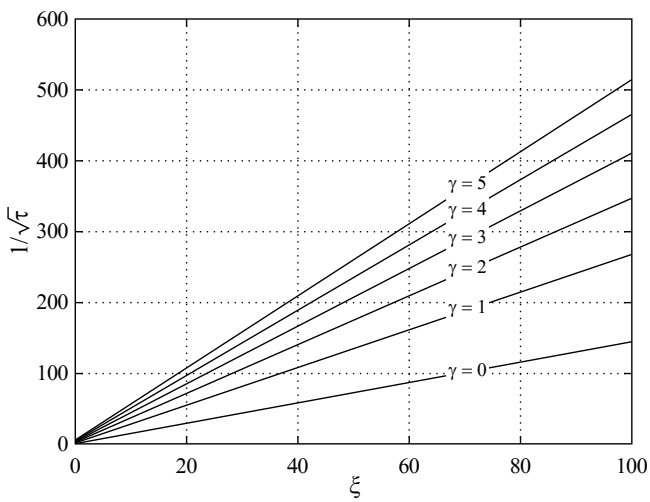

Figure 7. Stress in the bulk material outside the crack due to increasing surface parameter γ ($\xi(x) \equiv x - 1$, $x > 1$).

outside the crack due to an increasing surface parameter γ ($\xi(x) \equiv x - 1, x > 1$). Full details can be found in [Lengyel 2011].

5.1. ***Remark.*** Finally, we remark that the stability and rapid convergence of our numerical model allows us to obtain an approximate expression quantifying the effect of γ on the displacement of the crack face in the case of a constant stress input (relatively small crack length). In fact, using curve-fitting analysis, our numerical results suggest the following convenient approximation for the displacement field across the crack face in the case of a constant mode-III load input stress

$$w(x, 0^{\pm}) \simeq \pm a\left(\frac{P_0}{\mu}\right)\frac{(1-(x_1/a)^2)^{(27.67\gamma+1)/(27.67\gamma+2)}}{2\gamma+1}, \quad -a \le x \le a. \tag{5.5}$$

We find that the expression (5.5) agrees with the corresponding numerical results obtained using the complete finite element discretization method to an error of less than 5%.

6. Conclusions

The incorporation of surface effects allows for the assumption of energy dispersion on the boundary which reduces the input shear stress (Figure 4, right). With the exception of the region in the vicinity of the crack tips, the adjusted input stress magnitude shows a reduction when γ increases. From this reduction of input shear stress, the displacement (u) and opposing stress (τ_x) are reduced and remain finite across the crack face (including at the crack tips). Figures 3 and 4, left, demonstrate this conclusively for both displacement ($\theta \propto u$) and slope ($\theta' \propto \tau_x$). The displacements and stress magnitudes in the bulk are also reduced accordingly.

Given the convergence demonstrated in Figures 5 and 6, it is apparent that the function $\theta(x)$ ($\propto u$) along with it's derivatives $\theta_x(x)$ ($\propto \tau_x$) and $\theta''(x)$ ($\propto \tau_y$) are convergent across the crack face. The function $\theta''(x)$ does not converge near the crack tips, however all three functions showed a reduction and convergence across the crack tip when γ increased. Consequently, the incorporation of surface effects leads to a more stable and convergent numerical model. This additional stability and convergence is directly related to the effect of γ on the displacement profile. As the solution transitions from a semicircle (when $\gamma \to 0$) to a quadratic function (when $\gamma \to \infty$), the stability of the displacement (u) and stress (τ_x and τ_y) increases.

7. Acknowledgements

Schiavone acknowledges the support of the Natural Sciences and Engineering Research Council of Canada. The authors would like to thank an anonymous reviewer for his detailed comments which have led to improvements in the paper.

References

[Altenbach et al. 2009] H. Altenbach, V. A. Eremeyev, and N. F. Morozov, "Linear theory of shells taking into account surface stresses", *Dokl. Phys.* **54** (2009), 531–535.

[Altenbach et al. 2010a] H. Altenbach, V. A. Eremeyev, and L. P. Lebedev, "On the existence of solution in the linear elasticity with surface stresses", *Z. Angew. Math. Mech.* **90**:3 (2010), 231–240.

[Altenbach et al. 2010b] H. Altenbach, V. A. Eremeyev, and N. F. Morozov, "On equations of the linear theory of shells with surface stresses taken into account", *Mech. Solids* **45** (2010), 331–342.

[Altenbach et al. 2011] H. Altenbach, V. A. Eremeyev, and L. P. Lebedev, "On the spectrum and stiffness of an elastic body with surface stresses", *Z. Angew. Math. Mech.* **91**:9 (2011), 699–710.

[Antipov and Schiavone 2011] Y. A. Antipov and P. Schiavone, "Integro-differential equation for a finite crack in a strip with surface effects", *Q. J. Mech. Appl. Math.* **64**:1 (2011), 87–106.

[Benveniste and Aboudi 1984] Y. Benveniste and J. Aboudi, "Continuum model for fiber reinforced materials with debonding", *Int. J. Solids Struct.* **20**:11-12 (1984), 935–951.

[Broberg 1998] K. Broberg, "Crack expanding with constant velocity in an anisotropic solid under anti-plane strain", *Int. J. Fract.* **93** (1998), 1–12.

[Cammarata 1994] R. C. Cammarata, "Surface and interface stress effects in thin films", *Prog. Surf. Sci* **46**:1 (1994), 1–38.

[Chan and Larché 1982] J. W. Chan and F. Larché, "Surface stress and chemical equilibrium of small crystals, II: Solid particles embedded in a solid matrix", *Acta Metall.* **30** (1982), 51–56.

[Gibbs 1906] J. W. Gibbs, *The scientific papers of J. Willard Gibbs, I*, Longmans Green, London, 1906.

[Gurtin and Murdoch 1975] M. E. Gurtin and A. I. Murdoch, "A continuum theory of elastic material surfaces", *Arch. Ration. Mech. Anal.* **57**:4 (1975), 291–323.

[Gurtin and Murdoch 1978] M. E. Gurtin and A. I. Murdoch, "Surface stress in solids", *Int. J. Solids Struct.* **14** (1978), 431–440.

[Kim et al. 2010a] C. I. Kim, C.-Q. Ru, and P. Schiavone, "Analysis of a mode-III crack in the presence of surface elasticity and a prescribed non-uniform surface traction", *Z. Angew. Math. Phys.* **61**:3 (2010), 555–564.

[Kim et al. 2010b] C. I. Kim, C.-Q. Ru, and P. Schiavone, "The effects of surface elasticity on an elastic solid with mode-III crack: complete solution", *J. Appl. Mech.* (*ASME*) **77**:2 (2010), Article ID #021011.

[Kim et al. 2013] C. I. Kim, C.-Q. Ru, and P. Schiavone, "A clarification of the role of crack-tip conditions in linear elasticity with surface effects", *Math. Mech. Solids* **18**:1 (2013), 59–66.

[Knowles and Pucik 1973] J. Knowles and T. A. Pucik, "Uniqueness for plane crack problems in linear elastostatics", *J. Elasticity* **3** (1973), 155–160.

[Kress 1999] R. Kress, *Linear integral equations*, 2nd ed., Applied Mathematical Sciences **82**, Springer, New York, 1999.

[Lengyel 2011] T. H. Lengyel, "Analysis of displacement in an elastic solid with a mode-III crack in the presence of surface elasticity", Masters thesis, University of Alberta, 2011, available at http://hdl.handle.net/10402/era.27830.

[Milne-Thompson 1962] L. M. Milne-Thompson, *Anti-plane elastic systems*, Academic Press, New York, 1962.

[Muskhelishvili 1963] N. I. Muskhelishvili, *Some basic problems of the mathematical theory of elasticity: fundamental equations, plane theory of elasticity, torsion and bending*, 2nd ed., Noordhoff, Groningen, 1963.

[Orowan 1970] E. Orowan, "Surface energy and surface tension in solids and fluids", *Proc. R. Soc. Lond. A* **316** (1970), 473–491.

[Ru 2010] C.-Q. Ru, "Simple geometrical explanation of Gurtin–Murdoch model of surface elasticity with clarification of its related versions", *Sci. China Phys. Mech. Astronom.* **53**:3 (2010), 536–544.

[Sih 1965] G. C. Sih, "Boundary problems for longitudinal shear cracks", pp. 117–130 in *Developments in theoretical and applied mechanics* (Atlanta, GA, 1964), vol. 2, edited by W. A. Shaw, Pergamon, Oxford, 1965.

[Steigmann and Ogden 1997a] D. J. Steigmann and R. W. Ogden, "A necessary condition for energy-minimizing plane deformations of elastic solids with intrinsic boundary elasticity", *Math. Mech. Solids* **2**:1 (1997), 3–16.

[Steigmann and Ogden 1997b] D. J. Steigmann and R. W. Ogden, "Plane deformations of elastic solids with intrinsic boundary elasticity", *Proc. R. Soc. Lond. A* **453**:1959 (1997), 853–877.

[Thomson and Chuang 1986] R. Thomson and T. J. Chuang, "The role of surface stress in fracture", *Acta Metall.* **34**:6 (1986), 1133–1143.

[Walton 2012] J. R. Walton, "A note on fracture models incorporating surface elasticity", *J. Elasticity* **109**:1 (2012), 95–102.

[Wang et al. 2007] G. F. Wang, X. Q. Feng, and S. W. Yu, "Surface buckling of a bending microbeam due to surface elasticity", *Europhys. Lett.* **77**:4 (2007), Article ID #44002.

[Wang et al. 2010a] J. S. Wang, Y. H. Cui, X. Q. Feng, G. F. Wang, and Q. H. Qin, "Surface effects on the elasticity of nanosprings", *Europhys. Lett.* **92** (2010), 16002–1–6.

[Wang et al. 2010b] Z. Q. Wang, Y. P. Zhao, and Z. P. Huang, "The effects of surface tension on the elastic properties of nanostructures", *Int. J. Eng. Sci.* **48** (2010), 140–150.

[Zhu 2008] H. X. Zhu, "The effects of surface and initial stresses on the bending stiffness of nanowires", *Nanotechnology* **19**:40 (2008), Article ID #405703.

Received 17 May 2012. Revised 30 Jul 2012. Accepted 2 Aug 2012.

TAMRAN H. LENGYEL: tamran.lengyel@gmail.com
Department of Mechanical Engineering, University of Alberta, 4-9 Mechanical Engineering Building, Edmonton, AB T6G 2G8, Canada

PETER SCHIAVONE: p.schiavone@ualberta.ca
Department of Mechanical Engineering, University of Alberta, 4-9 Mechanical Engineering Building, Edmonton, AB T6G 2G8, Canada
http://www.mece.ualberta.ca/~schiavone/schiavon.htm

JOURNAL OF MECHANICS OF MATERIALS AND STRUCTURES
Vol. 7, No. 8-9, 2012
dx.doi.org/10.2140/jomms.2012.7.795

msp

ON THE CHOICE OF FUNCTIONS SPACES IN THE LIMIT ANALYSIS FOR MASONRY BODIES

MASSIMILIANO LUCCHESI, MIROSLAV ŠILHAVÝ AND NICOLA ZANI

The kinematic and static problems of limit analysis of no-tension bodies are formulated. The kinematic problem involves the infimum of kinematically admissible multipliers, and the static problem the supremum of statically admissible multipliers. The central question of the paper is under which conditions these two numbers coincide. This involves choices of function spaces for the competitor displacements and competitor stresses. A whole ordered scale of these spaces is presented. These problems are formulated as convex variational problems considered by Ekeland and Témam. The static problem is unconditionally shown to be the dual problem (in the sense of the mentioned reference) of the kinematic problem. A *necessary and sufficient condition,* the normality, guarantees that the kinematic and static problems give the same result. The normality is not always satisfied, as examples show (one of which is presented here). The qualification hypothesis of Ekeland and Témam, *sufficient* for the equality of the static and kinematic problems, is never satisfied in the spaces of admissible displacements of bounded deformation or of functions integrable together with the gradient in the power p, $1 \le p < \infty$. In the cases of lipschitzian displacements and of smooth displacements, the qualification hypothesis is equivalent to simple conditions that can be satisfied in the case of the pure traction problem. However, it is shown that then the space of admissible stresses must be enlarged to contain stress fields represented by finitely or countably additive tensor-valued measures.

1. Introduction

No-tension (masonry-like) materials [Anzellotti 1985; Giaquinta and Giusti 1985; Del Piero 1989; Di Pasquale 1992; Lucchesi et al. 2008a] cannot support all stresses: only negative semidefinite stresses are possible. Therefore, bodies made of no-tension materials cannot support all loads, certain loads lead to the collapse of the body. The goal of limit analysis is to determine the limit load, i.e., the largest possible load prior to collapse. It is customary to assume that the loads depend affinely on a scalar parameter λ, the loading multiplier, as described in Section 2A, and the problem reduces to determining the collapse multiplier, i.e., the value of λ corresponding to the limit load. Limit analysis is traditionally based on the static and kinematic theorems, which determine the limit load as the supremum of statically admissible multipliers and the infimum of kinematically admissible multipliers, respectively. The traditional definition identifies the collapse multiplier as one with the collapse mechanism (called *strong mechanism* in Section 2C below). Under this assumption the supremum of statically admissible multipliers and the infimum of kinematically admissible multipliers are the same and coincide with the

This research was supported by the Regione of Toscana (project "Tools for modeling and assessing the structural behavior of ancient constructions: the NOSA-ITACA code", PAR FAS 2007-2013). Šilhavý's research was also supported by RVO: 67985840. Both forms of support are gratefully acknowledged.
Keywords: limit analysis, static and kinematic theorems, duality of displacements and forces.

collapse multiplier. The reader is referred to [Del Piero 1998] for the proofs of the static and kinematic theorems under this definition. There is no definition of the collapse multiplier in the present paper since the strong mechanism need not exist (see Example 7.6), and the supremum and infimum can be different, depending of the choice of the function spaces, as discussed in Example 7.12.

In this paper we call the definitions of the infimum and of the supremum mentioned above the kinematic and static problems of limit analysis of no-tension bodies. The kinematic problem involves the choice of the function space for admissible displacements. The static problem involves the choice of the function space for admissible stress fields. The central question of the paper is under which conditions these two numbers coincide. Various choices of the spaces are discussed in detail: for the space of displacements we consider the subspaces satisfying the null boundary condition on the fixed part of the boundary of (a) functions of bounded deformation, (b) the Sobolev spaces $W^{1,p}$, $1 \le p < \infty$, (c) the Sobolev space $W^{1,\infty}$ of lipschitzian displacements, and (d) the space C^1 of all smooth displacements on the closure of the body. Corresponding to these choices we are led to stress spaces which consist, respectively, of (a′) the space of continuous functions, (b′) the space L^q of stress fields that are integrable with the power q where q is the Hölder conjugate exponent of p, (c′) the stress fields represented by finitely additive measures on the body that are absolutely continuous with respect to the Lebesgue measure, and (d′) the stress fields represented by countably additive Borel measures on the closure of the body.

The problems mentioned are formulated as convex variational problems considered in [Ekeland and Témam 1999, Chapter III]. Following the similar application of the duality theory to the deformation (Hencky) theory of plasticity in [Témam and Strang 1980] and [Témam 1983], the static problem of the limit analysis is unconditionally shown to be the dual problem (in the sense of [Ekeland and Témam 1999]) of the kinematic problem. The theory provides a *necessary and sufficient condition* for the primal and dual variational problems giving the same result, the *normality.* This is particularized to the static and kinematic problems of no-tension bodies. The condition can be applied with any choice of function spaces, and different choices lead to different results. Another condition, called *qualification hypothesis* in [Ekeland and Témam 1999, Chapter III, Remark 2.4], provides a *sufficient condition.* However, normality is difficult to verify. The qualification hypothesis even cannot be satisfied, with some function spaces, by the no-tension material, at variance with the deformation theory of plasticity. This failure occurs in the spaces of admissible displacements as in (a) and (b), no matter how tame the loads. An example is presented in which the static and kinematic problems give different results. The necessary and sufficient condition and the qualification hypothesis can be satisfied with the choices (c) and (d). However, then the space of admissible stresses must be enlarged to contain measures as mentioned above.

Another application of the duality theory, different from the one employed in [Témam 1983], is used to derive a simple condition for the static admissibility of a given multiplier.

In the introductions to the subsequent sections we give brief outlines of the material presented. We also refer to the summary in Section 8 for a more detailed discussion of the results of the paper.

Throughout, we use the conventions for vectors and second order tensors identical with those in [Gurtin 1981]. Thus Lin denotes the set of all second order tensors on $\mathbb{R}^n$, i.e., linear transformations from $\mathbb{R}^n$ into itself, Sym is the subspace of symmetric tensors, Sym^+ the set of all positive semidefinite elements of Sym; additionally Sym^- is the set of all negative semidefinite elements of Sym. The scalar product of $\boldsymbol{A}, \boldsymbol{B} \in \mathrm{Lin}$ is defined by $\boldsymbol{A} \cdot \boldsymbol{B} = \mathrm{tr}(\boldsymbol{A}\boldsymbol{B}^{\mathrm{T}})$ and $|\cdot|$ denotes the associated euclidean norm on Lin. If $\boldsymbol{A}, \boldsymbol{B} \in \mathrm{Sym}$, we write $\boldsymbol{A} \ge \boldsymbol{B}$ to say that $\boldsymbol{A} - \boldsymbol{B} \in \mathrm{Sym}^+$. We denote by $\mathbf{1}$ the unit tensor in Sym.

2. Abstract setting of the limit analysis for no-tension materials

We start this section with an informal introduction to the no-tension body and applied loads, i.e., surface tractions and body forces. Section 2B formulates the problem abstractly, with the energy of the loads as linear functionals on displacements and stresses as linear functionals on strains. Section 2C gives definitions of kinematically and statically admissible multipliers, of the infima and suprema thereof, of the collapse mechanism, and strong collapse mechanism. Section 2D reviews the duality theory of Ekeland and Témam. It presents the normality condition, which is equivalent to the equality of the results of the primal and dual problems, and a sufficient condition, the qualification hypothesis. Section 2E particularizes Section 2D to the kinematic and static problems of limit analysis of no-tension bodies. Proposition 2.5 gives a necessary condition for the equality of the results of the kinematic and static problems (i.e., for the normality) and Proposition 2.6 a sufficient condition (i.e., the qualification hypothesis). Finally Proposition 2.8 gives a necessary and sufficient condition for a multiplier to be statically admissible.

2A. ***Loads and potential energy.*** Let Ω be a reference configuration of a continuous body made of a no-tension material; it is assumed that Ω is a bounded connected open set in $\mathbb{R}^n$ (typically $n = 2$ or $n = 3$) with Lipschitz boundary $\partial\Omega$ in the sense of [Ekeland and Témam 1999, Chapter X, Section 2.2], of outer normal $\boldsymbol{n}$. The body is fixed on an area measurable subset $\mathscr{D}$ of $\partial\Omega$ while on $\mathscr{S} := \partial\Omega \setminus \mathscr{D}$ the body is subjected to surface tractions depending on the loading multiplier as specified below. We consider displacements $\boldsymbol{v} : \Omega \to \mathbb{R}^n$ from a Banach space of displacements V. Several choices of V are given below, and in all these choices it is meaningful to speak about the values of $\boldsymbol{v}$ on the boundary $\partial\Omega$, and in particular it is meaningful to require that

$$\boldsymbol{v} = \boldsymbol{0} \quad \text{on } \mathscr{D}, \tag{2-1}$$

either in the classical or in some generalized sense. We denote by W the set of all displacements from V which satisfy (2-1).

We assume that the body is subjected to loads consisting of a surface traction on $\mathscr{S}$ and a body force in Ω; both the surface traction and the body force depend affinely on a real parameter λ called the *loading multiplier*. Thus if $\lambda \in \mathbb{R}$, the surface tractions $\boldsymbol{s}(\lambda) : \mathscr{S} \to \mathbb{R}^n$ and the body force $\boldsymbol{b}(\lambda) : \Omega \to \mathbb{R}^n$ are given by

$$\boldsymbol{s}(\lambda) = \boldsymbol{s}_\circ + \lambda\bar{\boldsymbol{s}}, \quad \boldsymbol{b}(\lambda) = \boldsymbol{b}_\circ + \lambda\bar{\boldsymbol{b}},$$

where $\boldsymbol{s}_\circ$ and $\bar{\boldsymbol{s}}$ are vector-valued functions on $\mathscr{S}$ and $\boldsymbol{b}_\circ$ and $\bar{\boldsymbol{b}}$ are vector-valued functions on Ω. The functions $\boldsymbol{s}_\circ$, $\bar{\boldsymbol{s}}$, $\boldsymbol{b}_\circ$, $\bar{\boldsymbol{b}}$ have to belong to appropriate spaces to make the discussion that follows meaningful. We call the pair $(\boldsymbol{s}(\lambda), \boldsymbol{b}(\lambda))$ the *loads corresponding to* λ, the pair $(\boldsymbol{s}_\circ, \boldsymbol{b}_\circ)$ the *permanent loads* and the pair $(\bar{\boldsymbol{s}}, \bar{\boldsymbol{b}})$ the *variable loads*. We define the *potential energy* $\langle \boldsymbol{l}(\lambda), \boldsymbol{v}\rangle$ of the loads corresponding to λ on a displacement $\boldsymbol{v}$ by

$$\langle \boldsymbol{l}(\lambda), \boldsymbol{v}\rangle = \langle \boldsymbol{l}_\circ, \boldsymbol{v}\rangle + \lambda\langle \bar{\boldsymbol{l}}, \boldsymbol{v}\rangle \tag{2-2}$$

where

$$\langle \boldsymbol{l}_\circ, \boldsymbol{v}\rangle = \int_\Omega \boldsymbol{b}_\circ \cdot \boldsymbol{v}\, d\mathscr{L}^n + \int_{\mathscr{S}} \boldsymbol{s}_\circ \cdot \boldsymbol{v}\, d\mathscr{H}^{n-1}, \tag{2-3}$$

and

$$\langle \bar{\boldsymbol{l}}, \boldsymbol{v} \rangle = \int_\Omega \bar{\boldsymbol{b}} \cdot \boldsymbol{v} \, d\mathscr{L}^n + \int_{\mathscr{S}} \bar{\boldsymbol{s}} \cdot \boldsymbol{v} \, d\mathscr{H}^{n-1}, \tag{2-4}$$

for $\boldsymbol{v} \in W$, with $\mathscr{L}^n$ and $\mathscr{H}^{n-1}$ the volume and area measures, i.e., the Lebesgue measure and the $(n-1)$-dimensional Hausdorff measure in $\mathbb{R}^n$. Here the integrals are interpreted either classically or in an appropriate generalized sense to be precisely specified below.

We further define the infinitesimal strain tensor $\hat{\boldsymbol{E}}(\boldsymbol{v})$ of the displacement $\boldsymbol{v} \in W$ by

$$\hat{\boldsymbol{E}}(\boldsymbol{v}) = \tfrac{1}{2}(\nabla \boldsymbol{v} + \nabla \boldsymbol{v}^{\mathrm{T}}), \tag{2-5}$$

which will be either a function defined for almost all points of Ω, taking the values in the space Sym, or a Sym-valued measure. Throughout, "almost all", "almost every" and "almost everywhere" mean with respect to the Lebesgue measure. It is then meaningful to consider the space W^+ of all displacements $\boldsymbol{v} \in W$ for which $\hat{\boldsymbol{E}}(\boldsymbol{v})$ is either a positive semidefinite tensor for almost every point of Ω or a measure taking values in the set of positive semidefinite tensors. This is a convex cone in W, i.e., we have the following implications:

$$\begin{aligned} \boldsymbol{v}, \boldsymbol{w} \in W^+ \quad &\Rightarrow \quad \boldsymbol{v} + \boldsymbol{w} \in W^+, \\ \boldsymbol{v} \in W^+ \text{ and } t \in \mathbb{R},\ t \geq 0 \quad &\Rightarrow \quad t\boldsymbol{v} \in W^+. \end{aligned}$$

We assume that for the selected space W, the strain tensors $\hat{\boldsymbol{E}}(\boldsymbol{v}) : \Omega \to \mathrm{Sym}$ belong to some Banach space Y, which will form either an appropriately chosen class of functions $\boldsymbol{F} : \Omega \to \mathrm{Sym}$, possibly defined only almost everywhere in Ω, or the space of Sym valued measures. We furthermore denote by Y^+ the convex cone of all $\boldsymbol{F} \in Y$ such that either $\boldsymbol{F}$ is positive semidefinite almost everywhere or a measure with values in the space of positive semidefinite tensors. Thus if $\boldsymbol{v} \in W^+$, then $\hat{\boldsymbol{E}}(\boldsymbol{v}) \in Y^+$.

Next, we consider the stress fields $\boldsymbol{T}$. In the classical cases, this will be a function from Ω to Sym, possibly defined only almost everywhere. We shall also consider stress fields $\boldsymbol{T}$ represented by a more general object, viz., a finitely additive or countably additive measure to be specified in the subsequent formal treatment. We denote by Y^* the linear space of all stress fields, which we assume to form a closed subspace of the Banach space Y' of all continuous linear functionals on Y, i.e., the dual of Y. We denote by $(\boldsymbol{T}, \boldsymbol{F})$ the pairing between elements $\boldsymbol{T} \in Y^*$ and elements $\boldsymbol{F} \in Y$, i.e., the value of the linear functional $\boldsymbol{T}$ on an element $\boldsymbol{F}$. In the classical case we have

$$(\boldsymbol{T}, \boldsymbol{F}) = \int_\Omega \boldsymbol{T} \cdot \boldsymbol{F} \, d\mathscr{L}^n; \tag{2-6}$$

the integral has to be interpreted in a generalized sense in the more general cases of Y and Y^*. The stress fields in the masonry bodies take negative semidefinite values. If $\boldsymbol{T} : \Omega \to \mathrm{Sym}$ is a negative semidefinite classical function, we have

$$(\boldsymbol{T}, \boldsymbol{F}) \leq 0 \quad \text{for all } \boldsymbol{F} \in Y^+. \tag{2-7}$$

In the classical case we denote by Y^{*-} the set of all stress fields on Ω which take negative semidefinite values almost everywhere on Ω. When the stress field $\boldsymbol{T} \in Y^*$ is not represented by a function, we define Y^{*-} as the set of all elements of Y^* which satisfy (2-7). (In the classical case this leads to the requirement posed previously.) We say that a stress field $\boldsymbol{T}$ is Y^* admissible if $\boldsymbol{T} \in Y^{*-}$.

2B. ***Abstract setting of the problem.*** We summarize the essential features of the discussion in the preceding section. We consider general objects

$$W,\ \boldsymbol{l},\ \boldsymbol{l}_\circ,\ Y,\ Y^*,\ \hat{\boldsymbol{E}},\ Y^+,\ Y^{*-} \tag{2-8}$$

of the following nature:

(i) W is a Banach space;

(ii) $\boldsymbol{l}_\circ$ and $\bar{\boldsymbol{l}}$ are elements in the dual W^* of W;

(iii) Y is a Banach space and Y^* is a closed subspace of the dual Y' of Y;

(iv) $\hat{\boldsymbol{E}}$ is a continuous linear transformation from W to Y;

(v) Y^+ and Y^{*-} are closed convex cones in Y and in the dual Y^* of Y, respectively, which are dual to each other in the sense that

$$\{\boldsymbol{F} \in Y : (\boldsymbol{T}, \boldsymbol{F}) \le 0 \text{ for every } \boldsymbol{T} \in Y^{*-}\} = Y^+,$$
$$\{\boldsymbol{T} \in Y^* : (\boldsymbol{T}, \boldsymbol{F}) \le 0 \text{ for every } \boldsymbol{F} \in Y^+\} = Y^{*-}.$$

We interpret W as the set of displacement fields over Ω satisfying the kinematical constraint (2-1), and $\boldsymbol{l}_\circ$ and $\bar{\boldsymbol{l}}$ as the energy functionals of the permanent and variable loads. We then define $\boldsymbol{l}(\lambda)$ by (2-2) for any $\lambda \in \mathbb{R}$. We denote by $\langle \cdot, \cdot \rangle$ the dual pairing between W^* and W; i.e., $\langle \boldsymbol{m}, \boldsymbol{v} \rangle \in \mathbb{R}$ denotes the value of the linear functional $\boldsymbol{m} \in W^*$ on an element $\boldsymbol{v} \in W$. The transformation $\hat{\boldsymbol{E}}(\cdot)$ associates with any displacement $\boldsymbol{v} \in W$ an element $\hat{\boldsymbol{E}}(\boldsymbol{v}) \in Y$, which we interpret as the strain field of $\boldsymbol{v}$. We define W^+ by

$$W^+ = \{\boldsymbol{v} \in W : \hat{\boldsymbol{E}}(\boldsymbol{v}) \in Y^+\}$$

and view W^+ as the set of all displacements with positive semidefinite strain tensor over Ω. We denote by $(\cdot, \cdot)$ the dual pairing between Y^* and Y, i.e., $(\boldsymbol{T}, \boldsymbol{F}) \in \mathbb{R}$ denotes the value of the linear functional $\boldsymbol{T} \in Y^*$ on the element $\boldsymbol{F} \in Y$. The stress fields are interpreted as the elements of Y^*, and Y^{*-} is interpreted as the set of all negative semidefinite stress fields. We say that $\boldsymbol{T} \in Y^*$ is an *admissible stress field* if $\boldsymbol{T} \in Y^{*-}$; to emphasize the space of stresses, we sometimes say that $\boldsymbol{T}$ is Y^* admissible. We say that a stress field $\boldsymbol{T} \in Y^*$ *equilibrates the loads corresponding to* λ if

$$(\boldsymbol{T}, \hat{\boldsymbol{E}}(\boldsymbol{v})) = \langle \boldsymbol{l}(\lambda), \boldsymbol{v} \rangle$$

for every $\boldsymbol{v} \in W$.

In Sections 2C and 2E, we will use the abstract setting described above. In subsequent sections we make concrete choices for the objects introduced here.

2C. ***Kinematically and statically admissible multipliers.*** We say that a multiplier λ is *kinematically admissible* if

$$\text{there exists a } \ \boldsymbol{v} \in W^+ \ \text{ such that } \ \langle \bar{\boldsymbol{l}}, \boldsymbol{v} \rangle = 1 \ \text{ and } \ \langle \boldsymbol{l}(\lambda), \boldsymbol{v} \rangle = 0. \tag{2-9}$$

The last notion depends on the choice of the space W, and to emphasize this, we will sometimes say that λ is W-kinematically admissible. We denote the set of all kinematically admissible multipliers by $\bar{\Lambda}$. If λ is given, we call the element $\boldsymbol{v}$ as in (2-9) a *mechanism corresponding to* λ.

We say that a multiplier $\lambda \in \mathbb{R}$ is *statically admissible* if there exists an admissible stress field $\boldsymbol{T}$ which equilibrates the loads corresponding to λ. We shall sometimes say that λ is Y^*-statically admissible. We denote by Λ the set of all statically admissible multipliers.

The sets $\bar{\Lambda}$ and Λ are intervals, possibly empty, singletons, bounded, unbounded, open, or semiopen. To see, e.g., that $\bar{\Lambda}$ is an interval, we note that if $\lambda,\ \mu \in \bar{\Lambda}$ and $s \geq 0,\ t \geq 0,\ s+t=1$, then also $s\lambda + t\mu \in \bar{\Lambda}$ since if $\boldsymbol{v}, \boldsymbol{w} \in W^+$ denote mechanisms corresponding to λ and μ, respectively, then $s\boldsymbol{v} + t\boldsymbol{w} \in W^+$ is a mechanism corresponding to $s\lambda + t\mu \in \bar{\Lambda}$. That Λ is an interval is proved similarly.

The interval Λ is situated to the left of the interval $\bar{\Lambda}$ in the sense that

$$\text{if } \ \lambda \in \Lambda \ \text{ and } \ \mu \in \bar{\Lambda} \ \text{ then } \ \lambda \leq \mu. \tag{2-10}$$

Hence the intersection of Λ and $\bar{\Lambda}$ can contain at most one point. To prove (2-10), we note that if μ is kinematically admissible and $\boldsymbol{v}$ is a mechanism corresponding to it, then $\mu = -\langle \boldsymbol{l}_\circ, \boldsymbol{v}\rangle$ while if λ is statically admissible and $\boldsymbol{T} \in Y^{*-}$ a corresponding stress field, then $0 \geq (\boldsymbol{T}, \hat{\boldsymbol{E}}(\boldsymbol{v})) = \langle \boldsymbol{l}(\lambda), \boldsymbol{v}\rangle$ and hence $\lambda \leq -\langle \boldsymbol{l}_\circ, \boldsymbol{v}\rangle$, which gives (2-10).

Central to our considerations are the numbers (or the symbols ∞ and $-\infty$)

$$\bar{\lambda}_W := \inf\{\lambda \in \mathbb{R} : \lambda \text{ is } W \text{ kinematically admissible}\} \tag{2-11}$$

and

$$\lambda_{Y^*} := \sup\{\lambda \in \mathbb{R} : \lambda \text{ is } Y^* \text{ statically admissible}\}. \tag{2-12}$$

We call (2-11) the *kinematic problem* and (2-12) the *static problem.* We furthermore call $\bar{\lambda}_W$ the *critical multiplier of the kinematic problem* and λ_{Y^*} the *critical multiplier of the static problem.* The implication in (2-10) gives

$$\lambda_{Y^*} \leq \bar{\lambda}_W. \tag{2-13}$$

We examine conditions under which we have the equality in (2-13). Example 7.12, below, shows that under common choices of function spaces and under bounded and piecewise continuous loads we have the strict inequality sign. In the following section we treat the equality in (2-13) by applying the duality theory of [Ekeland and Témam 1999].

We close this section with a simple sufficient condition for the equality in (2-13). We say that the multiplier $\lambda_c \in \mathbb{R}$ *admits a strong mechanism* if there exists a statically admissible stress field $\boldsymbol{T}_c \in Y^{*-}$ corresponding to λ_c and a $\boldsymbol{v}_c \in W$ such that

$$\langle \bar{\boldsymbol{l}}, \boldsymbol{v}_c\rangle = 1 \ \text{ and } \ (\boldsymbol{T} - \boldsymbol{T}_c, \hat{\boldsymbol{E}}(\boldsymbol{v}_c)) \leq 0 \quad \text{for every } \ \boldsymbol{T} \in Y^{*-}.$$

Proposition 2.1. *If λ_c admits a strong mechanism $\boldsymbol{v}_c$, then*

$$\lambda_{Y^*} = \bar{\lambda}_W = \lambda_c \tag{2-14}$$

and $\boldsymbol{v}_c$ is a corresponding mechanism.

Proof. The definition requires that λ_c be statically admissible and hence

$$\lambda_c \leq \lambda_{Y^*}. \tag{2-15}$$

We have $(\boldsymbol{T}-\boldsymbol{T}_c, \hat{\boldsymbol{E}}(\boldsymbol{v}_c)) \le 0$ for every $\boldsymbol{T} \in Y^{*-}$; replacing $\boldsymbol{T}$ by $t\boldsymbol{T}$ where $t>0$, we obtain another element of Y^{*-} and hence $(t\boldsymbol{T}-\boldsymbol{T}_c, \hat{\boldsymbol{E}}(\boldsymbol{v}_c)) \le 0$; dividing by t and letting $t \to \infty$ we thus obtain $(\boldsymbol{T}, \hat{\boldsymbol{E}}(\boldsymbol{v}_c)) \le 0$, which by the assumed duality of the cones Y^+ and Y^{*-} stated in the preceding section implies that $\hat{\boldsymbol{E}}(\boldsymbol{v}_c) \in Y^+$, and hence $\boldsymbol{v}_c \in W^+$. Setting $\boldsymbol{T}=\boldsymbol{0}$ in the inequality $(\boldsymbol{T}-\boldsymbol{T}_c, \hat{\boldsymbol{E}}(\boldsymbol{v}_c)) \le 0$ we obtain $(\boldsymbol{T}_c, \hat{\boldsymbol{E}}(\boldsymbol{v}_c)) \ge 0$ and as also $\boldsymbol{T}_c \in Y^{*-}$ and $\hat{\boldsymbol{E}}(\boldsymbol{v}) \in Y^+$, we have $(\boldsymbol{T}_c, \hat{\boldsymbol{E}}(\boldsymbol{v}_c)) \le 0$ and hence $(\boldsymbol{T}_c, \hat{\boldsymbol{E}}(\boldsymbol{v}_c)) = 0$. Since $\boldsymbol{T}_c$ balances the loads corresponding to λ_c, we have

$$0 = (\boldsymbol{T}_c, \hat{\boldsymbol{E}}(\boldsymbol{v}_c)) = \langle \boldsymbol{l}(\lambda_c), \boldsymbol{v}_c \rangle$$

and since $\langle \bar{\boldsymbol{l}}, \boldsymbol{v}_c \rangle = 1$ as part of the definition of the strong mechanism, we see that λ_c is kinematically admissible and $\boldsymbol{v}_c$ a mechanism corresponding to it. Thus

$$\bar{\lambda}_W \le \lambda_c. \tag{2-16}$$

Combining inequalities (2-15) and (2-16) with (2-13) we obtain (2-14). Then $\boldsymbol{v}_c$ is a corresponding mechanism. □

Remark 2.2. In [Del Piero 1998, IV.1], a definition is given of collapse mechanism for the general case of a normal linear material (of which the no-tension material is a special case) which eventually leads to the properties embodied in the present definition of strong mechanism. Indeed, as a consequence of Del Piero's definition and of the assumptions of his kinematic theorem in the same work, the collapse mechanism in the sense of [Del Piero 1998] is assumed to exist. If we denote it by $\bar{\boldsymbol{v}}_c$, it satisfies

$$\langle \bar{\boldsymbol{l}}, \bar{\boldsymbol{v}}_c \rangle > 0,$$
$$(\boldsymbol{T}-\boldsymbol{T}_c, \hat{\boldsymbol{E}}(\bar{\boldsymbol{v}}_c)) \le 0 \quad \text{for every} \quad \boldsymbol{T} \in Y^{*-}.$$

(Cf. the text between Equations (42) and (43), and the second sentence after Equation (37), respectively.) It then follows that $\boldsymbol{v}_c := \bar{\boldsymbol{v}}_c / \langle \bar{\boldsymbol{l}}, \bar{\boldsymbol{v}}_c \rangle$ is a strong mechanism in the present sense. Thus Del Piero's definition of collapse mechanism is more restrictive than the present definition of strong mechanism and, hence Proposition 2.1 covers all cases treated in the version of the kinematic theorem in [Del Piero 1998].

We consider the assumption of the existence of collapse mechanism as too restrictive. Indeed, in Example 7.6 (below) we present loads which satisfy (2-14) and yet there is no collapse mechanism in the sense of [Del Piero 1998, Definition IV.1] or strong mechanism in the present sense. In the subsequent treatment we seek to prove (2-14) under more general assumptions.

2D. ***Primal and dual variational problems of convex analysis.*** We here outline the duality theory for convex variational problems developed in [Ekeland and Témam 1999, Chapter III].

Consider the variational problem [loc. cit., Remark 4.2]

$$\bar{J} = \inf\{C(\boldsymbol{v}) + D(\hat{\boldsymbol{E}}(\boldsymbol{v})) : \boldsymbol{v} \in W\}, \tag{2-17}$$

where $C : W \to \mathbb{R} \cup \{\infty\}$, $D : Y \to \mathbb{R} \cup \{\infty\}$ are general convex functions on Banach spaces W, Y and $\hat{\boldsymbol{E}}(\cdot) : W \to Y$ is a general bounded linear transformation. We call (2-17) the *primal problem.*

The *dual problem* is defined by

$$J = \sup\{-C^*(-\hat{\boldsymbol{E}}^*\boldsymbol{T}) - D^*(\boldsymbol{T}) : \boldsymbol{T} \in Y^*\}, \tag{2-18}$$

where W^* is the dual of W and Y^* is a closed subspace of the dual space Y' of Y, $C^* : W^* \to \mathbb{R} \cup \{\infty\}$, $D^* : Y^* \to \mathbb{R} \cup \{\infty\}$ are the convex conjugates of C, D, respectively, and $\hat{\boldsymbol{E}}^* : Y^* \to W^*$ is the adjoint transformation of $\hat{\boldsymbol{E}}$. The convex conjugate functions are defined by

$$\boldsymbol{C}^*(\boldsymbol{m}) = \sup\{\langle \boldsymbol{m}, \boldsymbol{v}\rangle - C(\boldsymbol{v}) : \boldsymbol{v} \in W\},$$
$$D^*(\boldsymbol{T}) = \sup\{(\boldsymbol{T}, \boldsymbol{F}) - D(\boldsymbol{F}) : \boldsymbol{F} \in Y\},$$

for each $\boldsymbol{m} \in W^*$, $\boldsymbol{T} \in Y^*$, and the adjoint $\hat{\boldsymbol{E}}^*$ is a linear transformation defined by the relation

$$(\boldsymbol{T}, \hat{\boldsymbol{E}}(\boldsymbol{v})) = \langle \hat{\boldsymbol{E}}^* \boldsymbol{T}, \boldsymbol{v}\rangle$$

for each $\boldsymbol{v} \in W$, $\boldsymbol{T} \in Y^*$.

We assume that the functions C and D are proper, i.e., each of them is less than ∞ somewhere and bigger than $-\infty$ everywhere. One has generally

$$-\infty \le J \le \bar{J} \le \infty.$$

Let $H : Y \to \mathbb{R} \cup \{-\infty, \infty\}$ be defined by

$$H(\boldsymbol{F}) = \inf\{C(\boldsymbol{v}) + D(\hat{\boldsymbol{E}}(\boldsymbol{v}) - \boldsymbol{F}) : \boldsymbol{v} \in W\}, \tag{2-19}$$

for $\boldsymbol{F} \in Y$, so that $H(\boldsymbol{0}) = \bar{J}$. The function H is convex. The problem (2-17) is said to be *normal* if $H(\boldsymbol{0})$ is finite and H is lower semicontinuous at $\boldsymbol{0}$.

Proposition 2.3. *The following conditions are equivalent*:

(i) *The problem (2-17) is normal.*

(ii) *One has*

$$J = \bar{J} \tag{2-20}$$

and this number is finite.

The problem (2-17) is said to satisfy the *qualification hypothesis* if there exists a $\boldsymbol{v}_\circ \in W$ such that

$$C(\boldsymbol{v}_\circ) < \infty, \;\; D(\hat{\boldsymbol{E}}(\boldsymbol{v}_\circ)) < \infty \;\text{ and } D \text{ is continuous at } \hat{\boldsymbol{E}}(\boldsymbol{v}_\circ). \tag{2-21}$$

See [Ekeland and Témam 1999, Chapter III, Remark 2.4].

Proposition 2.4. *Suppose the problem (2-17) satisfies the qualification hypothesis. Then*:

(i) *Equation (2-20) holds.*

(ii) *If the number $J = \bar{J}$ is finite, the dual problem has a solution, i.e., there exists a $\boldsymbol{T} \in Y^*$ such that*

$$J = -C^*(-\hat{\boldsymbol{E}}^* \boldsymbol{T}) - D^*(\boldsymbol{T}).$$

We emphasize that the qualification hypothesis is sufficient for (2-20) but not necessary, the necessary and sufficient condition is the normality.

2E. ***Primal and dual variational problems of limit analysis.*** The definition (2-11) of $\bar{\lambda}_W$ is easily seen to be equivalent to

$$\bar{\lambda}_W = \inf\{-\langle \boldsymbol{l}_\circ, \boldsymbol{v}\rangle : \boldsymbol{v} \in W^+,\ \langle \bar{\boldsymbol{l}}, \boldsymbol{v}\rangle = 1\}. \tag{2-22}$$

Proposition 2.5. *Let* $H : Y \to \mathbb{R} \cup \{-\infty, \infty\}$ *be given by*

$$H(\boldsymbol{F}) = \inf\{-\langle \boldsymbol{l}_\circ, \boldsymbol{v}\rangle : \boldsymbol{v} \in W,\ \hat{\boldsymbol{E}}(\boldsymbol{v}) - \boldsymbol{F} \in Y^+,\ \langle \bar{\boldsymbol{l}}, \boldsymbol{v}\rangle = 1\}, \tag{2-23}$$

$\boldsymbol{F} \in Y$. *Then*:

(i) H *is convex and nondecreasing in the sense that* $H(\boldsymbol{F}) \le H(\boldsymbol{G})$ *whenever* $\boldsymbol{G} - \boldsymbol{F} \in Y^+$.

(ii) *We have*

$$\lambda_{Y^*} = \bar{\lambda}_W \in \mathbb{R}$$

if and only if $H(\mathbf{0})$ *is finite and* H *is lower semicontinuous at* $\mathbf{0}$.

Here the finiteness of $H(\mathbf{0})$ and the lower semicontinuity of H at $\mathbf{0}$ is the normality condition for (2-22).

Proof. The problem (2-22) can be rewritten as

$$\bar{\lambda}_W = \inf\{C(\boldsymbol{v}) + D(\hat{\boldsymbol{E}}(\boldsymbol{v})) : \boldsymbol{v} \in W\} \tag{2-24}$$

where

$$C : W \to \mathbb{R} \cup \{\infty\}, \quad D : Y \to \mathbb{R} \cup \{\infty\}$$

are the functions defined by

$$C(\boldsymbol{v}) = \begin{cases} -\langle \boldsymbol{l}_\circ, \boldsymbol{v}\rangle & \text{if } \boldsymbol{v} \in W \text{ and } \langle \bar{\boldsymbol{l}}, \boldsymbol{v}\rangle = 1, \\ \infty & \text{if } \boldsymbol{v} \in W \text{ and } \langle \bar{\boldsymbol{l}}, \boldsymbol{v}\rangle \ne 1, \end{cases} \tag{2-25}$$

$$D(\boldsymbol{F}) = \begin{cases} 0 & \text{if } \boldsymbol{F} \in Y^+, \\ \infty & \text{if } \boldsymbol{F} \in Y \setminus Y^+. \end{cases} \tag{2-26}$$

The dual problem reads

$$\lambda_{Y^*} = \sup\{\lambda \in \mathbb{R} : \lambda \text{ is statically admissible}\}. \tag{2-27}$$

To prove the last statement, calculate C^* and D^*. If $\boldsymbol{m} \in W^*$, then

$$C^*(\boldsymbol{m}) = \sup\{\langle \boldsymbol{m} + \boldsymbol{l}_\circ, \boldsymbol{v}\rangle : \boldsymbol{v} \in W, \langle \bar{\boldsymbol{l}}, \boldsymbol{v}\rangle = 1\}$$

and since this supremum is finite if and only if $\boldsymbol{m} + \boldsymbol{l}_\circ$ and $\bar{\boldsymbol{l}}$ are parallel, say $\boldsymbol{m} + \boldsymbol{l}_\circ = -\lambda\bar{\boldsymbol{l}}$ for some $\lambda \in \mathbb{R}$, and then $\langle \boldsymbol{m} + \boldsymbol{l}_\circ, \boldsymbol{v}\rangle = -\lambda$, we have

$$C^*(\boldsymbol{m}) = \begin{cases} -\lambda & \text{if there exists a } \lambda \in \mathbb{R} \text{ such that } \langle \boldsymbol{m}, \boldsymbol{v}\rangle + \langle \boldsymbol{l}(\lambda), \boldsymbol{v}\rangle = 0 \text{ for every } \boldsymbol{v} \in W, \\ \infty & \text{otherwise,} \end{cases} \tag{2-28}$$

$\boldsymbol{m} \in W^*$. Letting $\boldsymbol{T} \in Y^*$, setting $\boldsymbol{m} = -\hat{\boldsymbol{E}}^*\boldsymbol{T}$ and noting that the finite regime in (2-28) occurs if and only if $\boldsymbol{T}$ equilibrates the loads corresponding to λ, in the sense that $\big(\boldsymbol{T}, \hat{\boldsymbol{E}}(\boldsymbol{v})\big) = \langle \boldsymbol{l}(\lambda), \boldsymbol{v}\rangle$ for each $\boldsymbol{v} \in W$, we obtain

$$C^*(-\hat{\boldsymbol{E}}^*\boldsymbol{T}) = \begin{cases} -\lambda & \text{if } \boldsymbol{T} \text{ equilibrates the loads corresponding to } \lambda, \\ \infty & \text{otherwise.} \end{cases}$$

Furthermore, the definition (2-26) of D^* and the fact that Y^+ is a cone implies that

$$D^*(\boldsymbol{T}) = \begin{cases} 0 & \text{if } \boldsymbol{T} \in Y^{*-} \\ \infty & \text{if } \boldsymbol{T} \in Y^* \setminus Y^{*-} \end{cases}$$

$\boldsymbol{T} \in Y^*$. Thus the right-hand side of the dual variational problem (2-18) is

$$-C^*(-\hat{\boldsymbol{E}}^*\boldsymbol{T}) - D^*(\boldsymbol{T}) = \begin{cases} \lambda & \text{if } \boldsymbol{T} \text{ equilibrates the loads corresponding to } \lambda \text{ and } \boldsymbol{T} \in Y^{*-}, \\ -\infty & \text{otherwise,} \end{cases}$$

and (2-27) follows.

The function H of (2-19) is given by (2-23).

(i) H is convex (as stated generally in Section 2D). To prove the nondecreasing character of H, it suffices to note that if $\boldsymbol{G} - \boldsymbol{F} \in Y^+$ then

$$\{\boldsymbol{v} \in W,\ \hat{\boldsymbol{E}}(\boldsymbol{v}) - \boldsymbol{G} \in Y^+,\ \langle \bar{\boldsymbol{l}}, \boldsymbol{v}\rangle = 1\} \subset \{\boldsymbol{v} \in W,\ \hat{\boldsymbol{E}}(\boldsymbol{v}) - \boldsymbol{F} \in Y^+,\ \langle \bar{\boldsymbol{l}}, \boldsymbol{v}\rangle = 1\}.$$

(ii) This follows from Proposition 2.3. □

Proposition 2.6. *Assume that*

$$\text{there exists a } \bar{\boldsymbol{v}}_\circ \text{ in } W^+ \text{ satisfying } \langle \bar{\boldsymbol{l}}, \bar{\boldsymbol{v}}_\circ\rangle > 0 \text{ such that } \hat{\boldsymbol{E}}(\bar{\boldsymbol{v}}_\circ) \text{ is an interior point of } Y^+. \tag{2-29}$$

Then

$$\lambda_{Y^*} = \bar{\lambda}_W; \tag{2-30}$$

if, additionally, the number $\lambda_{Y^*} = \bar{\lambda}_W$ is finite, then $\bar{\lambda}_W$ is statically admissible.

Condition (2-29) is the qualification hypothesis for Problem (2-22).

Proof. Consider the problem (2-24) with C and D given by (2-25) and (2-26). This problem satisfies the qualification hypothesis if and only if there exists a $\bar{\boldsymbol{v}}_\circ$ as in (2-29). Indeed, assume that the problem satisfies the qualification hypothesis. Then there exists a point $\bar{\boldsymbol{v}}_\circ$ such that (2-21) hold; the first of these three conditions and the definition of C gives that $\langle \bar{\boldsymbol{l}}, \bar{\boldsymbol{v}}_\circ\rangle = 1$; the second of these conditions and the definition of D gives $\bar{\boldsymbol{v}}_\circ \in W^+$, and the third condition gives that D is finite in some neighborhood of $\hat{\boldsymbol{E}}(\bar{\boldsymbol{v}}_\circ)$. Then $\bar{\boldsymbol{v}}_\circ$ is as in (2-29). Conversely, if (2-29) holds, then the point $\boldsymbol{v}_\circ := \bar{\boldsymbol{v}}_\circ / \langle \bar{\boldsymbol{l}}, \bar{\boldsymbol{v}}_\circ\rangle$ satisfies (2-21).

Then the assertion of the proposition follows from Proposition 2.4. □

Remark 2.7. Condition (2-29) is never satisfied if one uses displacements from the space BD of functions of bounded deformation or if one uses displacements from the Sobolev space $W^{1,p}$ of functions integrable together with the gradient in the power p where $1 \le p < \infty$. Indeed, we shall see that then the cone Y^+ has empty interior; see Sections 3 and 4. The cone Y^+ has nonempty interior if one uses lipschitzian displacements or continuously differentiable displacements on the closure of Ω, see Sections 5 and 6. However, we shall see that in the case of continuously differentiable displacements, (2-29) can be satisfied essentially only in the pure traction problem, when $\mathscr{D} = \varnothing$. Condition (2-29) is only sufficient for (2-30); a necessary and sufficient condition is provided by 2.5: the finiteness of $H(\boldsymbol{0})$ and lower semicontinuity of H at $\boldsymbol{0}$. The last condition is difficult to verify in concrete cases. Only in the cases of lipschitzian displacements or of continuously differentiable displacements, the lower semicontinuity of H at $\boldsymbol{0}$ reduces to verifying lower semicontinuity of a real function of real variable.

Lower semicontinuity frequently holds even when (2-29) fails to hold, because in concrete cases of loads we often have the equality (2-30).

We now address the problem of statical admissibility of a given multiplier $\lambda \in \mathbb{R}$.

Proposition 2.8. *A multiplier λ is Y^*-statically admissible if and only if there exists a $c < \infty$ such that*

$$\sup\{\langle \boldsymbol{l}(\lambda), \boldsymbol{v}\rangle : \boldsymbol{v} \in W,\ \hat{\boldsymbol{E}}(\boldsymbol{v}) - \boldsymbol{F} \in Y^+\} \le c|\boldsymbol{F}| \tag{2-31}$$

for every $\boldsymbol{F} \in Y$, where $|\cdot|$ denotes the norm on Y.

Condition (2-31) is the normality of the problem of static admissibility of a given λ. This condition will be employed in Example 7.6. Clearly (2-31) implies that

$$\langle \boldsymbol{l}(\lambda), \boldsymbol{v}\rangle \le 0 \tag{2-32}$$

for every $\boldsymbol{v} \in W^+$. However, (2-32) does not suffice for the static admissibility of λ; see Example 7.12 and Remark 7.15, below. Inequality (2-31) says, roughly, that if we allow displacements with slightly negative strain, then $\langle \boldsymbol{l}(\lambda), \boldsymbol{v}\rangle$ can become positive, but not too much.

Proof. Consider the problem

$$\bar{I} = \inf\{-\langle \boldsymbol{l}(\lambda), \boldsymbol{v}\rangle : \boldsymbol{v} \in W^+\}. \tag{2-33}$$

This problem takes the form

$$\bar{I} = \inf\{C(\boldsymbol{v}) + D(\hat{\boldsymbol{E}}(\boldsymbol{v})) : \boldsymbol{v} \in W\} \tag{2-34}$$

with

$$C(\boldsymbol{v}) = -\langle \boldsymbol{l}(\lambda), \boldsymbol{v}\rangle \quad \text{and} \quad D(\boldsymbol{F}) = \begin{cases} 0 & \text{if } \boldsymbol{F} \in Y^+, \\ \infty & \text{otherwise,} \end{cases}$$

for $\boldsymbol{v} \in W$, $\boldsymbol{F} \in Y$, and with $\hat{\boldsymbol{E}}(\cdot)$ the small strain mapping. Problem (2-34) reads explicitly

$$\bar{I} = \begin{cases} 0 & \text{if } \langle \boldsymbol{l}(\lambda), \boldsymbol{v}\rangle \le 0 \text{ for every } \boldsymbol{v} \in W^+, \\ -\infty & \text{otherwise.} \end{cases} \tag{2-35}$$

Indeed, if $\langle \boldsymbol{l}(\lambda), \boldsymbol{v}\rangle \le 0$ for every $\boldsymbol{v} \in W^+$ then the infimum in (2-33) is taken over the set of nonnegative numbers and thus $\bar{I} \ge 0$; on the other hand, setting $\boldsymbol{v} = \boldsymbol{0}$ in (2-33) we obtain $\bar{I} \le 0$ and thus we have the first regime in (2-35). In the second regime we have $\langle \boldsymbol{l}(\lambda), \bar{\boldsymbol{v}}\rangle > 0$ for some $\bar{\boldsymbol{v}} \in W^+$; setting $\boldsymbol{v} = s\bar{\boldsymbol{v}}$ where $s > 0$ in (2-33) we obtain

$$\bar{I} \le -s\langle \boldsymbol{l}(\lambda), \bar{\boldsymbol{v}}\rangle;$$

as this must be satisfied for all $s > 0$; we have the value asserted by the second regime in (2-35).

We determine the dual of (2-34). We have

$$C^*(\boldsymbol{m}) = \begin{cases} 0 & \text{if } \boldsymbol{m} = -\boldsymbol{l}(\lambda), \\ \infty & \text{otherwise,} \end{cases} \tag{2-36}$$

$\boldsymbol{m} \in W^*$, and

$$D^*(\boldsymbol{T}) = \begin{cases} 0 & \text{if } \boldsymbol{T} \in Y^{*-}, \\ \infty & \text{otherwise,} \end{cases}$$

$\boldsymbol{T} \in Y^*$. Setting $\boldsymbol{m} = -\hat{\boldsymbol{E}}^*\boldsymbol{T}$ in (2-36), we obtain

$$C^*(-\hat{\boldsymbol{E}}^*\boldsymbol{T}) = \begin{cases} 0 & \text{if } \hat{\boldsymbol{E}}^*\boldsymbol{T} = \boldsymbol{l}(\lambda), \\ \infty & \text{otherwise,} \end{cases}$$

$\boldsymbol{T} \in Y^*$. Then

$$-C^*(-\hat{\boldsymbol{E}}^*\boldsymbol{T}) - D^*(\boldsymbol{T}) = \begin{cases} 0 & \text{if } \hat{\boldsymbol{E}}^*\boldsymbol{T} = \boldsymbol{l}(\lambda) \text{ and } \boldsymbol{T} \in Y^{*-}, \\ -\infty & \text{otherwise,} \end{cases}$$

$\boldsymbol{T} \in Y^*$. Noting that the conditions $\hat{\boldsymbol{E}}^*\boldsymbol{T} = \boldsymbol{l}(\lambda)$ and $\boldsymbol{T} \in Y^{*-}$ mean exactly that λ is Y^*-statically admissible, we have the following: the dual problem of (2-34) reads

$$I = \begin{cases} 0 & \text{if } \lambda \text{ is } Y^* \text{ statically admissible,} \\ -\infty & \text{otherwise.} \end{cases} \tag{2-37}$$

The function $H : Y \to \mathbb{R} \cup \{-\infty, \infty\}$ of (2-19) corresponding to Problem (2-34) is given by

$$H(\boldsymbol{F}) = \inf\{-\langle \boldsymbol{l}(\lambda), \boldsymbol{v}\rangle : \boldsymbol{v} \in W,\ \hat{\boldsymbol{E}}(\boldsymbol{v}) - \boldsymbol{F} \in Y^+\};$$

the function H has the following properties:

(i) H is convex.

(ii) H is nondecreasing in the sense that $H(\boldsymbol{F}) \le H(\boldsymbol{G})$ whenever $\boldsymbol{G} - \boldsymbol{F} \in Y^+$.

(iii) $H(\boldsymbol{F}) \le 0$ if $-\boldsymbol{F} \in Y^+$.

(iv) $H(s\boldsymbol{F}) = sH(\boldsymbol{F})$ for every $\boldsymbol{F} \in Y$ and $s > 0$.

(v) either $H(\boldsymbol{0}) = 0$ or $H(\boldsymbol{0}) = -\infty$.

Indeed, (i) follows from the convexity of the general H stated in Section 2D. (ii) follows from the fact that if $\boldsymbol{G} - \boldsymbol{F} \in Y^+$ then

$$\{\boldsymbol{v} \in W,\ \hat{\boldsymbol{E}}(\boldsymbol{v}) - \boldsymbol{G} \in Y^+\} \subset \{\boldsymbol{v} \in W,\ \hat{\boldsymbol{E}}(\boldsymbol{v}) - \boldsymbol{F} \in Y^+\}.$$

(iii) follows from the fact that if $-\boldsymbol{F} \in Y^+$ then

$$\boldsymbol{0} \in \{\boldsymbol{v} \in W,\ \hat{\boldsymbol{E}}(\boldsymbol{v}) - \boldsymbol{F} \in Y^+\}.$$

(iv) follows from the equation

$$\{\boldsymbol{v} \in W,\ \hat{\boldsymbol{E}}(\boldsymbol{v}) - s\boldsymbol{F} \in Y^+\} = s\{\boldsymbol{v} \in W,\ \hat{\boldsymbol{E}}(\boldsymbol{v}) - \boldsymbol{F} \in Y^+\}.$$

(v) is proved by noting that $H(\boldsymbol{0}) \le 0$ by (iii) and $H(\boldsymbol{0}) = sH(\boldsymbol{0})$ for every $s > 0$ by (iv).

By definition, the problem (2-34) is normal if and only if $H(\boldsymbol{0}) = 0$ and H is lower semicontinuous at $\boldsymbol{0}$. By Proposition 2.3 the normality is equivalent to $I = \bar{I} \in \mathbb{R}$ and this in turn is equivalent to the statical admissibility of λ. Thus, to prove that (2-31) is equivalent to the statical admissibility of λ, we have to show that the conditions $H(\boldsymbol{0}) = 0$ and H is lower semicontinuous at $\boldsymbol{0}$ are equivalent to (2-31).

Indeed, let $H(\boldsymbol{0}) = 0$ and let H be lower semicontinuous at $\boldsymbol{0}$. Then H is bounded from below on the unit ball in Y in the sense that there exists a $c > 0$ such that

$$H(\boldsymbol{F}) \ge -c \quad \text{for all } \boldsymbol{F} \in Y \text{ with } |\boldsymbol{F}| \le 1.$$

The positive homogeneity of H asserted in (iv) then implies

$$H(\boldsymbol{F}) \geq -c|\boldsymbol{F}| \quad \text{for all } \boldsymbol{F} \in Y, \tag{2-38}$$

and the definition of H gives (2-31). Conversely, if (2-31) holds then we have (2-38) and this in turn implies that $H(\mathbf{0}) \geq 0$. As by (v) we have $H(\mathbf{0}) \leq 0$, this implies $H(\mathbf{0}) = 0$, and (2-38) gives that H is lower semicontinuous at $\mathbf{0}$. □

Proposition 2.9. *Let $\lambda \in \mathbb{R}$. If there exists a $\boldsymbol{v}_\circ \in W^+$ such that $\hat{\boldsymbol{E}}(\boldsymbol{v}_\circ)$ is an interior point of Y^+ then λ is Y^* statically admissible if and only if $\langle \boldsymbol{l}(\lambda), \boldsymbol{v}\rangle \leq 0$ for all $\boldsymbol{v} \in W^+$.*

The hypothesis of this proposition is the qualification condition for the problem of the static admissibility of λ.

Proof. Problem (2-33) satisfies the qualification hypothesis if and only if there exists a $\boldsymbol{v}_\circ \in W^+$ such that $\hat{\boldsymbol{E}}(\boldsymbol{v}_\circ)$ is an interior point of Y^+. This is proved in the same way as in Proposition 2.6. Under the qualification hypothesis we have the equality $I = \bar{I}$ by Proposition 2.4 and the explicit forms (2-35) and (2-37) of the primal and dual problems show that λ is Y^*-statically admissible if and only if $\langle \boldsymbol{l}(\lambda), \boldsymbol{v}\rangle \leq 0$ for all $\boldsymbol{v} \in W^+$. □

3. Displacements in *BD* and continuous stresses

This section presents the kinematic and static problems with the choice of displacements of bounded deformation and with the choice of continuous tensor fields as the space of stresses. The qualification hypothesis as a sufficient condition for the equality of the results of the kinematic and static problems can never be satisfied with this choice.

3A. ***Displacements, loads, and energies in the setting of BD.*** We define the objects (2-8) as follows. We put

$$W = W_{BD} := \{\boldsymbol{v} \in BD(\Omega) : \boldsymbol{v} = \mathbf{0} \text{ in the sense of trace on } \mathscr{D}\},$$
$$Y = \mathscr{M}(\Omega, \mathrm{Sym}),$$

so that $\hat{\boldsymbol{E}}(\,\cdot\,)$, defined by (2-5), is a bounded linear transformation from W_{BD} to $\mathscr{M}(\Omega, \mathrm{Sym})$. (We refer to the Appendix for an outline of the notation for the functions spaces employed here and in the subsequent treatment.) Furthermore, we put

$$Y^+ = \mathscr{M}(\Omega, \mathrm{Sym}^+) := \{\boldsymbol{F} \in \mathscr{M}(\Omega, \mathrm{Sym}) : \boldsymbol{F}(A) \geq \mathbf{0} \text{ for every Borel subset of } \Omega\},$$
$$W^+ = W^+_{BD} := \{\boldsymbol{v} \in W_{BD} : \hat{\boldsymbol{E}}(\boldsymbol{v}) \in \mathscr{M}(\Omega, \mathrm{Sym}^+)\}.$$

Finally, we set

$$Y^* = C^0(\mathrm{cl}\,\Omega, \mathrm{Sym})$$

and the duality pairing is given by

$$(\boldsymbol{T}, \boldsymbol{F}) = \int_\Omega \boldsymbol{T} \cdot d\boldsymbol{F}$$

for every $\boldsymbol{T} \in C^0(\mathrm{cl}\,\Omega, \mathrm{Sym})$ and every $\boldsymbol{F} \in \mathscr{M}(\Omega, \mathrm{Sym})$. The cone Y^{*-} is given by

$$Y^{*-} = C^0(\mathrm{cl}\,\Omega, \mathrm{Sym}^-) = \{\boldsymbol{T} \in C^0(\mathrm{cl}\,\Omega, \mathrm{Sym}) : \boldsymbol{T} \leq \mathbf{0} \text{ on } \Omega\}.$$

Remark 3.1. It is possible to introduce a duality between stresses and strains under different hypotheses on these objects. Namely the duality theory in [Dal Maso et al. 2007, Section 3] gives the following result (see also [Anzellotti 1983] and [Kohn and Témam 1983]): if $\boldsymbol{T}$ is a stress field in the set

$$S := \{\boldsymbol{T} \in L^\infty(\Omega, \mathrm{Sym}) : \operatorname{div} \boldsymbol{T} \in L^n(\Omega, \mathbb{R}^n)\}$$

and $\boldsymbol{v} \in BD(\Omega)$ then there exists a measure $[\boldsymbol{T}, \hat{\boldsymbol{E}}(\boldsymbol{v})] \in \mathcal{M}(\Omega, \mathbb{R})$ which behaves well under the weak convergence of $\boldsymbol{T}$ and such that $[\boldsymbol{T}, \hat{\boldsymbol{E}}(\boldsymbol{v})] = \boldsymbol{T} \cdot \hat{\boldsymbol{E}}(\boldsymbol{v})$ if $\boldsymbol{T}$ is continuous on $\operatorname{cl}\Omega$. The measure thus plays the role of the product $\boldsymbol{T} \cdot \hat{\boldsymbol{E}}(\boldsymbol{v})$ if $\boldsymbol{T}$ is not continuous on $\operatorname{cl}\Omega$ and the value $[\boldsymbol{T}, \hat{\boldsymbol{E}}(\boldsymbol{v})](\Omega)$ the role of $\int_\Omega \boldsymbol{T} \cdot d\hat{\boldsymbol{E}}(\boldsymbol{v})$. We can define the duality pairing between any $\boldsymbol{T} \in S$ and $\boldsymbol{F}$ in the space

$$Z := \{\boldsymbol{F} = \hat{\boldsymbol{E}}(\boldsymbol{v}) + \boldsymbol{G} : \boldsymbol{v} \in BD(\Omega),\ \boldsymbol{G} \in L^1(\Omega, \mathrm{Sym})\}$$

by

$$(\boldsymbol{T}, \boldsymbol{F}) = [\boldsymbol{T}, \hat{\boldsymbol{E}}(\boldsymbol{v})](\Omega) + \int_\Omega \boldsymbol{T} \cdot \boldsymbol{G}\, d\mathscr{L}^n.$$

It is easily shown that the value of $(\boldsymbol{T}, \boldsymbol{F})$ is independent of the choice of $\boldsymbol{v}$ and $\boldsymbol{G}$. We do not follow this possibility here, as the results under this duality are analogous to the results presented below.

To ensure that the energies of the loads, interpreted as functionals of displacements, are in W^*, we assume that the loads are represented by functions

$$\boldsymbol{s}_\circ,\ \bar{\boldsymbol{s}} \in L^\infty(\mathscr{S}, \mathbb{R}^n), \quad \boldsymbol{b}_\circ,\ \bar{\boldsymbol{b}} \in L^n(\Omega, \mathbb{R}^n),$$

and define $\boldsymbol{l}_\circ$ and $\bar{\boldsymbol{l}}$ classically by the integrals in (2-3) and (2-4).

3B. ***Limit analysis in the BD setting.*** We define $\bar{\lambda}_W$ and λ_{Y^*} by

$$\begin{aligned} \bar{\lambda}_W = \bar{\lambda}_{BD} &:= \inf\{\lambda \in \mathbb{R} : \lambda \text{ is } W_{BD} \text{ kinematically admissible}\}, \\ \lambda^*_Y = \lambda_\circ &:= \sup\{\lambda \in \mathbb{R} : \lambda \text{ is } C^0(\operatorname{cl}\Omega, \mathrm{Sym}) \text{ statically admissible}\}. \end{aligned} \tag{3-1}$$

The sufficient condition of Proposition 2.6 for the equality $\lambda_\circ = \bar{\lambda}_{BD}$ (i.e., the qualification hypothesis) is never satisfied in the present case since $\mathcal{M}(\Omega, \mathrm{Sym}^+)$ has empty interior. To see the last, let $\boldsymbol{F}$ be any element of $\mathcal{M}(\Omega, \mathrm{Sym}^+)$, let $\Omega_j \subset \Omega$ be a decreasing sequence of Borel sets such that $\mathscr{L}^n(\Omega_j) > 0$ for all j and $\bigcap_{j=1}^\infty \Omega_j = \varnothing$, and let the sequence $\boldsymbol{F}_j$ be defined by

$$\boldsymbol{F}_j(A) = \boldsymbol{F}(A \cap (\Omega \setminus \Omega_j)) - \mathscr{L}^n(A \cap \Omega_j)\mathbf{1}$$

for every Borel subset A of $\mathbb{R}^n$. Then $\boldsymbol{F}_j \notin \mathcal{M}(\Omega, \mathrm{Sym}^+)$ for all j and $\boldsymbol{F}_j \to \boldsymbol{F}$ in $\mathcal{M}(\Omega, \mathrm{Sym})$ as $j \to \infty$. Thus every point of $\mathcal{M}(\Omega, \mathrm{Sym}^+)$ is on the boundary of $\mathcal{M}(\Omega, \mathrm{Sym}^+)$.

4. Displacements in $W^{1,p}$, $1 \le p < \infty$, and stresses in L^q, $\infty \ge q > 1$

In Section 4A we consider the Sobolev spaces with finite exponent as the space of displacements and the space of power integrable tensor fields as stresses. Section 4B defines the corresponding multipliers for the kinematic and static problems, and shows that the qualification hypothesis can never be satisfied with this choice. Finally, in Section 4C a density condition is formulated to guarantee that the infimum of the

kinematic problem with the space of displacements of bounded deformation equals the infimum of the kinematic problem with the Sobolev space. Section 7B gives a sufficient condition for this density.

4A. ***Displacements, loads, and energies in the setting of power integrable functions.*** We assume that $1 \le p < \infty$ is a given number and denote by

$$q := \begin{cases} p/(p-1) & \text{if } p > 1, \\ \infty & \text{if } p = 1, \end{cases}$$

the Hölder conjugate exponent. We define the objects (2-8) as follows. We put

$$W = W_p := \{\boldsymbol{v} \in W^{1,p}(\Omega, \mathbb{R}^n) : \boldsymbol{v} = \boldsymbol{0} \text{ in the sense of trace on } \mathfrak{D}\},$$
$$Y = L^p(\Omega, \mathrm{Sym}),$$

so that $\hat{\boldsymbol{E}}(\,\cdot\,)$, defined by (2-5), is a bounded linear transformation from W_p to $L^p(\Omega, \mathrm{Sym})$. We also put

$$Y^+ = L^p(\Omega, \mathrm{Sym}^+) := \{\boldsymbol{F} \in Y : \boldsymbol{F} \ge \boldsymbol{0} \text{ almost everywhere on } \Omega\},$$
$$W^+ = W_p^+ := \{\boldsymbol{v} \in W_p : \hat{\boldsymbol{E}}(\boldsymbol{v}) \in L^p(\Omega, \mathrm{Sym}^+)\}.$$

Finally, Y^* is set equal to the dual of Y, i.e.,

$$Y^* = L^q(\Omega, \mathrm{Sym}),$$

and the duality pairing $(\boldsymbol{T}, \boldsymbol{F})$ is given by (2-6), as is well known. The cone Y^{*-} is given by

$$Y^{*-} = L^q(\Omega, \mathrm{Sym}^-) = \{\boldsymbol{T} \in L^q(\Omega, \mathrm{Sym}) : \boldsymbol{T} \le \boldsymbol{0} \text{ almost everywhere on } \Omega\}.$$

To ensure that the energies of the loads, interpreted as functionals of displacements, are in W^*, we distinguish the cases $p < n$, $p = n$ and $p > n$. If $p < n$, we assume that the loads are represented by functions

$$\boldsymbol{s}_\circ,\ \bar{\boldsymbol{s}} \in L^s(\mathcal{S}, \mathbb{R}^n), \quad \boldsymbol{b}_\circ,\ \bar{\boldsymbol{b}} \in L^t(\Omega, \mathbb{R}^n), \tag{4-1}$$

where

$$s = \frac{(n-1)p}{n(p-1)}, \quad t = \frac{np}{np - n + p},$$

and define $\boldsymbol{l}_\circ$ and $\bar{\boldsymbol{l}}$ classically by the integrals in (2-3) and (2-4). If $p = n$, we assume that the loads are represented by functions as in (4-1), with some s, t satisfying

$$1 < s \le \infty, \quad 1 < t \le \infty$$

and again define $\boldsymbol{l}_\circ$ and $\bar{\boldsymbol{l}}$ classically by the integrals in Equations (2-3) and (2-4). The Sobolev imbedding theorem [Adams and Fournier 2003, Theorem 4.12, Case C] and the trace theorem [ibid., Theorem 5.36] imply that these definitions are well posed. If $p > n$, then the elements of W_p represent continuous functions on the closure $\mathrm{cl}\,\Omega$ of Ω. In this case the loads can be more general. Namely, the surface tractions can be represented by vector-valued measures $\boldsymbol{s}_\circ$ and $\bar{\boldsymbol{s}}$ in $\mathcal{M}(\mathcal{S}, \mathbb{R}^n)$ and the body forces by

vector-valued measures $\boldsymbol{b}_\circ$ and $\bar{\boldsymbol{b}}$ in $\mathcal{M}(\Omega, \mathbb{R}^n)$. For this we assume that $\mathcal{S}$ is a Borel set. Then $\boldsymbol{l}_\circ$ and $\bar{\boldsymbol{l}}$ are given by

$$\langle \boldsymbol{l}_\circ, \boldsymbol{v}\rangle = \int_\Omega \boldsymbol{v}\cdot d\boldsymbol{b}_\circ + \int_{\mathcal{S}} \boldsymbol{v}\cdot d\boldsymbol{s}_\circ, \tag{4-2}$$

$$\langle \bar{\boldsymbol{l}}, \boldsymbol{v}\rangle = \int_\Omega \boldsymbol{v}\cdot d\bar{\boldsymbol{b}} + \int_{\mathcal{S}} \boldsymbol{v}\cdot d\bar{\boldsymbol{s}}, \tag{4-3}$$

for each $\boldsymbol{v} \in W_p$. This formalism includes concentrated loads. The distributed case, when the loads are represented by ordinary functions, is included by setting

$$\boldsymbol{s}_\circ = \boldsymbol{s}_\circ \mathscr{H}^{n-1} \llcorner \mathcal{S}, \quad \bar{\boldsymbol{s}} = \bar{\boldsymbol{s}} \mathscr{H}^{n-1} \llcorner \mathcal{S}, \quad \boldsymbol{b}_\circ = \boldsymbol{b}_\circ \mathscr{L}^n \llcorner \Omega, \quad \bar{\boldsymbol{b}} = \bar{\boldsymbol{b}} \mathscr{L}^n \llcorner \Omega,$$

where now the functions can belong to the spaces as follows:

$$\boldsymbol{s}_\circ,\ \bar{\boldsymbol{s}} \in L^1(\mathcal{S}, \mathbb{R}^n), \quad \boldsymbol{b}_\circ,\ \bar{\boldsymbol{b}} \in L^1(\Omega, \mathbb{R}^n)$$

and the notation of the Appendix has been employed. Then (4-2) and (4-3) reduce to (2-3) and (2-4).

4B. ***Limit analysis in the setting of power integrable functions.*** We define $\bar{\lambda}_W$ and λ_{Y^*} by

$$\begin{aligned} \bar{\lambda}_W = \bar{\lambda}_p &:= \inf\{\lambda \in \mathbb{R} : \lambda \text{ is } W_p \text{ kinematically admissible}\},\\ \lambda_{Y^*} = \lambda_q &:= \sup\{\lambda \in \mathbb{R} : \lambda \text{ is } L^q(\Omega, \mathrm{Sym}) \text{ statically admissible}\}. \end{aligned} \tag{4-4}$$

The sufficient condition of Proposition 2.6 for the equality $\lambda_q = \bar{\lambda}_p$ (i.e., the qualification hypothesis) is never satisfied in the present case, since $L^p(\Omega, \mathrm{Sym}^+)$ has empty interior for all $p \in [1, \infty)$. To see the last, let $\boldsymbol{F}$ be any element of $L^p(\Omega, \mathrm{Sym}^+)$, let $\Omega_j \subset \Omega$ be a decreasing sequence of measurable sets such that $\mathscr{L}^n(\Omega_j) > 0$ for all j and $\bigcap_{j=1}^\infty \Omega_j = \varnothing$, and let the sequence $\boldsymbol{F}_j$ be defined by

$$\boldsymbol{F}_j = \begin{cases} \boldsymbol{F} & \text{on } \Omega \setminus \Omega_j,\\ -\mathbf{1} & \text{on } \Omega_j. \end{cases}$$

Then $\boldsymbol{F}_j \notin L^p(\Omega, \mathrm{Sym}^+)$ for all j and $\boldsymbol{F}_j \to \boldsymbol{F}$ in $L^p(\Omega, \mathrm{Sym})$ as $j \to \infty$. Thus every point of $L^p(\Omega, \mathrm{Sym}^+)$ is on the boundary of $L^p(\Omega, \mathrm{Sym}^+)$.

Remark 4.1. Example 7.12 (below) shows that under very tame loads of a panel in the plane one can have $\lambda_q < \bar{\lambda}_p$.

Remark 4.2. The choice of W_p and $L^q(\Omega, \mathrm{Sym})$ with $p = q = 2$ plays a special role. The square integrable admissible equilibrating stress fields have a dynamical motivation in terms of the behavior of processes of masonry bodies with dissipation for large times [Padovani et al. 2008]: if $\lambda < \lambda_2$, then under the loads corresponding to λ, the processes starting from arbitrary initial data stabilize and converge to the set of equilibrium states; on the other hand, if $\lambda > \lambda_2$, the processes blow up in the sense of norms, i.e., the collapse occurs. Further, in [Lucchesi et al. 2010] it was shown that the existence of admissible square integrable stress fields balancing the loads is a necessary and sufficient condition for the total energy of a masonry body to be bounded from below. In [Lucchesi et al. 2011] the equilibrium of panels subjected both to distributed loads and concentrated forces is studied, and equilibrated tensor-valued measures are determined. Then, by using an integration procedure for parametric measures, equilibrated stress fields

that are represented by integrable functions are explicitly determined. Note also that $L^2(\Omega, \mathrm{Sym})$ is also the space of stress fields employed in [Del Piero 1998].

4C. ***Comparison of the critical multipliers in the BD and $W^{1,p}$ settings.*** Let $1 \le p < \infty$, and let $q \in (1, \infty]$ be the Hölder conjugate exponent, and assume that the energies $\boldsymbol{l}_\circ$ and $\bar{\boldsymbol{l}}$ are continuous functionals on W_{BD}. (See the conditions in Section 3.) Since $W_p \subset W_{BD}$ and the inclusion is continuous, the restriction of $\boldsymbol{l}_\circ$ and $\bar{\boldsymbol{l}}$ to W_p are continuous linear functionals on W_p as well (we denote these restrictions by the original symbols). Then in general we have

$$\bar{\lambda}_{BD} \le \bar{\lambda}_p$$

because the infimum in the definition of $\bar{\lambda}_p$ is taken over a smaller set than in the definition of $\bar{\lambda}_{BD}$. Similarly, we have

$$\lambda_\circ \le \lambda_q,$$

since the supremum for λ_q is taken over a larger set than that for $\lambda_\circ$. Under the condition that

$$\text{for each } \bar{\boldsymbol{v}} \in W^+_{BD} \text{ such that } \langle \bar{\boldsymbol{l}}, \bar{\boldsymbol{v}} \rangle > 0, \text{ there exists a sequence } \bar{\boldsymbol{v}}_j \in W^+_p \text{ such that } \bar{\boldsymbol{v}}_j \to \bar{\boldsymbol{v}} \text{ in } L^{n/(n-1)}(\Omega, \mathbb{R}^n) \text{ and } \bar{\boldsymbol{v}}_j \to \bar{\boldsymbol{v}} \text{ in } L^1(\partial\Omega, \mathbb{R}^n), \quad (4\text{-}5)$$

we have

$$\bar{\lambda}_{BD} = \bar{\lambda}_p.$$

Indeed, one takes the infimum in (4-4) over a dense subset of the set in the infimum in (3-1). In particular, if (4-5) holds for every $p \in [1, \infty)$, then $\bar{\lambda}_p$ is independent of p and equal to $\bar{\lambda}_{BD}$.

It does not seem that there exists a relatively easily verifiable condition to guarantee the equality $\lambda_q = \lambda_\circ$. In Section 7D, below, the function $q \mapsto \lambda_q$ is not constant and hence the equality $\lambda_q = \lambda_\circ$ cannot hold for all $q \in (1, \infty]$.

5. Lipschitzian displacements and finitely additive measures representing stresses

Sections 5A and 5B formulate the kinematic and static problems for lipschitzian displacements and for stresses modeled as finitely additive bounded measures that are absolutely continuous with respect to the Lebesgue measure. A necessary and sufficient condition of Section 2 is particularized to the present choice of spaces in Theorem 5.1 and results in an examination of a real-valued function of the real variable. The qualification hypothesis is derived in Theorem 5.2. Theorem 5.3 gives a very simple necessary and sufficient condition for the static admissibility of a general multiplier. Finally, Section 5C gives a density condition for the equality of the kinematic multipliers in the lipschitzian and Sobolev spaces settings.

5A. ***Lipschitzian displacements and the representation of stresses.*** We define the objects (2-8) as follows. We put

$$W = W_\infty := \{\boldsymbol{v} \in W^{1,\infty}(\Omega, \mathbb{R}^n) : \boldsymbol{v} = \boldsymbol{0} \text{ in the classical sense on } \mathcal{D}\},$$
$$Y = L^\infty(\Omega, \mathrm{Sym}),$$

so that $\hat{\boldsymbol{E}}(\cdot)$, defined by (2-5), is a bounded linear transformation from W to Y. Furthermore, we put

$$Y^+ = L^\infty(\Omega, \mathrm{Sym}^+) := \{\boldsymbol{F} \in Y : \boldsymbol{F} \geq \boldsymbol{0} \text{ almost everywhere on } \Omega\},$$
$$W^+ = W^+_\infty := \{\boldsymbol{v} \in W_\infty : \hat{\boldsymbol{E}}(\boldsymbol{v}) \in L^\infty(\Omega, \mathrm{Sym}^+)\}.$$

Under our assumption on Ω, the elements of $W^{1,\infty}(\Omega, \mathbb{R}^n)$ are represented by lipschitzian functions on the closure $\mathrm{cl}\,\Omega$ of Ω, i.e., by functions $\boldsymbol{v} : \mathrm{cl}\,\Omega \to \mathbb{R}^n$ satisfying

$$|\boldsymbol{v}(\boldsymbol{x}) - \boldsymbol{v}(\boldsymbol{y})| \leq k|\boldsymbol{x} - \boldsymbol{y}|$$

for all $\boldsymbol{x}, \boldsymbol{y} \in \mathrm{cl}\,\Omega$ and some k; see [Ekeland and Témam 1999, Chapter X, Section 2.2].

The loads can be represented by measures, as in the case $p > n$ in the preceding section, and $\boldsymbol{l}_\circ$ and $\bar{\boldsymbol{l}}$ are given by (4-2) and (4-3), respectively.

We denote by $Y^* = X_{\mathrm{ba}}$ the dual of $L^\infty(\Omega, \mathrm{Sym})$. We say that $\boldsymbol{T} \in X_{\mathrm{ba}}$ is negative semidefinite if $(\boldsymbol{T}, \boldsymbol{F}) \leq 0$ for each $\boldsymbol{F} \in L^\infty(\Omega, \mathrm{Sym}^+)$ and denote by X^-_{ba} the set of all negative semidefinite $\boldsymbol{T} \in X_{\mathrm{ba}}$. We interpret X^-_{ba} as the set of admissible stress fields. The elements $\boldsymbol{T}$ of X_{ba} are in general no longer representable by ordinary functions. Rather, the space X_{ba} is isomorphic to the space $\mathrm{ba}(\Omega, \mathfrak{M}, \mathscr{L}^n; \mathrm{Sym})$ of bounded finitely additive Sym valued measures that are absolutely continuous with respect to the Lebesgue measure. Thus to each element $\boldsymbol{T} \in X_{\mathrm{ba}}$ there exists a unique element $\mathfrak{T} \in \mathrm{ba}(\Omega, \mathfrak{M}, \mathscr{L}^n; \mathrm{Sym})$ such that we have

$$(\boldsymbol{T}, \boldsymbol{F}) = \int_\Omega \boldsymbol{F} \cdot d\mathfrak{T} \tag{5-1}$$

for each $\boldsymbol{F} \in L^\infty(\Omega, \mathrm{Sym})$, and conversely. We refer to [Fonseca and Leoni 2007, Sections 1.3.2 and Theorem 2.44] for details in the scalar case (in particular to the definition of the integral in (5-1)) and to an outline of the tensorial case in the Appendix. An important subset of $\mathrm{ba}(\Omega, \mathfrak{M}, \mathscr{L}^n; \mathrm{Sym})$ consists of measures of the form

$$\mathfrak{T} = \boldsymbol{T}\mathscr{L}^n \llcorner \Omega$$

where $\boldsymbol{T} \in L^1(\Omega, \mathrm{Sym})$. In this case the measure $\mathfrak{T}$ is actually countably additive.

5B. ***Limit analysis in the setting of lipschitzian displacements.*** We define $\bar{\lambda}_W$ and λ_{Y^*} by

$$\begin{aligned} \bar{\lambda}_W = \bar{\lambda}_\infty &:= \inf\{\lambda \in \mathbb{R} : \lambda \text{ is } W_\infty \text{ kinematically admissible}\}, \\ \lambda_{Y^*} = \lambda_{\mathrm{ba}} &:= \sup\{\lambda \in \mathbb{R} : \lambda \text{ is } X_{\mathrm{ba}} \text{ statically admissible}\}. \end{aligned} \tag{5-2}$$

Theorem 5.1. *Let $h : \mathbb{R} \to \mathbb{R} \cup \{-\infty, \infty\}$ be defined by*

$$h(t) = \inf\{-\langle \boldsymbol{l}_\circ, \boldsymbol{v}\rangle : \boldsymbol{v} \in W_\infty,\ \hat{\boldsymbol{E}}(\boldsymbol{v}) \geq t\boldsymbol{1} \text{ almost everywhere on } \Omega,\ \langle \bar{\boldsymbol{l}}, \boldsymbol{v}\rangle = 1\},$$

$t \in \mathbb{R}$. Then:

(i) *h is nondecreasing, convex and $h(0) = \bar{\lambda}_\infty$.*

(ii) *$h(0)$ is finite and $\lim_{\substack{t\to 0,\\ t<0}} h(t) = h(0)$ if and only if $\lambda_{\mathrm{ba}} = \bar{\lambda}_\infty \in \mathbb{R}$.*

Proof. The function H defined generally in (2-23) provides $h(t) = H(t\boldsymbol{1})$. The convexity and the nondecreasing character of H, asserted by Proposition 2.5(i) gives the same properties of h. Furthermore, clearly $h(0) = H(\boldsymbol{0}) = \bar{\lambda}_\infty$, which completes the proof of (i).

(ii) By Proposition 2.5(ii) then $\lambda_{\mathrm{ba}} = \bar{\lambda}_\infty \in \mathbb{R}$ if and only if $H(\mathbf{0}) = h(0)$ is finite and H is lower semicontinuous at $\mathbf{0}$. If the last holds, then $h(0) \in \mathbb{R}$ and h is lower semicontinuous at 0 and as h is nondecreasing, this in turn implies that

$$\lim_{\substack{t\to 0\\ t<0}} h(t) = h(0). \tag{5-3}$$

Conversely, let $h(0)$ be finite and let (5-3) hold. If $|\boldsymbol{F}|$ denotes the L^∞ norm of a general $\boldsymbol{F} \in L^\infty(\Omega, \mathrm{Sym})$ then $-|\boldsymbol{F}|\mathbf{1} \le \boldsymbol{F}$ and hence the monotonicity of H implies

$$h(-|\boldsymbol{F}|) \equiv H(-|\boldsymbol{F}|\mathbf{1}) \le H(\boldsymbol{F})$$

and thus

$$H(\mathbf{0}) \equiv h(0) = \lim_{\boldsymbol{F}\to\mathbf{0}} h(-|\boldsymbol{F}|) \equiv \lim_{\boldsymbol{F}\to\mathbf{0}} H(-|\boldsymbol{F}|\mathbf{1}) \le \liminf_{\boldsymbol{F}\to\mathbf{0}} H(\boldsymbol{F}).$$

Thus H is lower semicontinuous at $\mathbf{0}$. □

Theorem 5.2. *Assume that*

there exists a $\bar{\boldsymbol{v}}_\circ$ *in* W^+_∞ *satisfying* $\langle \bar{\boldsymbol{l}}, \bar{\boldsymbol{v}}_\circ\rangle > 0$

such that $\hat{\boldsymbol{E}}(\bar{\boldsymbol{v}}_\circ) \ge \alpha\mathbf{1}$ *for some* $\alpha > 0$ *and almost every point of* Ω. (5-4)

Then $\lambda_{\mathrm{ba}} = \bar{\lambda}_\infty$; *if additionally* $\lambda_{\mathrm{ba}} = \bar{\lambda}_\infty \in \mathbb{R}$ *then* $\bar{\lambda}_\infty$ *is statically admissible, i.e., there exists a bounded finitely additive negative semidefinite measure* $\mathfrak{T}$ *that is absolutely continuous with respect to* $\mathscr{L}^n$ *such that*

$$\int_\Omega \hat{\boldsymbol{E}}(\boldsymbol{v}) \cdot d\mathfrak{T} = \langle \boldsymbol{l}(\bar{\lambda}_\infty), \boldsymbol{v}\rangle$$

for all $\boldsymbol{v} \in W_\infty$.

Paroni [2012], dealing with inextensible nets with slack, and applying the duality theory of Ekeland & Témam, obtained balancing stresses represented by bounded finitely additive measures that are "almost absolutely continuous" with respect to the Lebesgue measure (see the cited paper for a precise statement).

Proof. If (5-4) holds, $\hat{\boldsymbol{E}}(\bar{\boldsymbol{v}}_\circ)$ is an interior point of $L^\infty(\Omega, \mathrm{Sym}^+)$. Indeed, the interior of $L^\infty(\Omega, \mathrm{Sym}^+)$ consists of all $\boldsymbol{F} \in L^\infty(\Omega, \mathrm{Sym})$ which satisfy $\boldsymbol{F}(\boldsymbol{x}) \ge \alpha\mathbf{1}$ for some positive α and almost every point $\boldsymbol{x}$ of Ω. To see the sufficiency of this condition, note that if $\boldsymbol{G} \in L^\infty(\Omega, \mathrm{Sym})$ satisfies $|\boldsymbol{F} - \boldsymbol{G}| < \alpha/2$, where $|\cdot|$ is the L^∞ norm on $L^\infty(\Omega, \mathrm{Sym})$, then $\boldsymbol{G}(\boldsymbol{x}) \ge \frac{1}{2}\alpha\mathbf{1}$ for almost every $\boldsymbol{x} \in \Omega$. The necessity is proved similarly.

Thus $\bar{\boldsymbol{v}}_\circ$ satisfies (2-29) and Proposition 2.6 implies the present proposition. □

Next we consider the statical admissibility of a general multiplier $\lambda \in \mathbb{R}$.

Theorem 5.3. *A multiplier* $\lambda \in \mathbb{R}$ *is* X_{ba}*-statically admissible if and only if*

$$\sup\{\langle \boldsymbol{l}(\lambda), \boldsymbol{v}\rangle : \boldsymbol{v} \in W_\infty,\ \hat{\boldsymbol{E}}(\boldsymbol{v}) \ge -\mathbf{1} \text{ almost everywhere on } \Omega\} < \infty. \tag{5-5}$$

The proof will show that (5-5) implies that $\langle \boldsymbol{l}(\lambda), \boldsymbol{v}\rangle \le 0$ for every $\boldsymbol{v} \in W^+_\infty$.

Proof. Assume that λ is X_{ba}-statically admissible and denote by $\boldsymbol{T} \in X_{\mathrm{ba}}^-$ an admissible equilibrating stress field. If $\boldsymbol{v} \in W_\infty$ is such that $\hat{\boldsymbol{E}}(\boldsymbol{v}) \geq -\mathbf{1}$ almost everywhere on Ω then

$$\langle \boldsymbol{l}(\lambda), \boldsymbol{v} \rangle = (\boldsymbol{T}, \hat{\boldsymbol{E}}(\boldsymbol{v})) \leq (\boldsymbol{T}, -\mathbf{1}) = -(\boldsymbol{T}, \mathbf{1})$$

and thus the value of the supremum in (5-5) is less than or equal to $-(\boldsymbol{T}, \mathbf{1})$. This completes the proof of the direct implication.

Conversely, let (5-5) hold. We must prove that (2-31) also holds. We prove first that (5-5) implies

$$\langle \boldsymbol{l}(\lambda), \boldsymbol{v} \rangle \leq 0 \tag{5-6}$$

for every $\boldsymbol{v} \in W_\infty^+$. Indeed, (5-5) asserts that there exists a $c \in \mathbb{R}$ such that

$$\langle \boldsymbol{l}(\lambda), \boldsymbol{v} \rangle < c \tag{5-7}$$

for every $\boldsymbol{v} \in W_\infty$ with $\hat{\boldsymbol{E}}(\boldsymbol{v}) \geq -\mathbf{1}$. Assume that $\boldsymbol{v} \in W_\infty^+$. Then for every $t > 0$ we have $\hat{\boldsymbol{E}}(t\boldsymbol{v}) \geq -\mathbf{1}$ and thus (5-7) gives

$$\langle \boldsymbol{l}(\lambda), t\boldsymbol{v} \rangle < c.$$

Fixing $\boldsymbol{v}$, dividing by $t > 0$ and letting $t \to \infty$ we obtain the desired conclusion $\langle \boldsymbol{l}(\lambda), \boldsymbol{v} \rangle \leq 0$.

Let us now prove that (2-31) holds. Let $\boldsymbol{F} \in L^\infty(\Omega, \mathrm{Sym})$, $\boldsymbol{F} \neq \mathbf{0}$, and let $\boldsymbol{v} \in W_\infty$ satisfy $\hat{\boldsymbol{E}}(\boldsymbol{v}) \geq \boldsymbol{F}$ almost everywhere on Ω. Then $\hat{\boldsymbol{E}}(\boldsymbol{v}/|\boldsymbol{F}|) \geq -\mathbf{1}$ almost everywhere on Ω, where $|\boldsymbol{F}|$ denotes the L^∞ norm of $\boldsymbol{F}$. Thus (5-5) implies

$$\langle \boldsymbol{l}(\lambda), \boldsymbol{v} \rangle \leq c|\boldsymbol{F}|,$$

i.e., (2-31). If $\boldsymbol{F} = \mathbf{0}$, this argument does not hold but then $\hat{\boldsymbol{E}}(\boldsymbol{v}) \geq \mathbf{0}$ almost everywhere on Ω and (2-31) holds again by (5-6). □

5C. ***Comparison of the critical multipliers in the lipschitzian and p integrable settings.*** Let $1 \leq p < \infty$, and let $q \in (1, \infty]$ be the Hölder conjugate exponent, and assume that the energies $\boldsymbol{l}_\circ$ and $\bar{\boldsymbol{l}}$ are continuous functionals on W_p. (See the conditions in Section 4.) Since $W_\infty \subset W_p$ and the inclusion is continuous, the restriction of $\boldsymbol{l}_\circ$ and $\bar{\boldsymbol{l}}$ to W_∞ are continuous linear functionals on W_∞ as well. Then in general we have

$$\bar{\lambda}_p \leq \bar{\lambda}_\infty$$

because the infimum in the definition of $\bar{\lambda}_\infty$ is taken over a smaller set than in the definition of $\bar{\lambda}_p$. Similarly, we have

$$\lambda_q \leq \lambda_{\mathrm{ba}},$$

since the supremum for λ_{ba} is taken over a larger set than that for λ_q. Under the condition that

$$\text{for each } \bar{\boldsymbol{v}} \in W_p^+ \text{ such that } \langle \bar{\boldsymbol{l}}, \bar{\boldsymbol{v}} \rangle > 0 \text{ there exists a sequence } \bar{\boldsymbol{v}}_j \in W_\infty^+ \text{ such that } \bar{\boldsymbol{v}}_j \to \bar{\boldsymbol{v}} \text{ in } W_p, \tag{5-8}$$

we have

$$\bar{\lambda}_p = \bar{\lambda}_\infty.$$

Indeed, one takes the infimum in (5-2) over a dense subset of the set in the infimum in (4-4). In particular, if (5-8) holds for every $p \in [1, \infty)$, then $\bar{\lambda}_p$ is independent of p and equal to $\bar{\lambda}_\infty$.

As in the preceding choices of function spaces, it does not seem that there exists a condition to guarantee the equality $\lambda_q = \lambda_{\mathrm{ba}}$.

6. Smooth displacements and countably additive measures representing stresses

Sections 6A and 6B formulate the kinematic and static problems within the context of smooth displacements and stress fields modeled as countably additive measures. The qualification hypothesis specialized in Theorem 6.1 is shown to hold only in the case of the pure traction problem. Theorem 6.3 provides a necessary and sufficient condition for the equality of the results of the kinematic and static problems and Theorem 6.4 a necessary and sufficient condition for the static admissibility of a general multiplier. Sections 6C and 6D provide sufficient conditions for the equality of the kinematic multiplier as defined here with those defined in the preceding sections.

6A. ***Smooth displacements and the representation of stresses.*** We define the objects (2-8) as follows. We put

$$W = C_1 := \{\boldsymbol{v} \in C^1(\mathrm{cl}\,\Omega, \mathbb{R}^n) : \boldsymbol{v} = \boldsymbol{0} \text{ in the classical sense on } \mathscr{D}\},$$
$$Y = C^0(\mathrm{cl}\,\Omega, \mathrm{Sym}),$$

so that $\hat{\boldsymbol{E}}(\,\cdot\,)$, defined by (2-5), is a bounded linear transformation from C_1 to $C^0(\mathrm{cl}\,\Omega, \mathrm{Sym})$. Furthermore, we put

$$Y^+ = C^0(\mathrm{cl}\,\Omega, \mathrm{Sym}^+) := \{\boldsymbol{F} \in C^0(\mathrm{cl}\,\Omega, \mathrm{Sym}) : \boldsymbol{F} \geq \boldsymbol{0} \text{ on } \mathrm{cl}\,\Omega\},$$
$$W^+ = C_1^+ := \{\boldsymbol{v} \in C_1 : \hat{\boldsymbol{E}}(\boldsymbol{v}) \in C^0(\mathrm{cl}\,\Omega, \mathrm{Sym}^+)\}.$$

The loads can be represented by measures as in the case $p > n$ in Section 4; $\boldsymbol{l}_\circ$ and $\bar{\boldsymbol{l}}$ are given by (4-2) and (4-3), respectively.

We denote by $Y^* = X_{\mathscr{M}}$ the dual of $C^0(\mathrm{cl}\,\Omega, \mathrm{Sym})$. We say that $\boldsymbol{T} \in X_{\mathscr{M}}$ is negative semidefinite if $(\boldsymbol{T}, \boldsymbol{F}) \leq 0$ for each $\boldsymbol{F} \in C^0(\mathrm{cl}\,\Omega, \mathrm{Sym}^+)$, and denote by $X_{\mathscr{M}}^-$ the set of all negative semidefinite $\boldsymbol{T} \in Y_{\mathscr{M}}$. We interpret the elements $\boldsymbol{T}$ of $X_{\mathscr{M}}^-$ as admissible stress fields. The elements $\boldsymbol{T}$ of $X_{\mathscr{M}}$ are in general not representable by ordinary functions. Rather, the space $X_{\mathscr{M}}$ is isomorphic with the space $\mathscr{M}(\mathrm{cl}\,\Omega, \mathrm{Sym})$ of bounded countably additive Sym-valued Borel measures on $\mathrm{cl}\,\Omega$. Thus for each element $\boldsymbol{T} \in X_{\mathscr{M}}$ there exists a unique element $\boldsymbol{T} \in \mathscr{M}(\mathrm{cl}\,\Omega, \mathrm{Sym})$ such that

$$(\boldsymbol{T}, \boldsymbol{F}) = \int_\Omega \boldsymbol{F} \cdot d\boldsymbol{T}$$

for each $\boldsymbol{F} \in C^0(\mathrm{cl}\,\Omega, \mathrm{Sym})$, and conversely. We refer to [Fonseca and Leoni 2007, Theorem 1.196] for details in the scalar case and to the Appendix. for the tensorial case. Recalling Section 5, we note that neither of the sets $\mathrm{ba}(\Omega, \mathfrak{M}, \mathscr{L}^n; \mathrm{Sym})$ and $\mathscr{M}(\mathrm{cl}\,\Omega, \mathrm{Sym})$ is a subset of the other, since the measures from $X_{\mathscr{M}}$ need not be absolutely continuous with respect to the Lebesgue measure and the measures from $\mathrm{ba}(\Omega, \mathfrak{M}, \mathscr{L}^n; \mathrm{Sym})$ need not be countably additive. With general elements of $\mathscr{M}(\mathrm{cl}\,\Omega, \mathrm{Sym})$ there may be stresses concentrated on sets of dimension strictly less than n. An important subset of $\mathscr{M}(\mathrm{cl}\,\Omega, \mathrm{Sym})$ consists of measures of the form

$$\boldsymbol{T} = \boldsymbol{T}\mathscr{L}^n \llcorner \Omega$$

where $\boldsymbol{T} \in L^1(\Omega, \mathrm{Sym})$.

The set $X_{\mathcal{M}}^-$ is just the set of all Borel measures on $\mathrm{cl}\,\Omega$ which take negative semidefinite values on every Borel subset of $\mathrm{cl}\,\Omega$.

6B. ***Limit analysis in the setting of smooth displacements.*** We define $\bar{\lambda}_W$ and λ_{Y^*} by

$$\bar{\lambda}_W = \bar{\lambda}_\circ := \inf\{\lambda \in \mathbb{R} : \lambda \text{ is } C_1 \text{ kinematically admissible}\},$$
$$\lambda_{Y^*} = \lambda_{\mathcal{M}} := \sup\{\lambda \in \mathbb{R} : \lambda \text{ is } X_{\mathcal{M}} \text{ statically admissible}\}.$$

Theorem 6.1. *Assume that*

$$\text{there is } \bar{\boldsymbol{v}}_\circ \text{ in } C_1^+ \text{ such that } \langle \bar{\boldsymbol{l}}, \bar{\boldsymbol{v}}_\circ \rangle > 0 \text{ and } \hat{\boldsymbol{E}}(\bar{\boldsymbol{v}}_\circ) \geq \alpha \mathbf{1} \text{ for some } \alpha > 0 \text{ and every point of } \mathrm{cl}\,\Omega. \quad (6\text{-}1)$$

Then we have $\lambda_{\mathcal{M}} = \bar{\lambda}_\circ$; if, additionally, this number is finite, then $\bar{\lambda}_\circ$ is statically admissible, i.e., there exists a bounded countably additive negative semidefinite Borel measure $\boldsymbol{T}$ such that

$$\int_\Omega \hat{\boldsymbol{E}}(\boldsymbol{v}) \cdot d\boldsymbol{T} = \langle \boldsymbol{l}(\bar{\lambda}_\circ), \boldsymbol{v} \rangle$$

for all $\boldsymbol{v} \in C_1$.

Proof. The interior of $C^0(\mathrm{cl}\,\Omega, \mathrm{Sym}^+)$ consists of all $\boldsymbol{F} \in C_\circ$ such that there exists a positive α satisfying $\boldsymbol{F} \geq \alpha \mathbf{1}$ for all points of $\mathrm{cl}\,\Omega$. We thus see that the displacement $\bar{\boldsymbol{v}}_\circ$ as in (6-1) satisfies the hypothesis of Proposition 2.6. The same proposition then gives the assertions of the present proposition. □

Remark 6.2. Let $\boldsymbol{v} \in C_1$, and let $\boldsymbol{x}$ be a point in $\mathcal{D}$ and $\boldsymbol{t}$ a vector that is tangent to $\mathcal{D}$ in the sense that there is a smooth curve γ contained in $\mathcal{D}$ and containing $\boldsymbol{x}$ with the tangent vector $\boldsymbol{t}$ at $\boldsymbol{x}$. Differentiating the equation $\boldsymbol{v} = \mathbf{0}$ along γ at $\boldsymbol{x}$ we obtain $\nabla \boldsymbol{v}(\boldsymbol{x})\boldsymbol{t} = \mathbf{0}$. Thus $\hat{\boldsymbol{E}}(\boldsymbol{v})(\boldsymbol{x})\boldsymbol{t} \cdot \boldsymbol{t} = 0$ and (6-1) cannot hold. This applies also to points of $\mathcal{D}$ at the corners or edges. Thus (6-1) can be effective essentially only in the case of the pure traction problem, when $\mathcal{D} = \varnothing$.

Negative semidefinite measures with nonzero singular part equilibrating the loads in no-tension materials were proposed in [Lucchesi et al. 2006]. The general theory of stresses represented by Borel measures is given in [Šilhavý 2008].

The following two results are proved in essentially the same way as Theorems 5.1 and 5.3. The proofs are therefore omitted.

Theorem 6.3. *Let $h : \mathbb{R} \to \mathbb{R} \cup \{-\infty, \infty\}$ be defined by*

$$h(t) = \inf\{-\langle \boldsymbol{l}_\circ, \boldsymbol{v} \rangle : \boldsymbol{v} \in C_1,\ \hat{\boldsymbol{E}}(\boldsymbol{v}) \geq t\mathbf{1} \text{ on } \mathrm{cl}\,\Omega,\ \langle \bar{\boldsymbol{l}}, \boldsymbol{v} \rangle = 1\},$$

$t \in \mathbb{R}$. Then:

(i) *h is nondecreasing, convex and $h(0) = \bar{\lambda}_\circ$.*

(ii) *$h(0)$ is finite and $\lim_{\substack{t \to 0 \\ t<0}} h(t) = h(0)$ if and only if $\lambda_{\mathcal{M}} = \bar{\lambda}_\circ \in \mathbb{R}$.*

Theorem 6.4. *A multiplier $\lambda \in \mathbb{R}$ is $X_{\mathcal{M}}$-statically admissible if and only if*

$$\sup\{\langle \boldsymbol{l}(\lambda), \boldsymbol{v} \rangle : \boldsymbol{v} \in C_1,\ \hat{\boldsymbol{E}}(\boldsymbol{v}) \geq -\mathbf{1} \text{ on } \Omega < \infty\} \quad (6\text{-}2)$$

This condition implies that $\langle \boldsymbol{l}(\lambda), \boldsymbol{v} \rangle \leq 0$ for every $\boldsymbol{v} \in C_1$, but it is stronger.

6C. ***Comparison of the critical multipliers in the smooth and p integrable settings.*** Let $1 \le p < \infty$, and let $q \in (1, \infty]$ be the Hölder conjugate exponent, and assume that $\boldsymbol{l}_\circ$ and $\bar{\boldsymbol{l}}$ are continuous functionals on W_p and hence also on C_1. Then in general we have

$$\bar{\lambda}_p \le \bar{\lambda}_\circ,$$

because the infimum in the definition of $\bar{\lambda}_\circ$ is taken over a smaller set than in the definition of $\bar{\lambda}_p$. Similarly, we have

$$\lambda_q \le \lambda_{\mathcal{M}}.$$

Under the condition that

$$\text{for each } \bar{\boldsymbol{v}} \in W_p^+ \text{ such that } \langle \bar{\boldsymbol{l}}, \bar{\boldsymbol{v}} \rangle > 0 \text{ there is a sequence } \bar{\boldsymbol{v}}_j \in C_1^+ \text{ such that and } \bar{\boldsymbol{v}}_j \to \bar{\boldsymbol{v}} \text{ in } W_p, \quad (6\text{-}3)$$

we have

$$\bar{\lambda}_p = \bar{\lambda}_\circ.$$

This is completely analogous to (5-8).

Lucchesi et al. [2008b; 2011] have given conditions and examples under which the loads equilibrated by measures from a certain class can be also equilibrated by stress fields represented by ordinary functions from $L^\infty(\Omega, \mathrm{Sym}^+)$.

6D. ***Comparison of the critical multipliers in the smooth and lipschitzian settings.*** Assume that $\boldsymbol{l}_\circ$ and $\bar{\boldsymbol{l}}$ are continuous functionals on W_∞ and hence also on C_1. Then in general we have

$$\bar{\lambda}_\infty \le \bar{\lambda}_\circ$$

because the infimum in the definition of $\bar{\lambda}_\circ$ is taken over a smaller set than that in the definition of $\bar{\lambda}_\infty$. Under the condition that

$$\text{for each } \bar{\boldsymbol{v}} \in W_\infty^+ \text{ such that } \langle \bar{\boldsymbol{l}}, \bar{\boldsymbol{v}} \rangle > 0 \text{ there is a sequence } \bar{\boldsymbol{v}}_j \in C_1^+ \text{such that } \bar{\boldsymbol{v}}_j \to \bar{\boldsymbol{v}} \text{ in } L^\infty(\Omega, \mathbb{R}^n), \quad (6\text{-}4)$$

we have

$$\bar{\lambda}_\infty = \bar{\lambda}_\circ.$$

This is completely analogous to (5-8) and (6-3).

We have

$$\lambda_{\mathrm{ba}} \le \lambda_{\mathcal{M}}$$

Indeed, each X_{ba}-statically admissible multiplier is also $X_{\mathcal{M}}$-statically admissible, because if an admissible stress field $\boldsymbol{T} \in X_{\mathrm{ba}}^-$ balances the loads corresponding to λ then the restriction $\tilde{\boldsymbol{T}}$ of $\boldsymbol{T}$ to $C^0(\mathrm{cl}\,\Omega, \mathrm{Sym})$ is $X_{\mathcal{M}}$ statically admissible and balances the same loads.

Remark 6.5. Returning to the functionals $\boldsymbol{T}$ and $\tilde{\boldsymbol{T}}$ from the preceding paragraph, we note that corresponding to $\boldsymbol{T}$ there exists a bounded finitely additive Sym-valued measure $\mathfrak{T}$ on the class $\mathfrak{M}$ of all Lebesgue measurable subsets of Ω, absolutely continuous with respect to the Lebesgue measure, such that

$$(\boldsymbol{T}, \boldsymbol{F}) = \int_\Omega \boldsymbol{F} \cdot d\mathfrak{T}$$

for all $\boldsymbol{F} \in L^\infty(\Omega, \mathrm{Sym})$. It appears that generally $\mathfrak{T}$ need not be countably additive, despite the extra information of balancing. At the same time there exists a finite, countably additive measure $\boldsymbol{T}$ on the class $\mathfrak{B}$ of all Borel subsets of $\operatorname{cl}\Omega$, such that

$$(\tilde{\boldsymbol{T}}, \boldsymbol{F}) \equiv (\boldsymbol{T}, \boldsymbol{F}) = \int_{\operatorname{cl}\Omega} \boldsymbol{F} \cdot d\boldsymbol{T}$$

for all $\boldsymbol{F} \in C^0(\operatorname{cl}\Omega, \mathrm{Sym})$. It appears that generally $\boldsymbol{T}$ need not be absolutely continuous with respect to the Lebesgue measure. A natural question arises of what is the relationship between $\mathfrak{T}$ and $\boldsymbol{T}$. Easy examples based on the extension of $\tilde{\boldsymbol{T}}$ by using the Hahn Banach theorem show that without the conditions of negative semidefiniteness and of balancing, there need not be any immediate relationship. However, with the two extra conditions just mentioned, the situation does not seem to be clear.

7. Monotonicity, density, and examples

Section 7A first shows that the displacements from the Sobolev spaces with positive semidefinite strain are monotone. Next, the same section shows that each displacement with positive semidefinite strain has to vanish, roughly speaking, on the interior of the convex hull of the set $\mathfrak{D}$. Section 7B proves the density of the smooth displacements with positive semidefinite strain in the wider spaces of displacements considered above. Some of the results of these two sections are employed in Sections 7C and 7D which present two examples: a collapse without a corresponding mechanism, and loads for which the kinematic and static problems give different results.

7A. ***Monotonicity and the convex hull.*** If $\boldsymbol{v}$ lies in $BD(\Omega)$ (in particular, if $\boldsymbol{v} \in W^{1,p}(\Omega, \mathbb{R}^n)$, where $1 \le p \le \infty$), we define the *precise representative* $\tilde{\boldsymbol{v}}$ of $\boldsymbol{v}$ on Ω by setting, for every $\boldsymbol{x} \in \operatorname{cl}\Omega$,

$$\tilde{\boldsymbol{v}}(\boldsymbol{x}) = \begin{cases} \lim_{r\to 0} \frac{1}{\mathscr{L}^n(B(\boldsymbol{x},r)\cap\Omega)} \int_{B(\boldsymbol{x},r)\cap\Omega} \boldsymbol{v}\, d\mathscr{L}^n & \text{if the limit exists,} \\ \boldsymbol{0} & \text{otherwise,} \end{cases} \tag{7-1}$$

where $B(\boldsymbol{x}, r)$ is the open ball of center $\boldsymbol{x}$ and radius r. Denote by $G(\boldsymbol{v})$ the set of all points $\boldsymbol{x} \in \operatorname{cl}\Omega$ for which the limit in (7-1) exists and, moreover, if $\boldsymbol{x} \in \partial\Omega$, it satisfies

$$\lim_{r\to 0} \frac{1}{\mathscr{L}^n(B(\boldsymbol{x}, r) \cap \Omega)} \int_{B(\boldsymbol{x},r)\cap\Omega} |\boldsymbol{v} - \tilde{\boldsymbol{v}}(\boldsymbol{x})|\, d\mathscr{L}^n = 0. \tag{7-2}$$

If $\boldsymbol{v} \in BD(\Omega)$ then $\mathscr{L}^n(\Omega \setminus G(\boldsymbol{v})) = 0$ and $\mathscr{H}^{n-1}(\partial\Omega \setminus G(\boldsymbol{v})) = 0$. The first assertion is the standard assertion about Lebesgue points (and actually holds for any $\boldsymbol{v} \in L^1(\Omega, \mathbb{R}^n)$); for the second assertion, see the trace theorem in [Témam 1983, Chapter II]. If $\boldsymbol{v} \in W^{1,p}(\Omega, \mathbb{R}^n)$ where $1 \le p \le \infty$ then $\mathscr{H}^{n-1}(\operatorname{cl}\Omega \setminus G(\boldsymbol{v})) = 0$. Indeed, $\mathscr{H}^{n-1}(\Omega \setminus G(\boldsymbol{v})) = 0$ by [Evans and Gariepy 1992, Theorem 1 in Section 4.8, Theorem 2 in Section 5.6.3, and Theorem 4 in Section 4.7.2] and $\mathscr{H}^{n-1}(\partial\Omega \setminus G(\boldsymbol{v})) = 0$ by [ibid., Definition and Remark, p. 133]. For every direction $\boldsymbol{t} \in \mathbb{S}^{n-1} := \{\boldsymbol{t} \in \mathbb{R}^n : |\boldsymbol{t}| = 1\}$, and for almost every line $\mathfrak{l}$ parallel to $\boldsymbol{t}$, $\tilde{\boldsymbol{v}}$ is absolutely continuous on $\mathfrak{s} := \mathfrak{l} \cap \operatorname{cl}\Omega$ (cf. [ibid., Theorem 2, Subsection 4.9.2] for lines parallel to the coordinate axes).

Remark 7.1. Let $\Omega \subset \mathbb{R}^n$ be a bounded convex set with Lipschitz boundary and $\boldsymbol{v} \in BD(\Omega)$ (respectively, $\boldsymbol{v} \in W^{1,p}(\Omega, \mathbb{R}^n)$ where $1 \le p \le \infty$), and let $\tilde{\boldsymbol{v}}$ be the precise representative. Then the following conditions are equivalent:

(i) $\hat{\boldsymbol{E}}(\boldsymbol{v})(B) \geq \boldsymbol{0}$ for every Borel subset B of Ω (respectively, $\hat{\boldsymbol{E}}(\boldsymbol{v}) \geq \boldsymbol{0}$ almost everywhere on Ω).

(ii) We have

$$(\tilde{\boldsymbol{v}}(\boldsymbol{x}) - \tilde{\boldsymbol{v}}(\boldsymbol{y})) \cdot (\boldsymbol{x} - \boldsymbol{y}) \geq 0 \tag{7-3}$$

for every $\boldsymbol{x}, \boldsymbol{y} \in G(\boldsymbol{v})$.

Note that condition (ii) can be formulated even for nondifferentiable displacements.

Proof. Let σ be a smooth mollifier, i.e., a nonnegative class ∞ function on $\mathbb{R}^n$ with the support in the open ball with center $\boldsymbol{0}$ and radius 1, and $\int_{\mathbb{R}^n} \sigma \, d\mathscr{L}^n = 1$. For each $\epsilon > 0$, let $\boldsymbol{v}_\epsilon$ be the ϵ mollification of $\boldsymbol{v}$, i.e., a map $\boldsymbol{v}_\epsilon : \Omega_\epsilon \to \mathbb{R}^n$ given by

$$\boldsymbol{v}_\epsilon(\boldsymbol{x}) = \epsilon^{-n} \int_\Omega \boldsymbol{v}(\boldsymbol{y}) \sigma((\boldsymbol{x} - \boldsymbol{y})/\epsilon) \, d\mathscr{L}^n(\boldsymbol{y})$$

for every $\boldsymbol{x}$ from the set

$$\Omega_\epsilon := \{\boldsymbol{x} \in \Omega : B(\boldsymbol{x}, \epsilon) \subset \Omega\}.$$

(i) $\Rightarrow$ (ii) The tensor $\hat{\boldsymbol{E}}(\boldsymbol{v}_\epsilon)$ is an ϵ mollification of $\hat{\boldsymbol{E}}(\boldsymbol{v})$ on Ω_ϵ (under either assumptions on $\boldsymbol{v}$) and hence $\hat{\boldsymbol{E}}(\boldsymbol{v}_\epsilon) \geq \boldsymbol{0}$ on Ω_ϵ. We have

$$\frac{d}{ds} \boldsymbol{v}_\epsilon(\boldsymbol{a} + s\boldsymbol{t}) \cdot \boldsymbol{t} = \nabla \boldsymbol{v}_\epsilon(\boldsymbol{a} + s\boldsymbol{t})\boldsymbol{t} \cdot \boldsymbol{t} = \hat{\boldsymbol{E}}(\boldsymbol{v}_\epsilon)(\boldsymbol{a} + s\boldsymbol{t})\boldsymbol{t} \cdot \boldsymbol{t} \geq 0$$

for every $\boldsymbol{a} \in \mathbb{R}^n$, every $s \in \mathbb{R}$, and every $\boldsymbol{t} \in \mathbb{S}^{n-1}$ for which $\boldsymbol{a} + s\boldsymbol{t} \in \operatorname{int} \Omega_\epsilon$. Thus the integration gives

$$(\boldsymbol{v}_\epsilon(\boldsymbol{x}) - \boldsymbol{v}_\epsilon(\boldsymbol{y})) \cdot (\boldsymbol{x} - \boldsymbol{y}) \geq 0$$

for every $\boldsymbol{x}, \boldsymbol{y} \in \operatorname{int} \Omega_\epsilon$. If $\boldsymbol{x}, \boldsymbol{y} \in \Omega$, then $\boldsymbol{x}, \boldsymbol{y} \in \operatorname{int} \Omega_\epsilon$ for all sufficiently small ϵ. We have $\boldsymbol{v}_\epsilon(\boldsymbol{x}) \to \tilde{\boldsymbol{v}}(\boldsymbol{x})$ as $\epsilon \to 0$ for every $\boldsymbol{x} \in G(\boldsymbol{v}) \cap \Omega$. This limit gives (7-3) for every $\boldsymbol{x}, \boldsymbol{y} \in G(\boldsymbol{v}) \cap \Omega$. Next assume that $\boldsymbol{x} \in G(\boldsymbol{v}) \cap \partial\Omega$ and $\boldsymbol{y} \in G(\boldsymbol{v}) \cap \Omega$. By the preceding case, we have

$$(\tilde{\boldsymbol{v}}(\boldsymbol{x}') - \tilde{\boldsymbol{v}}(\boldsymbol{y})) \cdot (\boldsymbol{x}' - \boldsymbol{y}) \geq 0$$

for every $\boldsymbol{x}' \in G(\boldsymbol{v}) \cap \Omega$. Hence, if $r > 0$, we have

$$\frac{1}{\mathscr{L}^n(B(\boldsymbol{x}, r) \cap \Omega)} \int_{B(\boldsymbol{x}, r) \cap \Omega} (\tilde{\boldsymbol{v}}(\boldsymbol{x}') - \tilde{\boldsymbol{v}}(\boldsymbol{y})) \cdot (\boldsymbol{x}' - \boldsymbol{y}) \, d\mathscr{L}^n(\boldsymbol{x}') \geq 0$$

and the limit $r \to 0$ using (7-1) and (7-2) gives (7-3). Finally, if $\boldsymbol{x}, \boldsymbol{y} \in G(\boldsymbol{v}) \cap \partial\Omega$, we proceed in the same way as above to establish (7-3) generally.

(ii) $\Rightarrow$ (i) Condition (ii) implies that if $\boldsymbol{t} \in \mathbb{S}^{n-1}$, and if $\mathfrak{l}$ is a line parallel to $\boldsymbol{t}$ then the function $\tilde{\boldsymbol{v}} \cdot \boldsymbol{t}$, defined on $\tilde{\mathfrak{l}} := \mathfrak{l} \cap G(\boldsymbol{v})$, is nondecreasing. By Fubini's theorem we have $\mathscr{H}^1((\mathfrak{l} \cap \Omega) \setminus \tilde{\mathfrak{l}}) = 0$ for $\mathscr{H}^{n-1}$ almost every line parallel to $\boldsymbol{t}$. Then $\boldsymbol{v}_\epsilon \cdot \boldsymbol{t}$ is nondecreasing on every closed line segment parallel to $\boldsymbol{t}$ in Ω_ϵ. Thus

$$0 \leq \frac{d}{ds} \boldsymbol{v}_\epsilon(\boldsymbol{a} + s\boldsymbol{t})\Big|_{s=0} \cdot \boldsymbol{t} = \hat{\boldsymbol{E}}(\boldsymbol{v}_\epsilon)(\boldsymbol{a})\boldsymbol{t} \cdot \boldsymbol{t}$$

for every point $\boldsymbol{a}$ of Ω_ϵ. We now let $\epsilon \to 0$ and obtain (i) under either assumption on $\boldsymbol{v}$. □

Proposition 7.2. *Assume that* $\Omega \subset \mathbb{R}^n$ *is open and convex, let* $\mathcal{D} \subset \partial\Omega$, *denote by* $\operatorname{int}\mathcal{D}$ *the relative interior of* $\mathcal{D}$ *in* $\partial\Omega$ *and assume that* $\operatorname{int}\mathcal{D}$ *is a class* 1 *surface. Define the sets* Z_i, $i = 1, \ldots,$ *by*

$$Z_1 = \{z \in \Omega : z = (1-t)\boldsymbol{x} + t\boldsymbol{y} \text{ for some } \boldsymbol{x}, \boldsymbol{y} \in \operatorname{int}\mathcal{D},\ \boldsymbol{x} \neq \boldsymbol{y},\ 0 < t < 1\}$$

and

$$Z_i = \{(1-t)\boldsymbol{x} + t\boldsymbol{y} : \boldsymbol{x}, \boldsymbol{y} \in Z_{i-1}, 0 \leq t \leq 1\}$$

if $i \geq 2$. *Then*:

(a) *The sequence* Z_i *is nondecreasing.*

(b) Z_i *is open for every* $i = 1, \ldots$.

(c) $Z_i \subset \Omega$ *for every* $i = 1, \ldots$.

(d) $Z_i = \operatorname{co} Z_1$ *for every* $i \geq n+1$, *where* $\operatorname{co} Z_1$ *denotes the convex hull of* Z_1.

Here by the relative interior of $\mathcal{D}$ we mean the interior with respect to the relative topology on $\partial\Omega$, defined by intersections of $\partial\Omega$ with open subsets of $\mathbb{R}^n$.

Proof. (a) The nondecreasing character of the sequence Z_i is immediate.

(b), (c) We work by induction on i. We have $Z_1 \subset \Omega$. To prove that Z_1 is open, let $z \in Z_1$ and $z = (1-t)\boldsymbol{x} + t\boldsymbol{y}$ for some $\boldsymbol{x}, \boldsymbol{y} \in \operatorname{int}\mathcal{D}$, $\boldsymbol{x} \neq \boldsymbol{y}$, $0 < t < 1$. Define the map $\Phi : \operatorname{int}\mathcal{D} \times (0,1) \to \Omega$ by

$$\Phi(\boldsymbol{y}', t') = (1-t')\boldsymbol{x} + t'\boldsymbol{y}', \tag{7-4}$$

$\boldsymbol{y}' \in \operatorname{int}\mathcal{D}$, $t' \in (0,1)$; hence

$$\Phi(\boldsymbol{y}, t) = z.$$

Then the continuity implies that Φ maps some neighborhood $\mathcal{N}$ of $(\boldsymbol{y}, t)$ in $\operatorname{int}\mathcal{D} \times (0,1)$ into some neighborhood $\mathcal{M}$ of z that is contained in Ω. One then has $\mathcal{M} \subset Z_1$ by the definition of Z_1. We now employ the implicit function theorem to show that there exists a neighborhood $\mathcal{M}' \subset \mathcal{M}$ of z and a class 1 map $\Psi : \mathcal{M}' \to \mathcal{N}$ such that $\Phi(\Psi(z')) = z'$ for all $z' \in \mathcal{M}'$. Indeed, the map Φ is continuously differentiable. To apply the implicit function theorem, we have to prove that the derivative $\mathrm{D}\,\Phi(\boldsymbol{y}, t) : \operatorname{Tan}(\operatorname{int}\mathcal{D}, \boldsymbol{y}) \times \mathbb{R} \to \mathbb{R}^n$ is nonsingular, where $\operatorname{Tan}(\operatorname{int}\mathcal{D}, \boldsymbol{y})$ is the tangent space to $\operatorname{int}\mathcal{D}$ at $\boldsymbol{y}$. If the local description of $\operatorname{int}\mathcal{D}$ near $\boldsymbol{y}$ is $\varphi(\boldsymbol{y}') = 0$ where φ is a class 1 function with $\nabla\varphi(\boldsymbol{y}) \neq \boldsymbol{0}$, then $\operatorname{Tan}(\operatorname{int}\mathcal{D}, \boldsymbol{y}) = \{\dot{\boldsymbol{y}} \in \mathbb{R}^n : \nabla\varphi(\boldsymbol{y}) \cdot \dot{\boldsymbol{y}} = 0\}$. The equation $\mathrm{D}\,\Phi(\boldsymbol{y}, t)(\dot{\boldsymbol{y}}, \dot{t}) = \boldsymbol{0}$ reads

$$\dot{t}(\boldsymbol{y} - \boldsymbol{x}) + t\dot{\boldsymbol{y}} = \boldsymbol{0}. \tag{7-5}$$

Multiplying scalarly by $\nabla\varphi(\boldsymbol{y})$ and using $\nabla\varphi(\boldsymbol{y}) \cdot \dot{\boldsymbol{y}} = 0$ we obtain

$$\nabla\varphi(\boldsymbol{y}) \cdot (\boldsymbol{y} - \boldsymbol{x})\dot{t} = 0. \tag{7-6}$$

Let us now show that

$$\nabla\varphi(\boldsymbol{y}) \cdot (\boldsymbol{y} - \boldsymbol{x}) \neq 0. \tag{7-7}$$

Indeed, the equation $\nabla\varphi(\boldsymbol{y}) \cdot (\boldsymbol{y} - \boldsymbol{x}) = 0$ means that the vector $\boldsymbol{x} - \boldsymbol{y}$ belongs to the tangent space of $\partial\Omega$ at $\boldsymbol{y}$ or equivalently that $\boldsymbol{x}$ belongs to the affine space $\boldsymbol{y} + \operatorname{Tan}(\operatorname{int}\mathcal{D}, \boldsymbol{y})$. Since Ω is convex and $\boldsymbol{x} \in \partial\Omega$, it follows that the line segment with endpoints $\boldsymbol{x}$ and $\boldsymbol{y}$ belongs to $\partial\Omega$ and hence in particular $z \in \partial\Omega$.

However, this is a contradiction as we assume that $z \in \Omega$. This contradiction shows that we have (7-7). Equation (7-6) then implies $\dot{t} = 0$ and (7-5) that $\dot{y} = \mathbf{0}$. Thus $\mathrm{D}\,\Phi(y, t)$ is nonsingular and the implicit function theorem gives a class 1 map $\Psi : \mathcal{M}' \to \mathcal{N}$ such that $\Phi(\Psi(z')) = z'$ for all $z' \in \mathcal{M}'$. This in turn means that Ψ maps some neighborhood of (y, t) in $\operatorname{int}\mathcal{D} \times (0, 1)$ onto some neighborhood of z. Thus Z_1 is open.

Let $i \geq 2$. Then (c) follows from the induction hypothesis and the convexity of Ω. To prove (b), let $z = (1-t)x + ty$ for some $x, y \in Z_{i-1}$ and $0 \leq t \leq 1$. To prove that there exist a neighborhood of z that is contained in Z_i, note that if $x = y$ or $t \in \{0, 1\}$ then $z \in Z_{i-1}$ and the induction hypothesis says that there exists a neighborhood of z that is contained in $Z_{i-1} \subset Z_i$. Thus we can assume that $x \neq y$ and $0 < t < 1$. Defining $\Gamma : Z_{i-1} \to \mathbb{R}^n$ by

$$\Gamma(y') = (1-t)x + ty'$$

for every $y' \in Z_{i-1}$ we find that Γ has the inverse Δ given by

$$\Delta(z') = (z' - (1-t)x)/t,$$

for $z' \in \mathbb{R}^n$. Hence Γ maps some neighborhood $\mathcal{N} \subset Z_{i-1}$ of y onto some neighborhood of z that is in Z_i. This completes the proof of (b) and (c).

(d) This follows from Carathéodory's theorem on the convex hull [Rockafellar 1970, Theorem 17.1]. □

Proposition 7.3. *Let $1 \leq p \leq \infty$, let Ω be convex, let $\mathcal{D} \subset \partial\Omega$ and assume that $\operatorname{int}\mathcal{D}$ is a class 1 surface. Let Z_i be the sequence defined in Proposition 7.2. If $v \in W^+_p$ then its precise representative $\tilde{v}$ satisfies*

$$\tilde{v} = \mathbf{0} \ \text{ everywhere on } \operatorname{co} Z_1. \tag{7-8}$$

Proof. We shall prove that

$$\tilde{v} = \mathbf{0} \ \text{ everywhere on } Z_i \tag{7-9}$$

for every $i = 1, \ldots$ by induction on i. Then (7-8) will follow from Proposition 7.2(d).

We prove (7-9) for $i = 1$. Note that if $x \in \Omega \cap G(v)$ and if $y \in \operatorname{int}\mathcal{D}$ then

$$\tilde{v}(x) \cdot (x - y) \geq 0. \tag{7-10}$$

Inequality (7-10) follows from Remark 7.1 if $y \in \operatorname{int}\mathcal{D} \cap G(v)$ since then $\tilde{v}(y) = \mathbf{0}$. Finally, if $x \in \Omega \cap G(v)$ and y in $\mathcal{D}$ is arbitrary, we make a limit in $\tilde{v}(x) \cdot (x - y') \geq 0$ as $y' \to y$ and $y' \in \operatorname{int}\mathcal{D} \cap G(v)$.

Let now $z \in Z_1 \cap G(v)$ and write $z = (1-t)x + ty$ for some $x, y \in \operatorname{int}\mathcal{D}$, $x \neq y$, $0 < t < 1$. Then (7-10) implies

$$\tilde{v}(z) \cdot (z - x) \geq 0 \quad \text{and} \quad \tilde{v}(z) \cdot (z - y) \geq 0.$$

This reads

$$t\tilde{v}(z) \cdot (y - x) \geq 0 \quad \text{and} \quad (1-t)\tilde{v}(z) \cdot (x - y) \geq 0,$$

and hence

$$\tilde{v}(z) \cdot t = 0, \tag{7-11}$$

where $t = (y - x)/|y - x|$. Define now a map Θ from $\mathbb{S}^{n-1}$ to $\partial\Omega \times \partial\Omega$ by the requirement that for each $t' \in \mathbb{S}^{n-1}$ we put $\Theta(t') = (x', y')$ where $x', y' \in \partial\Omega$ are uniquely determined by the conditions

that $\boldsymbol{t}' = (\boldsymbol{y}' - \boldsymbol{x}')/|\boldsymbol{y}' - \boldsymbol{x}'|$ and that the point $\boldsymbol{z}$ is on the (closed) line segment with endpoints $\boldsymbol{x}'$, $\boldsymbol{y}'$. Since $\operatorname{int}\mathcal{D} \times \operatorname{int}\mathcal{D}$ is a relatively open subset of $\partial\Omega \times \partial\Omega$, the continuity of Θ yields that there exists a neighborhood $\mathcal{N}$ of $\boldsymbol{t}$ in $\mathbb{S}^{n-1}$ such that Θ maps $\mathcal{N}$ onto some subset of $\operatorname{int}\mathcal{D} \times \operatorname{int}\mathcal{D}$. For all $\boldsymbol{t}' \in \mathcal{N}$ we have $\tilde{\boldsymbol{v}}(\boldsymbol{z}) \cdot \boldsymbol{t}' = 0$, which is possible only if $\tilde{\boldsymbol{v}}(\boldsymbol{z}) = \boldsymbol{0}$. Thus $\tilde{\boldsymbol{v}} = \boldsymbol{0}$ on $Z_1 \cap G(\boldsymbol{v})$ and hence $\tilde{\boldsymbol{v}} = \boldsymbol{0}$ everywhere on Z_1.

Let $i \geq 2$. Let $\boldsymbol{z} \in Z_i$ and let $\boldsymbol{z} = (1-t)\boldsymbol{x} + t\boldsymbol{y}$ where $\boldsymbol{x}, \boldsymbol{y} \in Z_{i-1}$, $0 \leq t \leq 1$. To prove that $\tilde{\boldsymbol{v}}(\boldsymbol{z}) = \boldsymbol{0}$, we can assume that $\boldsymbol{x} \neq \boldsymbol{y}$ and $0 < t < 1$ since otherwise $\boldsymbol{z} \in Z_{i-1}$ and the equation $\tilde{\boldsymbol{v}}(\boldsymbol{z}) = \boldsymbol{0}$ follows from the induction hypothesis. Let $\boldsymbol{x}', \boldsymbol{y}' \in Z_{i-1} \cap G(\boldsymbol{v})$ be such that $\boldsymbol{z} = (1-t)\boldsymbol{x}' + t\boldsymbol{y}'$. The induction hypothesis says that $\tilde{\boldsymbol{v}}(\boldsymbol{x}') = \tilde{\boldsymbol{v}}(\boldsymbol{y}') = \boldsymbol{0}$ and using this, we obtain $\tilde{\boldsymbol{v}}(\boldsymbol{z}) \cdot \boldsymbol{t}' = 0$ where $\boldsymbol{t}' = (\boldsymbol{y}' - \boldsymbol{x}')/|\boldsymbol{y}' - \boldsymbol{x}'|$; varying $\boldsymbol{x}' \in Z_{i-1} \cap G(\boldsymbol{v})$ and $\boldsymbol{y}' \in Z_{i-1} \cap G(\boldsymbol{v})$ in such a way that $\boldsymbol{z} := (1-t)\boldsymbol{x}' + t\boldsymbol{y}'$ remains fixed, we obtain the validity of $\tilde{\boldsymbol{v}}(\boldsymbol{z}) \cdot \boldsymbol{t}' = 0$ for almost every $\boldsymbol{t}'$ from a nonempty open subset of $\mathbb{S}^{n-1}$, which is possible only if $\tilde{\boldsymbol{v}}(\boldsymbol{z}) = \boldsymbol{0}$. □

7B. ***Density of monotone displacements satisfying boundary condition.*** Let $M \subset C^1(\operatorname{cl}\Omega, \mathbb{R}^n)$ and $M^+ \subset M$ be defined by

$$M := \{\boldsymbol{v} \in C^1(\operatorname{cl}\Omega, \mathbb{R}^n) : \boldsymbol{v} = \boldsymbol{0} \text{ in a neighborhood of } \mathcal{D}\},$$
$$M^+ := \{\boldsymbol{v} \in M : \hat{\boldsymbol{E}}(\boldsymbol{v}) \geq \boldsymbol{0} \text{ on } \operatorname{cl}\Omega\}.$$

We indicate here situations when

(α) M is dense in W_{BD} or in W_p, $1 \leq p \leq \infty$, in an appropriate sense, and

(β) M^+ is dense in W^+_{BD} or in W^+_p. The following result deals with Problem (α).

Proposition 7.4. *Suppose that $\mathcal{D}$ is relatively open in $\partial\Omega$. Let $1 \leq p \leq \infty$, and let $\boldsymbol{u} \in W_p$. Then there exists a sequence $\boldsymbol{u}_k \in M$ such that*

(i) *if $p < \infty$ then $\boldsymbol{u}_k \to \boldsymbol{u}$ in $W^{1,p}(\Omega, \mathbb{R}^n)$;*

(ii) *if $p = \infty$ then $\boldsymbol{u}_k \to \boldsymbol{u}$ uniformly on $\operatorname{cl}\Omega$, $\hat{\boldsymbol{E}}(\boldsymbol{u}_k) \to \hat{\boldsymbol{E}}(\boldsymbol{u})$ almost everywhere on Ω and*

$$\sup_{k=1,\ldots} |\nabla \boldsymbol{u}_k|_\infty < \infty,$$

where $|\cdot|_\infty$ is the L^∞ norm.

This is proved in a way similar to [Témam 1977, Theorem I.1 and I.3].

Problem (β) is more difficult. The standard results for the density of $C^\infty(\operatorname{cl}\Omega, \mathbb{R}^n)$ in $BD(\Omega)$ or in $W^{1,p}(\Omega, \mathbb{R}^n)$, employ constructions based on the multiplication of the function $\boldsymbol{v}$ by members θ_i of a suitable partition of unity. This operation does not preserve the positive semidefinite character of the strain tensor: One has

$$\hat{\boldsymbol{E}}(\theta_i \boldsymbol{v}) = \theta_i \hat{\boldsymbol{E}}(\boldsymbol{v}) + \tfrac{1}{2}(\boldsymbol{v} \otimes \nabla\theta_i + \nabla\theta_i \otimes \boldsymbol{v}),$$

and the expression in the bracket is not positive semidefinite in general. It is essentially only the homothetic extension that preserves positive semidefiniteness. We are therefore forced to impose strong hypotheses on Ω and $\mathcal{D}$ to be able to apply homothety to prove the density of M^+ in W^+_p.

Proposition 7.5. *Let $\Omega \subset \mathbb{R}^n$ be an open bounded convex set with Lipschitz boundary and let $\mathcal{D} \subset \partial\Omega$. Assume that one of the following conditions is satisfied*:

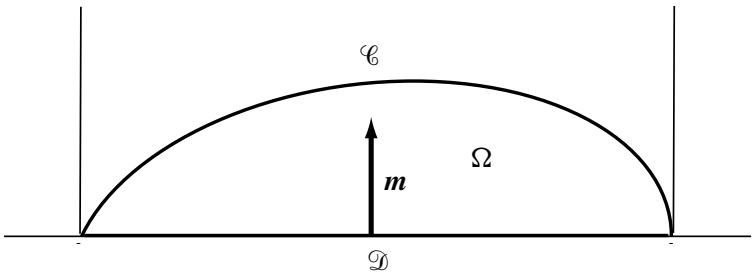

(1) (See figure above.) *The set $\mathscr{D}$ is nonempty, convex, is contained in some hyperplane H of normal $\boldsymbol{m}$, is open in H, and*

$$\Omega \subset \mathscr{C} := \{\boldsymbol{x} \in \mathbb{R}^n : \boldsymbol{x} = \boldsymbol{a} + s\boldsymbol{m} \text{ for some } \boldsymbol{a} \in \mathscr{D} \text{ and some } s > 0\}.$$

(2) $\operatorname{int}\mathscr{D}$ *is a class* 1 *surface and the set Z_1 defined in Proposition 7.2 is nonempty.*

(3) $\mathscr{D} = \varnothing$.

Let $1 \le p \le \infty$. Let $\boldsymbol{u} \in W^+_p$. Then there exists a sequence $\boldsymbol{u}_k \in M^+$ such that assertions (i) *and* (ii) *of Proposition 7.4 are satisfied.*

Proof. Suppose that (a) holds. We can assume that $\mathbf{0} \in \mathscr{D}$. For each $\epsilon > 0$ let

$$\Omega_\epsilon := (1+\epsilon)\Omega \cup \{\boldsymbol{a} + s\boldsymbol{m} \in \mathbb{R}^n : \boldsymbol{a} \in (1+\epsilon)\mathscr{D},\ -\epsilon < s \le 0\}.$$

We have $\operatorname{cl}\Omega \subset \Omega_\epsilon$ and Ω_ϵ is convex. Let $\boldsymbol{v}_\epsilon : \Omega_\epsilon \to \mathbb{R}^n$ be defined by

$$\boldsymbol{v}_\epsilon(\boldsymbol{x}) = \begin{cases} \boldsymbol{u}(\boldsymbol{x}/(1+\epsilon)) & \text{if } \boldsymbol{x} \in (1+\epsilon)\Omega, \\ \mathbf{0} & \text{if } \boldsymbol{x} \in \Omega_\epsilon \setminus (1+\epsilon)\Omega. \end{cases}$$

Since $\boldsymbol{u} = \mathbf{0}$ on $\mathscr{D}$, we have $\boldsymbol{v}_\epsilon \in BD(\Omega_\epsilon)$ or $\boldsymbol{v}_\epsilon \in W^{1,p}(\Omega_\epsilon, \mathbb{R}^n)$ for each $\epsilon > 0$; moreover, $\hat{\boldsymbol{E}}(\boldsymbol{v}_\epsilon)$ is positive semidefinite. Let $\boldsymbol{w}_\epsilon$ be an $\epsilon/4$ mollification of $\boldsymbol{v}_\epsilon$, i.e., a map on $\Omega_{3\epsilon/4}$ with values in $\mathbb{R}^n$ given by

$$\boldsymbol{w}_\epsilon(\boldsymbol{y}) = (\epsilon/4)^{-n} \int_{\Omega_\epsilon} \boldsymbol{v}_\epsilon(\boldsymbol{x}) \sigma\left(\frac{\boldsymbol{y}-\boldsymbol{x}}{\epsilon/4}\right) d\mathscr{L}^n(\boldsymbol{x})$$

for every $\boldsymbol{y} \in \operatorname{cl}\Omega_{3\epsilon/4}$. Here σ is a mollifier (see the proof of Remark 7.1). Then $\boldsymbol{w}_\epsilon \in C^\infty(\operatorname{cl}\Omega_{\epsilon/2}, \mathbb{R}^n)$, $\boldsymbol{w}_\epsilon(\boldsymbol{y}) = \mathbf{0}$ for every $\boldsymbol{y}$ from the set $\{\boldsymbol{y} \in \mathbb{R}^n : \boldsymbol{y} = \boldsymbol{a} + s\boldsymbol{m} : \boldsymbol{a} \in (1+\epsilon/2)\mathscr{D},\ -\epsilon/2 < s < -\epsilon/4\}$. Moreover, $\hat{\boldsymbol{E}}(\boldsymbol{w}_\epsilon) \ge \mathbf{0}$ on $\operatorname{cl}\Omega_{3\epsilon/4}$ since $\hat{\boldsymbol{E}}(\boldsymbol{w}_\epsilon)$ is the $\epsilon/4$ mollification of $\hat{\boldsymbol{E}}(\boldsymbol{v}_\epsilon)$. Let $\boldsymbol{u}_\epsilon : \Omega \to \mathbb{R}^n$ be defined by

$$\boldsymbol{u}_\epsilon(\boldsymbol{x}) = \boldsymbol{w}_\epsilon(\boldsymbol{x} - \epsilon\boldsymbol{m})$$

for every $\boldsymbol{x} \in \Omega$. Then $\boldsymbol{u}_\epsilon \in M^+$ and an argument similar to that of [Adams and Fournier 2003, proof of Proposition 3.22, pp. 69–70] shows that $\boldsymbol{u}_\epsilon \to \boldsymbol{u}$ in the sense of assertions (i)–(iii) of Proposition 7.4 as $\epsilon \to 0$. This completes the proof under hypothesis (a).

Suppose that (b) takes place. We may suppose that $\mathbf{0} \in Z_1 \subset \operatorname{co} Z_1$. For each $\epsilon > 0$, let

$$\Omega_\epsilon := (1+\epsilon)\Omega$$

so that the convexity implies that $\operatorname{cl}\Omega \subset \Omega_\epsilon$. Let $\boldsymbol{v}_\epsilon : \Omega_\epsilon \to \mathbb{R}^n$ be defined by

$$\boldsymbol{v}_\epsilon(\boldsymbol{x}) = \boldsymbol{u}(\boldsymbol{x}/(1+\epsilon)), \quad \boldsymbol{x} \in \Omega_\epsilon.$$

Since $\boldsymbol{u} = \boldsymbol{0}$ on $\operatorname{co} Z_1$ by Proposition 7.3, we have

$$\boldsymbol{v}_\epsilon = \boldsymbol{0} \quad \text{on } A_\epsilon := (1+\epsilon)\operatorname{co} Z_1.$$

Let $\boldsymbol{v}_\epsilon$ be the $\epsilon/4$ mollification of $\boldsymbol{v}_\epsilon$, so that

$$\boldsymbol{v}_\epsilon \in C^\infty(\Omega_{3\epsilon/4}, \mathbb{R}^n), \quad \hat{\boldsymbol{E}}(\boldsymbol{v}_\epsilon) \geq \boldsymbol{0} \text{ on } \Omega_{3\epsilon/4}, \quad \boldsymbol{v}_\epsilon = \boldsymbol{0} \text{ on } A_{3\epsilon/4}.$$

Then the restriction $\boldsymbol{u}_\epsilon$ of $\boldsymbol{v}_\epsilon$ to Ω satisfies $\boldsymbol{u}_\epsilon \in M^+$ and $\boldsymbol{u}_\epsilon \to \boldsymbol{u}$ in the sense of assertions (i) and (ii) of Proposition 7.4.

If (c) holds, one proceeds similarly, but the proof is easier, as no boundary condition has to be satisfied. □

7C. ***Example of collapse without collapse mechanism.*** In the example to be given here, the value $\lambda = \frac{1}{4}$ corresponds to the collapse, and yet there is no corresponding mechanism.

Example 7.6. (See figure below.) Let $\Omega = (0,1)^2$ and let $\mathscr{D} = [0,1] \times \{0\}$,

$$\boldsymbol{s}_\circ(\boldsymbol{r}) = \begin{cases} -\boldsymbol{j} & \text{if } \boldsymbol{r} \in \mathscr{S}_t := (0,1) \times \{1\}, \\ \boldsymbol{0} & \text{if } \boldsymbol{r} \in \mathscr{S} \setminus \mathscr{S}_t, \end{cases} \qquad \bar{\boldsymbol{s}}(\boldsymbol{r}) = \begin{cases} (4(x-1/2)^2 - 1)\boldsymbol{i} & \text{if } \boldsymbol{r} \in \mathscr{S}_t := (0,1) \times \{1\}, \\ \boldsymbol{0} & \text{if } \boldsymbol{r} \in \mathscr{S} \setminus \mathscr{S}_t, \end{cases}$$

and $\boldsymbol{b}_\circ = \bar{\boldsymbol{b}} = \boldsymbol{0}$ on Ω. (Here $\boldsymbol{i} = (1,0)$ and $\boldsymbol{j} = (0,1)$.) Then:

(i) $\lambda_q = \bar{\lambda}_p = \frac{1}{4}$ for all $p, q \in [1, \infty]$.

(ii) If $|\lambda| < \frac{1}{4}$ then λ is $L^q(\Omega, \mathrm{Sym})$-statically admissible for any $q \in [1, \infty]$.

(iii) If $|\lambda| = \frac{1}{4}$ then λ is $L^q(\Omega, \mathrm{Sym})$-statically admissible for any $q \in [1, 3)$.

(iv) If $q \in [1, \infty]$ then there is no $L^q(\Omega, \mathrm{Sym})$ mechanism corresponding to $\lambda = \frac{1}{4}$.

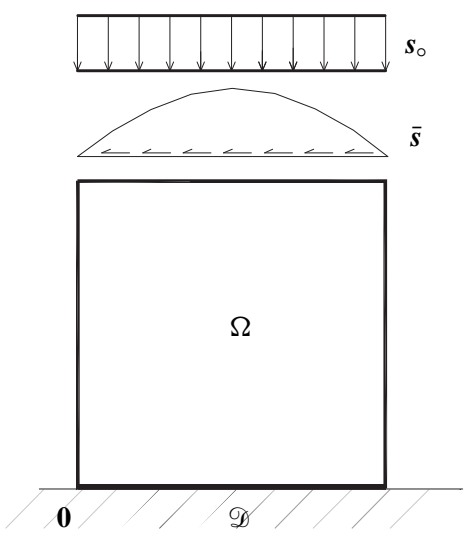

Remarks. (a) We do not know if $\lambda = \pm\frac{1}{4}$ is $L^q(\Omega, \mathrm{Sym})$-statically admissible for $q \geq 3$.

(b) The case $p = q = 2$ has been treated in [Lucchesi et al. 2010, Example 2.3]. It was shown that $\lambda_2 = \bar{\lambda}_2 = \frac{1}{4}$, and an admissible stress field $\boldsymbol{T}(\lambda)$ determined in [Lucchesi and Zani 2003] was shown to balance the loads for all $\lambda \in [-\frac{1}{4}, \frac{1}{4}]$. The stress field $\boldsymbol{T}(\lambda)$ was shown to be bounded if $|\lambda| < \frac{1}{4}$ and to belong to $L^2(\Omega, \mathrm{Sym})$ if $|\lambda| = \frac{1}{4}$. Furthermore, it was shown that no corresponding mechanism exists in W_2. Actually, $\boldsymbol{T}\left(\frac{1}{4}\right) \in L^q(\Omega, \mathrm{Sym})$ for all $q \in [1, 3)$, as a closer examination shows, and thus (ii), (iii) above follow from the construction in the cited references. Here we shall prove the existence of $\boldsymbol{T}$ balancing the loads for multipliers as in (ii), (iii), without giving an explicit formula for it, by using Proposition 2.8.

Lemma 7.7. *Let either* $0 \leq \lambda < \frac{1}{4}$ *and* $q \in [1, \infty]$ *or let* $\lambda = \frac{1}{4}$ *and* $q \in [1, 3)$. *Then* λ *is* $L^q(\Omega, \mathrm{Sym})$-*statically admissible.*

Proof. We employ Proposition 2.8. Hence we seek to show that corresponding to λ and q there exists a constant c such that

$$\sup\{\langle \boldsymbol{l}(\lambda), \boldsymbol{v}\rangle : \boldsymbol{v} \in W_p,\ \hat{\boldsymbol{E}}(\boldsymbol{v}) \geq \boldsymbol{F} \text{ almost everywhere on } \Omega\} \leq\ c|\boldsymbol{F}|_p$$

for every $\boldsymbol{F} \in L^p(\Omega, \mathrm{Sym})$, where p is the Hölder conjugate exponent to q and $|\boldsymbol{F}|_p$ is the L^p norm of $\boldsymbol{F}$.

Thus let $\boldsymbol{F} \in L^p(\Omega, \mathrm{Sym})$ and let $\boldsymbol{v} \in W_p$ satisfy

$$\hat{\boldsymbol{E}}(\boldsymbol{v}) \geq \boldsymbol{F} \text{ almost everywhere on } \Omega \tag{7-12}$$

and prove that

$$\langle \boldsymbol{l}(\lambda), \boldsymbol{v}\rangle \leq c|\boldsymbol{F}|_p. \tag{7-13}$$

Write $\boldsymbol{m}(\alpha) := \boldsymbol{s}(\lambda)(\alpha, 1)$ for every $\alpha \in [0, 1]$. For any $\alpha \in [0, 1]$ let

$$\mathfrak{l}(\alpha) := \{\boldsymbol{a}(\alpha) + z\boldsymbol{m}(\alpha) : z \in \mathbb{R}\}$$

be the line through the point $\boldsymbol{a}(\alpha) := (\alpha, 1) \in \mathcal{S}_t$ and of direction parallel to $\boldsymbol{m}(\alpha)$. The line $\mathfrak{l}(\alpha)$ always intersects the x-axis because $\boldsymbol{m}(\alpha)$ is never horizontal, viz., at the point

$$\boldsymbol{b}(\alpha) = (\beta(\alpha), 0)$$

where

$$\beta(\alpha) = \alpha + \lambda(4(\alpha - 1/2)^2 - 1).$$

One has

$$\beta(0) = 0, \quad \beta(1) = 1.$$

If $0 \leq \lambda \leq \frac{1}{4}$, then β is a nondecreasing function on the interval $[0, 1]$ thus

$$0 \leq \beta(\alpha) \leq 1 \text{ for every } \alpha \in [0, 1];$$

in other words, the line $\mathfrak{l}(\alpha)$ intersects the x-axis at some point $\boldsymbol{b}(\alpha)$ of the base $\mathcal{D}$, where the panel is fixed. We now consider the segment $\mathfrak{s}(\alpha) = \mathfrak{l}(\alpha) \cap \mathrm{cl}\,\Omega$ with endpoint $\boldsymbol{a}(\alpha)$, $\boldsymbol{b}(\alpha)$. The precise representative

$\tilde{\boldsymbol{v}}$ of $\boldsymbol{v}$ is absolutely continuous on the segment $\mathfrak{s}(\alpha)$ and $\boldsymbol{F}(\alpha)$ is defined for $\mathscr{H}^1$-almost every point of $\mathfrak{s}(\alpha)$ and $\boldsymbol{F}$ is $\mathscr{H}^1$ integrable on $\mathfrak{s}(\alpha)$. Equation (7-12) then gives

$$\frac{d}{dz}\boldsymbol{v}(\boldsymbol{a}(\alpha)+z\boldsymbol{t})\cdot\boldsymbol{t}=\hat{\boldsymbol{E}}(\boldsymbol{v})(\boldsymbol{a}(\alpha)+z\boldsymbol{t})\boldsymbol{t}\cdot\boldsymbol{t}\geq\boldsymbol{F}(\boldsymbol{a}(\alpha)+z\boldsymbol{t})\boldsymbol{t}\cdot\boldsymbol{t}$$

for $\mathscr{L}^1$-almost every $z\in[0,1]$, where we write $\boldsymbol{t}=\boldsymbol{m}(\alpha)$ for brevity. Thus integrating with respect to z over the interval $[0,1]$ and using $\boldsymbol{v}(\boldsymbol{a}(\alpha)+\boldsymbol{t})\equiv\boldsymbol{v}(\boldsymbol{b}(\alpha))=\boldsymbol{0}$, we find that

$$\boldsymbol{v}(\boldsymbol{a}(\alpha))\cdot\boldsymbol{t}\leq-\int_0^1\boldsymbol{F}(\boldsymbol{a}(\alpha)+z\boldsymbol{t})\boldsymbol{t}\cdot\boldsymbol{t}\,dz\leq\int_0^1|\boldsymbol{F}(\boldsymbol{a}(\alpha)+z\boldsymbol{t})||\boldsymbol{t}|^2\,dz.$$

We have $|\boldsymbol{t}|=|\boldsymbol{m}(\alpha)|\leq d<\infty$ for all $\boldsymbol{a}(\alpha)\in\mathscr{S}_t$ and thus we obtain that

$$\boldsymbol{v}(\boldsymbol{a}(\alpha))\cdot\boldsymbol{m}(\alpha)\leq d^2\int_0^1|\boldsymbol{F}(\boldsymbol{a}(\alpha)+z\boldsymbol{m}(\alpha))|\,dz \tag{7-14}$$

and hence, integrating (7-14) over $\mathscr{T}_t$ and using $\boldsymbol{m}(\alpha):=\boldsymbol{s}(\lambda)(\alpha,1)$ we obtain

$$\langle\boldsymbol{l}(\lambda),\boldsymbol{v}\rangle\leq d^2\int_0^1\int_0^1|\boldsymbol{F}(\boldsymbol{a}(\alpha)+z\boldsymbol{m}(\alpha))|\,dz\,d\alpha. \tag{7-15}$$

Let us now estimate the integral

$$I:=\int_0^1\int_0^1|\boldsymbol{F}((\alpha,1)+z\boldsymbol{m}(\alpha))|\,dz\,d\alpha.$$

Consider a change of variables Φ from (z,α) to $(x,y)=(\alpha,1)+z\boldsymbol{m}(\alpha))$, i.e.,

$$x=\alpha+z\lambda(4(\alpha-1/2)^2-1),\quad y=1-z.$$

The Jacobian of this transformation $J:=|\det\mathrm{D}\,\Phi|$ is

$$J=1+8\lambda\alpha z-4\lambda z.$$

Applying Hölder's inequality to the measure $J\,dz\,d\alpha$ we obtain

$$I=\int_0^1\int_0^1|\boldsymbol{F}((\alpha,1)+z\boldsymbol{m}(\alpha))|J^{-1}J\,dz\,d\alpha\leq K^{1/p}L^{1/q}$$

where

$$K=\int_0^1\int_0^1|\boldsymbol{F}((\alpha,1)+z\boldsymbol{m}(\alpha))|^pJ\,dz\,d\alpha\equiv\int_0^1\int_0^1|\boldsymbol{F}(x,y)|^p\,dx\,dy\equiv|\boldsymbol{F}|_p^p,$$

and

$$L=\int_0^1\int_0^1J^{1-q}\,dz\,d\alpha=\int_0^1\int_0^1(1+8\lambda\alpha z-4\lambda z)^{1-q}\,dz\,d\alpha.$$

We now distinguish two cases.

Case (a): Let $0\leq\lambda<\frac{1}{4}$. Then $1+8\lambda\alpha z-4\lambda z\geq1-4\lambda$ and thus

$$I\leq(1-4\lambda)^{(1-q)/q}|\boldsymbol{F}|_p.$$

Inequality (7-15) then yields

$$\langle \boldsymbol{l}(\lambda), \boldsymbol{v}\rangle \le d^2(1-4\lambda)^{(1-q)/q}|\boldsymbol{F}|_p$$

and thus we have (7-13) with $c = d^2(1-4\lambda)^{(1-q)/q}$. Consequently, the conclusion of Proposition 7.3 holds and thus λ is $L^q(\Omega, \mathrm{Sym})$-statically admissible for every $q \in [1, \infty]$.

Case (b): $\lambda = \frac{1}{4}$. Then

$$L = \int_0^1 \int_0^1 (1 + 2z\alpha - z)^{1-q}\, dz\, d\alpha \tag{7-16}$$

and hence

$$\begin{aligned} L &= (2-q)^{-1} \int_0^1 (2\alpha-1)^{-1}(1+2z\alpha-z)^{2-q}\big|_{z=0}^{z=1}\, d\alpha \\ &= (2-q)^{-1} \int_0^1 (2\alpha-1)^{-1}((2\alpha)^{2-q}-1)\, d\alpha, \end{aligned}$$

provided $q \neq 2$. Under this assumption, it is easily found that the integrand of the last integral has the only singularity at $\alpha = 0$, where it behaves as a constant multiple of α^{2-q}. The apparent singularity at $\alpha = 1/2$ does not occur as

$$\lim_{\alpha \to 1/2} (2\alpha-1)^{-1}((2\alpha)^{2-q}-1) = 1 - q/2.$$

Thus, if $2 - q > -1$, i.e., if $1 \le q < 3$, and $q \neq 2$, the integral in (7-16) thus converges. It is easily found that the integral in (7-16) converges also if $q = 2$. Thus (7-15) yields

$$\left\langle \boldsymbol{l}\left(\tfrac{1}{4}\right), \boldsymbol{v}\right\rangle \le d^2 L^{1/q}|\boldsymbol{F}|_p$$

for every $\boldsymbol{F} \in L^p(\Omega, \mathrm{Sym})$ and we have (7-13) with $c = d^2 L^{1/q}$. □

Remark 7.8. Assertions (ii) and (iii) follow from Lemma 7.7 by noting that any $\lambda \in \mathbb{R}$ is $L^q(\Omega, \mathrm{Sym})$-statically admissible if and only if $-\lambda$ is too (it suffices to change the orientation of the x-axis). It also follows from (ii) (or from Lemma 7.7) that $\lambda_q \le \frac{1}{4}$ for each $q \in [1, \infty]$.

Lemma 7.9. *For each $\lambda > \frac{1}{4}$ and $p \in [1, \infty]$ there exists a W_p mechanism corresponding to λ.*

Proof. Let $p \in [1, \infty]$ be arbitrary. If $\omega : \mathbb{R} \to \mathbb{R}$ is any nonincreasing C^1 function vanishing on $(1, \infty)$ that does not vanish identically on $(0, 1)$ then $\boldsymbol{v} : \Omega \to \mathbb{R}^2$, given by

$$\boldsymbol{v}(\boldsymbol{r}) = \omega(x/y)\boldsymbol{r}^\perp, \tag{7-17}$$

$\boldsymbol{r} = (x, y) \in \Omega$, $\boldsymbol{r}^\perp := (-y, x)$ satisfies $\boldsymbol{v} \in W_p$ and $\hat{\boldsymbol{E}}(\boldsymbol{v}) \in L^p(\Omega, \mathrm{Sym}^+)$. Indeed, one finds that $\boldsymbol{v} \in W^{1,p}(\Omega, \mathbb{R}^2)$ and since ω vanishes on $(1, \infty)$, $\boldsymbol{v}$ vanishes on

$$\Omega^- := \{\boldsymbol{r} \in \Omega : x/y > 1\}$$

and thus in particular on $\mathfrak{D}$ (in the sense of trace). Hence $\boldsymbol{v} \in W_p$. Furthermore,

$$\hat{\boldsymbol{E}}(\boldsymbol{v})(\boldsymbol{r}) = -y^{-2}\omega'(x/y)\boldsymbol{r}^\perp \otimes \boldsymbol{r}^\perp$$

$\boldsymbol{r} \in \Omega$, and as $\omega' \leq 0$ we have $\hat{\boldsymbol{E}}(\boldsymbol{v}) \in L^p(\Omega, \mathrm{Sym}^+)$. One has

$$\langle \boldsymbol{l}_\circ, \boldsymbol{v} \rangle = -\int_{\mathcal{T}} \omega(x/y) x \, d\mathcal{H}^1(\boldsymbol{r}) = -\int_0^1 \omega(x) x \, dx$$
$$\langle \bar{\boldsymbol{l}}, \boldsymbol{v} \rangle = 4\int_{\mathcal{T}} \omega(x/y) yx(1-x) \, d\mathcal{H}^1(\boldsymbol{r}) = 4\int_0^1 \omega(x) x(1-x) \, dx;$$

noting that the last expression and the hypotheses on ω imply that $\langle \bar{\boldsymbol{l}}, \boldsymbol{v} \rangle > 0$, we thus deduce that the value

$$\lambda = -\frac{\langle \boldsymbol{l}_\circ, \boldsymbol{v} \rangle}{\langle \bar{\boldsymbol{l}}, \boldsymbol{v} \rangle} = 4^{-1} \int_0^1 \omega(x) x \, dx \Big/ \int_0^1 \omega(x) x(1-x) \, dx \tag{7-18}$$

is a kinematically admissible multiplier. Fixing $\epsilon \in (0, 1)$ and taking a sequence of functions of the type of ω that converges to the function ω_ϵ given by

$$\omega_\epsilon(t) = \begin{cases} 1 & \text{if } t \leq \epsilon, \\ 0 & \text{otherwise,} \end{cases}$$

$t \in \mathbb{R}$, we deduce from (7-18) by evaluating the integrals that the value

$$\lambda = \tfrac{1}{4}(1 - 2\epsilon/3)$$

is kinematically admissible. Varying $\epsilon \in (0, 1)$ we obtain the interval $\left(\frac{1}{4}, \frac{3}{4}\right)$. □

Remark 7.10. It follows from Lemma 7.9 that $\bar{\lambda}_p \leq \frac{1}{4}$ for each $p \in [1, \infty]$. Combining $\frac{1}{4} \leq \bar{\lambda}_p \leq \lambda_q \leq \frac{1}{4}$ we obtain (i).

Lemma 7.11. *If $\lambda = \frac{1}{4}$ and $p \in [1, \infty]$ then there is no corresponding W_p mechanism.*

Proof. We prove that if $\boldsymbol{v} \in W_p^+$ and $\langle \boldsymbol{l}\left(\frac{1}{4}\right), \boldsymbol{v} \rangle = 0$ then $\boldsymbol{v} = \boldsymbol{0}$ almost everywhere on Ω. For any $\alpha \in [0, 1]$ let $\boldsymbol{a}(\alpha) \in \mathcal{S}_t$ and $\boldsymbol{b}(\alpha) \in \mathcal{D}$ be as in the proof of Lemma 7.7. Then for $\mathcal{L}^1$-almost every $\alpha \in [0, 1]$ we have

$$\big(\boldsymbol{v}(\boldsymbol{a}(\alpha)) - \boldsymbol{v}(\boldsymbol{b}(\alpha))\big) \cdot \big(\boldsymbol{a}(\alpha) - \boldsymbol{b}(\alpha)\big) \geq 0;$$

using that $\boldsymbol{v}(\boldsymbol{b}(\alpha)) = \boldsymbol{0}$, we obtain

$$\boldsymbol{v}(\boldsymbol{a}(\alpha)) \cdot \boldsymbol{s}\left(\tfrac{1}{4}\right)(\alpha, 1) \leq 0.$$

Comparing this with

$$\left\langle \boldsymbol{l}\left(\tfrac{1}{4}\right), \boldsymbol{v} \right\rangle = \int_0^1 \boldsymbol{v} \cdot \boldsymbol{s}\left(\tfrac{1}{4}\right)(\alpha, 1) \, d\alpha = 0$$

we obtain

$$\boldsymbol{v}(\boldsymbol{a}(\alpha)) \cdot \boldsymbol{s}\left(\tfrac{1}{4}\right)(\alpha, 1) = 0 \tag{7-19}$$

for $\mathcal{L}^1$-almost every $\alpha \in (0, 1)$. Furthermore, for almost every $\alpha \in (0, 1)$ we have

$$\big(\boldsymbol{v}(\boldsymbol{a}(\alpha)) - \boldsymbol{v}(\boldsymbol{0})\big) \cdot \boldsymbol{a}(\alpha) \geq 0, \quad \big(\boldsymbol{v}(\boldsymbol{a}(\alpha)) - \boldsymbol{v}(\boldsymbol{i})\big) \cdot \big(\boldsymbol{a}(\alpha) - \boldsymbol{i}\big) \geq 0,$$

which reduces to

$$\boldsymbol{v}(\boldsymbol{a}(\alpha)) \cdot \boldsymbol{a}(\alpha) \geq 0, \quad \boldsymbol{v}(\boldsymbol{a}(\alpha)) \cdot \big(\boldsymbol{a}(\alpha) - \boldsymbol{i}\big) \geq 0 \tag{7-20}$$

for $\mathscr{L}^1$-almost every $\alpha \in (0, 1)$. It is now easily seen that (7-19) and (7-20) imply that $\boldsymbol{v}(\boldsymbol{a}(\alpha)) = \boldsymbol{0}$ for $\mathscr{L}^1$-almost every $\alpha \in (0, 1)$. We thus have $\boldsymbol{v} = \boldsymbol{0}$ on $\mathscr{S}_t$ and on $\mathscr{D}$ and thus Proposition 7.3 implies that $\boldsymbol{v} = \boldsymbol{0}$ on $\operatorname{co} Z_1$ which is Ω. □

7D. ***Example of the violation of the kinematic theorem.*** We here give an example in which the supremum of statically admissible multipliers depends dramatically on the choice of function spaces.

Example 7.12. (See figure below.) Let $\Omega = (0, 1)^2$, $\mathscr{D} = (0, 1) \times \{0\}$, $\mathscr{S} = \partial\Omega \setminus \mathscr{D}$,

$$\boldsymbol{s}(\lambda)(\boldsymbol{r}) = \begin{cases} (1-\lambda)\boldsymbol{r} & \text{if } \boldsymbol{r} \in \mathscr{S}_t := (0, 1) \times \{1\}, \\ (\lambda/2 - 1)(\boldsymbol{i} + \boldsymbol{j}) & \text{if } \boldsymbol{r} \in \mathscr{S}_r := \{1\} \times (0, 1), \\ \boldsymbol{0} & \text{if } \boldsymbol{r} \in \mathscr{S}_l := \{0\} \times (0, 1), \end{cases}$$

$$\boldsymbol{b}(\lambda) = \boldsymbol{0} \quad \text{on } \Omega,$$

for $\lambda \in \mathbb{R}$. Then

$$\bar{\lambda}_p = 2 \text{ for all } p \in [1, \infty], \tag{7-21}$$

$$\lambda_q = \begin{cases} 2 & \text{if } q \in [1, 2), \\ 1 & \text{if } q \in [2, \infty]. \end{cases} \tag{7-22}$$

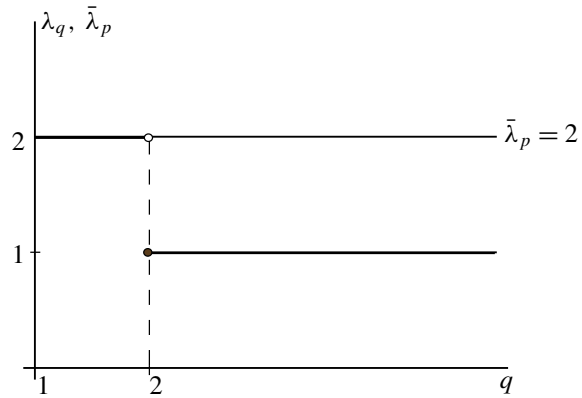

Lemma 7.13. *For any* $\lambda \in \mathbb{R}$, *let* $\boldsymbol{T}(\lambda) : \Omega \to \operatorname{Sym}$ *be defined by*

$$\boldsymbol{T}(\lambda)(\boldsymbol{r}) = \begin{cases} (1-\lambda)\boldsymbol{r} \otimes \boldsymbol{r}/y^3 & \text{if } \boldsymbol{r} \in \Omega^+ := \{\boldsymbol{r} \in \Omega : y/x > 1\}, \\ (\lambda/2 - 1)(\boldsymbol{i} + \boldsymbol{j}) \otimes (\boldsymbol{i} + \boldsymbol{j}) & \text{if } \boldsymbol{r} \in \Omega^- := \{\boldsymbol{r} \in \Omega : y/x < 1\}. \end{cases}$$

Then $\boldsymbol{T}(\lambda)$ *equilibrates the loads in the sense that*

$$(\boldsymbol{T}(\lambda), \boldsymbol{v}) = \langle \boldsymbol{l}(\lambda), \boldsymbol{v} \rangle \tag{7-23}$$

for each $\boldsymbol{v}$ *from the set*

$$M := \{\boldsymbol{v} \in C^1(\operatorname{cl}\Omega, \mathbb{R}^2) : \boldsymbol{v} = \boldsymbol{0} \text{ near } \mathscr{D}\};$$

moreover,

$$\left.\begin{array}{ll} \boldsymbol{T}(\lambda) \in L^q(\Omega, \operatorname{Sym}) & \text{for all } q \in [1, 2) \text{ and all } \lambda \in \mathbb{R}, \\ \boldsymbol{T}(1) \in L^q(\Omega, \operatorname{Sym}) & \text{for all } q \in [1, \infty], \\ \boldsymbol{T}(\lambda) \notin L^q(\Omega^+, \operatorname{Sym}) & \text{for all } q \in [2, \infty] \text{ and all } \lambda \in \mathbb{R}, \lambda \neq 1, \end{array}\right\} \tag{7-24}$$

and

$$\boldsymbol{T}(\lambda) \le \mathbf{0} \quad \mathscr{L}^2\text{-almost everywhere on } \Omega \quad \Longleftrightarrow \quad 1 \le \lambda \le 2. \tag{7-25}$$

Proof. One finds that (a) $\boldsymbol{T}(\lambda)$ can be continuously extended to $\partial\Omega^+ \setminus \{\mathbf{0}\}$ and also to $\partial\Omega^-$; (b) $\boldsymbol{T}(\lambda)$ satisfies the boundary condition

$$\boldsymbol{T}(\lambda)\boldsymbol{n} = \boldsymbol{s}(\lambda) \quad \text{on } \mathscr{S} \setminus \{\mathbf{0}\},$$

in the classical sense; (c) $\boldsymbol{T}(\lambda)$ is discontinuous across the segment $\mathfrak{l} := \{\boldsymbol{r} \in \Omega : y = x\}$, but the normal component of $\boldsymbol{T}(\lambda)$ is continuous across $\mathfrak{l}$; (d) $\boldsymbol{T}(\lambda)$ is of class ∞ on Ω^+ and Ω^- with the classical divergence vanishing on each of these two regions:

$$\operatorname{div} \boldsymbol{T}(\lambda) = \mathbf{0} \quad \text{on } \Omega^{\pm}.$$

If $\boldsymbol{v} \in M$ then there exists an $\epsilon > 0$ such that $\boldsymbol{v}$ vanishes on the line segment $\{\boldsymbol{r} \in \Omega : y = \epsilon\}$. Applying of the classical divergence theorem to $\Omega^+_\epsilon = \{\boldsymbol{r} \in \Omega^+ : y > \epsilon\}$ and $\Omega^-_\epsilon = \{\boldsymbol{r} \in \Omega^- : y > \epsilon\}$ separately (using of the properties (a)–(d)), and adding the results gives (7-23).

To prove the properties (7-24), we note that $\boldsymbol{T}(\lambda)$ is bounded on Ω^- while $\boldsymbol{T}(\lambda)$ has a singularity on Ω^+ at $\mathbf{0}$. Thus we have $\boldsymbol{T}(\lambda) \in L^q(\Omega, \mathrm{Sym})$ if and only if $\boldsymbol{T}(\lambda) \in L^q(\Omega^+, \mathrm{Sym})$. We have

$$|1 - \lambda|/y \le |\boldsymbol{T}(\lambda)(\boldsymbol{r})| \le \sqrt{2}|1 - \lambda|/y$$

for each $\boldsymbol{r} \in \Omega^+$. Thus

$$|1 - \lambda|^q I_q \le \int_{\Omega^+} |\boldsymbol{T}(\lambda)|^q \, d\mathscr{L}^2 \le (\sqrt{2})^q |1 - \lambda|^q I_q$$

where

$$I_q = \int_{\Omega^+} y^{-q} \, d\mathscr{L}^2.$$

One has $I_q < \infty$ if and only if $q \in [1, 2)$ and (7-24) follows.

Assertion (7-25) is immediate. □

Lemma 7.14. *All λ satisfying $1 \le \lambda < 2$ are W_p-kinematically inadmissible for all $p \in [1, \infty]$, and every $\lambda \in (2, 7)$ is W_p-kinematically admissible. In particular, we have (7-21).*

Proof. Let $1 \le \lambda < 2$. By (7-23) and (7-25) we have

$$0 \ge (\boldsymbol{T}(\lambda), \hat{\boldsymbol{E}}(\boldsymbol{v})) = \langle \boldsymbol{l}(\lambda), \boldsymbol{v} \rangle$$

for all $\boldsymbol{v} \in M^+ := \{\boldsymbol{v} \in M : \hat{\boldsymbol{E}}(\boldsymbol{v}) \ge \mathbf{0} \text{ on } \operatorname{cl}\Omega\}$. The continuity of the loads on W_p for every $p \in [1, \infty]$ and the density of M^+ in W^+_p (Proposition 7.5(a)) then imply that the inequality $\langle \boldsymbol{l}(\lambda), \boldsymbol{v} \rangle \le 0$ can be extended to W^+_p, i.e., we have $\langle \boldsymbol{l}(\lambda), \boldsymbol{v} \rangle \le 0$ for all $\boldsymbol{v} \in W^+_p$, and all $\lambda \in [1, 2)$. This implies that no $\lambda \in [1, 2)$ is kinematically admissible, as we now show. Indeed, one easily verifies from the definition that if $\lambda \in \mathbb{R}$ is kinematically admissible then for every $\mu > \lambda$ there exists a $\boldsymbol{v} \in W^+_p$ such that $\langle \boldsymbol{l}(\mu), \boldsymbol{v} \rangle > 0$. Thus the hypothesis that some $\lambda \in [1, 2)$ is kinematically admissible would imply that for every $\mu > \lambda$ there is a $\boldsymbol{v} \in W^+_p$ such that $\langle \boldsymbol{l}(\mu), \boldsymbol{v} \rangle > 0$. However, we have shown that $\langle \boldsymbol{l}(\lambda), \boldsymbol{v} \rangle \le 0$ for all $\boldsymbol{v} \in W^+_p$, and all $\lambda \in [1, 2)$; in particular $\langle \boldsymbol{l}(\mu), \boldsymbol{v} \rangle \le 0$ for all $\boldsymbol{v} \in W^+_p$, and all $\mu \in (\lambda, 2)$. Thus λ cannot be kinematically admissible.

Next we prove that every $\lambda \in (2, 7)$ is W_p-kinematically admissible for every $p \in [1, \infty]$ by exhibiting a mechanism corresponding to λ which is in all W_p. Let s be a number satisfying $0 < s < 1$, put

$$\boldsymbol{m} = (1, s),$$

denote by Ω_s the set

$$\Omega_s = \{\boldsymbol{r} : y \geq 1 - sx\},$$

and define $\boldsymbol{v}_s$ by

$$\boldsymbol{v}_s(\boldsymbol{r}) = \begin{cases} (\boldsymbol{r} \cdot \boldsymbol{m} - 1)\boldsymbol{m} & \text{if } \boldsymbol{r} \in \Omega_s, \\ \boldsymbol{0} & \text{if } \boldsymbol{r} \in \Omega \setminus \Omega_s. \end{cases}$$

Then $\boldsymbol{v}_s \in W_p^+$ for all $p \in [1, \infty]$ with

$$\hat{\boldsymbol{E}}(\boldsymbol{v}_s) = \begin{cases} \boldsymbol{m} \otimes \boldsymbol{m} & \text{on } \Omega_s, \\ \boldsymbol{0} & \text{on } \Omega \setminus \Omega_s. \end{cases}$$

Calculations give

$$\begin{aligned} \langle \boldsymbol{l}(\lambda), \boldsymbol{v}_s \rangle &= \tfrac{1}{6}\big((-2s^3 - 3s^2 + 3 + 3s)\lambda + 2s^3 + 3s^2 - 6s - 6\big), \\ \langle \boldsymbol{l}_\circ, \boldsymbol{v}_s \rangle &= \tfrac{1}{6}(-2s^3 - 3s^2 + 3 + 3s). \end{aligned}$$

If $s \in (0, 1)$ then one finds that

$$\langle \boldsymbol{l}(\lambda_s), \boldsymbol{v}_s \rangle = 0$$

for

$$\lambda_s = \frac{2s^3 + 3s^2 - 6s - 6}{2s^3 + 3s^2 - 3s - 3}.$$

The function $s \mapsto \lambda_s$ is increasing and maps the interval $(0, 1)$ onto the interval $(2, 7)$, as one easily finds. Moreover,

$$\langle \boldsymbol{l}_\circ, \boldsymbol{v}_s \rangle > 0$$

for all $s \in (0, 1)$. It therefore follows that for every $\lambda \in (2, 7)$ there exist a s_λ such that $\boldsymbol{v}_{s_\lambda}$ is a mechanism corresponding to λ. This proves that every $\lambda \in (2, 7)$ is kinematically admissible. □

Remark 7.15. The proof of Lemma 7.14 shows that if $1 \leq \lambda \leq 2$ and $p \in [1, \infty]$ then $\langle \boldsymbol{l}(\lambda), \boldsymbol{v} \rangle \leq 0$ for each $\boldsymbol{v} \in W_p^+$. Despite of this, for $q \in [2, \infty]$ the multiplier λ is not statically admissible, which shows that the condition that $\langle \boldsymbol{l}(\lambda), \boldsymbol{v} \rangle \leq 0$ for each $\boldsymbol{v} \in W_p^+$ is only necessary, but not sufficient for the static admissibility. Cf. the discussion following Proposition 2.8.

Lemma 7.16. *A $\lambda \in \mathbb{R}$ is $L^q(\Omega, \mathrm{Sym})$-statically admissible if and only if*

$$\lambda \in \Lambda_q := \begin{cases} [1, 2] & \text{if } 1 \leq p < 2, \\ \{1\} & \text{if } 2 \leq p \leq \infty. \end{cases}$$

In particular, we have (7-22).

Proof. All $\lambda < 1$ are $L^q(\Omega, \mathrm{Sym})$-statically inadmissible for all $q \in [1, \infty]$. Indeed, if they were to be statically admissible, then we would have $\boldsymbol{s}(\lambda) \cdot \boldsymbol{n} \le 0$ on $\mathcal{S}_t$ by [Lucchesi et al. 2010, Proposition 2.1(i)], where $\boldsymbol{n}$ is the outer normal to Ω on $\mathcal{S}_t$, while we have $\boldsymbol{s}(\lambda) \cdot \boldsymbol{n} > 0$ everywhere on $\mathcal{S}_t$ for $\lambda < 1$.

Further, $\lambda = 1$ is $L^q(\Omega, \mathrm{Sym})$-statically admissible for all $q \in [1, \infty]$. Indeed, the stress field $\boldsymbol{T}(1)$ is bounded on Ω, is admissible, and equilibrates the loads $\boldsymbol{l}(1)$.

If $1 \le q < 2$, then every $\lambda \in [1, 2]$ is $L^q(\Omega, \mathrm{Sym})$-statically admissible. Indeed, the stress field $\boldsymbol{T}(\lambda)$ is admissible, is in $L^q(\Omega, \mathrm{Sym})$, and equilibrates the loads in the sense that (7-23) holds for every $\boldsymbol{v} \in W_p$ where p is the Hölder conjugate of q. This is proved by using (7-23) for $\boldsymbol{v} \in M$ and applying the density of M in W_p (Proposition 7.4) and the continuity of loads on W_p.

If $2 \le q \le \infty$, then every $\lambda \in (1, 2)$ is $L^q(\Omega, \mathrm{Sym})$ statically inadmissible. Let $1 < \lambda \le 2$ and prove that there is no admissible stress field in $L^q(\Omega, \mathrm{Sym})$ equilibrating the loads $\boldsymbol{l}(\lambda)$. Assume, on the contrary, that $\boldsymbol{T}$ is an admissible stress field equilibrating the loads. If $\omega : \mathbb{R} \to \mathbb{R}$ is any nonincreasing C^1 function vanishing on $(1, \infty)$ and with $\omega' < 0$ on $(0, 1)$, let $\boldsymbol{v} : \Omega \to \mathbb{R}^2$, defined by (7-17). As in the proof of Lemma 7.9, we have $\boldsymbol{v} \in W_p^+$. Furthermore, one finds that

$$\langle \boldsymbol{l}(\lambda), \boldsymbol{v} \rangle = 0.$$

From $\langle \boldsymbol{l}(\lambda), \boldsymbol{v} \rangle = (\boldsymbol{T}, \hat{\boldsymbol{E}}(\boldsymbol{v})) = 0$ and $\boldsymbol{T} \le \boldsymbol{0}$, $\hat{\boldsymbol{E}}(\boldsymbol{v}) \ge \boldsymbol{0}$ on Ω we derive that $\boldsymbol{T} \cdot \hat{\boldsymbol{E}}(\boldsymbol{v}) = 0$ for $\mathscr{L}^2$ a.e. point of Ω. We have $\omega'(x/y) \ne 0$ for every point of Ω^+. Then $\boldsymbol{T}(\boldsymbol{r}) \cdot (\boldsymbol{r}^\perp \otimes \boldsymbol{r}^\perp) = 0$ for a.e. point of Ω^+ and must be proportional to $\boldsymbol{r} \otimes \boldsymbol{r}$ and hence we write

$$\boldsymbol{T}(\boldsymbol{r}) = \eta(\boldsymbol{r}) \boldsymbol{r} \otimes \boldsymbol{r} / y^3$$

for $\mathscr{L}^2$ a.e. $\boldsymbol{r} = (x, y) \in \Omega^+$ where $\eta : \Omega^+ \to \mathbb{R}$ is a $\mathscr{L}^2$ measurable function.

As in [Lucchesi et al. 2010, proof of Example 2.4], we deduce from $\operatorname{div} \boldsymbol{T} = \boldsymbol{0}$ in Ω^+ and $\boldsymbol{T}\boldsymbol{n} = \boldsymbol{s}(\lambda)$ on $\mathcal{S}_t$ that

$$\boldsymbol{T}(\boldsymbol{r}) = \boldsymbol{T}(\lambda) \quad \text{on } \Omega^+ . \tag{7-26}$$

Indeed, the equation $\operatorname{div} \boldsymbol{T} = \boldsymbol{0}$ gives $\boldsymbol{r}(\boldsymbol{r} \cdot \nabla \eta) + 3\boldsymbol{r}\eta = \boldsymbol{0}$ which gives

$$\boldsymbol{r} \cdot \nabla \eta + 3\eta = 0.$$

The substitution $\eta = \hat{\eta}/y^3$ then provides

$$\boldsymbol{r} \cdot \nabla \hat{\eta} = 0.$$

Thus the directional derivative of $\hat{\eta}$ along any segment $\{\boldsymbol{r} \in \Omega^+ : \boldsymbol{r} = c\boldsymbol{d}, 0 < c < d\}$ is constant for any $\boldsymbol{d} \in \mathcal{S}_t$. The segment is completely characterized by the slope y/x and thus there exists a function $\tilde{\eta}$ on $(1, \infty)$ such that $\hat{\eta}(\boldsymbol{r}) = \tilde{\eta}(y/x)$ for every $\boldsymbol{r} \in \Omega^+$. Thus

$$\boldsymbol{T}(\lambda)(\boldsymbol{r}) = \tilde{\eta}(y/x) \boldsymbol{r} \otimes \boldsymbol{r} / y^3 \quad \text{on } \Omega^+.$$

The boundary condition $\boldsymbol{T}\boldsymbol{n} = \boldsymbol{s}(\lambda)$ on $\mathcal{S}_t$ then leads to $\tilde{\eta}(\boldsymbol{d}) = (\lambda - 1)$ for any $\boldsymbol{d} \in \mathcal{S}_t$ and we obtain finally (7-26). The argument above applies to the case when $\boldsymbol{T}$ is continuously differentiable. The general argument in case $\boldsymbol{T}$ is only measurable is given in [Lucchesi et al. 2010, proof of Example 2.4]. This part of the proof is omitted.

To complete the proof, we note that $\boldsymbol{T}(\lambda) \notin L^q(\Omega^+, \mathrm{Sym})$ and thus we arrive at a contradiction: Starting from arbitrary balancing stress field in $L^q(\Omega, \mathrm{Sym})$ we obtain that $\boldsymbol{T} \notin L^q(\Omega, \mathrm{Sym})$. Thus λ is not $L^q(\Omega, \mathrm{Sym})$-statically admissible. □

8. Summary

(i) A decreasing continuous sequence of function spaces

$$W_{BD} \supset \cdots \supset W_{p_1} \supset W_{p_2} \supset \cdots \supset W_\infty \supset C_1$$

($1 \le p_1 < p_2 < \infty$) has been presented. The kinematic problem with this decreasing sequence is more and more restrictive in the competitors space which results in apriori inequalities for the corresponding critical multipliers of the kinematic problems

$$\bar{\lambda}_{BD} \le \bar{\lambda}_{p_1} \le \bar{\lambda}_{p_2} \le \cdots \le \bar{\lambda}_\infty \le \bar{\lambda}_\circ. \tag{8-1}$$

Density conditions have been given which guarantee that the sequence (8-1) is constant.

(ii) A continuous sequence of function spaces $C^0(\mathrm{cl}\,\Omega, \mathrm{Sym})$, $L^q(\Omega, \mathrm{Sym})$, X_{ba}, $X_{\mathscr{M}}$ for static problems has been given. This sequence is better wieved as *increasing* if the parameter q is *decreasing*:

$$C^0(\mathrm{cl}\,\Omega, \mathrm{Sym}) \subset \cdots \subset L^{q_1}(\Omega, \mathrm{Sym}) \subset L^{q_2}(\Omega, \mathrm{Sym}) \subset \cdots \subset X_{\mathrm{ba}} \subset X_{\mathscr{M}} \tag{8-2}$$

($\infty \ge q_1 > q_2 > 1$). (With this way of ordering of the set of all q's, we can consider q_1 and q_2 as the Hölder conjugates of p_1 and p_2 above, respectively.) The static problem with the sequence (8-2) admits wider and wider competitors space which results in apriori inequalities for the corresponding critical multipliers of the static problems

$$\lambda_\circ \le \cdots \le \lambda_{q_1} \le \lambda_{q_2} \le \cdots \le \lambda_{\mathrm{ba}} \le \lambda_{\mathscr{M}}. \tag{8-3}$$

In the case of the choice of the spaces W_∞ or C_1 in the kinematic problem, the set of all admissible stresses has to be enlarged to contain stresses represented by either finitely or countably additive tensor-valued measures. No condition is currently available to the authors that would guarantee that the sequence (8-3) is constant. We also note in passing that all the multipliers in (8-1) and (8-3) coincide if

$$\lambda_\circ = \bar{\lambda}_\circ \tag{8-4}$$

that is, if the supremum of the statically admissible multipliers over the continuous stress fields coincides with the infimum of the kinematically admissible multipliers over the smooth displacement fields. In this case, the critical multipliers become independent of the choice of the function spaces. However, we do not know any condition guaranteeing (8-4).

(iii) A necessary and sufficient condition has been given under which the supremum of statically admissible multipliers equals the infimum of kinematically admissible multipliers. Two sufficient conditions for the last equality have been given. A simple sufficient condition involves the assumption of the existence of the strong mechanism. An example is given to show that this is not always satisfied, even with very regular loads.

(iv) An example has been given of loads in which the function $q \mapsto \lambda_q$ ($\infty \ge q > 1$) has an increasing jump at $q = 2$ as q moves along $[1, \infty]$ *from right to left.* Moreover, $\lambda_q < \bar{\lambda}_p$ for $q \in [1, 2)$.

The above shows that the limit analysis problems are sensitive to the choice of function spaces.

Appendix: Notation for function spaces

We here describe briefly and somewhat informally the function spaces used in the main text. All spaces below are Banach spaces but we do not specify the corresponding norms.

If Z is a finite dimensional real inner product space and $1 \le p \le \infty$ then $L^p(\Omega, Z)$ is the set of all Lebesgue measurable functions $\beta : \Omega \to Z$ such that

$$\begin{cases} \int_\Omega |\beta|^p \, d\mathscr{L}^n < \infty & \text{if } p < \infty, \\ \operatorname{ess\,sup}\{|\beta(\boldsymbol{x})| : \boldsymbol{x} \in \Omega\} < \infty & \text{if } p = \infty. \end{cases}$$

The spaces $L^p(\mathscr{S}, Z)$ are defined analogously, with the Lebesgue measure replaced by the Hausdorff measure $\mathscr{H}^{n-1}$. See, e.g., [Fonseca and Leoni 2007, Chapter 2] for the scalar-valued case. In the general case the space Z is isometrically isomorphic to $\mathbb{R}^k$ for a suitable k, and one employs the procedures of the scalar case to components. The same applies also to the other objects with values in Z, $\mathbb{R}^n$ or Sym to be considered below, without mentioning it. (The references we give below deal exclusively with the scalar case.)

If $1 \le p \le \infty$ then $W^{1,p}(\Omega, \mathbb{R}^n)$ denotes the Sobolev space of all $\boldsymbol{v} : \Omega \to \mathbb{R}^n$ such that $\boldsymbol{v} \in L^p(\Omega, \mathbb{R}^n)$ and $\nabla \boldsymbol{v} \in L^p(\Omega, \mathrm{Lin})$. See e.g., [Adams and Fournier 2003, Chapter 3].

If Z is as above and A a Borel subset of $\operatorname{cl}\Omega$ then $\mathscr{M}(A, Z)$ denotes the space of all countably additive Z-valued measures, i.e., functions $\mu : \mathfrak{B} \to Z$, where $\mathfrak{B}$ is the set of all Borel subsets of $\mathbb{R}^n$, such that

$$\mu\Big(\bigcup_{i=1}^{\infty} B_i\Big) = \sum_{i=1}^{\infty} \mu(B_i)$$

for each disjoint sequence of Borel subsets of $\mathbb{R}^n$, and

$$\mu(B) = 0$$

if B is a Borel subset of $\mathbb{R}^n$ such that $A \cap B = \varnothing$. The elements $\mu \in \mathscr{M}(A, Z)$ are called Z-valued countably additive measures on A. See, e.g., [Fonseca and Leoni 2007, Section 1.3.1]. Furthermore, if μ stands for the Lebesgue measure in $\mathbb{R}^n$ or for the $n-1$ dimensional Hausdorff measure and A is a μ measurable subset of $\mathbb{R}^n$, then $\mu \llcorner A$ denotes the restriction of μ to A, defined as the measure on $\mathbb{R}^n$ by

$$(\mu \llcorner A)(B) = \mu(A \cap B)$$

for every μ measurable set B. In this context, if β is a $\mu \llcorner A$ integrable function with values in Z then $\beta\mu \llcorner A$ denote the multiple of $\mu \llcorner A$ by β, defined as an element of $\mathscr{M}(A, Z)$, by

$$(\beta\mu \llcorner A)(B) = \int_{A \cap B} \beta \, d\mu$$

for all μ measurable sets B.

The space $\mathrm{ba}(\Omega, \mathfrak{M}, \mathscr{L}^n; \mathrm{Sym})$ of bounded finitely additive Sym-valued measures that are absolutely continuous with respect to the Lebesgue measure is the set of all $\mathfrak{T} : \mathfrak{M} \to \mathrm{Sym}$, where $\mathfrak{M}$ is the system of all Lebesgue measurable subsets of $\mathbb{R}^n$, such that

(a) $\mathfrak{T}(A \cup B) = \mathfrak{T}(A) + \mathfrak{T}(B)$ for every $A, B \in \mathfrak{M}$ with $A \cap B = \varnothing$;

(b) $\sup\left\{\sum_{i=1}^{j} |\mathfrak{T}(A_i)| : \{A_i\} \subset \mathfrak{M} \text{ is a finite partition of } \mathbb{R}^n\right\} < \infty$;

(c) $\mathfrak{T}(A) = \mathbf{0}$ for each $A \in \mathfrak{M}$ with $\mathscr{L}^n(A) = 0$;

(d) $\mathfrak{T}(A) = \mathbf{0}$ for each $A \in \mathfrak{M}$ with $A \cap \Omega = \varnothing$.

See, e.g., [Fonseca and Leoni 2007, pp. 169–171].

$BD(\Omega)$ is the set of all $\boldsymbol{v} \in L^1(\Omega, \mathbb{R}^n)$ such that $\hat{\boldsymbol{E}}(\boldsymbol{v})$, interpreted as a distribution, is in $\mathscr{M}(\Omega, \mathrm{Sym})$. See [Témam 1983, Chapter II].

$C^1(\mathrm{cl}\,\Omega, \mathbb{R}^n)$ is the set of all continuously differentiable functions $\boldsymbol{v} : \Omega \to \mathbb{R}^n$ such that both $\boldsymbol{v}$ and $\nabla \boldsymbol{v}$ have continuous extensions from Ω to the closure $\mathrm{cl}\,\Omega$ of Ω. We often identify $\boldsymbol{v}$ and $\nabla \boldsymbol{v}$ with these extensions.

$C^0(\mathrm{cl}\,\Omega, \mathrm{Sym})$ is the space of all continuous functions $\boldsymbol{F} : \mathrm{cl}\,\Omega \to \mathrm{Sym}$. See, e.g., [Fonseca and Leoni 2007, p. 126].

Acknowledgment

We thank the anonymous referee for many valuable remarks and suggestions.

References

[Adams and Fournier 2003] R. A. Adams and J. J. F. Fournier, *Sobolev spaces*, 2nd ed., Pure and Applied Mathematics **140**, Elsevier/Academic Press, Amsterdam, 2003.

[Anzellotti 1983] G. Anzellotti, "Pairings between measures and bounded functions and compensated compactness", *Ann. Mat. Pura Appl.* (4) **135** (1983), 293–318.

[Anzellotti 1985] G. Anzellotti, "A class of convex noncoercive functionals and masonry-like materials", *Ann. Inst. H. Poincaré Anal. Non Linéaire* **2**:4 (1985), 261–307.

[Dal Maso et al. 2007] G. Dal Maso, A. Demyanov, and A. DeSimone, "Quasistatic evolution problems for pressure-sensitive plastic materials", *Milan J. Math.* **75** (2007), 117–134.

[Del Piero 1989] G. Del Piero, "Constitutive equation and compatibility of the external loads for linear elastic masonry-like materials", *Meccanica* (*Milano*) **24**:3 (1989), 150–162.

[Del Piero 1998] G. Del Piero, "Limit analysis and no-tension materials", *Int. J. Plast.* **14** (1998), 259–271.

[Di Pasquale 1992] S. Di Pasquale, "New trends in the analysis of masonry structures", *Meccanica* (*Milano*) **27** (1992), 173–184.

[Ekeland and Témam 1999] I. Ekeland and R. Témam, *Convex analysis and variational problems*, Classics in Applied Mathematics **28**, Society for Industrial and Applied Mathematics, Philadelphia, 1999.

[Evans and Gariepy 1992] L. C. Evans and R. F. Gariepy, *Measure theory and fine properties of functions*, CRC Press, Boca Raton, FL, 1992.

[Fonseca and Leoni 2007] I. Fonseca and G. Leoni, *Modern methods in the calculus of variations: L^p spaces*, Springer, New York, 2007.

[Giaquinta and Giusti 1985] M. Giaquinta and E. Giusti, "Researches on the equilibrium of masonry structures", *Arch. Ration. Mech. Anal.* **88**:4 (1985), 359–392.

[Gurtin 1981] M. E. Gurtin, *An introduction to continuum mechanics*, Mathematics in Science and Engineering **158**, Academic Press, New York, 1981.

[Kohn and Témam 1983] R. Kohn and R. Témam, "Dual spaces of stresses and strains, with applications to Hencky plasticity", *Appl. Math. Optim.* **10**:1 (1983), 1–35.

[Lucchesi and Zani 2003] M. Lucchesi and N. Zani, "Some explicit solutions to plane equilibrium problem for no-tension bodies", *Struct. Eng. Mech.* **16**:3 (2003), 295–316.

[Lucchesi et al. 2006] M. Lucchesi, M. Šilhavý, and N. Zani, "A new class of equilibrated stress fields for no–tension bodies", *J. Mech. Mater. Struct.* **1** (2006), 503–539.

[Lucchesi et al. 2008a] M. Lucchesi, C. Padovani, G. Pasquinelli, and N. Zani, *Masonry constructions: mechanical models and numerical applications*, Springer, Berlin, 2008.

[Lucchesi et al. 2008b] M. Lucchesi, M. Šilhavý, and N. Zani, "Integration of measures and admissible stress fields for masonry bodies", *J. Mech. Mater. Struct.* **3** (2008), 675–696.

[Lucchesi et al. 2010] M. Lucchesi, C. Padovani, and M. Šilhavý, "An energetic view on the limit analysis of normal bodies", *Quart. Appl. Math.* **68**:4 (2010), 713–746.

[Lucchesi et al. 2011] M. Lucchesi, M. Šilhavý, and N. Zani, "Integration of parametric measures and the statics of masonry panels", *Ann. Solid Struct. Mech.* **2** (2011), 33–44.

[Padovani et al. 2008] C. Padovani, G. Pasquinelli, and M. Šilhavý, "Processes in masonry bodies and the dynamical significance of collapse", *Math. Mech. Solids* **13**:7 (2008), 573–610.

[Paroni 2012] R. Paroni, "An existence theorem for inextensible nets with slack", *Math. Mech. Solids* **17** (2012), 460–472.

[Rockafellar 1970] R. T. Rockafellar, *Convex analysis*, Princeton Mathematical Series **28**, Princeton Univ. Press, Princeton, NJ, 1970.

[Šilhavý 2008] M. Šilhavý, "Cauchy's stress theorem for stresses represented by measures", *Contin. Mech. Therm.* **20**:2 (2008), 75–96.

[Témam 1977] R. Témam, *Navier–Stokes equations: theory and numerical analysis*, Studies in Math. and its Applications **2**, North-Holland, Amsterdam, 1977.

[Témam 1983] R. Témam, *Problèmes mathématiques en plasticité*, Méthodes Mathématiques de l'Informatique **12**, Gauthier-Villars, Montrouge, 1983.

[Témam and Strang 1980] R. Témam and G. Strang, "Duality and relaxation in the variational problems of plasticity", *J. Méc.* **19**:3 (1980), 493–527.

Received 1 Jun 2012. Revised 27 Sep 2012. Accepted 4 Oct 2012.

MASSIMILIANO LUCCHESI: massimiliano.lucchesi@unifi.it
Dipartimento di Ingegneria Civile e Ambientale, Università di Firenze, Piazza Brunelleschi 6, I-50121 Firenze, Italy

MIROSLAV ŠILHAVÝ: silhavy@math.cas.cz
Institute of Mathematics, Academy of Sciences of the Czech Republic, Žitná 25, 115 67 Praha 1, Czech Republic

NICOLA ZANI: nicola.zani@unifi.it
Dipartimento di Ingegneria Civile e Ambientale, Università di Firenze, Piazza Brunelleschi 6, I-50121 Firenze, Italy

JOURNAL OF MECHANICS OF MATERIALS AND STRUCTURES
Vol. 7, No. 8-9, 2012
dx.doi.org/10.2140/jomms.2012.7.837

EDGE STIFFNESS EFFECTS ON THIN-FILM LAMINATED DOUBLE GLAZING SYSTEM DYNAMICAL BEHAVIOR BY THE OPERATIONAL MODAL ANALYSIS

ALI AKROUT, MARIEM MILADI CHAABANE, LOTFI HAMMAMI AND MOHAMED HADDAR

We apply operational modal analysis (OMA) to determine the eigenfrequencies and the eigenmode shapes of a thin-film laminated double glazing system. For this purpose, the dynamic behaviors of both a laminate alone and a coupled system (double-wall structure) for specific boundary conditions are investigated. Here, the laminated plate which is composed of two elastic skins joined with an adhesive ultra-thin film is bonded by an elastic joint. Thus, two configurations of the thin-film laminated glass plate elastic boundary conditions are considered. The first one assumes that the structure is bonded by a translational stiffness (linear springs). In the second one, besides the translational stiffness, a rotational stiffness (angular springs) is introduced in order to improve the developed model. The modal recombination results of a thin-film laminated glass plate as well as those of the thin-film laminated double glazing system are presented and compared to the estimated modes achieved by OMA. Since a good agreement is obtained, the OMA technique can be used to determine the modal parameters by considering the experimental vibratory responses of the studied system. In addition, the vibration's amplitude of two laminated glass plates linked from edge to edge with both linear and angular springs can be much reduced compared to the one of the same structure bonded only by linear springs.

1. Introduction

In recent years, several structural damping calculations have been carried out in order to control vibration amplitudes and sound transmissions through windows. Thus, as presented in works such as [Antonio et al. 2003] and [Cheng et al. 2005], double panel systems offers improved vibro-acoustic behaviors and can be used in building constructions, medication equipments, automobiles and aeronautical industries. In fact, to calculate the dynamic responses of a fluid-structure coupled problem, some mathematical models can be mixed. In this context, Bouhioui [1993] combined a finite element model with an integral equation formulation in order to determine the sound transmission loss through an elastic double glazing system. This model is recently improved by Basten et al. [2001] who developed an acousto-elastic model for a double elastic panel in which the viscothermal fluid cavity effects are taken into account. Besides, in [Akrout et al. 2008b; 2009; 2010], a structural damping model of simple and laminated plates is coupled to the viscothermal fluid model developed by Basten et al. in order to obtain a new configuration of fluid-structure coupled system. In this case, the classical modal analysis is mixed with an iterative procedure in order to calculate the vibro-acoustic modes.

Furthermore, the lamination effects give more damping to a considered vibrating panel excited by mechanical force and/or acoustical pressure; see for example [Zenkert 1995; Reddy 1997; Khdeir and

Keywords: thin-film laminated double glazing, rotational stiffness, translational stiffness, operational modal analysis, blind source separation, eigenmodes.

Reddy 1999; Carrera 2004]. In this context, Assaf [1991] analyzed the dynamic effects of a viscoelastic core on standard sandwich plate vibratory behavior by taking into account essentially the shearing work in the core and the coupling between membranous and bending effects. In the same context, Abdennadher et al. [2005b] developed a dynamic model in order to characterize the modal damping induced by a double sandwich panels. Recently, Akrout et al. [2008a] showed that the lamination process based on ultra-thin film at the skin's interface let's to provide reduced plate's deflection amplitudes. Additionally, stiffness boundary conditions have considerable effects on dynamic responses of plates. In fact, the study of a double panel system dynamic behavior for various boundary conditions have been carried out by many researchers; see for example [Abbès et al. 2011; Abdennadher et al. 2005a]. Then, if a damping and/or a stiffness of plate edge is considered, the vibro-acoustic responses amplitude can be much reduced. For this purpose, Park et al. [2003] examined the effect of viscoelastic supports at the level of plate's edges. It has been shown that the plate's velocity and the sound energy are effectively affected by the damping on the level of the edges inducing reduced vibration amplitudes. Also, Vallaban et al. [1997] considered a structural joint at the level of a glass panel edges. It has been concluded that the dynamic behavior of the plate-joint can be improved by increasing the stress in the joint produced by the shearing forces on the level of the edges.

As a resolution method, we can use especially the Operational Modal Analysis (OMA) formulation which has been previously established by many researchers in neuroscience and signal processing; see for example [Hérault and Ans 1984; 1985; Nguyen et al. 1994]. In this context, independent component analysis, one of the major techniques of the BSS method, can be exploited in order to solve BSS problems in the case of linear or nonlinear convolutive mixtures as presented in [Zarzoso and Comon 2008; Antoni et al. 2004; 2005]. This method needs to know only the sensor's measurement or the FE vibratory responses in order to estimate the eigenfrequencies of a studied structure. It's defined by a separation procedure applied on independent linear mixture signal by using only the measured vibratory response of the system. Poncelet et al. [2007] used ICA in order to exploit the virtual source theory by studying an output-only modal analysis. Kerschen et al. [2007] used the modal assurance criterion to establish the relation between exact and estimated modes. In this work, the OMA method is presented and exploited in order to extract the eigenmodes of a thin-film laminated double glazing system with elastic boundary conditions. In this case, both translational and rotational stiffness are considered at the level of the plate's edges. The model validation is obtained by comparing the exact (numerical) and estimated eigenfrequencies of a thin-film laminated glass plate for two cases of elastic boundary conditions: the first model assumes that the laminated plate is fixed only by a linear springs. In the second one, the same structure is fixed by both linear and angular springs. Moreover, the dynamic responses of each case are presented and discussed. Also, the exact and estimated eigenmodes shapes of a thin-film laminated double glazing system are presented and compared. Thus, the influence of the system's edge stiffness can be analyzed.

2. Mathematical formulation

2.1. ***The OMA method.*** As presented in [Hérault and Ans 1984; 1985; Nguyen et al. 1994], the operational modal analysis (OMA) method is based on independent component analysis (ICA), a recent approach used in signal treatment. We briefly describe the setup. Consider N_s source signals emitted

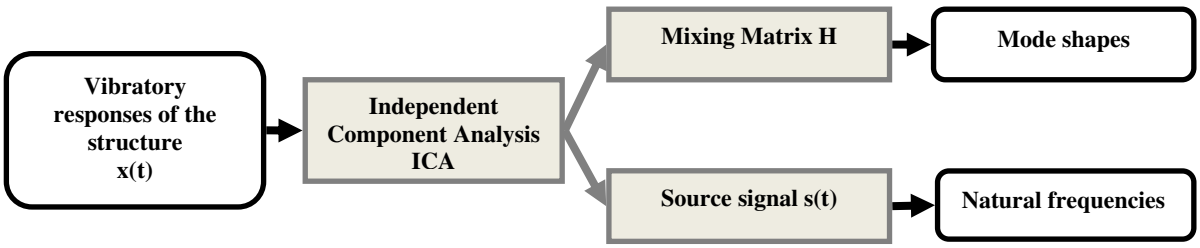

Figure 1. Separation procedure: ICA concept.

through a dynamic system modeled by a mixture matrix of dimension $N_s \times N_c$ and received by N_c sensors. Then, the model equation can be expressed as (see [Abbès et al. 2011; Zarzoso and Comon 2008; Poncelet et al. 2007])

$$x_i = \sum_{j=1}^{N_s} h_{ij} s_j + b_i, \quad i = 1, \ldots, N_c. \tag{1}$$

Equation (1) can be written in matrix form as

$$\{x\} = [H]\{s\} + \{b\}, \tag{2}$$

where $\{x\} = \langle x_1, \ldots, x_{N_c} \rangle^T$ represents the N_c observations vector, $\{s\} = \langle s_1, \ldots, s_{N_s} \rangle^T$ represents the N_s signals sources vector, $[H] = [\{h_1\}, \ldots, \{h_{Ns}\}]$ is the mixture matrix of dimension $N_c \times N_s$, $\{h_j\} = \langle h_{1j}, \ldots, h_{Ncj} \rangle^T$, $j = 1, \ldots, N_s$, is the j-th column vector of the mixture matrix $[H]$, $\{b\}$ is a possible additive noise.

When ICA is applied in OMA, the structure physical responses defined as virtual sources with different spectral contents can be interpreted. In this case, ICA provides the mixing matrix and the modal response of the structure (Figure 1).

The dynamic response of a given mechanical system can be obtained by the modal recombination method as (see [Akrout et al. 2008a; Abbès et al. 2011])

$$\{x\} = [\Psi]\{y\}, \tag{3}$$

where $\{x\}$ is the measured nodal vector, $[\Psi]$ represents the modal matrix and $\{y\}$ is the vector containing the modal responses. Then, by using only the output signal $\{x\}$, OMA is carried out in order to determine the eigenmode shapes existing in the modal matrix $[\Psi]$ and the eigenfrequencies contained in the modal response vector $\{y\}$.

2.2. ***Thin-film laminated plate dynamic model.*** As presented in Figure 2, the kinematical behavior of the laminate is based on the theory that introduce a specific behavior law for an ultra-thin adhesive film of stiffness k_{film} confined at the interface of two skin plies of thicknesses (h_1, h_2) which satisfy for the Kirchhoff plate's theory. In this case, ℓ_x and ℓ_y are the half dimensions of the laminate with respect to directions x and y.

Then, the vibratory behavior of the laminated glass plate is described by both dynamics of skins and the ultra-thin adhesive film.

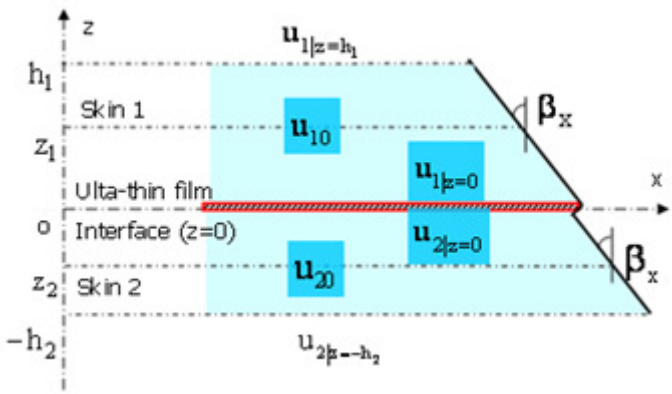

Figure 2. In plane (x, z) thin-film laminate kinematic model.

Consequently, the displacement field in the thin-film laminated glass plate can be expressed as follows [Akrout et al. 2008a]:

$$x\text{-direction}: \begin{cases} u_1 = u_m + \frac{[u_\tau]}{2} + (z - z_m)\beta_x \\ u_2 = u_m - \frac{[u_\tau]}{2} + (z - z_m)\beta_x \end{cases} \tag{4}$$

$$y\text{-direction}: \begin{cases} v_1 = v_m + \frac{[v_\tau]}{2} + (z - z_m)\beta_y \\ v_2 = v_m - \frac{[v_\tau]}{2} + (z - z_m)\beta_y \end{cases} \tag{5}$$

$$z\text{-direction}: w(x, y, z) = w(x, y) \tag{6}$$

The dynamic of the ultra-thin film can be written as a function of the shear interfacial displacements with respect to directions x and y ($[u_\tau] = u_{1|z=0} - u_{2|z=0}$ and $[v_\tau] = v_{1|z=0} - v_{2|z=0}$) as follows:

$$\begin{aligned} \tau_x &= k_{\text{film}}[u_\tau] \\ \tau_y &= k_{\text{film}}[v_\tau] \end{aligned} \tag{7}$$

where (τ_x, τ_y) are the shear interfacial stresses [Akrout et al. 2008a].

Consequently, we can use the stress-strain relations in order to determine the energy functional of the laminate as follows:

$$\vartheta_L = (E_{\text{str.}} + E_{\text{kin.}})_{\text{skins}} + E_{\text{film}} \tag{8}$$

where $(E_{\text{str.}})_{\text{skins}}$, E_{film} and $(E_{\text{kin.}})_{\text{skins}}$ are respectively the skin's strain energy, the film strain energy and the skin's kinetic energy (by neglecting inertial terms of rotations) calculated as follows [Akrout et al.

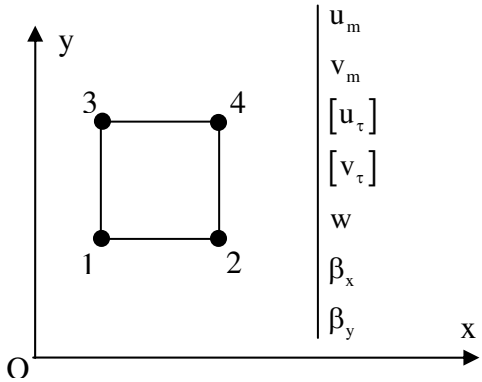

Figure 3. Laminate quadrilateral FE.

2008a]:

$$(E_{\text{str.}})_{\text{skins}} = \frac{1}{2}\int_{\Sigma}\left(\int_{-h_2}^{0}\langle\sigma\rangle_2\{\epsilon\}_2\,dz + \int_{0}^{h_1}\langle\sigma\rangle_1\{\epsilon\}_1\,dz\right)d\Sigma \tag{9}$$

$$E_{\text{film}} = \frac{1}{2}\int_{\Sigma}\langle[u_\tau][v_\tau]\rangle\begin{bmatrix}k_{\text{film}} & 0\\ 0 & k_{\text{film}}\end{bmatrix}\begin{Bmatrix}[u_\tau]\\ [v_\tau]\end{Bmatrix}d\Sigma \tag{10}$$

$$E_{\text{kin.}} = \frac{1}{2}\sum_{i=1}^{2}\int_{\Sigma}\left(\int_{-h_2}^{h_1}\rho_i(\dot{u}_i^2+\dot{v}_i^2+\dot{w}^2)\,dz\right)d\Sigma \tag{11}$$

The homogenous energy functional of the laminated glass plate can be obtained by integrating (9) and (11) with respect to z.

As sketched in Figure 3, the homogenous laminate energy functional is discretized by a four nodes linear quadrilateral finite element (FE). In this case, the laminate nodal vector at node 'i' contain seven degrees of freedom:$\{U\}_{\text{node }'i'} = \langle u_m, v_m, [u_\tau], [v_\tau], w, \beta_x, \beta_y\rangle^T_{\text{node }'i'}$.

The FE discretization of the thin-film laminated plate energy functional gives after minimization the following eigenmodes symmetrical matrix system:

$$([K_L]-\omega^2[M_L])\{U_L\} = \{0\} \tag{12}$$

where $[K_L]$ and $[M_L]$ are respectively the stiffness and mass matrices of the thin-film laminated plate. $\{U_L\}$ is the laminate nodal displacement vector.

2.3. ***Elastic joint model.*** As discussed in [Vallaban et al. 1997; Park et al. 2003; Abbès et al. 2011], the modal characteristics of a given structure (beams or plates) are strongly affected by specified boundary conditions. Then, an elastic joint model can be considered in order to confer better vibratory behavior to the thin-film laminate. So, the dynamic model developed in this work is based on both translational and rotational stiffness modeled by both linear and angular springs at the level of its edge (see Figure 4).

By taking into account the stiffness effects introduced above, the dynamic behavior law of the elastic joint can be defined via the relation between the force and displacements (translation w and rotations

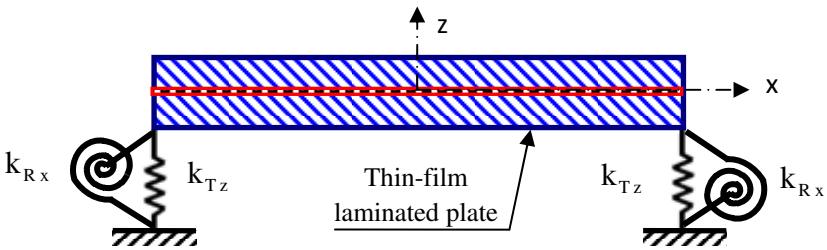

Figure 4. Thin-film laminate elastic boundary conditions.

(β_x, β_y)) at node 'N_i' of the laminate edge as follows:

$$\begin{aligned} F_{Tz\cdot Ni} &= k_{Tz} w_{Ni} \\ F_{Rx\cdot Ni} &= k_{Rx} \beta_{x\cdot Ni} \\ F_{Ry\cdot Ni} &= k_{Ry} \beta_{y\cdot Ni} \end{aligned} \tag{13}$$

Relations (13) can be written in matrix form as follows:

$$\{F_{Ni}\} = [K_{Je}]\{U_{Ni}\} \tag{14}$$

where $\{U_{Ni}\} = \langle w_{Ni} \;\; \beta_{x\cdot Ni} \;\; \beta_{y\cdot Ni} \rangle^T$ is the transversal displacement and deflection rotations vector. $\{F_{Ni}\} = \langle F_{Tz\cdot Ni} \;\; F_{Rx\cdot Ni} \;\; F_{Ry\cdot Ni} \rangle^T$ represents the force vector applied by the joint on the plate boundary. $[K_{Je}]$ is an elementary elastic joint matrix written as follows:

$$[K_{Je}] = \begin{bmatrix} k_{Tz} & 0 & 0 \\ 0 & k_{Rx} & 0 \\ 0 & 0 & k_{Ry} \end{bmatrix} \tag{15}$$

Thus, when the laminate edge contains N_n nodes, a global matrix $[K_J]$ of the elastic joint effect at the edge of the laminate can be derived as follows:

$$[K_J] = \begin{bmatrix} \begin{bmatrix} [0]_{4\times4} & [0]_{4\times3} \\ [0]_{3\times4} & [K_{Je}] \end{bmatrix}_{\text{node}N_1} & [0]_{7\times7} & \cdots & \cdots & [0]_{7\times7} \\ [0]_{7\times7} & \begin{bmatrix} [0]_{4\times4} & [0]_{4\times3} \\ [0]_{3\times4} & [K_{Je}] \end{bmatrix}_{\text{node}N_2} & [0]_{7\times7} & \cdots & [0]_{7\times7} \\ \vdots & [0]_{7\times7} & \ddots & & \vdots \\ \vdots & \vdots & & \ddots & [0]_{7\times7} \\ [0]_{7\times7} & [0]_{7\times7} & \cdots & [0]_{7\times7} & \begin{bmatrix} [0]_{4\times4} & [0]_{4\times3} \\ [0]_{3\times4} & [K_{Je}] \end{bmatrix}_{\text{node}N_n} \end{bmatrix} \tag{16}$$

The developed model of the elastic joint is combined with the thin-film laminated plate model allow modeling a new configuration of laminated double glazing system.

2.4. ***Dynamic model of a thin-film laminated double glazing system.*** The considered double glazing system is composed of two thin-film laminated plate bonded by the elastic joint defined in Section 2.3.

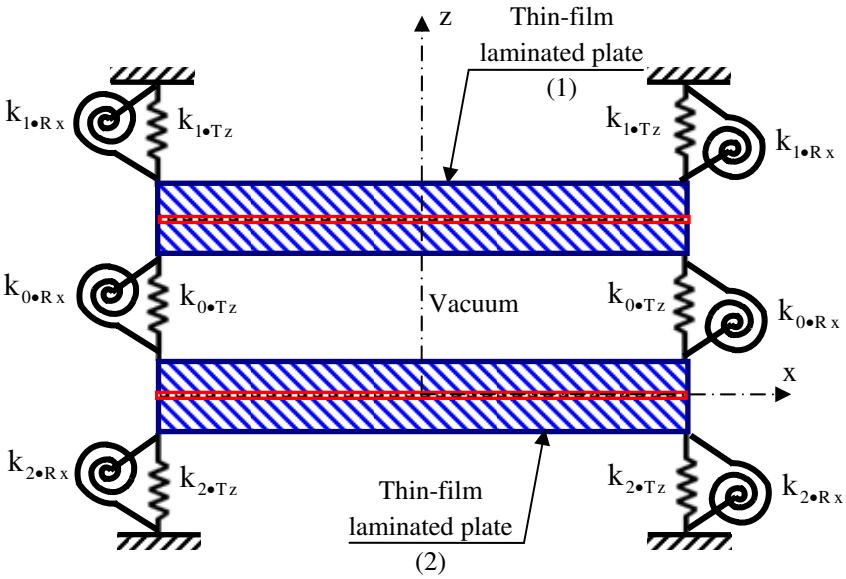

Figure 5. In plane (x, z) double laminate-joint model.

In this case, the two laminates are coupled by elastic linear and angular springs of stiffness $k_{0\cdot Tz}$ and $k_{0\cdot Rx}$. The obtained coupled system is related to a rigid body by two elastic joints $(k_{1\cdot Tz}, k_{1\cdot Rx})$ and $(k_{2\cdot Tz}, k_{2\cdot Rx})$as presented in Figure 5.

The double glazing system energy functional can be obtained by calculating the associated energy of each part composing the system. Then, we can write:

$$\vartheta_{\text{D.G.S}} = \Big(\sum_{i=1}^{2}[(E_{\text{str.}} + E_{\text{kin.}})_{\text{skins}} + E_{\text{film}}]_{Li}\Big) + \Big(\sum_{i=1}^{2}(E_{\text{str.}})_{Ji0}\Big) + (E_{\text{coupling}})_{J_0\cdot L_1\cdot L_2} \tag{17}$$

where $(E_{\text{str.}})_{Ji0}$ $(i = 1, 2)$ and $(E_{\text{coupling}})_{J_0\cdot L_1\cdot L_2}$ represent respectively the strain energies due to the joint effect at the edge of the laminate Li $(i = 1, 2)$ and the laminates-joint coupling energy expressed as follows:

$$(E_{\text{str.}})_{Ji0} = \tfrac{1}{2}[(k_{0\cdot Tz} + k_{i\cdot Tz})\int_{\ell} w_i^2\, d\ell + (k_{0\cdot Rx} + k_{i\cdot Rx})\int_{\ell}\beta_{xi}^2\, d\ell + (k_{0\cdot Ry} + k_{i\cdot Ry})\int_{\ell}\beta_{yi}^2\, d\ell] \tag{18}$$

$$(E_{\text{coupling}})_{J_0\cdot L_1\cdot L_2} = -\tfrac{1}{2}[(2k_{0\cdot Tz}\int_{\ell} w_1 w_2\, d\ell) + (2k_{0\cdot Rx}\int_{\ell}\beta_{x1}\beta_{x2}\, d\ell) + (2k_{0\cdot Ry}\int_{\ell}\beta_{y1}\beta_{y2}\, d\ell)] \tag{19}$$

The discretization and the minimization of the double glazing system energy functional by the finite element method (FE) give the following symmetrical coupled matrix equation:

$$\left(\begin{bmatrix}[K_{L_1}]+[K_{J_{10}}] & -[K_{J_0\cdot L_1\cdot L_2}] \\ -[K_{J_0\cdot L_1\cdot L_2}]^T & [K_{L_2}]+[K_{J_{20}}]\end{bmatrix} - \omega^2\begin{bmatrix}[M_{L_1}] & [0] \\ [0] & [M_{L_2}]\end{bmatrix}\right)\begin{Bmatrix}\{U_1\} \\ \{U_2\}\end{Bmatrix} = \begin{Bmatrix}\{0\} \\ \{0\}\end{Bmatrix} \tag{20}$$

where $([K_{L_1}], [K_{L_2}])$ and $([M_{L_1}], [M_{L_2}])$ represent respectively the stiffness and mass matrices of the laminates. $[K_{J_{10}}]$ and $[K_{J_{20}}]$ are respectively the stiffness matrices due to the joints effects at the edge of the laminates; obtained from the FE discretization of Equation (18) and expressed as follows:

$$\begin{aligned}[K_{J_{10}}] &= [K_{J_1}] + [K_{J_0}] \\ [K_{J_{20}}] &= [K_{J_2}] + [K_{J_0}]\end{aligned} \tag{21}$$

with: $[K_{J_0}]$, $[K_{J_1}]$ and $[K_{J_2}]$ represent respectively the stiffness matrices of the elastic joints J_0, J_1, and J_2 defined at the laminate boundary nodes.

$[K_{J_0 \cdot L_1 \cdot L_2}]$ is a stiffness matrix resulting from the coupling between the boundaries of two laminates (L_1, L_2) and the joint J_0 obtained from the FE discretization of Equation (19).

$\{U_1\}$ and $\{U_2\}$ represent respectively the nodal displacement vectors of laminates 1 and 2.

2.5. ***Modal analysis of the laminated double glazing system.*** The eigenmodes of the coupled system are solution of Equation (20) which can be written in the following form:

$$\begin{bmatrix} [K_{S_1}] - \omega^2 [M_{S_1}] & [C_S] \\ [C_S]^T & [K_{S_2}] - \omega^2 [M_{S_2}] \end{bmatrix} \begin{Bmatrix} \{U_1\} \\ \{U_2\} \end{Bmatrix} = \begin{Bmatrix} \{0\} \\ \{0\} \end{Bmatrix} \tag{22}$$

where $[K_{S_i}] = [K_{L_i}] + [K_{J_{i0}}]$, $[M_{S_i}] = [M_{L_i}]$ $(i = 1, 2)$, $[C_S] = -[K_{J_0 \cdot L_1 \cdot L_2}]$.

The eigenmodes $[\Phi_{S_1}]$ and $[\Phi_{S_2}]$ of each laminate alone can be used in order to reduce the size of the coupled system (22). Then, the modal matrices of each plate alone can be written as follows:

$$[\mathbf{K}_{S_i}] = [\Phi_{S_i}]^T [K_{S_i}] [\Phi_{S_i}] = \begin{bmatrix} \ddots & & \\ & \omega^2_{r \cdot S_i} & \\ & & \ddots \end{bmatrix} \text{ for } \begin{cases} r = 1 \ldots N_{\text{eig}} \\ i = 1, 2 \end{cases} \tag{23}$$

$$[\mathbf{M}_{S_i}] = [\Phi_{S_i}]^T [M_{S_i}] [\Phi_{S_i}] = \begin{bmatrix} \ddots & & \\ & 1 & \\ & & \ddots \end{bmatrix} \text{ for } \begin{cases} r = 1 \ldots N_{\text{eig}} \\ i = 1, 2 \end{cases} \tag{24}$$

N_{eig} represent the number of eigenmodes retained.

Consequently, the coupled matrix system (22) can be much reduced and written as follows:

$$\begin{bmatrix} \omega^2_{r \cdot S_1} - \omega^2 & [\mathbf{C_S}] \\ [\mathbf{C_S}]^T & \omega^2_{r \cdot S_2} - \omega^2 \end{bmatrix} \begin{Bmatrix} \{\mathbf{U}_1\} \\ \{\mathbf{U}_2\} \end{Bmatrix} = \begin{Bmatrix} \{\mathbf{0}\} \\ \{\mathbf{0}\} \end{Bmatrix} \tag{25}$$

where $\{\mathbf{U}_1\}$ and $\{\mathbf{U}_2\}$ represent, respectively the modal displacement vectors of laminates 1 and 2 defined by:

$$\begin{aligned}\{\mathbf{U}_1\} &= [\Phi_{S_1}]^T \{U_1\} \\ \{\mathbf{U}_2\} &= [\Phi_{S_2}]^T \{U_2\}\end{aligned} \tag{26}$$

$[\mathbf{C_S}]$ represents the laminate-joint modal coupling matrix written as follows:

$$[\mathbf{C_S}] = [\Phi_{S_1}]^T [C_S] [\Phi_{S_2}] \tag{27}$$

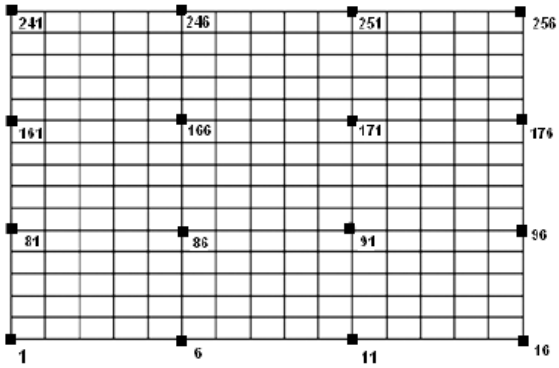

Figure 6. Laminated plate dynamic response nodes.

As discussed in [Akrout et al. 2008b; 2009; 2010], the resolution of the coupled system (25) allows determining the coupled eigenfrequencies $\omega_{r\cdot C}$ $(r = 1, \ldots\ldots N_{C\cdot\text{eig}})$ and a coupled eigenmodes basis $[\Phi_C] = [\{\Phi_1\} \ldots\ldots\ldots \{\Phi_{N_{C\cdot\text{eig}}}\}]$. So, we can calculate the modal responses of the laminated double glazing system which is in free vibration and under initial excitations of the first laminate. The considered initial conditions are the following:

$$\text{for } t = 0, \begin{cases} \langle\{U_1\}\{U_2\}\rangle_{t=0} = \langle\{U_{10}\}\{0\}\rangle \\ \langle\{\dot{U}_1\}\{\dot{U}_2\}\rangle_{t=0} = \langle\{\dot{U}_{10}\}\{0\}\rangle \end{cases} \tag{28}$$

In this case, the nodal vibratory responses are obtained by the modal recombination method.

Hence, the calculated numerical responses are used as inputs in the ICA concept which is applied in the OMA method in order to obtain estimated results of the eigenfrequencies and eigenmode shapes.

3. Numerical procedure validation: case of thin-film laminated plate alone

In this part, the OMA approach is used in order to estimate the eigenmodes of a thin-film laminated glass plate alone for two cases of elastic boundary conditions:

- only a linear springs is considered at the level of the edge.
- both linear and angular springs are considered at the level of the edge.

In order to estimate the eigenfrequencies and the eigenmode shapes by the OMA method, 16 vibratory responses of the laminate x $(1, \ldots, 16)$ are calculated at the indicated nodes (see Figure 6). Note that, the plate is in free vibration under initial conditions.

The physical and geometrical properties of the studied structure are the following:

- skin's laminate properties: in-plane dimensions: $\ell_x = 0.6\,\text{m}$, $\ell_y = 0.4\,\text{m}$, Young modulus: $E_1 = E_2 = 7.2 \times 10^4\,\text{MPa}$, Poisson's ratio: $\nu_1 = \nu_2 = 0.22$, density: $\rho_1 = \rho_2 = 2500\,\text{Kg/m}^3$ skin's thickness: $h_1 = h_2 = 3\,\text{mm}$.
- ultra-thin film stiffness: $k_{\text{film}} = 1.362 \times 10^7\,\text{N/mm}^3$ (Araldite),
- linear stiffness per length unit: $k_{Tz} = 0.264 \times 10^4\ \text{N/m}^2$,

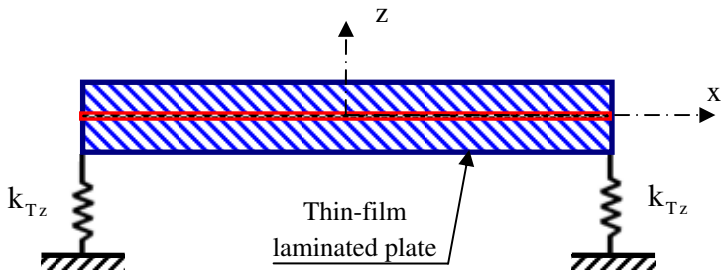

Figure 7. Laminated plate bonded by translational joint.

- angular stiffness per length unit: $k_{Rx} = k_{Ry} = 0.264 \times 10^4$ N/rad.

In the next sections, the ICA results can be compared to those obtained numerically (by the classical modal analysis). Also, the effect of angular springs added to the linear spring is presented and analyzed.

3.1. ***Case of translational stiffness 'T'.*** In this section, the considered laminate is supported only by a translational joint as sketched in Figure 7. The laminate is supposed to be in free vibration and under arbitrary initial conditions satisfying to a standard statistical rule.

The eigenmodes of the laminate bonded by translational joint are solution of the following matrix system:

$$([[K_L] + [K_J]] - \omega^2[M_L])\{U_L\} = \{0\}$$
$$\text{for } t = 0 \begin{cases} \{U_L\} = \{U_{L0}\} \\ \{\dot{U}_L\} = \{\dot{U}_{L0}\} \end{cases} \tag{29}$$

where $([K_L], [K_J])$ and $[M_L]$ are respectively the laminate-joint stiffness matrices and the mass matrix of the structure. $\{U_{L0}\}$ and $\{\dot{U}_{L0}\}$ are respectively the initial displacement and velocity vectors applied on the laminate.

Figure 8 presents the observed signals at nodes $x(3)$: node 11, $x(10)$: node 166, $x(12)$: node 176 and $x(14)$: node 246 which are used for the eigenmodes estimation. In analyzing the spectrum of those observed signals, we remark the existence of four dominant picks characteristics of the main natural frequencies of the laminate.

Table 1 regroups the exact and estimated eigenfrequencies of the laminated glass plate with translational boundary conditions (linear springs). The OMA results are validated by calculating the following performance criteria [Zhou and Chelidze 2007; Abbès et al. 2011]:

- The Modal Assurance Criterion defined as follows:

$$\text{MAC}_i = \frac{(\psi_i^T \bar{\psi}_i)}{(\psi_i^T \psi_i)(\bar{\psi}_i^T \bar{\psi}_i)} \tag{30}$$

  where ψ_i and $\bar{\psi}_i$ are respectively the numerical (exact) and estimated eigenmodes of the laminate.

- The Euclidean distance between two vectors of the modal matrix in order to calculate the approximation error of eigenmodes as follows:

$$E_{ri} = \|\psi_i - \bar{\psi}_i\| \tag{31}$$

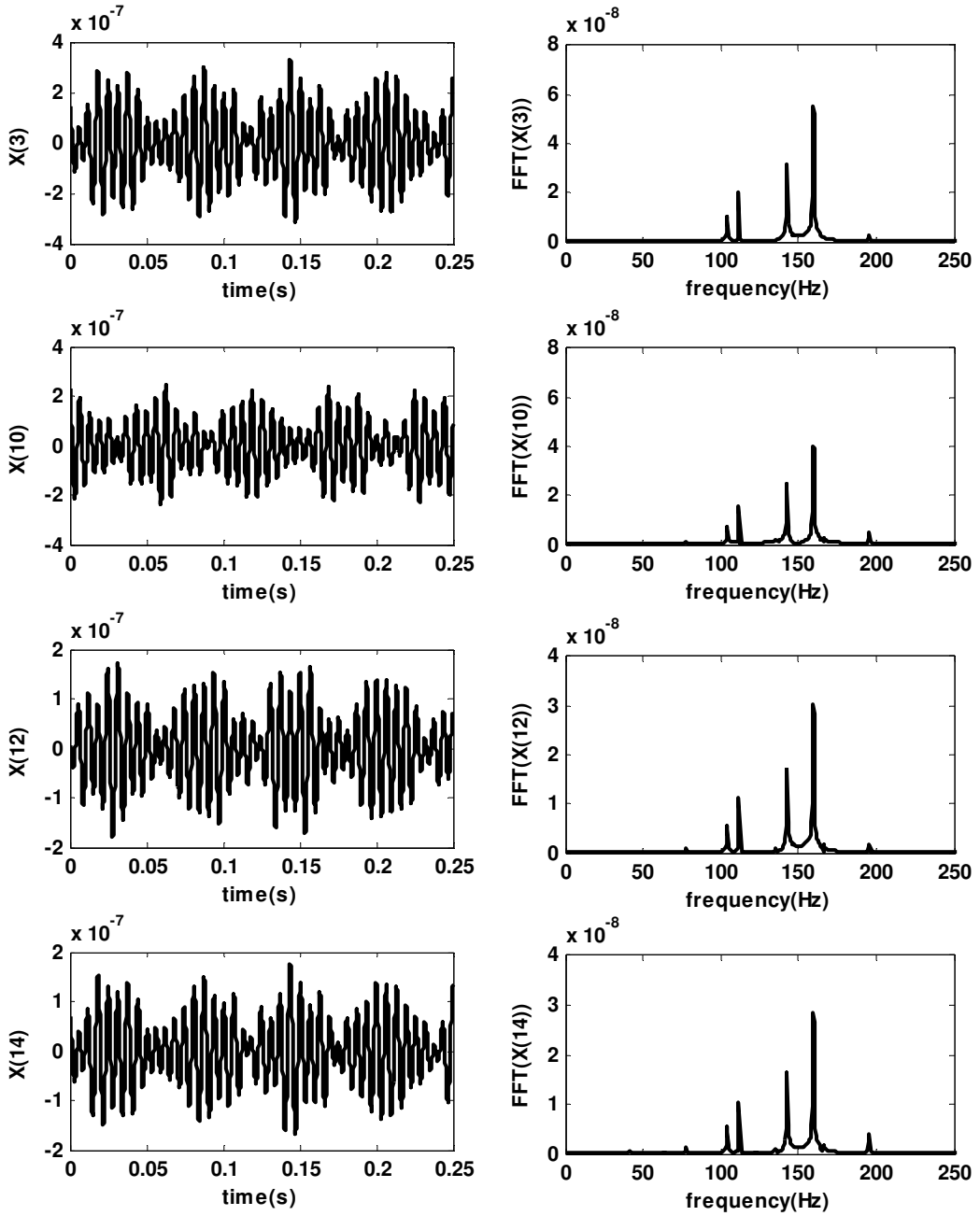

Figure 8. Some observed signals: case of laminated plate bonded by translational joint.

- The relative error Ef_i between the exact and estimated eigenfrequencies present good performance criteria defined as follows:

$$Ef_i(\%) = 100\frac{f_i - \bar{f}_i}{f_i} \tag{32}$$

Mode	Exact eigenfreq. (Hz)	Estimated eigenfreq. (Hz)	Er	MAC	$Ef(\%)$
1	23.7771	24	0.0006	0.9979	0.9376
2	41.7990	42	0.0014	0.9996	0.4810
3	62.5867	62.5	0.0007	0.9999	0.1385
4	70.7569	71	0.0008	0.9966	0.3436
5	77.8571	78	0.0002	1.0000	0.1836
6	104.2231	104	0.0007	1.0000	0.2141
7	111.5364	111.5	0.0003	1.0000	0.0326
8	121.9734	122	0.0006	0.9998	0.0218
9	135.7371	135.5	0.0004	0.9999	0.1747
10	142.7350	142.5	0.0001	1.0000	0.1647
11	159.7369	159.5	0.0001	1.0000	0.1483
12	166.2010	166	0.0005	0.9998	0.1209
13	195.1359	195	0.0030	0.9557	0.0696
14	195.3606	195.5	0.0003	1.0000	0.0714
15	201.8061	202	0.0040	0.9972	0.0961
16	214.2604	214.5	0.0024	0.9666	0.1118

Table 1. Eigenfrequencies of a laminated plate alone bonded by translational joint.

where f_i and $\bar{f}_i$ represent respectively the exact and estimated eigenfrequencies.

Then, the performance criteria presented in Table 1 show that an excellent accord is achieved by comparing the numerical (exact) and the estimated eigenfrequencies (obtained by OMA).

As a next result, we present in Figure 9 the exact and estimated eigenmode shapes for the tree first eigenfrequencies of the laminate. Hence, a good accord is obtained.

3.2. ***Case of both translational and rotational stiffness 'T + R'.*** The model of the structure is presented in Figure 4. In this case, the same nodes $\{x(3)$: node11, $x(10)$: node 166, $x(12)$: node 176 and $x(14)$: node 246$\}$ are used for the estimation of the laminate eigenmodes. So, according to those nodes, Figure 10 present the observed signals and the corresponding spectra. In analyzing the evolution of the dynamic responses versus time, we can see a reduced vibration amplitude for the laminate fixed by both translational and rotational joints compared to the one fixed only by translational joint. Also, some eigenfrequencies have vanished in the spectrum of joint '$\mathbf{R}+\mathbf{T}$' (Figure 10) compared to the spectrum of joint '**T**' presented in Figure 8.

Table 2 contains the numerical and estimated eigenfrequencies of the laminated glass plate with elastic (translational and rotational) boundary conditions. The OMA results are validated by calculating the same performance criteria [Zhou and Chelidze 2007; Abbès et al. 2011] defined by (30), (31) and (32). Also, the eigenfrequencies of the laminate-joint '$\mathbf{R}+\mathbf{T}$' (Table 2) increased compared to those of the laminate-joint '**T**' (Table 1). Thus, more rigidity can be conferred to the structure.

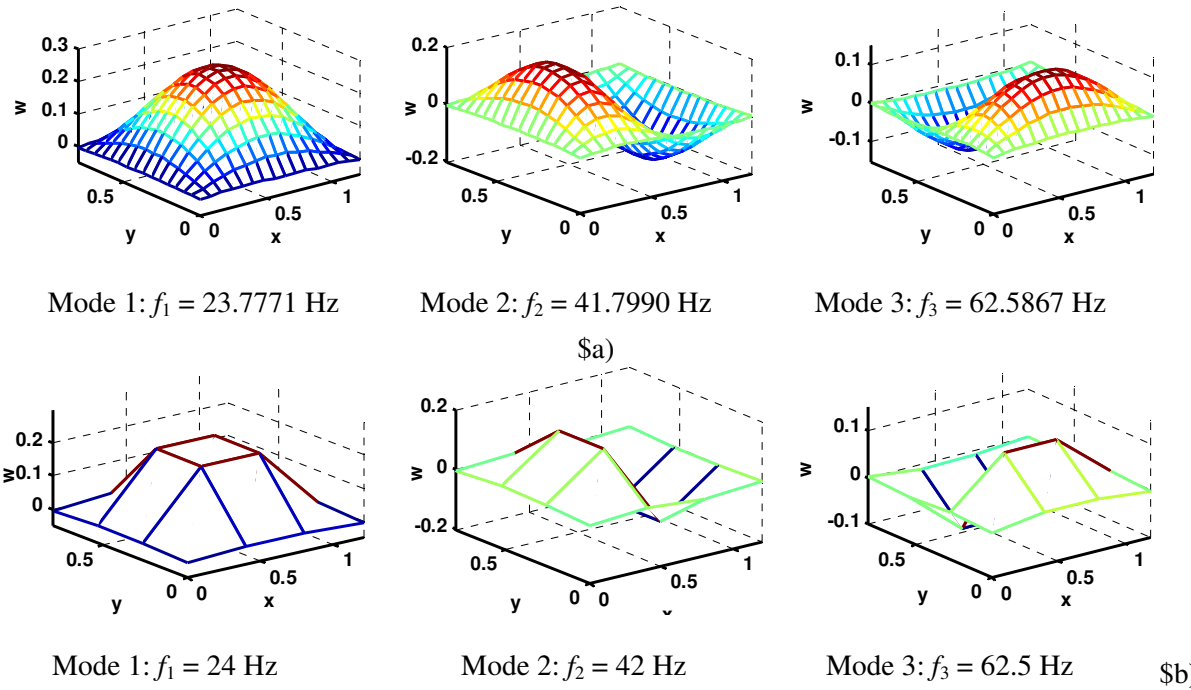

Figure 9. Eigenmode shapes of a laminated plate bonded by translational joint. (a) Exact eigenmode shapes. (b) Estimated eigenmode shapes.

In addition, Figure 11 shows the numerical (exact) and estimated eigenmode shapes of a thin-film laminated glass plate bonded by both translational and rotational joints. The same form is observed by comparing each corresponding mode presented in Figure 11(a) (exact) to the one presented in Figure 11(b) (estimated).

4. OMA application: case of thin-film laminated double glazing system

In this section, the OMA method is applied in order to identify the modal characteristics of a laminated double glazing system bonded by an elastic joint. Figure 12 presents the corresponding nodes used for the calculation of 32 vibratory responses corresponding to the coupled system.

The double glazing system is composed of two identical laminated glass plate which each one is made of two similar skins connected by an adhesive ultra-thin film.

The physical and geometrical properties of the laminate are given in Section 3.

A same elastic joint is used as boundary conditions of the coupled system (see Figure 5):

- linear stiffness per length unit: $k_{i\cdot Tz} = k_{Tz},\ (i = 0, 1, 2)$.
- angular stiffness per length unit: $k_{i\cdot Rx} = k_{i\cdot Ry} = k_{Rx} = k_{Ry},\ (i = 0, 1, 2)$.

The value of k_{Tz}, k_{Rx} and k_{Ry} are given in Section 3.

In the next sections, the ICA results can be compared to those obtained numerically (by the classical modal analysis). Also, the effect of angular springs added to the linear spring is presented and analyzed.

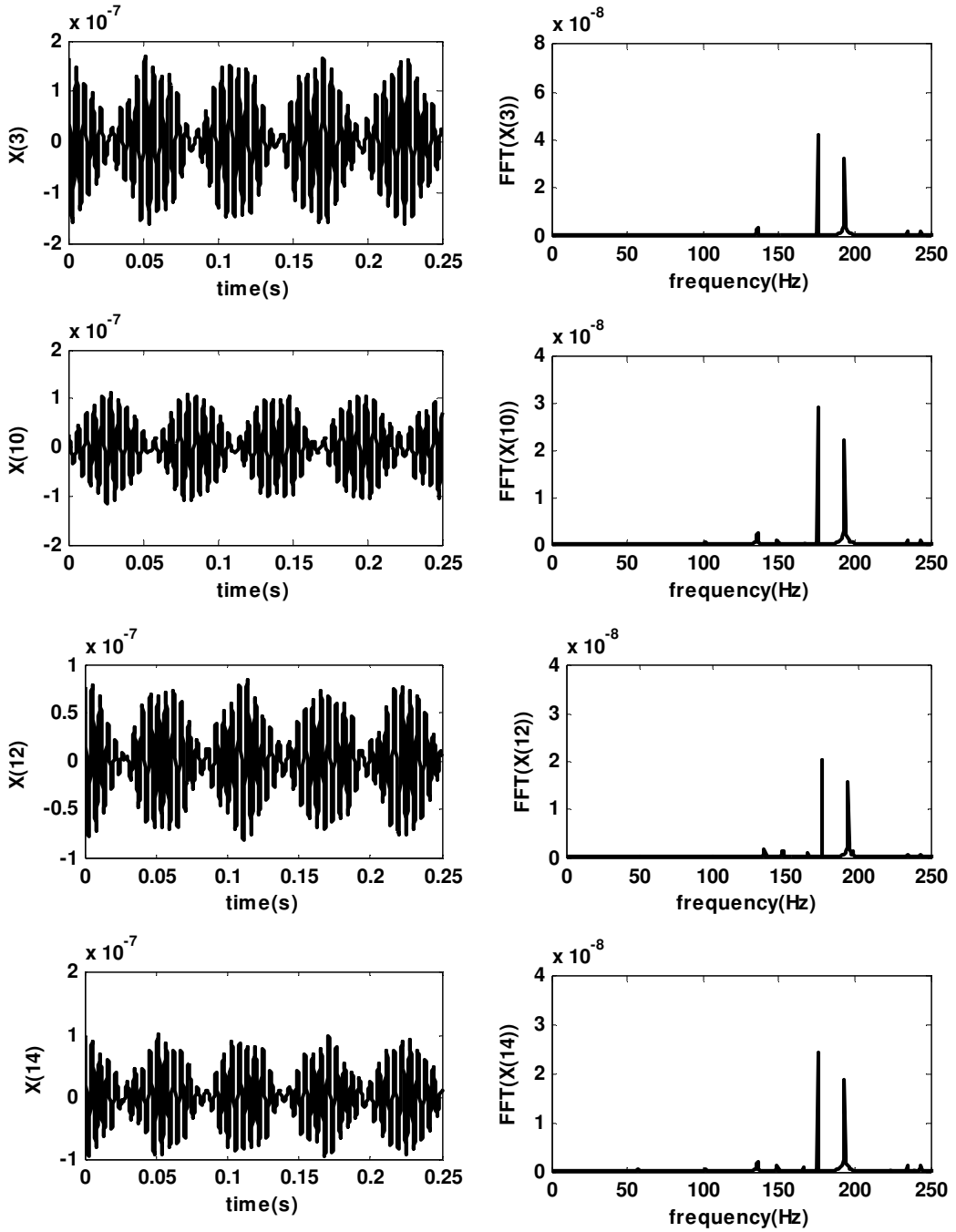

Figure 10. Some observed signals: case of laminated plate bonded by both translational and rotational joints.

Mode	Numerical eigenfreq. (Hz)	Estimated eigenfreq. (Hz)	Er	MAC	$Ef(\%)$
1	37.1843	37	0.0051	0.9779	0.4956
2	57.2723	57.5	0.0002	1.0000	0.3975
3	84.6944	84.5	0.0008	0.9999	0.2295
4	90.1553	90	0.0001	1.0000	0.1722
5	101.7795	102	0.0007	0.9997	0.2166
6	131.6648	131.5	0.0003	1.0000	0.1251
7	135.7660	136	0.0029	0.9999	0.1723
8	148.7430	149	0.0001	1.0000	0.1727
9	166.0922	166	0.0001	1.0000	0.0555
10	175.4942	175.5	0.0010	1.0000	0.0033
11	193.3816	193.5	0.0002	1.0000	0.0612
12	196.6265	196.5	0.0001	1.0000	0.0643
13	222.3098	222.5	0.0003	0.9999	0.0855
14	234.4725	234.5	0.0002	1.0000	0.0117
15	238.1860	238	0.0006	0.9999	0.0780
16	243.3318	243.5	0.0002	1.0000	0.0691

Table 2. Eigenfrequencies of a laminated plate alone bonded by both translational and rotational joints.

4.1. ***Observed signals of the laminated double glazing system.*** As observed signals, we report in the same graph (Figures 13, 14, 15 and 16) the dynamic responses of both a thin film laminated double glazing fixed by '**T**' joint and the same system fixed by '$\mathbf{R}+\mathbf{T}$' joint. These vibratory responses are determined at nodes: 166: $x(10)$ and 246: $x(14)$ for laminate 1 and at nodes: 417: $x(25)$ and 502: $x(30)$ for laminate 2.

By analyzing the vibratory responses of the laminated double glazing system with translational stiffness boundary conditions (dashed line, '**T**') to those of the same system with both translational and rotational stiffness boundary conditions (solid line, '$\mathbf{R}+\mathbf{T}$'), we remark a reduced vibration amplitude for the '$\mathbf{R}+\mathbf{T}$' system compared to the one for the '**T**' system. Also, the rotational stiffness can be clearly seen in the observed signals of laminate 1 (Figures 13 and 14) on which the initial excitation conditions are applied.

4.2. ***Eigenfrequencies of the coupled system.*** Table 3 regroups the numerical (exact) and estimated (via OMA) eigenfrequencies of the two configurations '**T**' and '$\mathbf{R}+\mathbf{T}$' laminated double glazing system. Besides the obtained good agreement between the exact and estimated values, one can clearly see that the eigenfrequencies of the coupled system have increased when a rotational stiffness is added.

4.3. ***Eigenmodes shapes of the laminated double glazing system bonded by '$\mathbf{R}+\mathbf{T}$' joint.*** In this section, the exact and estimated eigenmode shapes of the laminated double glazing system are presented and

	Translational stiffness '**T**'					Translational + Rotational stiffness '**R** + **T**'				
Mode	Num. Efreq. (Hz)	Estim. Efreq. (Hz)	Er	MAC	$Ef(\%)$	Num. Efreq. (Hz)	Estim. Efreq. (Hz)	Er	MAC	$Ef(\%)$
1	23.77	23	0.0095	0.7819	3.2394	37.18	37	0.0019	0.9976	0.4955
2	24.02	24	0.0263	0.8856	0.0833	37.81	38	0.0023	0.9994	0.4973
3	41.79	41.5	0.0019	0.9994	0.6939	57.27	57.5	0.0086	0.9913	0.3976
4	42.37	42.5	0.0006	0.9986	0.3068	58.21	58	0.0022	0.9969	0.3634
5	62.58	62.5	0.0163	0.8626	0.1278	84.69	84.5	0.0032	0.9963	0.2295
6	63.86	64	0.0001	1.0000	0.2192	88.28	88.5	0.0008	1.0000	0.2423
7	70.75	71	0.0053	0.9999	0.3534	90.15	90	0.0024	1.0000	0.1723
8	71.94	72	0.0025	0.9959	0.0834	91.96	92	0.0058	0.9883	0.0335
9	77.85	78	0.0061	0.9765	0.1927	101.77	102	0.0106	0.9602	0.2166
10	79.94	80	0.0022	1.0000	0.0751	105.34	105.5	0.0019	1.0000	0.1517
11	104.22	104	0.0037	0.9999	0.2111	131.66	131.5	0.0006	1.0000	0.1252
12	107.66	107.5	0.0058	0.9796	0.1486	135.52	135.5	0.0011	0.9995	0.0147
13	111.53	111.5	0.0102	0.6315	0.0269	135.76	136	0.0133	0.9035	0.1723
14	113.92	114	0.0025	0.9989	0.0702	139.91	140	0.0030	0.9989	0.0606
15	121.97	122	0.0319	0.8447	0.0246	148.74	149	0.0016	0.9997	0.1728
16	126.59	126.5	0.0267	0.1735	0.0711	162.01	162	0.0028	0.9949	0.0099
17	135.73	135.5	0.0093	0.9840	0.1695	166.09	166	0.0006	1.0000	0.0555
18	141.78	142	0.0011	0.9998	0.1552	175.49	175.5	0.0052	0.9965	0.0033
19	142.73	142.5	0.0018	0.9994	0.1611	177.83	178	0.0020	0.9994	0.0941
20	148.30	148.5	0.0026	0.9708	0.1349	180.59	180.5	0.0024	0.9962	0.0530
21	159.73	195.5	0.0057	0.9798	0.1440	193.38	193.5	0.0005	0.9999	0.0612
22	166.20	166	0.0003	1.0000	0.1203	196.62	196.5	0.0012	1.0000	0.0643
23	168.15	168	0.0037	0.9999	0.0892	204.28	204.5	0.0011	1.0000	0.1069
24	171.05	171	0.0033	0.9931	0.0292	205.99	206	0.0047	0.9922	0.0032
25	195.13	195	0.0959	0.1494	0.0666	222.30	222.5	0.0067	0.9841	0.0856
26	195.36	195.5	0.0046	0.9999	0.0717	234.47	234.5	0.0030	0.9999	0.0117
27	201.80	202	0.0011	1.0000	0.0991	238.18	238	0.0010	1.0000	0.0781
28	204.22	204	0.0426	0.4764	0.1077	242.95	243	0.0065	0.9850	0.0196
29	207.22	207	0.0675	0.0235	0.1062	243.33	243.5	0.0278	0.6943	0.0691
30	214.26	214.5	0.0385	0.7989	0.1120	248.59	248.5	0.0285	0.9056	0.0369
31	215.83	216	0.0421	0.8065	0.0788	259.04	259	0.0089	0.9902	0.4955
32	230.33	230.5	0.1840	0.8029	0.0738	265.25	265.5	0.0224	0.7569	0.4973

Table 3. Eigenfrequencies of the '**T**' and '**R** + **T**' coupled systems.

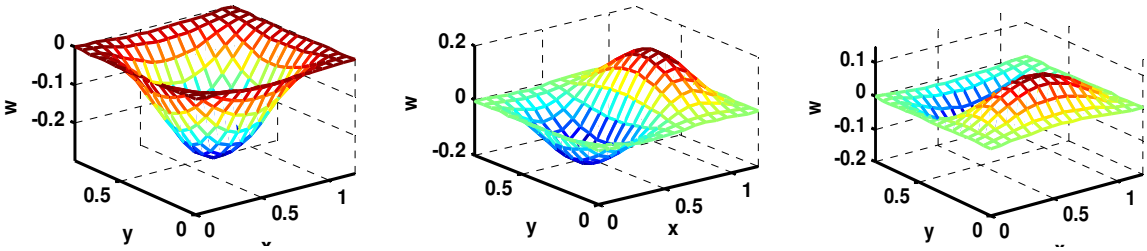

Mode 1: f_1 = 37.1843 Hz Mode 2: f_2 = 57.2723 Hz Mode 3: f_3 = 84.6944 Hz

$a)

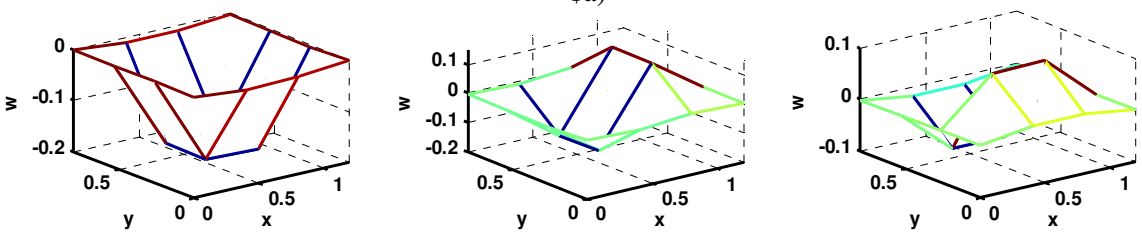

Mode 1: f_1 = 37 Hz Mode 2: f_2 = 57.5 Hz Mode 3: f_3 = 84.5 Hz

$b)

Figure 11. Eigenmode shapes of a laminated plate bonded by both translational and rotational joints. (a) Exact eigenmode shapes. (b) Estimated eigenmode shapes.

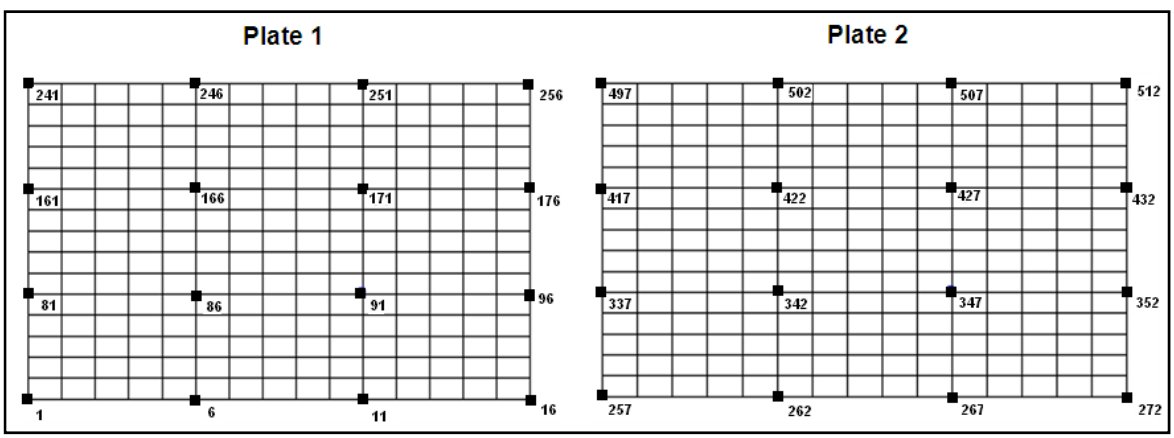

Figure 12. Coupled system vibratory response nodes.

commented. Consequently, the considered 32 coupled system vibratory response nodes let's to construct the investigated eigenmodes (Figures 17 and 18).

Here, four eigenmode shapes are estimated and presented and then, a good accord is obtained when comparing with numerical results. As discussed in [Basten et al. 2001; Akrout et al. 2009; 2010], two categories of eigenfrequencies are found. The first one regroups those of a laminate alone bonded by '**R**+**T**' joint. In this case, the two plates are vibrating in-phase. In fact, the middle joint doesn't generate a

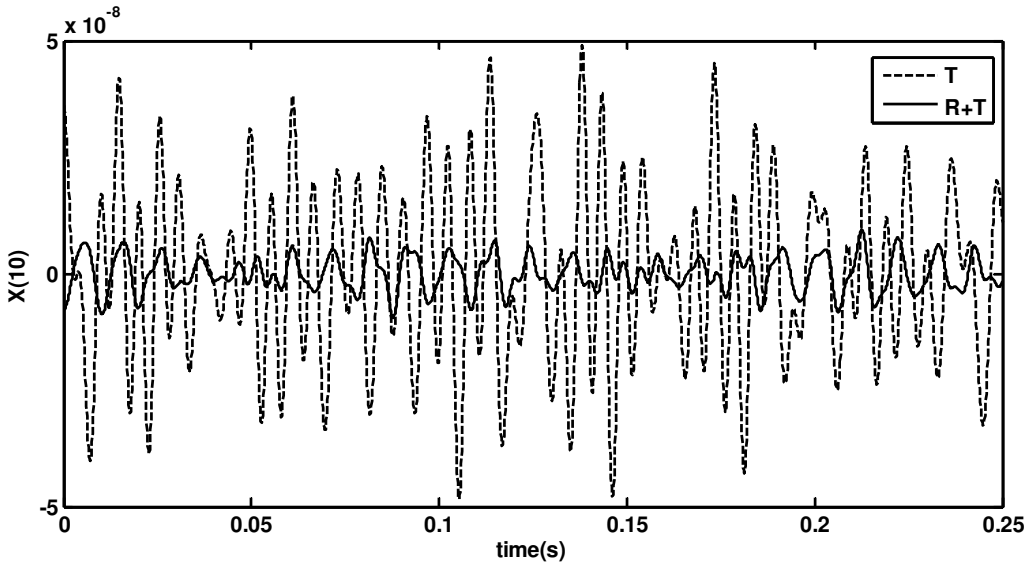

Figure 13. Observed signals of the first laminate at node 166.

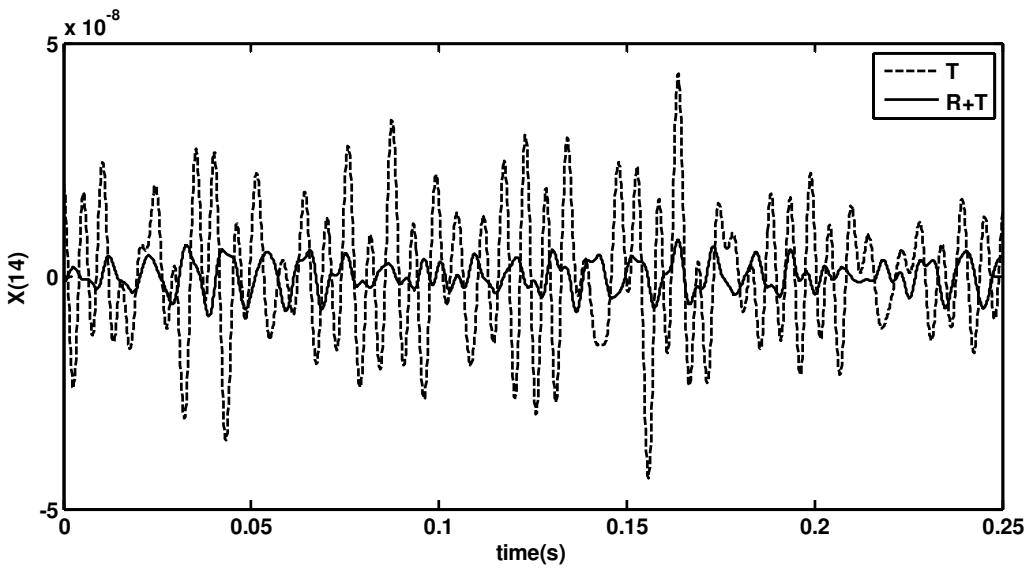

Figure 14. Observed signals of the first laminate at node 246.

coupling with laminates. The second category regroups the coupled eigenfrequencies which are affected by the coupling laminate-joint and where the two plates are vibrating in opposition.

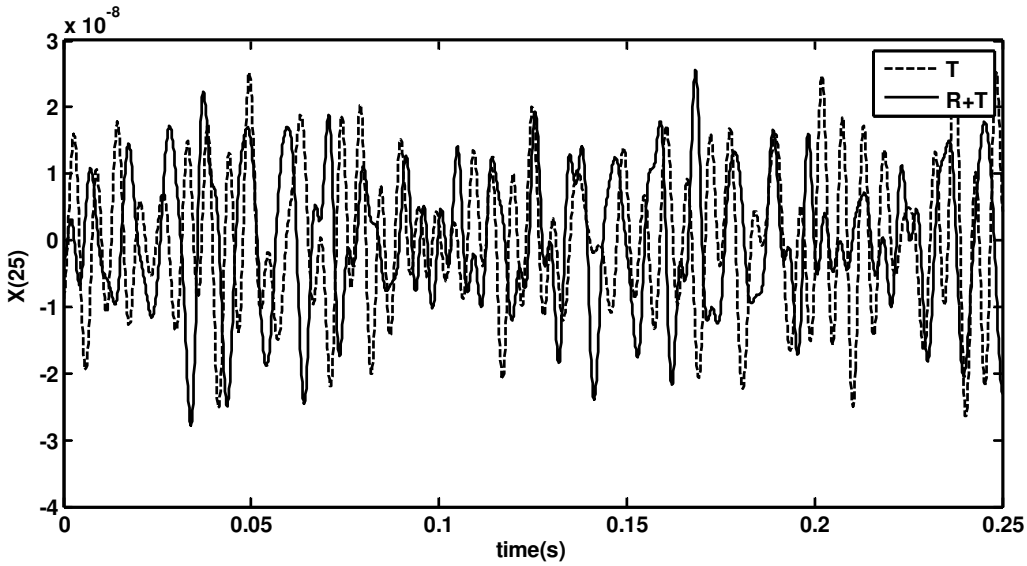

Figure 15. Observed signals of the second laminate at node 417.

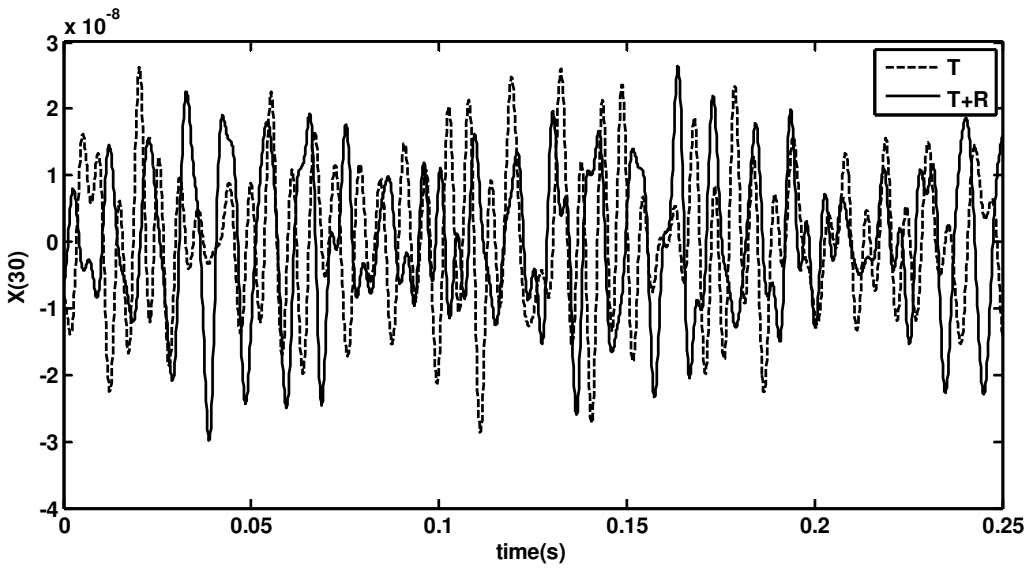

Figure 16. Observed signals of the second laminate at node 502.

5. Conclusion

In this work, the dynamic modal behavior of a thin-film laminated double glazing system is investigated. In this case, the edge stiffness boundary conditions associated to an elastic joint (translational and rotational effects) are modeled and its influence on a given structure (laminated plate alone or double glazing system) can be analyzed. For this purpose, the OMA method is presented and exploited in

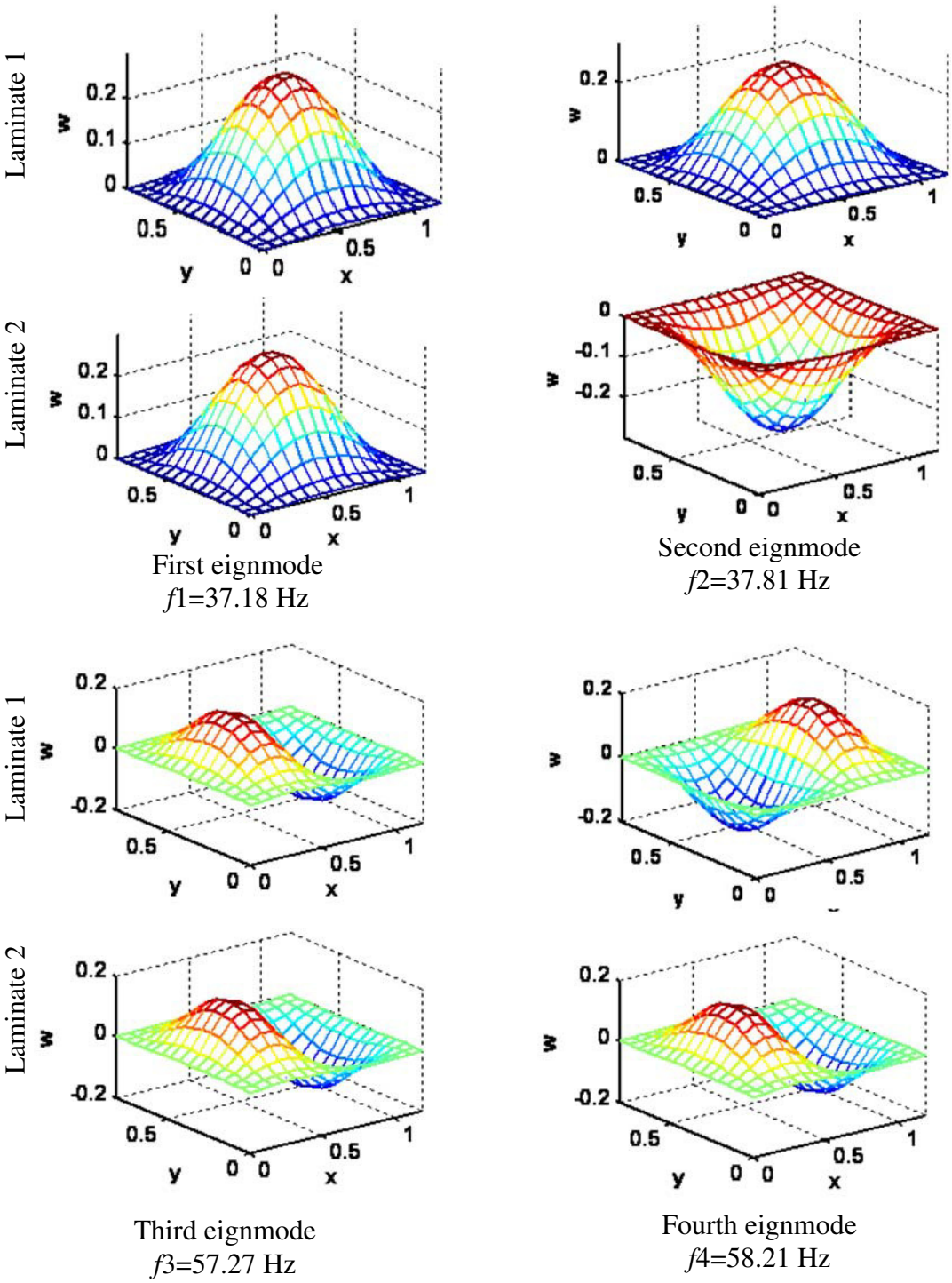

Figure 17. Exact eigenmodes shapes of the laminated double glazing system.

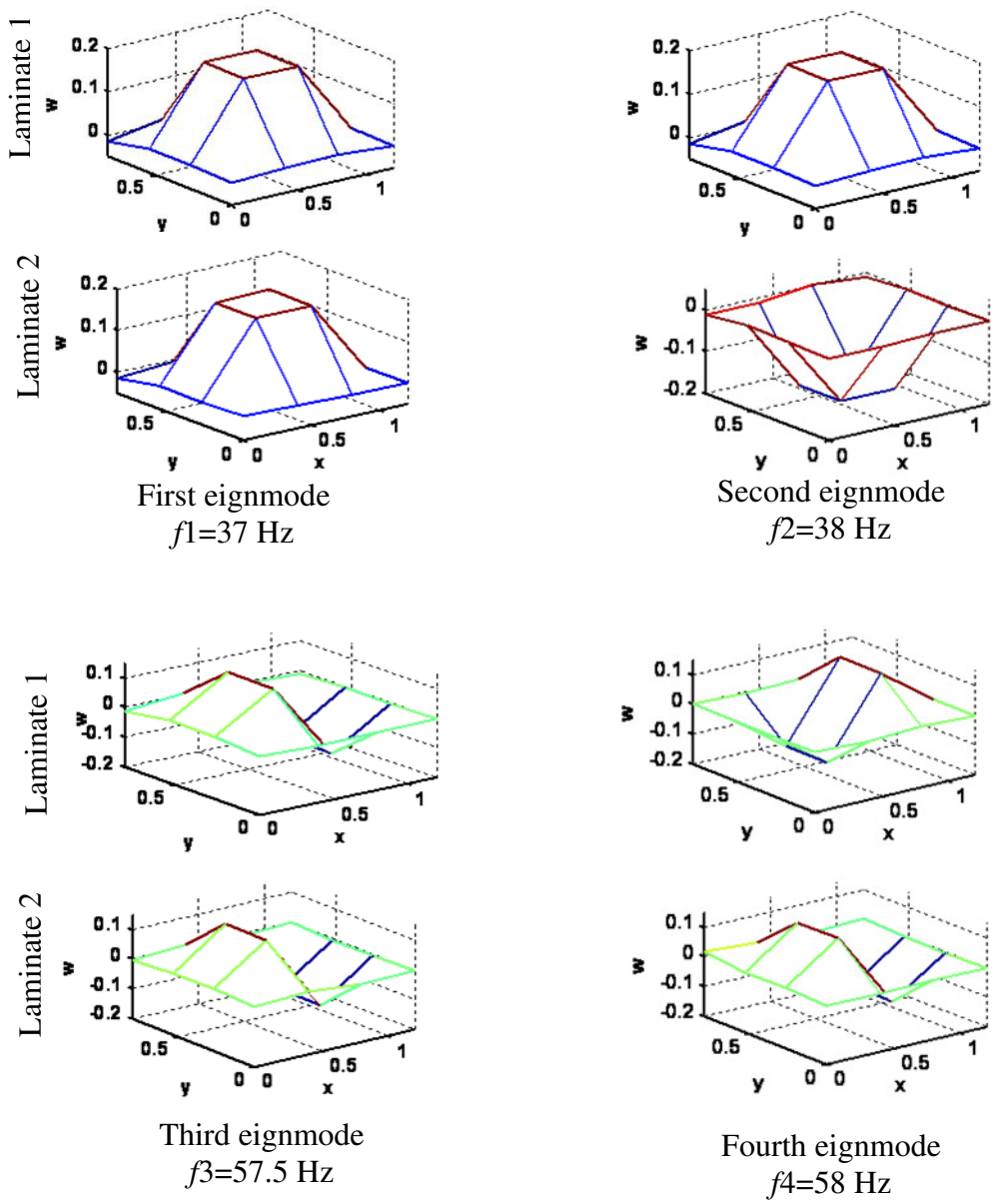

Figure 18. Estimated eigenmodes shapes of the laminated double glazing system.

order to determine the modal characteristics (eigenfrequencies and eigenmode shapes) of the coupled system. The modal procedure validation is based on the calculation of three performance criteria defined by the Modal Assurance Criterion (MAC), the approximation error of the eigenmode shapes (Er) and the relative error between numerical and estimated eigenfrequencies (Ef). Hence, a good agreement is achieved by comparing the exact (obtained by FE) and estimated (obtained by OMA) eigenmodes. Then, from the calculated results, it's deduced that when angular springs are added to linear springs at

the laminate's edges, the vibratory behavior of the studied system becomes much better. In fact, reduced vibration amplitudes are obtained and an improved rigidity can be conferred to the considered structure due to the increasing of its natural frequencies.

References

[Abbès et al. 2011] M. S. Abbès, M. Miladi Chaabane, A. Akrout, T. Fakhfakh, and M. Haddar, "Vibratory behavior of a double panel system by the operational modal analysis", *Int. J. Model. Simul. Sci. Comput.* **2**:4 (2011), 459–479.

[Abdennadher et al. 2005a] M. Abdennadher, S. Fenina, L. Hammami, and M. Haddar, "Double glazing vibroacoustic behaviour", *Electron. J. Tech. Acoust.* **6** (2005), 1–12.

[Abdennadher et al. 2005b] M. Abdennadher, S. Fenina, L. Hammami, and M. Haddar, "Vibro-acoustic analysis of a double sandwich panels system", *Int. J. Eng. Simul.* **6**:1 (2005), 3–9.

[Akrout et al. 2008a] A. Akrout, L. Hammami, M. Ben Tahar, and M. Haddar, "Inter-facial shear effects of ultra-thin film on laminated glass plate dynamical behaviour", *Proc. Inst. Mech. Eng. C, J. Mech. Eng. Sci.* **222**:8 (2008), 1421–1433.

[Akrout et al. 2008b] A. Akrout, C. Karra, L. Hammami, and M. Haddar, "Viscothermal fluid effects on vibro-acoustic behaviour of double elastic panels", *Int. J. Mech. Sci.* **50**:4 (2008), 764–773.

[Akrout et al. 2009] A. Akrout, L. Hammami, M. Ben Tahar, and M. Haddar, "Vibro-acoustic behaviour of laminated double glazing enclosing a viscothermal fluid cavity", *Appl. Acoust.* **70**:1 (2009), 82–96.

[Akrout et al. 2010] A. Akrout, L. Hammami, C. Karra, M. Ben Tahar, and M. Haddar, "Vibro-acoustic damping simulation of two laminated glass panels coupled to viscothermal fluid layer", *Int. J. Acoust. Vib.* **15**:2 (2010), 79–90.

[Antoni 2005] J. Antoni, "Blind separation of vibration components: principles and demonstration", *Mech. Syst. Signal Process.* **19**:6 (2005), 1166–1180.

[Antoni et al. 2004] J. Antoni, L. Garibaldi, S. Marchesiello, and M. Sidahmed, "New separation techniques for output-only modal analysis", *Shock Vib.* **11**:3 (2004), 227–242.

[Antonio et al. 2003] J. M. P. Antonio, A. Tadeu, and L. Godinho, "Analytical evaluation of the acoustic insulation provided by double infinite walls", *J. Sound Vib.* **263**:1 (2003), 113–29.

[Assaf 1991] S. Assaf, *Modélisation par la méthode des éléments finis du comportement vibratoire des poutres et plaques sandwiches: métal matériaux viscoélastiques*, Ph.D. thesis, University of Technology of Compiègne, Compiègne, 1991.

[Basten et al. 2001] T. G. H. Basten, P. J. M. van der Hoogt, R. M. E. J. Spiering, and H. Tijdeman, "On the acousto-elastic behaviour of double-wall panels with a viscothermal air layer", *J. Sound Vib.* **243**:4 (2001), 699–719.

[Bouhioui 1993] H. Bouhioui, *Étude vibro-acoustique d'un montage en double parois de verre*, Ph.D. thesis, University of Technology of Compiègne, Compiègne, 1993.

[Carrera 2004] E. Carrera, "On the use of Murakami's zig-zag function in the modeling of layered plates and shells", *Comput. Struct.* **82** (2004), 541–554.

[Cheng et al. 2005] L. Cheng, Y. Y. Li, and J. X. Gao, "Energy transmission in a mechanically linked double-wall structure coupled to an acoustic enclosure", *J. Acoust. Soc. Am.* **117**:5 (2005), 2742–51.

[Hérault and Ans 1984] J. Hérault and B. Ans, "Réseaux de neurones à synapses modifiables: décodage de messages sensoriels composites par un apprentissage non supervise et permanent", *C. R. Acad. Sci. III Sci. Vie* **209**:13 (1984), 525–528.

[Hérault et al. 1985] J. Hérault, C. Jutten, and B. Ans, "Détection de grandeurs primitives dans un message composite par une architecture de calcul neuromimétique en apprentissage non supervise", pp. 1017–1022 in *Dixième Colloque sur le Traitement du Signal et ses Applications* (Nice, 1985), Groupe de Recherche et d'Étude de Traitement du Signal et des Images, Gif-sur-Yvette, 1985.

[Kerschen et al. 2007] G. Kerschen, F. Poncelet, and J.-C. Golinval, "Physical interpretation of independent component analysis in structural dynamics", *Mech. Syst. Signal Process.* **21** (2007), 1561–1575.

[Khdeir and Reddy 1999] A. A. Khdeir and J. N. Reddy, "Free vibrations of laminate composite plate using second-order shear deformation theory", *Comput. Struct.* **71** (1999), 617–626.

[Nguyen et al. 1994] H. L. Nguyen, J. Caelen, and C. Jutten, "Réhaussement de la parole par la séparation de sources dans un mélange convolutif", *J. Phys.* (*France*) *IV* **4**:C5 (1994), 541–544.

[Park et al. 2003] J. Park, L. Mongeau, and T. Siegmund, "Influence of support properties on the sound radiated from the vibrations of rectangular plates", *J. Sound Vib.* **264** (2003), 775–794.

[Poncelet et al. 2007] F. Poncelet, G. Kerschen, J.-C. Golinval, and D. Verhelst, "Output-only modal analysis using blind source separation techniques", *Mech. Syst. Signal Process.* **21** (2007), 2335–2358.

[Reddy 1997] J. N. Reddy, *Mechanics of laminated composite plates: theory and analysis*, CRC, Boca Raton, FL, 1997.

[Vallaban et al. 1997] C. V. G. Vallaban, M. Z. Asik, and K. Kandil, "Analysis of structural glazing systems", *Comput. Struct.* **65** (1997), 231–239.

[Zarzoso and Comon 2008] V. Zarzoso and P. Comon, "Robust independent component analysis for blind source separation and extraction with application in electrocardiography", pp. 3344–3347 in *Personalized healthcare through technology: proceedings of the 30th Annual International of the IEEE Engineering in Medicine and Biology Society* (Vancouver, BC, 2008), IEEE, Piscataway, NJ, 2008.

[Zenkert 1995] D. Zenkert, *An introduction to sandwich construction*, Engineering Materials Advisory Services, London, 1995.

[Zhou and Chelidze 2007] W. Zhou and D. Chelidze, "Blind source separation based vibration mode identification", *Mech. Syst. Signal Process.* **21** (2007), 3072–3087.

Received 5 Jun 2012. Revised 3 Oct 2012. Accepted 16 Oct 2012.

ALI AKROUT: ali.akrout@enit.rnu.tn
Mechanical Engineering Department, National School of Engineers of Sfax, Unit of Mechanics, Modelling and Manufacturing (U2MP), BP. 1173, 3038 Sfax, Tunisia

MARIEM MILADI CHAABANE: mariam.mi@hotmail.fr
Mechanical Engineering Department, National School of Engineers of Sfax, Unit of Mechanics, Modelling and Manufacturing (U2MP), BP. 1173, 3038 Sfax, Tunisia

LOTFI HAMMAMI: lotfi.hammami@enis.rnu.tn
Mechanical Engineering Department, National School of Engineers of Sfax, Unit of Mechanics, Modelling and Manufacturing (U2MP), BP. 1173, 3038 Sfax, Tunisia

MOHAMED HADDAR: mohamed.haddar@enis.rnu.tn
Mechanical Engineering Departement, National Engineering School of Sfax, Unit of Mechanics, Modelling and Manufacturing (U2MP), BP. 1173, 3038 Sfax, Tunisia

JOURNAL OF MECHANICS OF MATERIALS AND STRUCTURES
Vol. 7, No. 8-9, 2012
dx.doi.org/10.2140/jomms.2012.7.861

NETWORK EVOLUTION MODEL OF ANISOTROPIC STRESS SOFTENING IN FILLED RUBBER-LIKE MATERIALS: PARAMETER IDENTIFICATION AND FINITE ELEMENT IMPLEMENTATION

ROOZBEH DARGAZANY, VU NGOC KHIÊM, UWE NAVRATH AND MIKHAIL ITSKOV

A purely micromechanical network evolution theory granting new insight into the damage mechanism was proposed previously by the authors (Dargazany and Itskov, 2009). In this follow-up paper, we further formulate the network evolution model for implementation into finite element simulations. To this end, a general internal variable formulation is developed which determines the inelastic response of the microstructure on the basis of the free energy function. The thermodynamical consistency of the network evolution model is then verified analytically. Next, the predictive capabilities of the model are demonstrated by means of several experiments especially designed to capture stress softening, permanent set, and induced anisotropy. Finally, the influence of the filler concentration on material parameters is studied.

1. Introduction

Constitutive modeling of the macroscopic behavior of rubber-like materials has long been the subject of interest; see [Treloar 2005] or [Mark and Erman 2007] for an introduction. In the behavior of rubbers, hyperelasticity and stress softening are the most studied phenomena.

Investigations of inelastic effects in rubber materials, as, for example, stress softening, date back to the beginning of the last century, starting with [Bouasse and Carrière 1903; Holt 1932]. Later, Mullins and his coworkers investigated rubber-like materials in detail and reported different inelastic features of filled rubbers [Mullins and Tobin 1957; 1965], which still can hardly be modeled micromechanically.

Bueche [1960; 1961] associated the Mullins effect with the breakage of weak bonds between polymer chains and filler particles (see [Aksel and Hübner 1996]). This assumption was redefined by some authors as the slippage of polymer chains on filler clusters [Houwink 1956; Killian et al. 1994]. This concept has been further developed by describing the chain entanglements between particles [Hamed and Hatfield 1989] and has consequently been employed as a basis for the thermodynamical representation of continuum damage mechanics [Simo 1987; Miehe and Keck 2000]. Following the lead of Bueche, Govindjee and Simo [1991; 1992] decomposed the rubber matrix into a pure rubber network and a polymer-filler network, the latter being subjected to damage. The model was based on the isotropic three-chain model [James and Guth 1943], in which the damage depends on the largest principal stretch. The main assumption of their model is that damage takes place only in the presence of fillers. Indeed, recent experiments show that only filled elastomers that can crystallize show stress softening [Diani et al. 2009].

Rajagopal and Wineman [1992] developed a set of integral-type constitutive equations governing the microstructural damage induced by the rupture of molecular bonds and recreation of new ones. Based

Keywords: Mullins effect, stress softening, constitutive behavior, microstructures, anisotropic material, rubber material.

on this approach, stress softening and permanent set in some applications were calculated based on a neo-Hookean-type model [Huntley et al. 1996]. Using a similar technique, Demirkoparan et al. [2009] generalized the two-reference configuration theory proposed in [Wineman and Rajagopal 1990] to fibrous soft matter by considering the material as a composition of two components, in which the microstructure change only occurs in the fibrous component. The resulting model was able to capture stress softening and permanent set in fibrous materials.

By categorizing polymer chains into two types, flexed and extended, Drozdov and Dorfmann [2001] developed a micromechanically motivated model that can take stress softening and permanent set into account.

Based on the concept of pseudoelasticity, Dorfmann and Ogden [2004] proposed a phenomenological approach to account for permanent set. Combining the three-chain [James and Guth 1943] and eight-chain [Arruda and Boyce 1993] models, Elías-Zúñiga and Beatty [2002] proposed a model that successfully predicted the constitutive behavior of rubber under multiaxial loading conditions. The model had a relatively simple formulation and only three model parameters. Next, by redistributing of the representative chains in all possible orientations, the full network model was attained [Beatty 2003]. In another approach, Elías-Zúñiga and Rodríguez [2010] proposed a phenomenological damage function and substituted it into the non-Gaussian full-network model. The final model showed good agreement with experimental results on equibiaxial tension tests.

Hanson et al. [2005] associated the anisotropic Mullins effect with the removal of the chain entanglements during slippage of chains on each other. Thus, despite the constant number of active chains, the density of entanglements changes under deformation.

In order to describe the anisotropic Mullins effect, the idea of network decomposition of [1991] was exploited by Göktepe and Miehe [2005]. They further presented a microsphere model with 21 material directions instead of the three principal directions proposed by Govindjee and Simo [1991; 1992]. By considering nonaffinity in the polymer–polymer network, the developed model is also efficient for unfilled elastomers. Zimmermann and Wineman [2005] derived the constitutive theories that characterize the implications of polymer chains debonding on the mechanical properties of the rubber matrix, particularly induced anisotropy, and permanent set.

In another approach, Diani et al. [2006] further generalized the one-dimensional network alteration model into a three-dimensional model. Then, by proposing a phenomenological damage function, the losses of energy in different directions were taken into account. The so-obtained model was then compared with quasistatic experiments and agreed well with the measured residual strain and induced anisotropy.

In [Dargazany and Itskov 2009], we proposed a micromechanical constitutive model for carbon black filled rubber-like materials, which can describe such anisotropic inelastic phenomena as the Mullins effect, permanent set, and induced anisotropy. The model is based on the idea of network decomposition of [Govindjee and Simo 1991], where the rubber network is decomposed into a pure rubber network and a polymer-filler network. Damage in the polymer-filler network is considered as a consequence of chain sliding on or debonding from aggregates. In contrast to previous works on anisotropy of the Mullins effect, no phenomenological damage function is introduced. Damage in different directions is governed by a network evolution concept which describes changes in the interaggregate distribution of polymer

chains. The proposed model demonstrates very good agreement with experimental data with respect to the above-mentioned inelastic effects, although it considers filler aggregates as rigid bodies.

Moreover, the model benefits from its simplicity, small number of physically motivated material parameters, and fast fitting procedure. However, the predictions of the model were validated by only one set of experimental data and, furthermore, the thermodynamical consistency and implementation procedure of the model into finite element code were not discussed. Addressing these issues is the main goal of this work.

The paper is organized as follows. The fundamentals of the network evolution model are reviewed in Section 2. Then, the constitutive modeling approach is discussed in Section 3. In Section 4, the thermodynamical consistency of the model is studied and verified analytically. In order to implement the network evolution model into finite element simulations, the tangent tensor is derived using a linearization procedure discussed in Section 5. Section 6 describes the experimental procedure which is used later in Section 7 for evaluation of the material parameters. The implementation of the proposed constitutive model into commercial FE code (ABAQUS) is presented in Section 8. Finally, the Appendix provides details of the derivation of the tangent tensor.

2. Network evolution model

2.1. ***Statistical mechanics of a single chain.*** According to Gaussian statistics, the probability that a segment of a freely rotating chain with n segments and end-to-end distance R exists is given by

$$P_G(n, R)\, dR = \sqrt{\frac{\alpha'}{\pi n l^2}} \exp\left(-\frac{\alpha' R^2}{n l^2}\right) dR, \tag{1}$$

where l denotes the segment length and $\alpha' = \frac{3}{2}(1-\cos\theta)/(1+\cos\theta)$ is expressed in terms of the supplement to the valence angle $\theta = 70.5°$. Accordingly, the probability of existence of a polymer chain connecting two constrained segments, so that none of the segments between numbers 1 and n is joined to an aggregate surface, is given by (see [Dargazany and Itskov 2009])

$$P(n, \bar{R}) = \kappa \sqrt{\frac{\alpha'}{\pi n}} \exp A, \quad \text{with} \tag{2}$$

$$A = -\alpha' \frac{\bar{R}^2}{n} - \kappa \sqrt{\frac{\alpha'}{\pi}} \left[2\sqrt{n} \exp\left(-\alpha' \frac{\bar{R}^2}{n}\right) + 2\bar{R}\sqrt{\pi\alpha'} \left(\operatorname{erf}\left(\bar{R}\sqrt{\frac{\alpha'}{n}}\right) - \operatorname{erf}\left(\bar{R}\sqrt{\alpha'}\right) \right) - 2\exp(-\alpha' \bar{R}^2) \right],$$

where κ denotes the average area of active adsorption sites available for one bond.

(A bar over a parameter denotes its normalized value with respect to the segment length l: thus $\bar{R} = R/l$, and so on.)

Let us denote the vectors connecting the two ends of the chain in the reference and deformed configurations by $\boldsymbol{R}$ and $\boldsymbol{r}$, and their lengths by R and r, respectively. Accordingly, one has

$$\boldsymbol{r} = \mathbf{F}_m \boldsymbol{R}, \qquad r = \overset{D}{\lambda} R, \tag{3}$$

where $\mathbf{F}_m$ denotes the deformation gradient at the microscale, and $\overset{D}{\lambda} = \sqrt{\boldsymbol{D}\mathbf{F}_m^T \mathbf{F}_m \boldsymbol{D}}$ the microstretch in the direction specified by the unit vector $\boldsymbol{D}$. Hereafter, the following font styles are used: for a scalar X, a vector $\boldsymbol{X}$, a second-order tensor $\mathbf{X}$, and a fourth-order tensor $\mathbb{X}$.

Based on non-Gaussian statistics, the strain energy density of a freely rotating chain is written as

$$\psi_c(n, \bar{r}) = bnKT\Big(\frac{\bar{r}}{abn}\beta + \ln\frac{\beta}{\sinh\beta}\Big), \tag{4}$$

where the coefficients a and b are calculated by [Treloar 2005]

$$a = \frac{3}{2\alpha'}\cos^{-1}\Big(\frac{\theta}{2}\Big), \qquad b = \frac{2}{3}\alpha'\cos^2\Big(\frac{\theta}{2}\Big), \tag{5}$$

and $\beta = \mathscr{L}^{-1}(\bar{r}/abn)$ is expressed in terms of the inverse Langevin function $\mathscr{L}^{-1}$, while K and T denote Boltzmann's constant and the absolute temperature.

2.2. ***Strain energy of the rubber matrix.*** By considering rubber as a nearly incompressible material, its strain energy function $\Psi_N(\mathbf{C})$ can be decoupled into isochoric and volumetric parts by (see, for example, [Holzapfel 2000])

$$\Psi_N(\mathbf{C}) = \Psi_M(\bar{\mathbf{C}}) + U(J), \tag{6}$$

where $\mathbf{C}$ denotes the right Cauchy–Green tensor, $J^2 = \det\mathbf{C}$, and $\bar{\mathbf{C}} = J^{-2/3}\mathbf{C}$.

The rubber matrix is then decomposed into a pure rubber network (CC) and a polymer-filler network (PP) which act parallel to each other (for details see [Dargazany and Itskov 2009]). Accordingly, the isochoric strain energy of the rubber matrix Ψ_M can be represented as

$$\Psi_M = \Psi_{cc} + \Psi_{pp}, \tag{7}$$

where Ψ_{cc} and Ψ_{pp} denote the strain energies of the CC and PP networks per unit reference volume of the material (see Figure 1).

2.3. ***Pure rubber network.*** The pure rubber network is considered as an ideally elastic network with affine motion of cross-links and identical chains that are initially in the unperturbed state, in which the mean end-to-end distance of a freely rotating chain is $R_0 = a\sqrt{bn}$. Accordingly, the entropic energy of a single chain subjected to elongation is represented by

$$\psi(n, \overset{p}{\chi}) := \psi_c(n, \overset{p}{\lambda}\bar{R}_0), \tag{8}$$

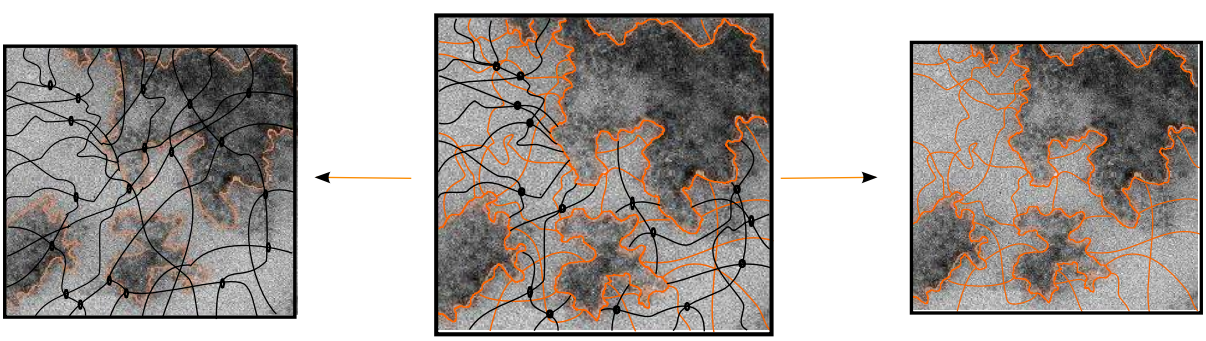

Figure 1. Illustration of the network decomposition concept.

where we keep in mind that in the CC network the microstretch $\overset{D}{\lambda}$ is equal to the macrostretch $\overset{D}{\chi}$. In order to obtain the strain energy of the CC network, N_c chains with n_c segments are considered in each spatial direction, so that

$$\Psi_{cc} = \frac{1}{A_s} \int_S N_c \psi(n_c, \overset{D}{\chi})\, d\overset{D}{u}, \tag{9}$$

where A_s represents the surface area of the microsphere S, and $\overset{D}{u}$ the unit area of the surface with the normal direction $\boldsymbol{D}$.

2.4. ***Polymer-filler network.*** The evolution of the polymer-filler network is assumed to be responsible for the already mentioned stress softening. Let $\tilde{N}(n, \bar{r})$ be the number of chains with number of segments (relative length) n, relative end-to-end distance $\bar{r}$, and end-to-end direction specified by the unit vector $\boldsymbol{D}$. The integration over the whole set D_A of relative chain lengths n available in the direction $\boldsymbol{D}$ further yields the free energy of chains in this direction as

$$\overset{D}{\Psi} = \int_{D_A} \tilde{N}(n, \bar{r}) \psi_c(n, \bar{r})\, dn. \tag{10}$$

The network evolution was described as an interaction of two simultaneous processes of aggregate-polymer debonding and network rearrangement. In the course of deformation, polymer chains begin to slide on or debond from the aggregates. This debonding starts with the shortest chain and gradually involves longer and longer chains. Under unloading, the debonded chains do not reattach back to the aggregate's active sites, and thus the maximal microstretch previously reached in the loading history,

$$\overset{D}{\lambda}_m = \max_{\tau \in (-\infty, t]} \overset{D}{\lambda}(\tau), \tag{11}$$

is crucial for the description of the polymer-filler debonding. Accordingly, the length of the shortest available chain in the deformed subnetwork is then obtained by (see also [Dargazany and Itskov 2009])

$$n_{c-f}(\overset{D}{\lambda}_m) = \frac{\nu \overset{D}{\lambda}_m \bar{R}}{ab}, \tag{12}$$

where $\nu > 1$ denotes a sliding ratio and is a material parameter.

Furthermore, we assume an upper limit for the length of a chain between two aggregates, denoted in the following by $n_{\max}$ (for details see [Dargazany and Itskov 2009]). Accordingly, the set of available relative lengths of chains bonded to aggregates in the direction $\boldsymbol{D}$ can be expressed by

$$D_A(\overset{D}{\lambda}_m) = \{n \mid n_{c-f}(\overset{D}{\lambda}_m) \le n \le n_{\max}\}. \tag{13}$$

By these means, the material behavior in the direction $\boldsymbol{D}$ is influenced by the loading history.

The concept of chain rearrangement in a rubber network suggests that the detachment of chains from the aggregate surface does not necessarily result in the complete loss of their role in the network entropic energy, but it may also lead to the activation of some new segments. Thus, all in all, one can assume that the total number of active segments remains constant. This assumption yields

$$\tilde{N}(n, \bar{r}) = N_0 \Phi(\overset{D}{\lambda}_m) P(n, \bar{R}) = N_0 \Phi(\overset{D}{\lambda}_m) \hat{P}(n), \tag{14}$$

where

$$\Phi(x) = \left(\int_{D_A(x)} \hat{P}(n) n\, dn \right)^{-1}. \tag{15}$$

We consider $\bar{R}$ as a material constant, and introduce the notation $\hat{P}(n) := P(n, \bar{R})$. The variable N_0 represents the number of active chains per unit undeformed volume, and will also be considered as a material parameter. Finally, considering (14) and (13) in (10), the energy of a subnetwork in direction $\boldsymbol{D}$ is obtained as

$$\overset{D}{\Psi} = N_0 \Phi(\overset{D}{\lambda}_m) \int_{D_A(\overset{D}{\lambda}_m)} \hat{P}(n) \psi_c(n, \overset{D}{\lambda} \bar{R})\, dn. \tag{16}$$

3. Constitutive modeling

3.1. ***Three-dimensional generalization.*** Assuming an isotropic spatial distribution of polymer chains in the rubber matrix, the macroscopic energy of a three-dimensional network can be written as

$$\Psi_{cc} = \frac{1}{A_s} \int_S N_c \psi(n_c, \overset{D}{\chi})\, d\overset{D}{u}, \qquad \Psi_{pp} = \frac{1}{A_s} \int_S \overset{D}{\Psi}\, d\overset{D}{u}. \tag{17}$$

The integration is carried out numerically by

$$\Psi_{cc} \cong \sum_{i=1}^{k} N_c \psi(n_c, \overset{D_i}{\chi}) w_i, \qquad \Psi_{pp} \cong \sum_{i=1}^{k} \overset{D_i}{\Psi} w_i, \tag{18}$$

where w_i are weight factors corresponding to the collocation directions $\boldsymbol{D}_i$ $(i = 1, 2, \ldots, k)$. As shown in [Ehret et al. 2010], the numerical scheme of [Heo and Xu 2001] demonstrates the least error in prediction of the induced anisotropy in comparison with the number of integration points and thus is used in this study. Accordingly, a set of $k = 45$ integration points on the half-sphere is chosen. Substitution of (16) into (18) yields the energy of the rubber matrix as

$$\Psi_M = \Psi_{cc} + \Psi_{pp} = \frac{\tilde{N}_c}{KT} \sum_{i=1}^{k} w_i \psi(n_c, \overset{D_i}{\chi}), + \frac{\tilde{N}_0}{KT} \sum_{i=1}^{k} w_i \int_{D_A(\overset{D_i}{\lambda}_m)} \Phi(\overset{D_i}{\lambda}_m)\, \hat{P}(n) \psi_c(n, \overset{D_i}{\lambda} \bar{R})\, dn, \tag{19}$$

where

$$\tilde{N}_c = N_c KT, \qquad \tilde{N}_0 = N_0 KT. \tag{20}$$

3.2. ***Strain amplification.*** In a filler-reinforced rubber network, the stretch of the polymer chains between aggregates (microstretch) generally exceeds the stretch applied to the rubber matrix (macrostretch). This strain amplification concept is based on the fact that filler aggregates are considerably stiffer than the polymer chains connecting them together [Rault et al. 2006]. This inhomogeneity of the material leads to the inhomogeneity in the microstretch distribution. Accordingly, the amplification function X is defined to establish a relationship between the microstretch $\overset{D}{\lambda}$ and the macrostretch $\overset{D}{\chi}$, and is written as

$$\overset{D}{\lambda} = X(\overset{D}{\chi}) = \frac{\overset{D}{\chi} - C^{\mathfrak{p}}}{1 - C^{\mathfrak{p}}}, \tag{21}$$

where $C \in (0, 1)$ represents the volume fraction of filler per unit volume of rubber matrix ($C < 0.3$ in most studies), and $\mathfrak{p}$ depends on the structure of the filler network. Bueche [1961] showed that $\mathfrak{p} = \frac{1}{3}$ in the case of a statistically homogeneous distribution of spherical particles (see, for example, [Govindjee 1997; Bergström and Boyce 1999]).

The strain amplification concept is based on the following assumptions.

(1) Filler aggregates are distributed and colonized randomly in three dimensions.

(2) The stiffness of the rubber matrix is negligible in comparison to that of the filler aggregates, and thus the filler aggregates can be considered as rigid inclusions.

(3) Changes in the aggregate's volume under deformation are negligible.

(4) There is no energy dissipation in the aggregates.

Let us represent parameters related to fillers, polymers, additives, and the rubber matrix by subscript f, p, a, and r, respectively. Then

$$C = \frac{V_f}{V_r}, \qquad V_r = V_f + V_p + V_a, \tag{22}$$

where $V_\bullet$ denotes the volume. In industrial applications, the amount of filler in a rubber sample is given by C_f which denotes the mass parts of filler per hundred parts of rubber (phr):

$$C_f = \frac{M_f}{M_p} = \frac{V_f}{V_p}\frac{\rho_f}{\rho_p}, \qquad M_r = M_f + M_p + M_a, \tag{23}$$

where $\rho_\bullet$ and $M_\bullet$ represent the density and mass of the corresponding ingredients, respectively. The amount of additive, which is mainly composed of processing agents, can be considered to be around 5–10 phr. Accordingly, one can simply express C as

$$C = \frac{V_f/V_p}{V_f/V_p + 1 + M_a/(\rho_a V_p)} = \frac{C_f \rho_p/\rho_f}{(1 + 0.1\rho_p/\rho_a) + C_f \rho_p/\rho_f}. \tag{24}$$

Note that (21) is valid as far as $\overset{D}{\chi} > C^{\mathfrak{p}}$, otherwise the deformation of aggregates should also be taken into account. Experimental results, however, show that the validity range of (21) lies within the elasticity range of samples.

The implementation of the strain amplification concept does not introduce any additional parameters into the model. It applies to microstretches and does not contradict the incompressibility constraint valid for the macroscale deformations. Indeed, this constraint is a purely macroscopic phenomenon and does not necessarily hold for microscopic deformations.

3.3. ***Macroscale behavior.*** Now, the total strain energy of the rubber matrix is given in (19). The constitutive equation for the first Piola–Kirchhoff stress tensor $\mathbf{P}$ can be written as

$$\mathbf{P} = \frac{\partial \Psi_M}{\partial \mathbf{F}} = \frac{\partial \Psi_{pp}}{\partial \mathbf{F}} + \frac{\partial \Psi_{cc}}{\partial \mathbf{F}}, \tag{25}$$

where

$$\begin{aligned}
\frac{\partial \Psi_{cc}}{\partial \mathbf{F}} &= \sum_{i=1}^{k} N_c w_i \left.\frac{\partial \psi(n_c, x)}{\partial x}\right|_{x=\overset{D_i}{\chi}} \frac{1}{2\overset{D_i}{\chi}} \frac{\partial \boldsymbol{D}_i \bar{\mathbf{C}} \boldsymbol{D}_i}{\partial \bar{\mathbf{F}}} : \frac{\partial \bar{\mathbf{F}}}{\partial \mathbf{F}}, \\
\frac{\partial \Psi_{pp}}{\partial \mathbf{F}} &= \sum_{i=1}^{k} w_i \frac{\partial \overset{D_i}{\Psi}}{\partial \overset{D_i}{\lambda}} \frac{\partial \overset{D_i}{\lambda}}{\partial \overset{D_i}{\chi}} \frac{1}{2\overset{D_i}{\chi}} \frac{\partial \boldsymbol{D}_i \bar{\mathbf{C}} \boldsymbol{D}_i}{\partial \bar{\mathbf{F}}} : \frac{\partial \bar{\mathbf{F}}}{\partial \mathbf{F}}.
\end{aligned} \tag{26}$$

These equations can be further simplified by means of the following identities:

$$\frac{\partial \psi_c(n, x\bar{R})}{\partial x} = \frac{1}{a}\bar{R}KT\mathcal{L}^{-1}\left(\frac{x\bar{R}}{abn}\right), \tag{27}$$

$$\frac{\partial \psi(n, x)}{\partial x} = \sqrt{bn}KT\mathcal{L}^{-1}\left(\frac{x}{\sqrt{bn}}\right), \tag{28}$$

$$\frac{\partial \overset{D}{\Psi}}{\partial \overset{D}{\lambda}} = N_0\Phi(\overset{D}{\lambda}_m)\int_{D_A(\overset{D}{\lambda}_m)} \hat{P}(n)\frac{\partial \psi_c(n, x\bar{R})}{\partial x}\bigg|_{x=\overset{D}{\lambda}} dn, \tag{29}$$

$$\frac{\partial \overset{D}{\lambda}}{\partial \overset{D}{\chi}} = \frac{1}{1-C^{\mathfrak{p}}}, \tag{30}$$

$$\frac{\partial \boldsymbol{D}\bar{\mathbf{C}}\boldsymbol{D}}{\partial \bar{\mathbf{F}}} : \frac{\partial \bar{\mathbf{F}}}{\partial \mathbf{F}} = 2\bar{\mathbf{F}}(\boldsymbol{D}\otimes\boldsymbol{D}) : J^{-1/3}\mathbb{I} = 2J^{-1/3}\bar{\mathbf{F}}(\boldsymbol{D}\otimes\boldsymbol{D}). \tag{31}$$

Thus, (25) yields

$$\mathbf{P} = \sum_{i=1}^{k}(P_{cc}(\boldsymbol{D}_i) + P_{pp}(\boldsymbol{D}_i))\frac{w_i}{\overset{D_i}{\chi}}J^{-1/3}\bar{\mathbf{F}}(\boldsymbol{D}_i\otimes\boldsymbol{D}_i), \tag{32}$$

where

$$P_{cc}(\boldsymbol{x}) = \tilde{N}_c\sqrt{bn_c}\mathcal{L}^{-1}\left(\frac{\overset{x}{\chi}}{\sqrt{bn_c}}\right), \tag{33}$$

$$P_{pp}(\boldsymbol{x}) = \frac{\bar{R}}{a}\frac{\tilde{N}_0}{1-C^{\mathfrak{p}}}\Phi(\overset{x}{\lambda}_m)\int_{D_A(\overset{x}{\lambda}_m)}\hat{P}(n)\mathcal{L}^{-1}\left(\frac{\overset{x}{\lambda}\bar{R}}{abn}\right)dn. \tag{34}$$

A proper approximation approach for the inverse Langevin function can be chosen depending on the elongation range of polymer chains. In this study, the elongation ratio at which the chains are debonded from the aggregate surface is described by ν. Depending on its value, two different functions approximating the inverse Langevin function are utilized.

In cases of moderate and large deformations, Taylor expansion is more favorable (see [Itskov et al. 2012]). However, if chain breakage occurs very close to the fully stretched state of the chains $\nu < 1.04$, then Padé approximants [Puso 2003] show better agreement with the exact values. Accordingly

$$\mathcal{L}^{-1}(x) \cong \begin{cases} \displaystyle\sum_{i=0}^{n} C_i x^i & \text{if } \nu \geq 1.04, \\ \dfrac{3x}{1-x^3} & \text{if } \nu < 1.04, \end{cases} \tag{35}$$

where the number of terms n and the values of C_i are given in [Itskov et al. 2012].

4. Thermodynamic consistency

Since the strain energy of the rubber matrix Ψ_M is influenced by a number of internal variables, namely $\overset{D}{\lambda}_m$, one can rewrite Ψ_M as

$$\Psi_M := \hat{\Psi}_M(\bar{\mathbf{C}}, \boldsymbol{\Omega}) = \tilde{\Psi}_M(\bar{\mathbf{F}}, \boldsymbol{\Omega}), \tag{36}$$

where

$$\boldsymbol{\Omega} = \{\overset{\boldsymbol{D}}{\lambda}_m : \boldsymbol{D} \in \mathbb{V}^3 \wedge |\boldsymbol{D}| = 1\}. \tag{37}$$

Accordingly, the Clausius–Duhem inequality resulting from the second law of thermodynamics can be reduced to

$$-\partial_{\overset{\boldsymbol{D}}{\lambda}_m} \Psi_M \cdot (\dot{\overset{\boldsymbol{D}}{\lambda}}_m) \geq 0 \quad \text{for all } \boldsymbol{D}. \tag{38}$$

Under unloading and reloading $\dot{\overset{\boldsymbol{D}}{\lambda}}_m = 0$ while $\dot{\overset{\boldsymbol{D}}{\lambda}}_m > 0$ in primary loading. Thus, the Clausius–Duhem inequality is satisfied if during the primary loading, the following inequality:

$$\frac{\partial \Psi_M}{\partial \overset{\boldsymbol{D}}{\lambda}_m} \leq 0 \quad \text{for all } \boldsymbol{D} \tag{39}$$

holds. With respect to (7) and (18), (38) yields

$$\frac{\partial \overset{\boldsymbol{D}}{\Psi}}{\partial \overset{\boldsymbol{D}}{\lambda}_m} \leq 0 \quad \text{for all } \boldsymbol{D}. \tag{40}$$

We will prove (40) for an arbitrary direction $\boldsymbol{D}$ and for the sake of brevity denote $\overset{\boldsymbol{D}}{\lambda}_m$ by x. Using (16) we further obtain

$$\frac{d\Phi(x)}{dx} \int_{n_{c-f}(x)}^{n_{\max}} \hat{P}(n)\psi_c(n, \lambda\bar{R})\, dn - \frac{dn_{c-f}(x)}{dx}\Phi(x)\hat{P}(n_{c-f}(x))\psi_c(n_{c-f}(x), \lambda\bar{R}) \leq 0, \tag{41}$$

where

$$\frac{d\Phi(x)}{dx} = -x\left(\frac{\upsilon\bar{R}}{ab}\right)^2 \Phi^2(x)\hat{P}(n_{c-f}(x)). \tag{42}$$

Since (41) should be verified just during the primary loading ($\dot{\overset{\boldsymbol{D}}{\lambda}}_m = \dot{\overset{\boldsymbol{D}}{\lambda}}$), it can be rewritten as

$$n_{c-f}(x)\left(\int_{n_{c-f}(x)}^{n_{\max}} \hat{P}(n)\psi_c(n, \lambda\bar{R})\, dn\right) - \left(\int_{n_{c-f}(x)}^{n_{\max}} \hat{P}(n)n\, dn\right)\psi_c(n_{c-f}(x), \lambda\bar{R}) \leq 0, \tag{43}$$

which holds since, in view of (2), we have the following inequalities:

$$n_{c-f}(x) \leq n \quad \text{for all } n \in \{n_{c-f}(x), n_{\max}\}, \qquad \text{hence} \qquad n_{c-f}(x) < \int_{n_{c-f}(x)}^{n_{\max}} \hat{P}(n)n\, dn;$$

and

$$\psi_c(n_{c-f}(x), x\bar{R}) \geq \psi_c(n, x\bar{R}) \quad \text{for all } n \in \{n_{c-f}(x), n_{\max}\},$$

hence

$$\int_{n_{c-f}(x)}^{n_{\max}} \hat{P}(n)\psi_c(n, x\bar{R})\, dn < \psi_c(n_{c-f}(x), x\bar{R}).$$

5. Finite element linearization

In the following we derive the tangent tensor defined by

$$\mathbb{C} = 2\frac{\partial \mathbf{S}}{\partial \mathbf{C}}, \tag{44}$$

where $\mathbf{S}$ denotes the second Piola–Kirchhoff stress tensor. By using the fourth-order deviatoric projection tensor in the Lagrangian description

$$\mathbb{P}_{\text{Dev}} = \mathbb{I}^s - \tfrac{1}{3}\mathbf{C}^{-1} \odot \mathbf{C}, \tag{45}$$

for a nearly incompressible material $\mathbf{S}$ is formulated as

$$\mathbf{S} = 2\frac{\partial \Psi_N(\mathbf{C}, \Omega)}{\partial \mathbf{C}} = 2\frac{\partial \Psi_M}{\partial \bar{\mathbf{C}}} : \frac{\partial \bar{\mathbf{C}}}{\partial \mathbf{C}} + 2\frac{\partial U}{\partial J}\frac{\partial J}{\partial \mathbf{C}} = \underbrace{J^{-2/3}(\mathbb{P}_{\mathrm{Dev}} : \bar{\mathbf{S}})}_{\mathbf{S}^{\mathrm{iso}}} + \underbrace{U' J \mathbf{C}^{-1}}_{\mathbf{S}^{\mathrm{vol}}}, \tag{46}$$

where $\bar{\mathbf{S}} = 2\partial \Psi_M / \partial \bar{\mathbf{C}}$.

Accordingly, the tangent tensor of the rubber matrix is given by

$$\mathbb{C} = 2\frac{\partial \mathbf{S}}{\partial \mathbf{C}} = \underbrace{2\frac{\partial \mathbf{S}^{\mathrm{iso}}}{\partial \mathbf{C}}}_{\mathbb{C}^{\mathrm{iso}}} + \underbrace{2\frac{\partial \mathbf{S}^{\mathrm{vol}}}{\partial \mathbf{C}}}_{\mathbb{C}^{\mathrm{vol}}}. \tag{47}$$

Substituting (46) into (47) gives

$$\mathbb{C}^{\mathrm{iso}} = J^{-4/3}\mathbb{P}_{\mathrm{Dev}} : \bar{\mathbb{C}} : \mathbb{P}^T_{\mathrm{Dev}} - \tfrac{2}{3} J^{-2/3}[\mathbf{C}^{-1} \odot \bar{\mathbf{S}} + \bar{\mathbf{S}} \odot \mathbf{C}^{-1}] + \tfrac{2}{3}(\bar{\mathbf{S}} : \bar{\mathbf{C}})\mathbb{Z}, \tag{48}$$

$$\mathbb{C}^{\mathrm{vol}} = J\big(U'' J + \tfrac{5}{3} U'\big)\mathbf{C}^{-1} \odot \mathbf{C}^{-1} - 2U' J \mathbb{Z}, \tag{49}$$

where the fourth-order tensor products are defined in [Itskov 2009].

Finally, the tangent tensor is obtained in view of (47) as

$$\mathbb{C} = J^{-4/3}\mathbb{P}_{\mathrm{Dev}} : \bar{\mathbb{C}} : \mathbb{P}^T_{\mathrm{Dev}} - \tfrac{2}{3} J^{-2/3}(\mathbf{C}^{-1} \odot \bar{\mathbf{S}} + \bar{\mathbf{S}} \odot \mathbf{C}^{-1}) + \tfrac{2}{3}(\bar{\mathbf{S}} : \bar{\mathbf{C}} - 3U' J)\mathbb{Z} + J\big(U'' J + \tfrac{5}{3} U'\big)\mathbf{C}^{-1} \odot \mathbf{C}^{-1}, \tag{50}$$

where $\mathbb{Z} = \big[\frac{1}{3}\mathbf{C}^{-1} \odot \mathbf{C}^{-1} + (\mathbf{C}^{-1} \otimes \mathbf{C}^{-1})^{s}\big]$ and $\bar{\mathbb{C}}$ is given by (see details in the Appendix)

$$\bar{\mathbb{C}} = 2\frac{\partial \bar{\mathbf{S}}}{\partial \bar{\mathbf{C}}} + 2\sum_{i=1}^{k} \frac{\partial \bar{\mathbf{S}}(\bar{\mathbf{C}}, \Omega)}{\partial \overset{\boldsymbol{D}_i}{\lambda}_m} \odot \frac{\partial \overset{\boldsymbol{D}_i}{\lambda}_m}{\partial \bar{\mathbf{C}}}. \tag{51}$$

6. Experiment

The experimental study[1] presented here consists of three parts: loading in two orthogonal directions to capture induced anisotropy, multiaxial tension tests to evaluate model accuracy, and cyclic tension tests on a compound with different filler concentrations to investigate the influence of material parameters.

6.1. ***Loading in two orthogonal directions.*** In this experiment we used a cross-shaped specimen (Figure 2) made of 50 phr carbon black filled polychloroprene rubber (CR). The exact composition of the elastomer used in this experiment is given in Table 1. The experiment was performed at room temperature with a strain rate of 40% /min.

The four arms of the cross-shaped specimens have multiple slits parallel to the sides to obtain a nearly homogeneous state of uniaxial tension in the measurement area (see, for example, [Pawelski 2001]). The specimens were loaded by a spindle-driven two-pillar universal tensile test machine. The machine provides a constant clamping force, which is important for measurement reproducibility [Itskov et al. 2006]. Fast clamping and unclamping procedures furthermore reduced the influence of time-dependent

[1]The experimental part of this work is a result of cooperation with Professor E. Haberstroh (Institute of Rubber Technology, RWTH Aachen University) whose contribution is gratefully acknowledged.

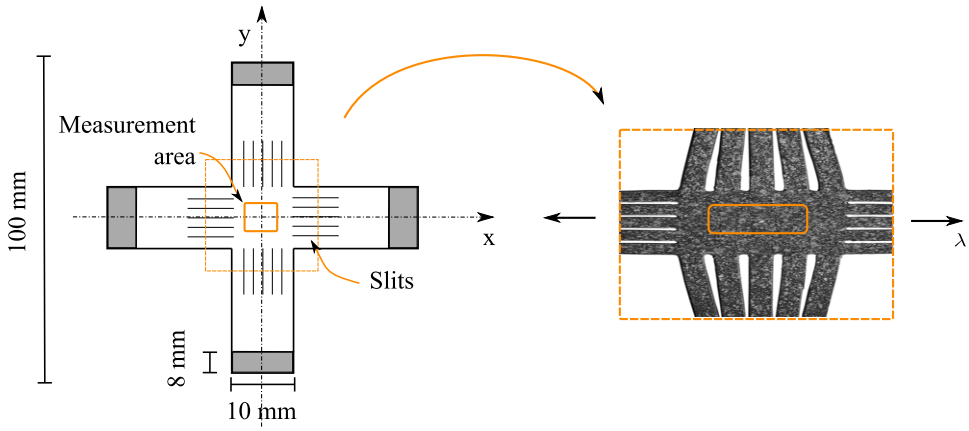

Figure 2. A cross-shaped specimen in its virgin and deformed states. The measurement area retains its rectangular form, which implies a homogeneous strain distribution there.

effects such as relaxation. Using an optical measuring system, stretches in the measurement area were evaluated by a noncontact method.

The experimental procedure was as follows: the virgin specimen was subjected to loading-unloading cycles of uniaxial tension (in the x-direction) with increasing stretch amplitudes of 1.15, 1.30, 1.45, 1.60, and 1.75. Five cycles were conducted for each stretch amplitude.

After unloading to the stress-free state, the sample was unclamped and reclamped for consequent loading in the orthogonal direction (the y-direction). Despite resulting residual strains from the previous loading cycles, the new configuration is considered as the reference configuration for the loading in the y-direction. The above-described loading procedure was repeated again in the y-direction.

The nominal stress P is plotted versus stretch χ in Figure 3a. Under tension in the x-direction, the classical Mullins effect and permanent set can be seen after the first loading cycle. Under tension in the y-direction, the strong anisotropy of the Mullins effect can be observed.

In order to resume the ideal Mullins effect, the hysteresis observed in the second and subsequent cycles is eliminated from the experimental data. Accordingly, Figure 3b illustrates the idealized Mullins effect, permanent set, and induced anisotropy.

Compound	phr	Density (kg/m^3)
Polychloroprene (CR)	100	1210
Carbon black (N330)	50	1800
Antioxidant	2	990
Processing aids	1.5	1230
Activator	2	3600
Cross-linker	5	2000
Plasticizer	2	970

Table 1. Compound specifications of the rubber sample used for the cross-shaped specimen.

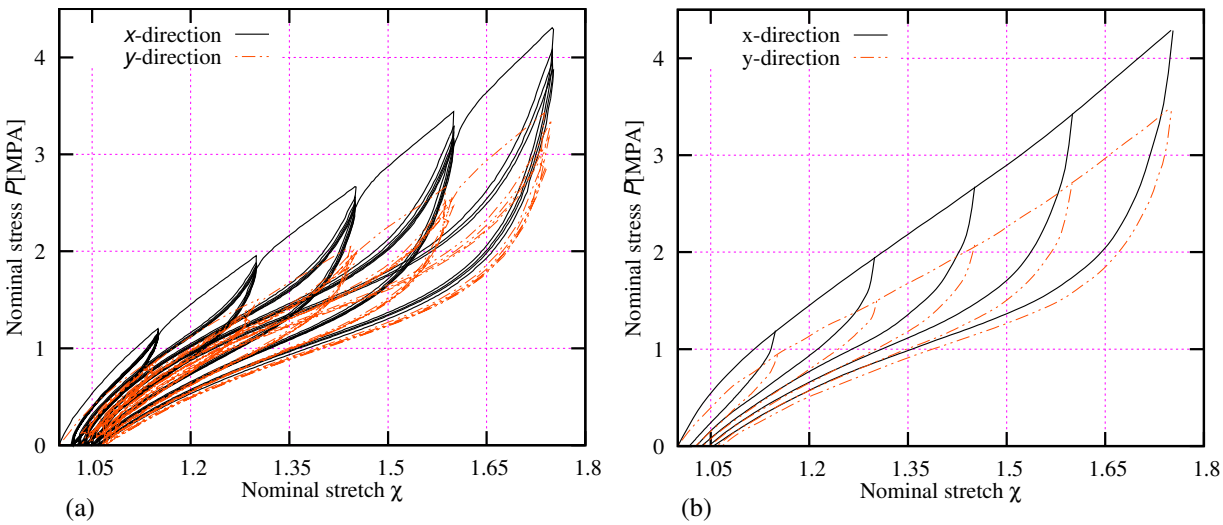

Figure 3. (a) Initial and (b) treated experimental results of the uniaxial tension test of the cross-shaped specimen in the two orthogonal directions.

6.2. ***Multiaxial tension test.*** To investigate the evolution of the deformation-induced anisotropy, its magnitude was studied by loading in different directions, in the following experiment.

A large specimen was elongated up to a certain stretch level then unloaded (one complete uniaxial tension cycle). Then, a small dumbbell-shaped specimen was cut from the prestretched specimen at an angle Φ inclined to the initial tension direction, with $\Phi = 0°, 15°, 22.5°, 45°, 67.5°, 90°$ (see Figure 4). The small samples were then loaded up to the same stretch level as the large sample and then unloaded.

Using this approach, one can study the mechanical response of the material in different directions. The comparison of the responses of the large and small specimens for $\Phi = 0°$ is shown in Figure 5.

The samples were made of 50 phr (24% by volume) carbon black filled polychloroprene rubber (CR) with the composition given in Table 2. The mechanical responses of the small samples for different

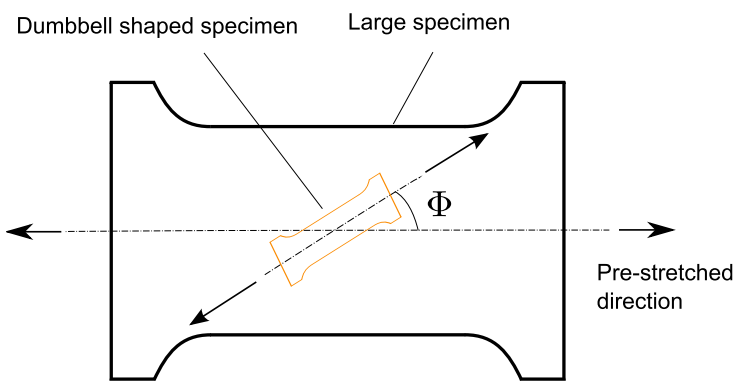

Figure 4. Sample preparation for multiaxial tension test. Small samples were cut under a certain angle Φ to the prestretch direction of the large sample.

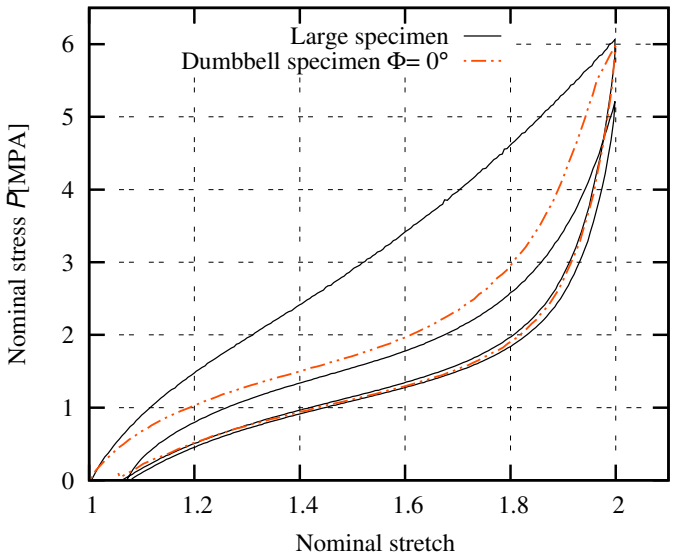

Figure 5. The mechanical response of the large sample in comparison with the smaller one.

Compound	phr	Density (kg/m^3)
Polychloroprene (CR)	100	1210
Carbon black (N330)	50	1800
Antioxidant	1	990
Processing aids	4	1230
Activator	1	3600
Cross-linker	5	2000
Plasticizer	10	970

Table 2. Compound specifications of the rubber sample used in the multiaxial experiment.

directions are depicted in Figure 6. One observes that the Mullins effect decreases with increasing angle Φ.

6.3. ***Influence of the filler concentration.*** It is expected that stress softening increases in compounds with higher filler concentrations. In this experiment, a compound with three different filler concentrations was used. The ingredients of the compound are given in Table 2, and the filler concentrations are 20, 40, and 60 phr (11, 20, and 28% by volume). The transverse loading experiment described in Section 6.1 is then applied to each sample. The results plotted in Figure 7 confirm that the Mullins effect, permanent set, and hysteresis are more pronounced in samples with higher filler concentrations.

7. Comparison with experimental results

The objective of this section is to assess the predictive capabilities of the proposed constitutive model by comparing it with the experimental data presented in Section 6.

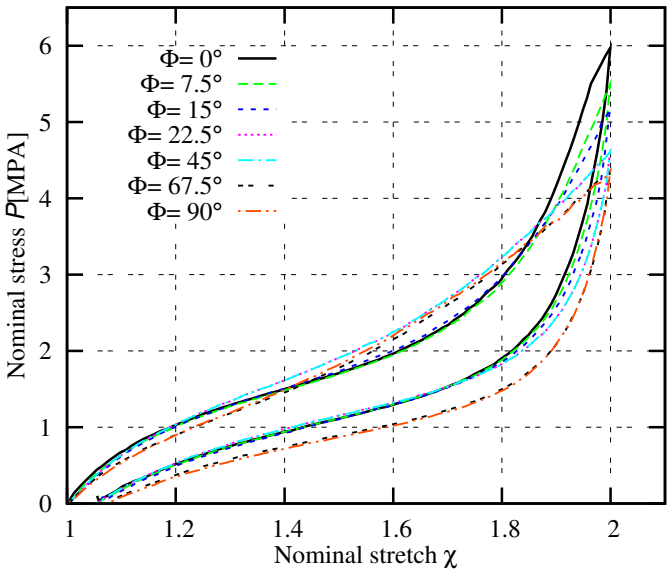

Figure 6. Experimental results of uniaxial tensile tests on small samples cut under different angles Φ from the large sample.

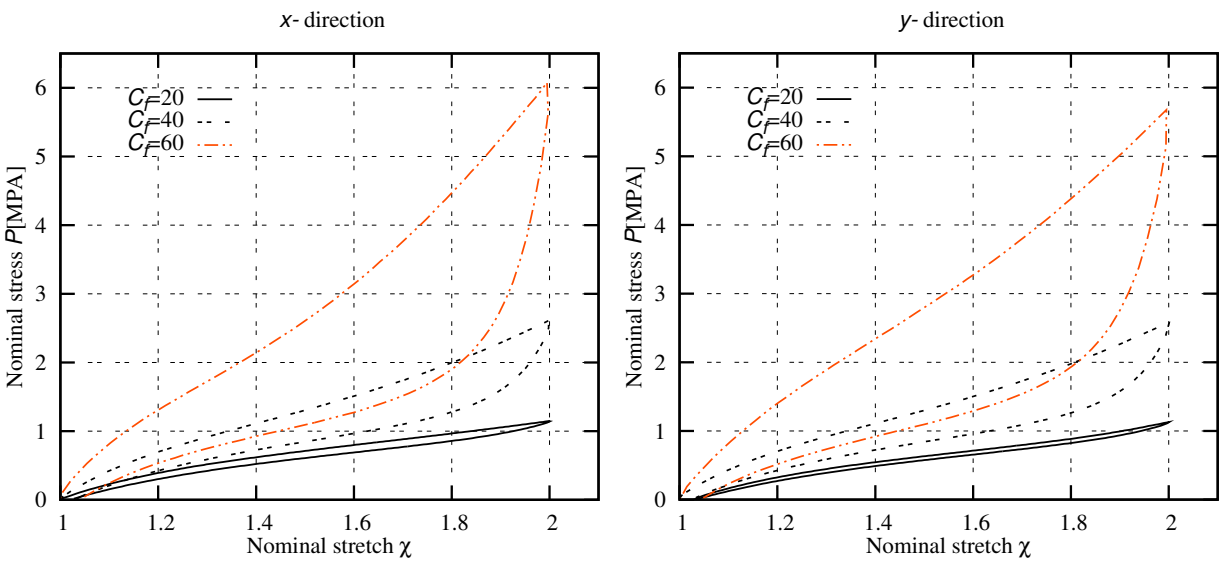

Figure 7. Experimental results of the uniaxial deformation of samples with different filler concentrations in the (left) x and (right) y-directions.

7.1. ***Transverse loading.*** By means of seven material parameters, the model was fitted to the transverse loading experimental data presented in Section 6.1. To this end, the least-square error function was minimized with the aid of the Levenberg–Marquardt algorithm. The obtained values of the material parameters are given in Table 3, while the predicted stress-stretch curves are plotted in Figure 8 against the experimental diagrams for the x and y-directions.

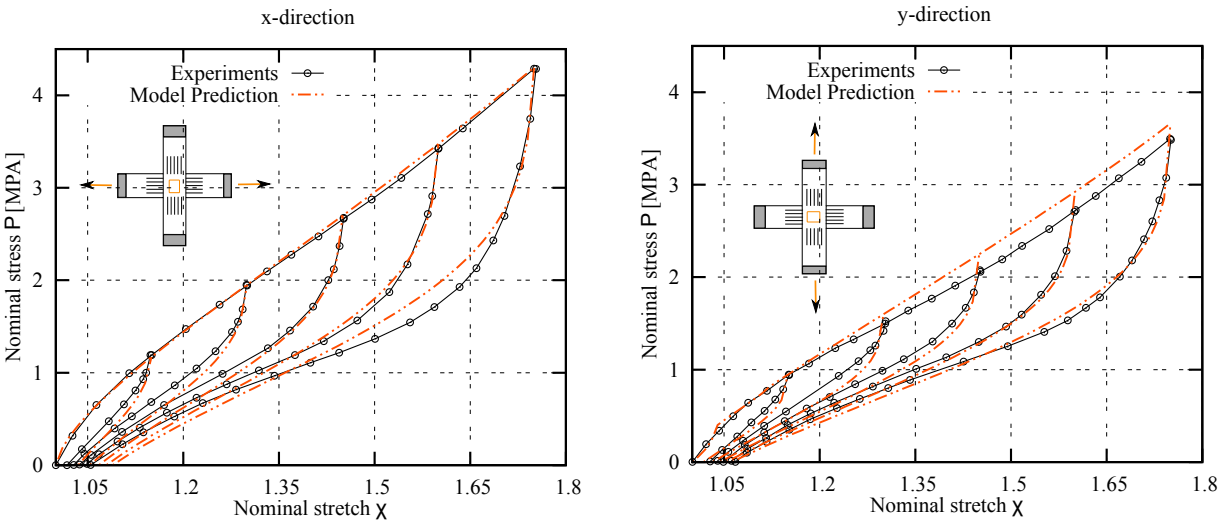

Figure 8. Comparison of the nominal stress-stretch curves of the model and the experiment for the uniaxial tension test in the (left) x and (right) y-directions.

κ	ν	$\bar{R}$	$n_{\max}$	n_c	$\tilde{N}_0$ (MPa)	$\tilde{N}_c$ (MPa)
14.824	1.0065	6.406	24.9135	100	2.8356	1.8141

Table 3. Parameters of the network evolution model for 50 phr CR used in the transverse loading experiment.

κ	ν	$\bar{R}$	$n_{\max}$	n_c	$\tilde{N}_0$ (MPa)	$\tilde{N}_c$ (MPa)
4.218	1.0057	5.558	26.425	100	6.722	1.167

Table 4. Parameters of the network evolution model for 50 phr CR used in the multiaxial loading experiment.

The loading-unloading cycle of the 1.6 stretch amplitude in the x-direction was used for the fitting. Thus, good agreement with other unloading curves in the x-direction and all loading-unloading curves in the y-direction was obtained automatically.

7.2. ***Multiaxial tension test.*** In the multiaxial tension test, the residual stretches in the small samples were taken into account in their new reference configurations.

The material parameters given in Table 4 were obtained by fitting the model to the experimental data on the large sample. Then, using these parameters, the multiaxial loading experiment was simulated and compared to the experimental data as shown in Figure 9.

7.3. ***Influence of the filler concentration.*** The aim of this experiment was to check the capabilities of our model to simulate rubbers with different filler concentrations. To this end, samples made of the same compound and different filler concentrations were analyzed.

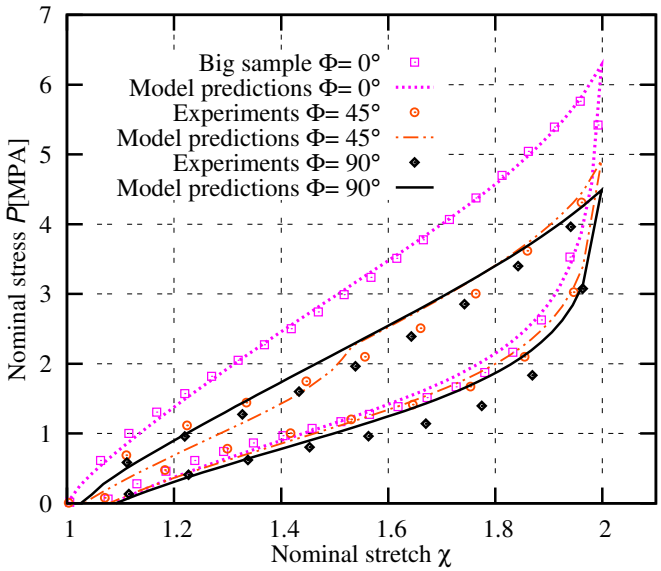

Figure 9. Comparison of the model predictions with the experimental results for the $\Phi = 0°, 45°, 90°$ small samples.

C_f (phr)	κ	ν	$\bar{R}$	$n_{\max}$	n_c	$\tilde{N}_0$ (MPa)	$\tilde{N}_c$ (MPa)
60	1.6203	1.0050	4.8700	24.7144	100	8.5121	1.0372
40	0.8094	1.0050	5.6747	38.7337	100	8.5121	1.0372
20	0.002552	1.0050	6.7090	97.1366	100	8.5121	1.0372

Table 5. Parameters of the network evolution model for fitting to compounds with different filler concentrations. Constant material parameters are shaded.

Since the sample materials differed from each other just in filler concentration, the material parameters independent of the filler concentration should remain constant for all simulations.

To verify this concept, we first calculated the seven material parameters of the model by fitting to the uniaxial loading result of 60 phr CR in the x-direction (see Table 5). Then, the model simulations were compared to the experimental results for this material in the x and y-directions (see Figure 10).

The parameters $\{\kappa, R, n_{\max}\}$ are directly influenced by the concentration of filler and ν by the type of filler. The parameters $\{n_c, \tilde{N}_0, \tilde{N}_c\}$ highly depend on the cross-linking and monomer properties, which are constant in the three samples. In addition, the number of active segments in a network, namely $\{\tilde{N}_0, \tilde{N}_c\}$, slightly changes with the filler concentration due to the immobilization of some segments around the aggregates, which are generally referred to as bound rubber. However, by excluding the effect of the bound rubber, the parameters $\{\nu, n_c, \tilde{N}_0, \tilde{N}_c\}$ can be assumed to be independent of the filler concentration.

In the next step, simulating the behavior of 40 and 20 phr CR, the material parameters $\{\nu, n_c, \tilde{N}_0, \tilde{N}_c\}$ were taken from the fitting to 60 phr CR experimental data, and the rest, $\{\kappa, R, n_{\max}\}$, approximated by phenomenological relations which take the forms of power functions in terms of the filler concentration.

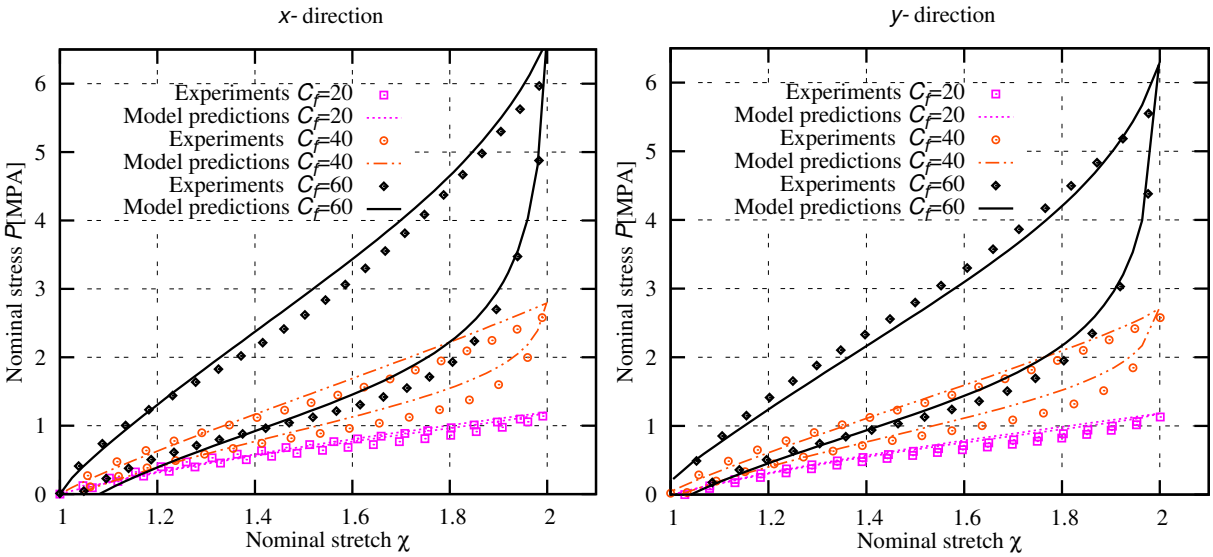

Figure 10. Comparison of the model predictions with the experimental results of samples with different filler concentrations. A transverse loading experiment is applied to each sample and the results in the (left) x and (right) y-directions are compared.

Despite the error induced by neglecting the effect of bound rubber, the predictions of the model using the aforementioned set of parameters show relatively good agreement with experimental results (see Figure 10). This further suggests that the changes in material parameters for different filler concentrations can be obtained by performing only one fitting procedure and enables one to simulate rubbers of the same compound with various filler concentrations based on only one set of fitting parameters.

8. Application examples

In this section, our model, implemented into the commercial FE code ABAQUS, is illustrated by two examples with large inhomogeneous deformations. First, the behavior of a thin rubber sheet with a hole in the middle is simulated and compared with experimental results under uniaxial tension. In the second test, the model predicts the behavior of an industrial damper under cyclic loading.

8.1. ***Rectangular rubber specimen with a central hole under uniaxial tension.*** The objective of this experiment is to assess the accuracy of the proposed constitutive model in predicting complex strain fields.

The specimen is made of a 60 phr carbon black filled rubber, with the exact compound given in Table 5. It has a rectangular shape ($100 \times 35 \times 2$ mm) with a hole of $D = 14$ mm at its center (see Figure 11). The hole was punched out by a mechanical cutting device.

The experiment is performed at room temperature with a strain rate of $\dot{\epsilon} = 0.4$ /s and stretch amplitude of $\epsilon = 0.75$. The strain field on the surface of the specimen is accurately measured by an optical measuring system (GOM Aramis), where the displacements of several points on the sample are captured and a detailed displacement field is provided.

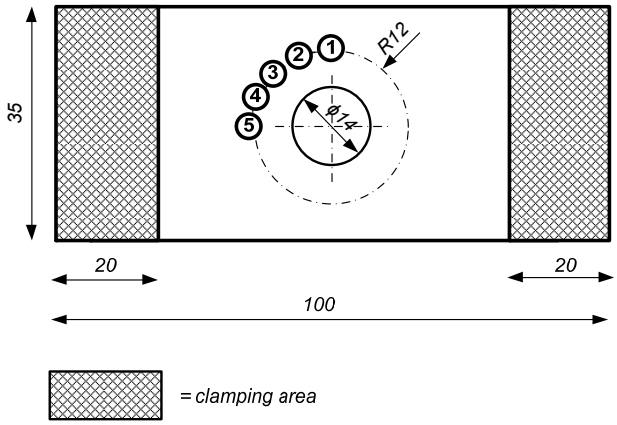

Figure 11. Shape of the test specimen.

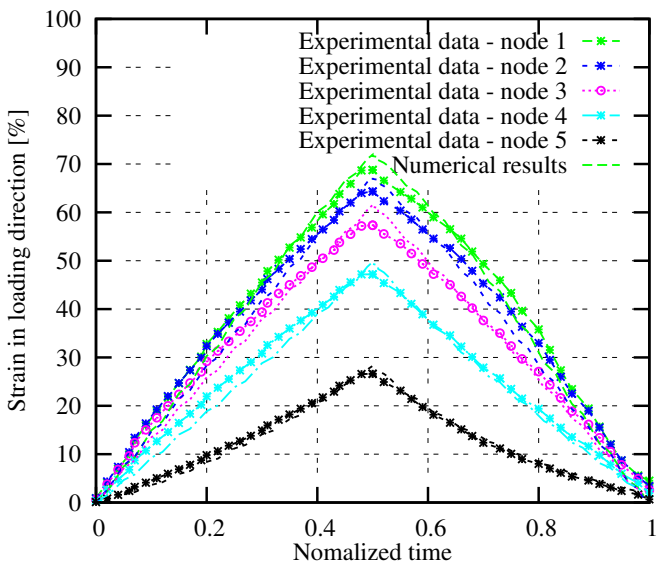

Figure 12. Comparison between strains in the loading direction from the FE results and the experimental data.

Five points on the specimen surface are chosen, as shown in Figure 11. Strains at these points are compared with the numerical results of the model simulations with 922 cubic elements. Good agreement between the experimental data and the numerical simulation is observed (see Figure 12).

8.2. ***Rubber suspension system.*** In another example, the model is used to simulate the behavior of a rubber component in an industrial application. To this end, cyclic loading of a cylindrical rubber string[2], shown in Figure 13, is simulated and compared with the measured data. The specimen is part of a suspension unit that is generally used as an impact stop, oscillation damper, or pivot bearing in machine constructions. The housing and the shaft of the bearing are made of steel. The string is made of carbon

[2]The samples used in this experiment are manufactured and provided by ROSTA AG.

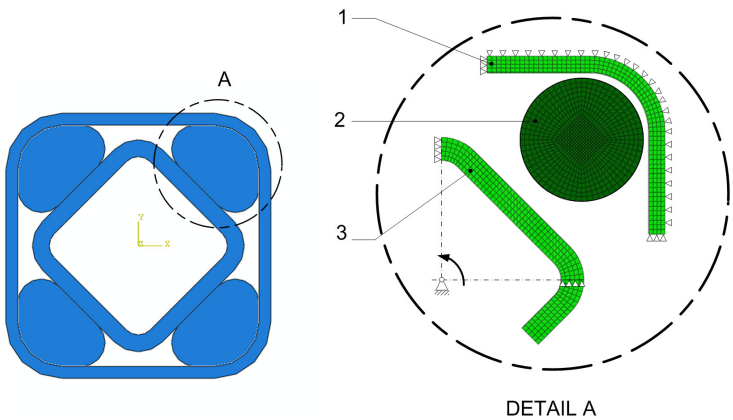

Figure 13. Assembled rubber suspension unit with housing (1), string (2), and shaft (3).

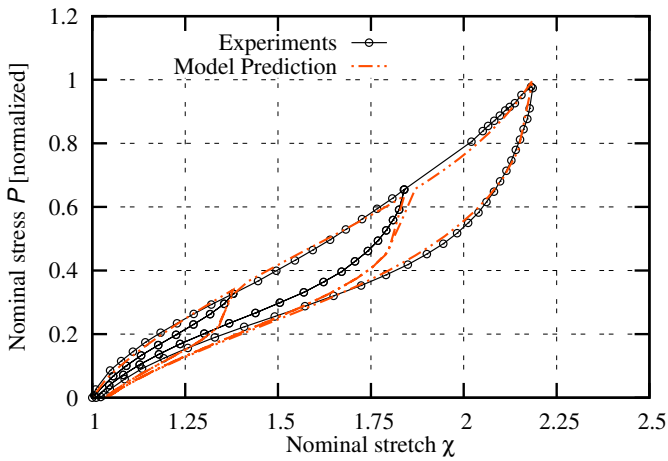

Figure 14. Comparison of the model predictions with the experimental results for the material of the string.

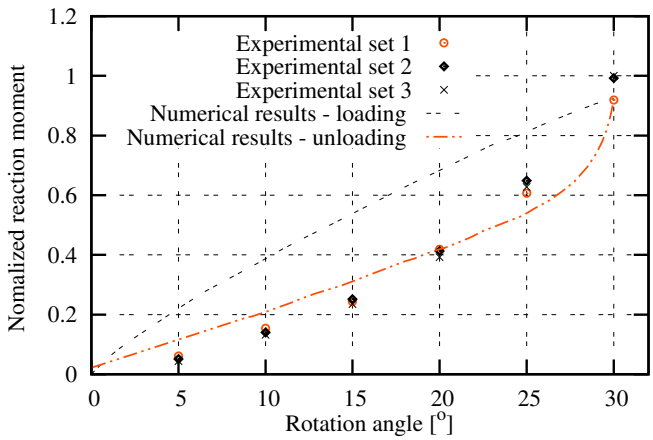

Figure 15. Comparison of the reaction moment at the center axis of the shaft for the FE results and the experiment.

black filled rubber with material constants obtained by fitting to the experimental data provided by the manufacturer, ROSTA AG (Figure 14).

Due to the symmetry of the structure, appropriate boundary conditions were applied to one-quarter of the rubber suspension unit, which was discretized by 2094 linear cubic elements. The simulation of the rubber suspension unit started with the assembly process from undeformed state (Figure 13), following by rotation of the shaft inside the bearing.

In Figure 15, the model predictions for the moment normalized with respect to the length of the string are plotted versus the angle and compared with the experimental data for the reaction moment. This was measured after five loading-unloading cycles, which corresponds to the unloading curve of our model. This curve demonstrates good agreement with the above-mentioned experimental data (see Figure 15).

9. Concluding remarks

The previously proposed network evolution model for carbon black filled rubbers exhibiting anisotropic Mullins effect is implemented here for finite elements simulations. To this end, the tangent moduli for elastic and nonelastic regimes are formulated in terms of internal variables. Additionally, the thermodynamical consistency of the model is proved.

In the next part, the concepts and predictive capabilities of the model are validated experimentally. The performance of the model is illustrated by comparing it to different sets of experimental data particularly designed to reveal the anisotropic Mullins effect and permanent set. Next, the predictive capabilities of the model are verified by comparing compounds with different filler concentrations. The model is also implemented into the FEM commercial code ABAQUS and its predictions for complex loading and geometrical problems are compared with the experimental data.

Everywhere, the model illustrated very good agreement with the experimental data. This fact, in addition to the simplicity of the proposed model, makes it a suitable option for commercial and industrial applications.

Appendix: Derivation of tangent tensors

In view of (36), the second Piola–Kirchhoff stress tensor $\bar{\mathbf{S}}$ is a nonlinear tensor valued-tensor function of state variables $\bar{\mathbf{C}}$ and Ω, defined as follows:

$$\bar{\mathbf{S}}(\bar{\mathbf{C}}, \Omega) = 2\frac{\partial \hat{\Psi}_M(\bar{\mathbf{C}}, \Omega)}{\partial \bar{\mathbf{C}}} = 2\frac{\partial \Psi_{cc}}{\partial \bar{\mathbf{C}}} + 2\frac{\partial \Psi_{pp}}{\partial \bar{\mathbf{C}}} = \bar{\mathbf{S}}_{cc} + \bar{\mathbf{S}}_{pp}. \tag{A.1}$$

Accordingly, in view of (27) one has

$$\begin{aligned}
\bar{\mathbf{S}}_{cc} &= 2\frac{\partial \Psi_{cc}}{\partial \bar{\mathbf{C}}} = \sum_{i=1}^{k} w_i \tilde{N}_c \sqrt{bn_c}\, \mathcal{L}^{-1}\left(\frac{\overset{D_i}{\chi}}{\sqrt{bn_c}}\right)\frac{1}{\overset{D_i}{\chi}}(\boldsymbol{D}_i \otimes \boldsymbol{D}_i),\\
\bar{\mathbf{S}}_{pp} &= 2\frac{\partial \Psi_{pp}}{\partial \bar{\mathbf{C}}} = \sum_{i=1}^{k} w_i \tilde{N}_0 \Phi(\overset{D_i}{\lambda}_m)\frac{\mu \xi_i}{\overset{D_i}{\chi}}(\boldsymbol{D}_i \otimes \boldsymbol{D}_i),
\end{aligned} \tag{A.2}$$

where $\mu = \dfrac{1}{1-C^{\mathfrak{p}}}$. Furthermore, the parameter ξ_i is defined by

$$\xi_i = \frac{\bar{R}}{a}\int_{D_A(\overset{D_i}{\lambda}_m)} \hat{P}(n)\mathcal{L}^{-1}\Big(\frac{\overset{D_i}{\lambda}\bar{R}}{abn}\Big)\,dn. \tag{A.3}$$

The standard Newton–Raphson procedure in finite element analysis requires a linearization of the relation between the second Piola–Kirchhoff stress tensor $\bar{\mathbf{S}}$ and the state variables $\bar{\mathbf{C}}$ and Ω. The modified tangent tensor $\bar{\mathbb{C}}$ is formulated by dropping the higher-order terms of the following Taylor expansion:

$$\begin{aligned}\bar{\mathbf{S}}(\bar{\mathbf{C}}+d\bar{\mathbf{C}},\,\Omega+d\Omega) &= \bar{\mathbf{S}}(\bar{\mathbf{C}},\,\Omega)+d\bar{\mathbf{S}}\\ &= \bar{\mathbf{S}}(\bar{\mathbf{C}},\,\Omega)+\frac{\partial\bar{\mathbf{S}}(\bar{\mathbf{C}},\,\Omega)}{\partial\bar{\mathbf{C}}}:d\bar{\mathbf{C}}+\sum_{i=1}^{k}\frac{\partial\bar{\mathbf{S}}(\bar{\mathbf{C}},\,\Omega)}{\partial\overset{D_i}{\lambda}_m}d\overset{D_i}{\lambda}_m+\Theta(d\bar{\mathbf{C}}^2,\,d\overset{D_i}{\lambda}{}^2_m).\end{aligned}$$

Thus, the linearization process yields

$$\begin{aligned}d\bar{\mathbf{S}} &= \frac{\partial\bar{\mathbf{S}}(\bar{\mathbf{C}},\,\Omega)}{\partial\bar{\mathbf{C}}}:d\bar{\mathbf{C}}+\sum_{i=1}^{k}\frac{\partial\bar{\mathbf{S}}(\bar{\mathbf{C}},\,\Omega)}{\partial\overset{D_i}{\lambda}_m}d\overset{D_i}{\lambda}_m=\frac{\partial\bar{\mathbf{S}}(\bar{\mathbf{C}},\,\Omega)}{\partial\bar{\mathbf{C}}}:d\bar{\mathbf{C}}+\sum_{i=1}^{k}\frac{\partial\bar{\mathbf{S}}(\bar{\mathbf{C}},\,\Omega)}{\partial\overset{D_i}{\lambda}_m}\Big(\frac{\partial\overset{D_i}{\lambda}_m}{\partial\bar{\mathbf{C}}}:d\bar{\mathbf{C}}\Big)\\ &= 2\Bigg[\frac{\partial\bar{\mathbf{S}}(\bar{\mathbf{C}},\,\Omega)}{\partial\bar{\mathbf{C}}}+\sum_{i=1}^{k}\frac{\partial\bar{\mathbf{S}}(\bar{\mathbf{C}},\,\Omega)}{\partial\overset{D_i}{\lambda}_m}\odot\frac{\partial\overset{D_i}{\lambda}_m}{\partial\bar{\mathbf{C}}}\Bigg]:\frac{1}{2}\,d\bar{\mathbf{C}},\end{aligned} \tag{A.4}$$

which finally gives $\bar{\mathbb{C}}$ as

$$\bar{\mathbb{C}} = 2\frac{\partial\bar{\mathbf{S}}}{\partial\bar{\mathbf{C}}}+2\sum_{i=1}^{k}\frac{\partial\bar{\mathbf{S}}(\bar{\mathbf{C}},\,\Omega)}{\partial\overset{D_i}{\lambda}_m}\odot\frac{\partial\overset{D_i}{\lambda}_m}{\partial\bar{\mathbf{C}}}. \tag{A.5}$$

In view of (A.1) and (A.5), the first part of the tangent tensor is given by

$$2\frac{\partial\bar{\mathbf{S}}}{\partial\bar{\mathbf{C}}} = 2\frac{\partial\bar{\mathbf{S}}_{cc}}{\partial\bar{\mathbf{C}}}+2\frac{\partial\bar{\mathbf{S}}_{pp}}{\partial\bar{\mathbf{C}}} = \bar{\mathbb{C}}_{cc}+\bar{\mathbb{C}}_{pp}. \tag{A.6}$$

Next, $\bar{\mathbb{C}}_{cc}$ is calculated by using (A.2) as

$$\begin{aligned}\bar{\mathbb{C}}_{cc} &= 2\sum_{i=1}^{k}w_i\tilde{N}_c\sqrt{bn_c}(\boldsymbol{D}_i\otimes\boldsymbol{D}_i)\odot\frac{\partial}{\partial\overset{D_i}{\chi}}\Bigg[\frac{1}{\overset{D_i}{\chi}}\mathcal{L}^{-1}\Big(\frac{\overset{D_i}{\chi}}{\sqrt{bn_c}}\Big)\Bigg]\frac{\partial\overset{D_i}{\chi}}{\partial\bar{\mathbf{C}}}\\ &= \sum_{i=1}^{k}w_i\tilde{N}_c\Delta_i(\boldsymbol{D}_i\otimes\boldsymbol{D}_i)\odot(\boldsymbol{D}_i\otimes\boldsymbol{D}_i),\end{aligned} \tag{A.7}$$

where the parameter Δ_i is written as

$$\Delta_i = -\frac{\sqrt{bn_c}}{\chi_i^3}\beta+\frac{1}{\overset{D_i}{\chi}{}^2}\frac{\beta^2\sinh^2\beta}{\sinh^2\beta-\beta^2}, \tag{A.8}$$

by knowing

$$\frac{d\mathscr{L}^{-1}(y)}{dy} = \frac{1}{d\mathscr{L}(\beta)/d\beta} = \frac{\beta^2 \sinh^2 \beta}{\sinh^2 \beta - \beta^2}.$$

Furthermore, with respect to (A.2), one has for $\bar{\mathbb{C}}_{pp}$:

$$\begin{aligned}\bar{\mathbb{C}}_{pp} &= 2\sum_{i=1}^{k} w_i \tilde{N}_0 \mu \Phi(\overset{D_i}{\lambda}_m)(\boldsymbol{D}_i \otimes \boldsymbol{D}_i) \odot \frac{\partial}{\partial \bar{\mathbf{C}}}\left[\frac{\xi_i}{\overset{D_i}{\chi}}\right] \\ &= \sum_{i=1}^{k} w_i \tilde{N}_0 \mu \Phi(\overset{D_i}{\lambda}_m)\left[-\frac{\xi_i}{\overset{D_i}{\chi}{}^3} + \frac{\mu\gamma_i}{\overset{D_i}{\chi}{}^2}\right](\boldsymbol{D}_i \otimes \boldsymbol{D}_i) \odot (\boldsymbol{D}_i \otimes \boldsymbol{D}_i),\end{aligned} \tag{A.9}$$

where $\gamma_i = d\xi_i / d\overset{D_i}{\lambda}$.

Finally, (A.6) is simplified to

$$2\frac{\partial \bar{\mathbf{S}}}{\partial \bar{\mathbf{C}}} = \sum_{i=1}^{k} w_i \left(\tilde{N}_c \Delta_i + \tilde{N}_0 \mu \Phi(\overset{D_i}{\lambda}_m)\left[-\frac{\xi_i}{\overset{D_i}{\chi}{}^3} + \frac{\mu\gamma_i}{\overset{D_i}{\chi}{}^2}\right]\right)\mathbb{D}_i, \tag{A.10}$$

where $\mathbb{D}_i = (\boldsymbol{D}_i \otimes \boldsymbol{D}_i) \odot (\boldsymbol{D}_i \otimes \boldsymbol{D}_i)$.

For the second term of the tangent tensor, one has

$$\frac{\partial \overset{D_i}{\lambda}_m}{\partial \bar{\mathbf{C}}} = \begin{cases} \dfrac{\partial \overset{D_i}{\lambda}}{\partial \bar{\mathbf{C}}} = \dfrac{\mu}{2\overset{D_i}{\chi}}(\boldsymbol{D}_i \otimes \boldsymbol{D}_i), & \overset{D_i}{\lambda} = \overset{D_i}{\lambda}_m \text{ (in primary loading)}, \\ \mathbf{0}, & \text{(in unloading or reloading)}, \end{cases} \tag{A.11}$$

which consequently gives

$$2\sum_{i=1}^{k} \frac{\partial \bar{\mathbf{S}}(\bar{\mathbf{C}}, \Omega)}{\partial \overset{D_i}{\lambda}_m} \odot \frac{\partial \overset{D_i}{\lambda}_m}{\partial \bar{\mathbf{C}}} = 2\sum_{i=1}^{k} \frac{\partial \bar{\mathbf{S}}(\bar{\mathbf{C}}, \Omega)}{\partial \overset{D_i}{\lambda}_m} \odot \frac{\mu}{2\overset{D_i}{\chi}}(\boldsymbol{D}_i \otimes \boldsymbol{D}_i)\delta(\boldsymbol{D}_i), \tag{A.12}$$

where

$$\delta(\boldsymbol{D}_i) = \begin{cases} 1 & \text{if } \overset{D_i}{\lambda} = \overset{D_i}{\lambda}_m, \\ 0 & \text{if } \overset{D_i}{\lambda} \neq \overset{D_i}{\lambda}_m. \end{cases}$$

Since the second term of the tangent tensor is nonzero just in the case of primary loading, one obtains the following identity based on (A.2):

$$\begin{aligned}\frac{\partial \bar{\mathbf{S}}(\bar{\mathbf{C}}, \Omega)}{\partial \overset{D_i}{\lambda}_m} &= \frac{\partial \bar{\mathbf{S}}_{cc}}{\partial \overset{D_i}{\lambda}_m} + \frac{\partial \bar{\mathbf{S}}_{pp}}{\partial \overset{D_i}{\lambda}_m} = \frac{\partial}{\partial \overset{D_i}{\lambda}_m}\left(w_i \tilde{N}_0 \Phi(\overset{D_i}{\lambda}_m)\frac{\mu\xi_i}{\overset{D_i}{\chi}}(\boldsymbol{D}_i \otimes \boldsymbol{D}_i)\right) \\ &= w_i \tilde{N}_0 \frac{\mu}{\overset{D_i}{\chi}}(\boldsymbol{D}_i \otimes \boldsymbol{D}_i)\left[\Phi(\overset{D_i}{\lambda}_m)\frac{\partial \xi_i}{\partial \overset{D_i}{\lambda}_m} + \xi_i \frac{\partial \Phi(\overset{D_i}{\lambda}_m)}{\partial \overset{D_i}{\lambda}_m}\right].\end{aligned} \tag{A.13}$$

Next, substituting (42) and

$$\frac{\partial \xi_i}{\partial \lambda_m} = -\frac{\upsilon \bar{R}^2}{a^2 b}\hat{P}\left(n_{c-f}(\lambda_m)\right)\mathscr{L}^{-1}\left(\frac{1}{\upsilon}\right), \tag{A.14}$$

into (A.13) gives

$$\frac{\partial \bar{\mathbf{S}}(\bar{\mathbf{C}}, \Omega)}{\partial \overset{D_i}{\lambda}_m} = w_i \tilde{N}_0 \Phi(\overset{D_i}{\lambda}_m)\eta_i \frac{1}{\overset{D_i}{\chi}}(\boldsymbol{D}_i \otimes \boldsymbol{D}_i), \tag{A.15}$$

where

$$\eta_i = -\left(\frac{\upsilon \bar{R}}{ab}\right)^2 \hat{P}\left(n_{c-f}(\overset{D_i}{\lambda}_m)\right)\left[\frac{b}{\upsilon}\mathscr{L}^{-1}\left(\frac{1}{\upsilon}\right) + \xi_i \overset{D_i}{\lambda}_m \Phi(\overset{D_i}{\lambda}_m)\right]. \tag{A.16}$$

Finally, the expanded formulation of the tangent tensor is obtained as

$$\bar{\mathbb{C}} = \sum_{i=1}^{k} w_i \left(\tilde{N}_c \Delta_i + \tilde{N}_o \mu \Phi(\overset{D_i}{\lambda}_m)\left[-\frac{\xi_i}{\overset{D_i}{\chi}{}^3} + \mu \frac{\gamma_i + \eta_i \delta(\boldsymbol{D}_i)}{\overset{D_i}{\chi}{}^2}\right]\right)\mathbb{D}_i. \tag{A.17}$$

Acknowledgments

The authors thank the German Research Foundation (DFG) for their financial support of this work. The experimental part of this study is the result of cooperation with Professor E. Haberstroh (Institute of Rubber Technology, RWTH Aachen University) whose contribution is also gratefully acknowledged.

References

[Aksel and Hübner 1996] N. Aksel and C. Hübner, "The influence of dewetting in filled elastomers on the changes of their mechanical properties", *Arch. Appl. Mech.* **66**:4 (1996), 231–241.

[Arruda and Boyce 1993] E. Arruda and M. Boyce, "A three-dimensional constitutive model for the large stretch behavior of rubber elastic materials", *J. Mech. Phys. Solids* **41**:2 (1993), 389–412.

[Beatty 2003] M. F. Beatty, "An average-stretch full-network model for rubber elasticity", *J. Elasticity* **70**:1-3 (2003), 65–86.

[Bergström and Boyce 1999] J. Bergström and M. Boyce, "Mechanical behavior of particle filled elastomers", *Rubber Chem. Technol.* **72**:4 (1999), 633–656.

[Bouasse and Carrière 1903] H. Bouasse and Z. Carrière, "Courbes de traction du caoutchouc vulcanisé", *Ann. Fac. Sci. Toulouse* (2) **5**:3 (1903), 257–283.

[Bueche 1960] F. Bueche, "Molecular basis for the Mullins effect", *J. Appl. Polym. Sci.* **4**:10 (1960), 107–114.

[Bueche 1961] F. Bueche, "Mullins effect and rubber-filler interaction", *J. Appl. Polym. Sci.* **5**:15 (1961), 271–281.

[Dargazany and Itskov 2009] R. Dargazany and M. Itskov, "A network evolution model for the anisotropic Mullins effect in carbon black filled rubbers", *Int. J. Solids Struct.* **46**:16 (2009), 2967–2977.

[Demirkoparan et al. 2009] H. Demirkoparan, T. J. Pence, and A. Wineman, "On dissolution and reassembly of filamentary reinforcing networks in hyperelastic materials", *Proc. R. Soc. Lond. A* **465**:2103 (2009), 867–894.

[Diani et al. 2006] J. Diani, M. Brieu, and J. Vacherand, "A damage directional constitutive model for Mullins effect with permanent set and induced anisotropy", *Eur. J. Mech. A Solids* **25**:3 (2006), 483–496.

[Diani et al. 2009] J. Diani, B. Fayolle, and P. Gilormini, "A review on the Mullins effect", *Eur. Polym. J.* **45**:3 (2009), 601–612.

[Dorfmann and Ogden 2004] A. Dorfmann and R. Ogden, "A constitutive model for the Mullins effect with permanent set in particle-reinforced rubber", *Int. J. Solids Struct.* **41**:7 (2004), 1855–1878.

[Drozdov and Dorfmann 2001] A. D. Drozdov and A. Dorfmann, "Stress-strain relations in finite viscoelastoplasticity of rigid-rod networks: applications to the Mullins effect", *Contin. Mech. Therm.* **13**:3 (2001), 183–205.

[Ehret et al. 2010] A. Ehret, M. Itskov, and H. Schmid, "Numerical integration on the sphere and its effect on the material symmetry of constitutive equations: a comparative study", *Int. J. Numer. Methods Eng.* **81**:2 (2010), 189–206.

[Elías-Zúñiga and Beatty 2002] A. Elías-Zúñiga and M. F. Beatty, "A new phenomenological model for stress-softening in elastomers", *Z. Angew. Math. Phys.* **53**:5 (2002), 794–814.

[Elías-Zúñiga and Rodríguez 2010] A. Elías-Zúñiga and C. A. Rodríguez, "A non-monotonous damage function to characterize stress-softening effects with permanent set during inflation and deflation of rubber balloons", *Int. J. Eng. Sci.* **48**:12 (2010), 1937–1943.

[Göktepe and Miehe 2005] S. Göktepe and C. Miehe, "A micro-macro approach to rubber-like materials, III: The micro-sphere model of anisotropic Mullins-type damage", *J. Mech. Phys. Solids* **53**:10 (2005), 2259–2283.

[Govindjee 1997] S. Govindjee, "An evaluation of strain amplification concepts via monte carlo simulations of an ideal composite", *Rubber Chem. Technol.* **70**:1 (1997), 25–37.

[Govindjee and Simo 1991] S. Govindjee and J. Simo, "A micro-mechanically based continuum damage model for carbon black-filled rubbers incorporating Mullins' effect", *J. Mech. Phys. Solids* **39**:1 (1991), 87–112.

[Govindjee and Simo 1992] S. Govindjee and J. Simo, "Transition from micro-mechanics to computationally efficient phenomenology: carbon black filled rubbers incorporating Mullins effect", *J. Mech. Phys. Solids* **40**:1 (1992), 213–233.

[Hamed and Hatfield 1989] G. L. Hamed and S. Hatfield, "On the role of bound rubber in carbon-black reinforcement", *Rubber Chem. Technol.* **62**:1 (1989), 143–156.

[Hanson et al. 2005] D. Hanson, M. Hawley, R. Houlton, K. Chitanvis, P. Rae, E. Orler, and D. Wrobleski, "Stress softening experiments in silica-filled polydimethylsiloxane provide insight into a mechanism for the Mullins effect", *Polymer* **46**:24 (2005), 10989–10995.

[Heo and Xu 2001] S. Heo and Y. Xu, "Constructing fully symmetric cubature formulae for the sphere", *Math. Comput.* **70**:233 (2001), 269–279.

[Holt 1932] W. L. Holt, "Behavior of rubber under repeated stresses", *Rubber Chem. Technol.* **5**:1 (1932), 79–89.

[Holzapfel 2000] G. A. Holzapfel, *Nonlinear solid mechanics: a continuum approach for engineering*, Wiley, Chichester, 2000.

[Houwink 1956] R. Houwink, "Slipping of molecules during the deformation of reinforced rubber", *Rubber Chem. Technol.* **29**:3 (1956), 888–893.

[Huntley et al. 1996] H. E. Huntley, A. S. Wineman, and K. R. Rajagopal, "Chemorheological relaxation, residual stress, and permanent set arising in radial deformation of elastomeric hollow spheres", *Math. Mech. Solids* **1**:3 (1996), 267–299.

[Itskov 2009] M. Itskov, *Tensor algebra and tensor analysis for engineers*, 2nd ed., Springer, Dordrecht, 2009.

[Itskov et al. 2006] M. Itskov, E. Haberstroh, A. E. Ehret, and M. C. Vöhringer, "Experimental observation of the deformation induced anisotropy of the Mullins effect in rubber", *Kautsch. Gummi Kunstst.* **59**:3 (2006), 93–96.

[Itskov et al. 2012] M. Itskov, R. Dargazany, and K. Hörnes, "Taylor expansion of the inverse function with application to the Langevin function", *Math. Mech. Solids* **17**:7 (2012), 693–701.

[James and Guth 1943] H. James and E. Guth, "Theory of the elastic properties of rubbers", *J. Chem. Phys.* **11**:10 (1943), 455–480.

[Killian et al. 1994] H. G. Killian, M. Strauss, and D. W. Hamm, "Universal properties in filler-loaded rubbers", *Rubber Chem. Technol.* **67**:1 (1994), 1–16.

[Mark and Erman 2007] J. E. Mark and B. Erman, *Rubberlike elasticity: a molecular primer*, 2nd ed., Cambridge University Press, Cambridge, 2007.

[Miehe and Keck 2000] C. Miehe and J. Keck, "Superimposed finite elastic-viscoelastic-plastoelastic stress response with damage in filled rubbery polymers: experiments", *J. Mech. Phys. Solids* **48**:2 (2000), 323–365.

[Mullins and Tobin 1957] L. Mullins and N. R. Tobin, "Theoretical model for the elastic behavior of filler-reinforced vulcanized rubbers", *Rubber Chem. Technol.* **30**:2 (1957), 555–571.

[Mullins and Tobin 1965] L. Mullins and N. R. Tobin, "Stress softening in rubber vulcanizates, I: Use of a strain amplification factor to describe the elastic behavior of filler-reinforced vulcanized rubber", *J. Appl. Polym. Sci.* **9**:9 (1965), 2993–3009.

[Pawelski 2001] H. Pawelski, "Softening behavior of elastomeric media after loading in changing directions", pp. 27–36 in *Constitutive models for rubber, II: Proceedings of the Second European Conference* (*ECCMR*) (Hannover, 2001), edited by D. Besdo et al., Balkema, Lisse, 2001.

[Puso 2003] M. Puso, *Mechanistic constitutive models for rubber elasticity and viscoelasticity*, Ph.D. thesis, University of California, Davis, CA, 2003, Available at http://e-reports-ext.llnl.gov/pdf/243854.pdf.

[Rajagopal and Wineman 1992] K. R. Rajagopal and A. S. Wineman, "A constitutive equation for nonlinear solids which undergo deformation induced microstructural changes", *Int. J. Plast.* **8**:4 (1992), 385–395.

[Rault et al. 2006] J. Rault, J. Marchal, P. Judeinstein, and P. Albouy, "Stress-induced crystallization and reinforcement in filled natural rubbers: 2H NMR study", *Macromolecules* **39**:24 (2006), 8356–8368.

[Simo 1987] J. Simo, "On a fully three-dimensional finite-strain viscoelastic damage model: formulation and computational aspects", *Comput. Methods Appl. Mech. Eng.* **60**:2 (1987), 153–173.

[Treloar 2005] L. R. G. Treloar, *The physics of rubber elasticity*, 3rd ed., Oxford University Press, New York, 2005.

[Wineman and Rajagopal 1990] A. S. Wineman and K. R. Rajagopal, "On a constitutive theory for materials undergoing microstructural changes", *Arch. Mech. Stos.* **42**:1 (1990), 53–75.

[Zimmermann and Wineman 2005] M. Zimmermann and A. Wineman, "On the elastic behavior of scission materials", *Math. Mech. Solids* **10**:1 (2005), 63–88.

Received 12 Jun 2012. Revised 10 Oct 2012. Accepted 16 Oct 2012.

ROOZBEH DARGAZANY: roozbeh@mit.edu
Department of Materials Science and Engineering, Massachusetts Institute of Technology, 77 Massachusetts Avenue, Room 12002, Cambridge, MA 02139, United States

and

Department of Continuum Mechanics, RWTH Aachen University, Kackertstraße 9, 52072 Aachen, Germany

VU NGOC KHIÊM: vu@km.rwth-aachen.de
Department of Continuum Mechanics, RWTH Aachen University, Kackertstraße 9, 52072 Aachen, Germany

UWE NAVRATH: navrath@km.rwth-aachen.de
Department of Continuum Mechanics, RWTH Aachen University, Kackertstraße 9, 52072 Aachen, Germany

MIKHAIL ITSKOV: itskov@km.rwth-aachen.de
Department of Continuum Mechanics, RWTH Aachen University, Kackertstraße 9, 52072 Aachen, Germany

SUBMISSION GUIDELINES

ORIGINALITY

Authors may submit manuscripts in PDF format online at the Submissions page. Submission of a manuscript acknowledges that the manuscript is original and has neither previously, nor simultaneously, in whole or in part, been submitted elsewhere. Information regarding the preparation of manuscripts is provided below. Correspondence by email is requested for convenience and speed. For further information, write to one of the Chief Editors:

Davide Bigoni	bigoni@ing.unitn.it
Iwona Jasiuk	ijasiuk@me.concordia.ca
Yasuhide Shindo	shindo@material.tohoku.ac.jp

LANGUAGE

Manuscripts must be in English. A brief abstract of about 150 words or less must be included. The abstract should be self-contained and not make any reference to the bibliography. Also required are keywords and subject classification for the article, and, for each author, postal address, affiliation (if appropriate), and email address if available. A home-page URL is optional.

FORMAT

Authors can use their preferred manuscript-preparation software, including for example Microsoft Word or any variant of TEX. The journal itself is produced in LATEX, so accepted articles prepared using other software will be converted to LATEX at production time. Authors wishing to prepare their document in LATEX can follow the example file at www.jomms.net (but the use of other class files is acceptable). At submission time only a PDF file is required. After acceptance, authors must submit all source material (see especially Figures below).

REFERENCES

Bibliographical references should be complete, including article titles and page ranges. All references in the bibliography should be cited in the text. The use of BibTEX is preferred but not required. Tags will be converted to the house format (see a current issue for examples); however, for submission you may use the format of your choice. Links will be provided to all literature with known web locations; authors can supply their own links in addition to those provided by the editorial process.

FIGURES

Figures must be of publication quality. After acceptance, you will need to submit the original source files in vector format for all diagrams and graphs in your manuscript: vector EPS or vector PDF files are the most useful. (EPS stands for Encapsulated PostScript.)

Most drawing and graphing packages—Mathematica, Adobe Illustrator, Corel Draw, MATLAB, etc.—allow the user to save files in one of these formats. Make sure that what you're saving is vector graphics and not a bitmap. If you need help, please write to graphics@msp.org with as many details as you can about how your graphics were generated.

Please also include the original data for any plots. This is particularly important if you are unable to save Excel-generated plots in vector format. Saving them as bitmaps is not useful; please send the Excel (.xls) spreadsheets instead. Bundle your figure files into a single archive (using zip, tar, rar or other format of your choice) and upload on the link you been given at acceptance time.

Each figure should be captioned and numbered so that it can float. Small figures occupying no more than three lines of vertical space can be kept in the text ("the curve looks like this:"). It is acceptable to submit a manuscript with all figures at the end, if their placement is specified in the text by means of comments such as "Place Figure 1 here". The same considerations apply to tables.

WHITE SPACE

Forced line breaks or page breaks should not be inserted in the document. There is no point in your trying to optimize line and page breaks in the original manuscript. The manuscript will be reformatted to use the journal's preferred fonts and layout.

PROOFS

Page proofs will be made available to authors (or to the designated corresponding author) at a Web site in PDF format. Failure to acknowledge the receipt of proofs or to return corrections within the requested deadline may cause publication to be postponed.

Journal of Mechanics of Materials and Structures

Volume 7, No. 8-9 October 2012